Cryogenic Heat Pipe for Cooling High Temperature Superconductors with Application to Electromagnetic Formation Flight Satellites

by

Daniel W. Kwon

S.B. Aeronautics and Astronautics, MIT 2002
S.B. Electrical Engineering and Computer Science, MIT 2002
S.M. Aeronautics and Astronautics, MIT 2005

SUBMITTED TO THE DEPARTMENT OF AERONAUTICS AND ASTRONAUTICS
IN PARTIAL FULLFILLMENT OF THE DEGREE OF
DOCTOR OF PHILOSOPHY IN AERONAUTICS AND ASTRONAUTICS
at the
MASSACHUSETTS INSTITUTE OF TECHNOLOGY
June 2009

Signature of Author..
Department of Aeronautics and Astronautics
February 1, 2009

Certified by..
Raymond J. Sedwick
Department of Aerospace Engineering, University of Maryland
Thesis Advisor

Certified by..
David W. Miller
Department of Aeronautics and Astronautics
Thesis Committee Chairman

Certified by..
John Brisson
Department of Mechanical Engineering

Accepted by..
David L. Darmofal
Department of Aeronautics and Astronautics
Chairman, Committee for Graduate Students

Cryogenic Heat Pipe for Cooling High Temperature Superconductors with Application to Electromagnetic Formation Flight Satellites

by

Daniel W. Kwon

Submitted to the Department of Aeronautics and Astronautics
on February 1, 2009 in partial fulfillment of the
requirements for the degree of
Doctor of Philosophy in Aeronautics and Astronautics
in the field of Space Systems

ABSTRACT

An emerging method of propellant-less formation flight propulsion is the use of electromagnets coupled with reaction wheels. This technique is called Electromagnetic Formation Flight (EMFF). In order to create a large magnetic field necessary for actuating formation flying spacecraft, EMFF uses high temperature superconducting (HTS) wire since it is able to carry a large current at low power. To achieve superconductivity, the HTS wire needs a cryogenic thermal control system to maintain the wire temperature below the critical temperature and this temperature must be maintained over the entire EMFF coil, which could be as large as two meters in diameter. For commercially available HTS wire, this critical temperature is 110 K. Since EMFF obviates the need for consumables for formation flying maneuvers, the thermal system must also be consumable-free.

The research in this thesis investigates a consumable-free method of maintaining isothermalization for a large scale HTS coil. The HTS coil resides inside a thermally conductive jacket which is used for isothermalization. A cryocooler is attached to the thermally conductive jacket and is used for heat extraction. Wrapped around the thermally conductive jacket is multilayer insulation which is used to reduce the heat load into the HTS coil. This thermal system has the ability to maintain constant temperature in the presence of a rapidly changing thermal environment, such as low Earth orbit. Both a solid conductor and a heat pipe were investigated for use as the thermally conductive jacket. Finite difference models were developed to model a single coil in space and a coil inside a vacuum chamber.

In addition, the research in this thesis investigates the design, operation, and testing of a cryogenic heat pipe. The heat pipe uses nitrogen as a working fluid and a stainless steel mesh as the wicking structure. As a proof of concept, an 86 cm long heat pipe was constructed as the thermally conductive jacket enclosing the HTS wire. The working fluid, at saturation condition, maintains a constant temperature below the HTS wire critical temperature. Testing of the heat pipe in a vacuum chamber was conducted to verify the power capacity of the heat pipe. Verifying the proof of concept cryogenic heat pipe led to construction of a full scale circular heat pipe for testing in a two meter diameter toroidal vacuum chamber. This system also achieved saturation condition and showed the potential for HTS cooling. The experiments in this thesis demonstrate the feasibility of operating large HTS coils for future formation flying missions.

Thesis Supervisor: Raymond J. Sedwick
Title: Assistant Professor of Aerospace Engineering

ACKNOWLEDGEMENTS

I'd like to thank Ray Sedwick and Dave Miller for their help supporting me for many years. Their tireless efforts are sincerely appreciated. Working for them has been a privilege and a pleasure throughout the years. I'd also like to thank John Brisson for being on my committee and providing useful feedback. Additional sources of wisdom and mentoring were provided by Edmund Kong and Alvar Saenz-Otero. I've learned a lot from everyone.

Technical assistance came from all corners. The solid foundation for any SSL project is Paul Bauer, and this research was no exception. The toroidal vacuum chamber was built by Stephan Pretorius and Payload Systems. This project alone was an amazing accomplishment. Tony Busalacchi helped provide vacuum chamber feedthroughs and assisted the heat pipe construction. Several UROPs helped with the EMFF testbed, including Amado DeHoyos, Dawn Wheeler, Kevin Liu, and Victoria Stolyar.

Sharon Brown and Marilyn Good deserve a special shout-out. Thanks for making things happen in the SSL.

I'd like to thank members of the EMFF team throughout the years: Laila Elias, Sam Schweighart, Umair Ahsun, Jaime Ramirez, Matt Neave, Aya Sakaguchi, Sang-il Lee and Dr. Kong. Propellant-less formation flight is not an easy topic. I think we have all done some pretty revolutionary and exciting things.

Graduate school has been a rewarding and fun time thanks to all members of the SSL. Web gem nominees go to all of those who have played and supported Aero/Astro sports. MVP awards go to the Tom McGuire, Carl Dietrich, the 2004 Red Sox, and Ryan Lang, who has raced through MIT with me since we first met in concert band over 10 years ago.

Finally, I'd like to thank my parents Hee-min and Sue and sister Sabina. Following in my parents' footsteps, I'm now proud of finishing the unwritten Kwon family rule: "get an advanced degree." But seriously, the best part of family is having a gifted and caring sibling who is making the world a better place.

Formation flying using only one satellite is a lonely business. I'd like to thank my wife Alicia for her love and support, again proving that life is better in pairs.

TABLE OF CONTENTS

LIST OF FIGURES

LIST OF TABLES

Chapter 1 Introduction

An increasing number of missions are considering multiple spacecraft flying in close proximity to replace traditional large monolithic space systems. Formation flying space interferometers are one example of this application. NASA's Terrestrial Planet Finder Interferometer and ESA's Darwin mission have the goal of directly detecting Earth-like planets in other solar systems. Both systems utilize multiple free-flying satellites in formation to perform as a nulling interferometer [1, 2]. A second example of the concept of replacing a large satellite with smaller entities is used by Darpa in their F6 program. The F6 program stands for Future, Flexible, Fast, Fractionated, Free-Flying Spacecraft united by Information eXchange [3]. F6 plans to demonstrate that a large satellite can be divided up into separate functional modules, whereby the new fractionated spacecraft has benefits such as launch flexibility, improved robustness from failures or attacks, and improved upgradeability.

One of the challenges for formation flying systems is that the amount of propellant available puts a constraint on mission lifetime and ΔV capabilities. An emerging method of propellant-less formation flight propulsion is the use of electromagnets coupled with reaction wheels. This technique is called Electromagnetic Formation Flight (EMFF). The system is powered by the Sun through solar arrays, meaning a satellite is no longer reliant on propellant for formation flying maneuvers. Reducing a satellite's dependence on propellant can change current design methods for future spacecraft formations. For example, the amount of propellant required is currently determined using the rocket equation and typically the ΔV required for formation flying is a parameter used in the calculation. For propellant-based systems, one method of minimizing propellant mass is to reduce the formation flying ΔV. Since EMFF is propellant-less, the rocket equation is not used. Therefore, by using EMFF, the formation flight propulsion system can be based on the desired formation performance, without any fuel constraints. As a result, EMFF opens up new capabilities for satellite formations that might have had ΔV requirements that before were too costly in terms of propellant to even consider. Another advantage of EMFF over traditional propellant-based thrusters is the elimination of impinging thruster plumes, which can cause ablation of nearby spacecraft surfaces and produce unwanted vibration excitation [4]. Applications of EMFF are not just restricted to stationkeeping fractionated spacecraft architectures or maintaining sparse aperture systems. The Electromagnetic (EM) coils can be used with multi-role functionality, such as power transmission, torque for slew control, or for passive offensive or defensive capabilities in military satellites [5, 6].

To implement EMFF, an EM dipole is created by running current through an electromagnetic coil. A conceptual drawing of an EMFF vehicle is shown in Figure 1.1. The EM dipole creates coupled forces and torques on nearby satellites which also have at least one EMFF coil. A satellite with three orthogonal coils can create a steerable dipole in three dimensions. Similarly, a set of three orthogonal reaction wheels are necessary to de-couple the forces and torques in three dimensions. Consequently, the EM coils in concert with reaction wheels allow for all the necessary actuation in relative degrees of freedom for a formation flight array [7]. An example of the forces and torques created by two EMFF vehicles are shown in Figure 1.2.

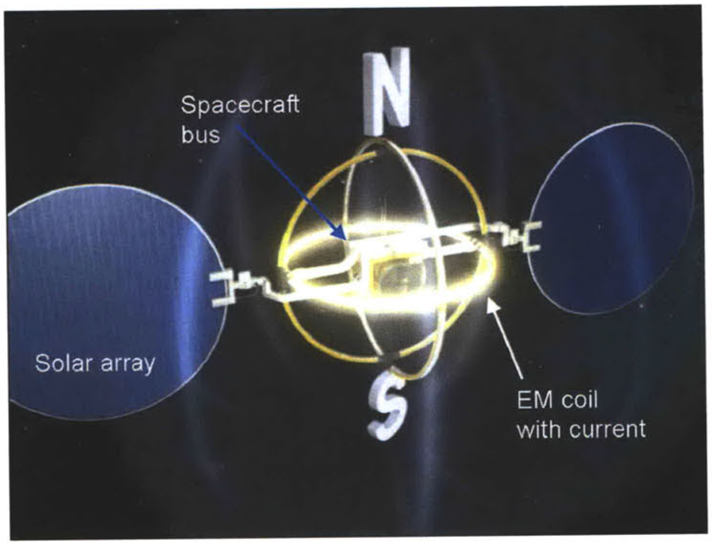

Figure 1.1 Conceptual drawing of an EMFF vehicle

The force between two vehicles with their dipole orientations axially aligned, such as in a repulsion configuration shown in Figure 1.2, is given by

$$F = \frac{3}{2\pi}\mu_o\frac{\mu_1\mu_2}{d^4} \tag{1.1}$$

where d is the separation distance between the vehicles and μ_o is the permeability of free space. The magnetic dipole for each vehicle is μ and is a function of the current (i), number of current loops (n), and the radius of the coil (R_c):

$$\mu = ni\pi R_c \tag{1.2}$$

In order to create a large magnetic moment to generate large forces, coils that can carry a large current and are large in size are favorable for EMFF.

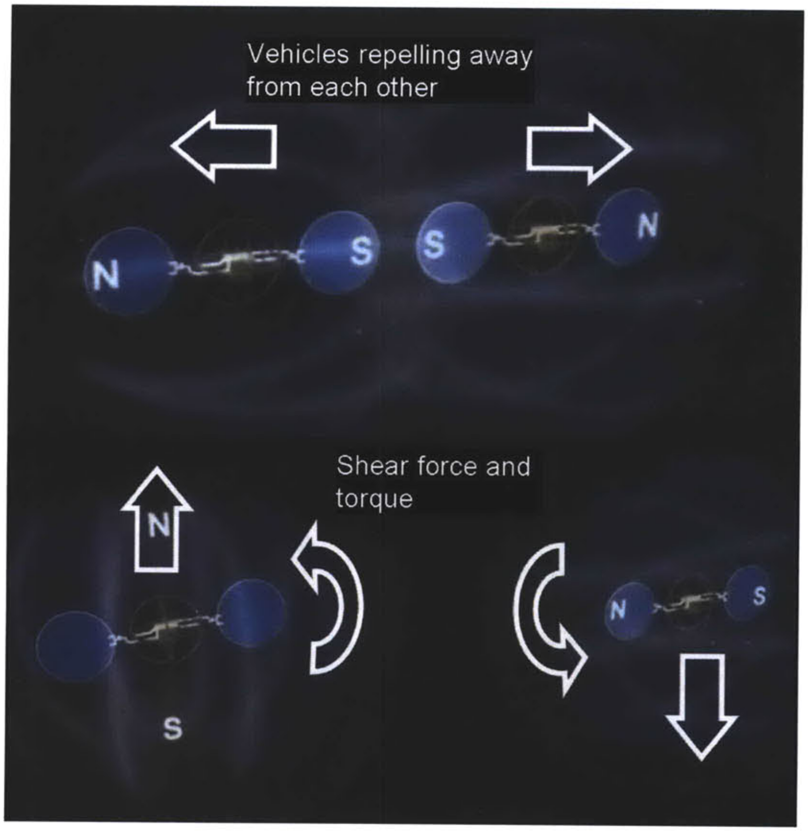

Figure 1.2 Example of forces and torques created by two EMFF vehicles

The high temperature superconducting (HTS) wire is an enabling technology for EMFF because it allows the creation of a large dipole moment. One of the challenges of using HTS is maintaining the cold temperature necessary for operation. The entire length of the superconducting wire must be maintained below a critical temperature in order for it to operate at superconducting levels. Commercial-off-the-shelf (COTS) wire from American Superconductor has a critical temperature, $T_{critical}$, of 110 K [8]. For EMFF satellites in the proximity of Earth, such as LEO or GEO, heat flux from the Sun and Earth needs to be rejected in order to maintain temperatures below $T_{critical}$. This heat flux has the potential to rapidly change in both magnitude and direction, depending on the satellites' orientation. Heat into the coils can be rejected using cryocoolers and various types of insulation such as Multilayer Insulation (MLI). One characteristic of the HTS wire is that at colder temperatures more current can be driven through the wires creating a larger dipole field and thus improving the performance of EMFF. However, this benefit comes at the expense of additional power and mass required by the thermal system. In addition to this coupled behavior, the thermal system must also be consumable-free since EMFF obviates the need for consumables for formation flying maneuvers. The EMFF thermal system is a unique problem in the topic of cooling large space structures without the use of consumables.

1.1 Current State of EMFF

In order to develop the necessary technology for EMFF, development of a ground EMFF testbed by the MIT Space Systems Laboratory (MIT-SSL) started in 2002 by an undergraduate design and build course. Two EMFF testbed vehicles were built, each with two coils allowing for a steerable dipole in two dimensions. The coils were made from Bi-2223 HTS wires from American Superconductor and have a diameter of approximately 80 cm. The EMFF testbed used a reservoir of liquid nitrogen (LN2) to cool the HTS coils. This first version of the EMFF testbed, built by the undergraduate course, used a gravity-fed LN2 reservoir and is shown in Figure 1.3a.

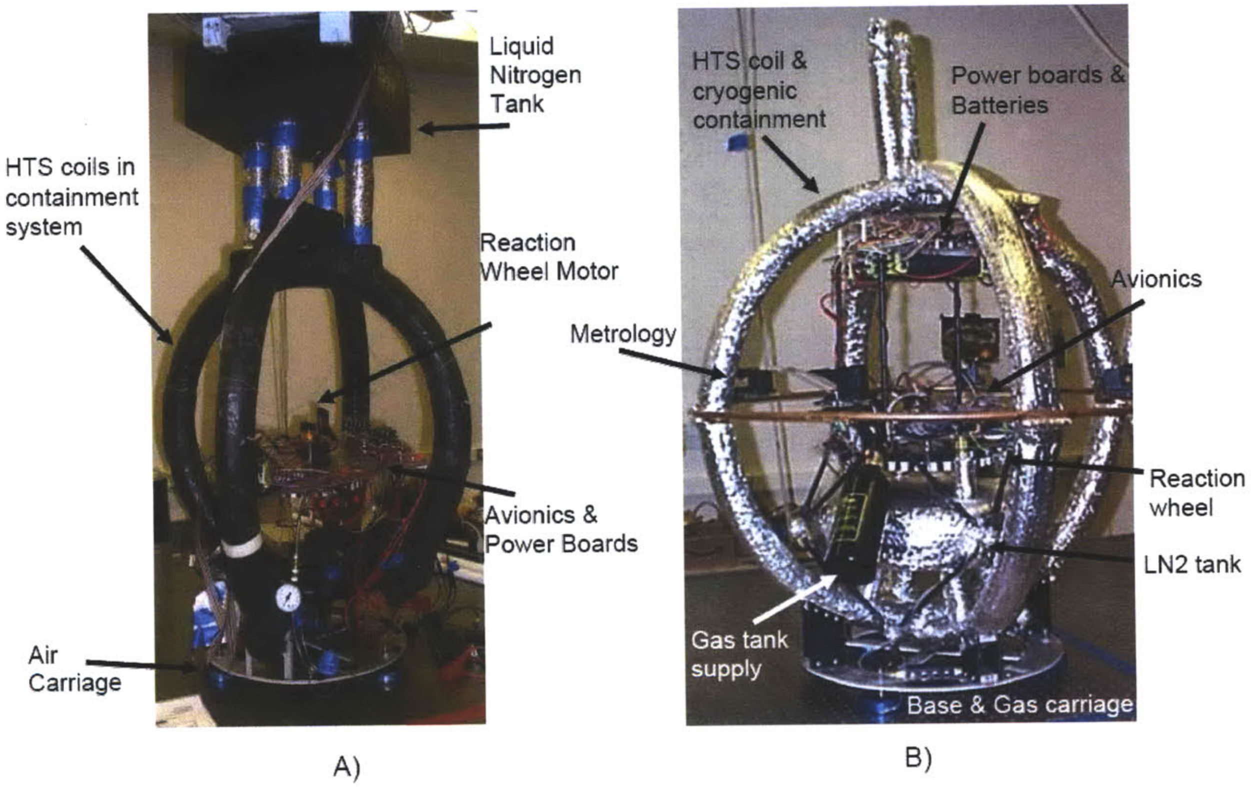

Figure 1.3 EMFF testbed with gravity-fed LN2 reservoir (A); testbed with pressurized LN2 reservoir (B)

For the first version of the testbed the source of cryogen was located above the HTS coil and flowed into the coil container replacing any boiloff. There were two problems with the design. First, the boiloff and liquid cryogen shared the same flow path making it difficult to determine how much liquid cryogen was actually inside the coil container cooling the HTS. Secondly, thermal cycling of the coil container led to cracking in the Styrofoam containment material and epoxy joints. Improvements to the thermal system were implemented in the second version of the EMFF testbed built by Kwon and Neave and is shown in Figure 1.3b [5, 9]. A coil container made of copper housed the HTS coils and contained the liquid nitrogen. A pressurized LN2 tank fed the LN2 from the bottom of the coils and maintained cryogen throughout the entire coil. Excess LN2 and boiloff were vented from the top of the vehicle via chimneys. The new thermal design on the testbed has allowed for the amount of cryogen in the system to be more accurately determined and has eliminated any problems associated with leaking cryogen.

Past research on a flight version of the thermal system determined that a cryocooler was necessary for heat extraction and COTS cryocoolers had the ability to extract the tens of watts necessary for steady-state cooling. In addition, a comparison of insulation systems consisting of a vacuum gap or aerogel was conducted in both LEO and in Earth-trailing orbit, which is outside of the Earth's heating environment. A quick summary of these details will also be discussed in Chapter 2.

In addition to developing the EMFF thermal system there are several other challenges to bringing EMFF to a flight-like state. These include the power system, magnetic shielding, and dynamics and control. The power system for EMFF supplies the high current for the HTS wires. A high current, low voltage and low power H-bridge design for the power circuit has been demonstrated on the EMFF testbed using COTS electronics components. The re-built EMFF testbed uses three D-cell batteries to supply 100 amps to a coil and the entire power system for two coils requires less than 100 Watts.

A large part of the EMFF research conducted by the MIT-SSL has been the dynamics and control of EMFF satellites. Control of EMFF satellites is challenging because of the coupled nature of the electromagnetics and the non-linearity of the EM force with distance. In LEO, the dynamics and control of an EMFF satellite are affected by the variation in the magnetic field and the J2 perturbation [10]. Non-linear controllers operating in real-time have the potential to burden the avionics system. Past research has investigated the dynamics and control for EMFF arrays in LEO and experimentally validated linear control techniques on the testbed [7]. Current EMFF research at MIT also includes examining control of n-vehicle arrays, non-linear controllers on the testbed, and use of smaller scale EMFF coils using conventional conductors for microsatellites [11, 12].

A concern that is commonly asked about EMFF is the effect the magnetic fields have on electronics. Kwon investigated the effect of the testbed coils on GPS avionics [5]. It was determined that the maximum field strength of the testbed, approximately 50 Gauss, did not affect the signal strength received by the GPS antenna and receiver. However, the effect of larger flight sized coils operating at possibly higher field strengths is unknown. To shield the avionics it has been suggested to enclose any sensitive electronic equipment in a box made of mu-metal to act as a sort of magnetic Faraday cage.

A group in Japan at the University of Tokyo and JAXA has also been independently researching the EMFF concept. The Japanese team has performed preliminary trade studies and dynamics and control simulations for two EMFF satellites in LEO [13]. In addition, a group at the Polish Academy of Sciences extended the two vehicle non-linear controller developed by Elias to a three vehicle linear array and a three vehicle triangular array [7, 14]. A sister technology to EMFF that has been investigated by Michigan Technological University is the use of Coulomb forces from charged spacecraft for formation flight propulsion [15]. Unfortunately this system is not capable of producing spacecraft torques or shear motions, degrees of freedom that are achievable using EMFF. The EMFF testbed at the MIT-SSL is the only known testbed for propellant-less formation flying using electromagnetics.

1.2 Research Objectives and Approach

The goal of this thesis is to develop a renewable method of cooling large space structures, such as the HTS coils used for EMFF, which can maintain uniform cryogenic temperatures across large one-dimensional structures operating in orbits where the thermal environment is characterized by time varying sources with substantial heat flux, such as Earth IR and solar reflection and eclipse. There are three challenges of this problem statement that are important.

First, a renewable method of cooling means that the thermal design must not be reliant on consumables, such as onboard cryogens. Both the method of extracting heat from the system and the distribution of heat should be consumable-free. On the testbed, the coils are immersed in a bath of liquid nitrogen to maintain a continuous temperature of 77 K. Liquid nitrogen is used on the testbed because it operates in a room temperature, one atmosphere environment where conduction and gravity-induced convection make thermal control a challenge. EMFF in LEO will face a high thermal flux environment, but the vacuum allows for other thermal management techniques such as MLI, heat pipes, and cryocoolers. More importantly, the use of liquid nitrogen on the testbed is not trace-able to a flight design because the liquid nitrogen is a consumable. Since one of the benefits of EMFF is to replace consumables the design of the thermal system must be self-contained. An active cooling system, such as a cryocooler, powered by solar arrays meets the requirements for a heat extraction method.

The second challenge of the problem is the scale of the thermal design since the HTS coils potentially can be as large as two meters in diameter. This eliminates devices intended for cooling concentrated point heat sources, such as detectors on space telescopes, and focuses the problem on distributed cooling techniques. It is important to maintain isothermalization of the coil, meaning that minimal temperature gradients exist across the entire coil because the warmest point in the coil will limit the performance of the HTS wire. The research in this thesis investigates locating the HTS wire inside a cryogenic heat pipe as a means of maintaining isothermalization. The research will also compare the performance of a cryogenic heat pipe with other consumable-free designs such as a solid conductor.

The third challenge of keeping the EMFF HTS coils at cryogenic temperatures is the constantly changing heating environment in Earth orbit. Because of the rapidly changing orientation of the vehicles heat from the Earth and Sun are not constant with respect to time or direction. For this reason sun shields are not practical for EMFF.

In summary, the objective of the research is to develop a flight-like design for an EMFF spacecraft concentrating on the implementation of the consumable-free cryogenic thermal control of the HTS coils. The core hypothesis of the thesis is that a consumable-free method of maintaining cryogenic temperatures for a large scale HTS coil that is independent of orbit exists using a cryogenic heat pipe, by which isothermalization of the coil is maintained by locating the HTS wire inside the vapor space of the heat pipe.

To accomplish the research objective the first task is to understand the scale of the thermal problem by developing simulation models. Insight can be gained by modeling a solid conductor with and without MLI to determine temperature performance of a system without working fluid, the effect of insulation, and the amount of heat into the system. In order to gain confidence in the simulation models, experimental testing is conducted. Also by testing in a vacuum chamber environment that has a heat flux greater than low Earth orbit gives confidence that the system will work in space. To determine the benefits of operating a system with working fluid, a heat pipe is designed and constructed. First, a proof-of-concept straight heat pipe is built to verify modeling and master the manufacturing process. Next, HTS wire is inserted into the straight heat pipe to demonstrate the ability of the thermal design to cool HTS. Finally, a circular heat pipe is designed and built to demonstrate the ability to cool a large scale HTS coil. Once the cooling methods, heat distribution, and heat rejection methods are modeled and experimentally verified, the thermal design can be migrated to a flight version with high confidence.

1.3 Literature Review

EMFF is just one application where superconducting wire was found to be an enabling technology. MRI machines in hospitals, particle accelerators, interplanetary propulsion concepts such as the VASIMR [16], nuclear fusion experiments, and future electrical power transmission systems all incorporate superconducting wires. Superconducting technology allows the ability to create large magnetic fields and carry high currents all without any cost in wire resistance. Of course, the cost of using superconductors is the cryogenic system necessary to allow materials into a superconducting state. The subject of cryogenics is best summarized by Dr. Steven Van Sciver of the National High Magnetic Field Laboratory [17]:

> “Cryogenics is a necessary but often undesirable part of a superconducting system because it increases cost, reduces reliability, and increases complexity.”

The task of the thermal design in this thesis, and in any superconducting system, is to minimize the costs incurred by the cryogenic system so that the full benefits of using superconducting wire can be realized.

1.3.1 Cryogenic Systems

Superconducting devices need refrigeration to overcome two sources of heat loading. The first is any heat leaking into the system from the surrounding environment. The second is any internal heat generation in the device. This could be from non-superconducting splices, leads, or AC losses [18]. AC losses are the result of induced time-varying electric fields in the normal-state regions of HTS wires, which lead to the occurrence of Joule dissipation. The time-varying electric field is caused by a time-varying magnetic field, which is the result of a time-varying current through the wire. In addition, a refrigeration device is needed to bring the superconductor from ambient to low temperature in a reasonable length of time. Currently, there are three main methods for cooling a superconducting magnet.

The most common method is immersing the magnet in a liquid cryogen by which heat is extracted by evaporation of the liquid. A common method of achieving an isothermal bath is to use liquid nitrogen or liquid Helium (LHe). Selection of a cryogen depends on the required operating temperature. Early high field metallic superconductors such as NbTi ($T_{critical}$ = 9 K) used LHe, which has a normal boiling point (NBP) of 4.2 K [17]. Recent developments of HTS wire allows the use of LN2 (NBP = 77 K), which is significantly cheaper than LHe. A limitation of using cryogens is that they have a narrow operating temperature which is restricted by the cost and suitability of available cryogens. More importantly, for space applications, the amount of cryogen available limits the lifetime of the superconducting device. Once the cryogen has evaporated it must be replenished making it a mission life limiting consumable. A common example of bath cooling is MRI magnets in hospitals and research facilities. MRI machines have very little evidence of cryogenics and typically only require annual service to top off liquid cryogen.

The second method for cooling superconducting magnets is to integrate the magnet with a closed cycle refrigeration system or cryocooler to circulate the cryogen to the magnet. This method is similar to bath cooling because the magnet is also ‘wet’, meaning that it is in direct contact with a liquid cryogen surrounding the magnet containment vessel. Heat is removed at a liquefier or refrigerator located outside the magnet vessel. The difference with bath cooling is that there is a refrigeration cycle that recovers the vapor and returns liquid to the magnet. A common example is the recuperative Collins refrigeration cycle, which uses a steady flow of Helium through refrigerator components, such as a compressor, heat exchangers, and expansion engines, to deliver liquid cryogen to the magnet [17]. Types of cryocoolers that have been used in these superconducting systems include pulse tube refrigerators, Gifford-McMahon cryocoolers, Stirling coolers, and Joule-Thomson coolers [19, 20]. Examples of closed cycle refrigeration systems are seen in high energy particle accelerator laboratories and nuclear fusion experiments. The disadvantages of using a closed cycle refrigeration system are that they can be capital intensive and require considerable technical support [17].

The third method for cooling superconducting magnets is conduction cooling a magnet in direct contact with a cryocooler, which extracts heat. In this method the magnet is 'dry' or cryogen-free. Cryogen-free magnets are an emerging method because of advances in cryocooler technology and the development of high temperature superconducting current leads. Dry magnets are beneficial because they are free of consumables, easy to operate and maintain, and make the magnet's cryogenic system less visible [18]. There are numerous challenges to designing a dry magnet system. The magnet must be extremely well insulated, which can potentially limit the size, operating current, and cool down time. In addition, dry magnets are inherently unstable due to the small heat capacity at low temperatures, especially for low temperature superconductors (LTS). There is no thermal storage capacity to allow for continued operation if the cryocooler fails. Reliability can be increased using multiple components, such as cold heads or compressors, but this solution takes up time, mass, and power. Therefore dry magnets must be very careful to minimize AC loss or other thermal disturbances that might induce quench. A quench is the process of a superconducting coil entering the normal or resistive state and can lead to rapid loss of superconductivity. Kopera designed an example of a small HTS magnet cooled by a single-stage cryocooler [21]. The magnet used HTS tapes based on the Bi-2223 material, which are similar to the EMFF testbed HTS wires. However, the magnet size is considerably smaller; its magnets were HTS "pancake" coils with a 5 cm inner diameter, and a 9.8 cm outer diameter.

There are also emerging hybrid methods of cooling. An example is MRI machines that use a cryocooler to recondense LHe boiloff [17]. Also some dry LTS magnets have used a small liquid Helium reservoir to increase thermal stability [22].

The thermal system in this thesis is a new type of hybrid approach. It uses a cryocooler to extract heat and a cryogenic heat pipe as the magnet vessel. Inside the magnet vessel, the HTS wire is not 'wet' since it is not in a bath of cryogen, but it is also not 'dry' since it is not conduction cooled. Instead it is vapor cooled by the working fluid. In addition, circulation of the working fluid or cryogen occurs passively inside the heat pipe, which is different from some closed refrigeration systems. There are several benefits to the hybrid system in this thesis. First, by using a cryocooler the lifetime of the system is not limited by stored cryogens. This is an advantage over bath cooling, which was the first method for cooling superconducting magnets discussed in this section. Second, the distribution of working fluid inside the heat pipe occurs passively and requires no active mechanical process or moving parts. This system is easier to maintain in space and is a benefit over the second method mentioned in this section. Lastly, the working fluid increases the thermal storage capacity of the entire cryogenic magnet system and avoids the thermal stability problems of purely 'dry' magnets, which were part of the third method. In summary, the hybrid approach is able to avoid limitations of each of the three conventional methods of cooling superconductors.

1.3.2 Related Flight Cryogenic Systems

Current and future space missions such as space telescopes and particle detectors require cryogenic components to cool devices. The Spitzer space telescope has a cryostat for its detector instruments. The cryogen tank contains 360 liters of superfluid Helium and has an expected lifetime of five years [23]. Past Helium cooled payloads include the Infrared Astronomical Satellite (IRAS) in 1983, Cosmic Background Explorer (COBE) in 1989, Superfluid Helium On-Orbit Transfer Flight Demonstration (SHOOT) in 1993, and the Infrared Space Observatory (ISO) in 1995 [24]. These missions had inventories of Helium as large as 2,300 L. The future Alpha Magnetic Spectrometer (AMS-02) experiment plans to have a He inventory of 2,500 L and is launched cold [24]. The James Webb Space Telescope (JWST) uses a deployable spacecraft sun shield to block heat from the Sun, Earth, and Moon [25]. In order to reduce the heat load, the planned orbit for JWST is ESL2, the second Lagrange point of the Earth-Sun system. Sun shields are a passive method of cooling devices in space, but there are also some disadvantages. Since the telescope is thermally 'open' there are straylight issues from two sources. There is light from celestial sources outside the field of view and thermal emission of the telescope and surrounding surfaces which can enter the detector [26]. While many space observatories demonstrate operation of cryogenic systems in space, many rely on consumables and JWST's system relies on a specific orbit. Therefore no current or future mission contains complete cryogenic thermal control systems that are applicable to EMFF operating Earth orbit. However, there are some various component technologies that are useful.

The main components of the EMFF HTS thermal system include the cryocooler and a cryogenic heat pipe. One benefit of these various cryogenic cooling technologies is that they have been demonstrated in space. An example of a cryocooler is one that has flown on the Hubble Space Telescope as part of the Creare NICMOS Cooling System [27]. In addition, Sunpower Inc. has flown their M77 cryocooler on the RHESSI mission in 2002 and Ball Aerospace flew a Joule-Thomson cryocooler on STS-85 in 1997 [28]. The Sunpower M87N Stirling cryocoolers will also be used on the AMS-02 experiment onboard the International Space Station. The cryocoolers are used to cool the outermost vapor cooled shields to extend the life of the stored cryogen. It will be the first space flight mission with Stirling-cycle cryocoolers operating with a substantial steady-state magnetic field. Ground tests have been conducted demonstrating the feasibility of operating the cryocooler in fields as high as 925 Gauss [29], which is over twenty times the field of the MIT-SSL EMFF ground testbed. JWST also plans to use a cryocooler. The interesting aspect of JWST's pulse tube cryocooler is that the cold head is located approximately 20 meters away from its compressor and the cryocooler electronics [25]. This is one example of cryogenic components operating at long distances. JWST is an example of a future large space structure operating at cryogenic temperatures. Using a sun shield, the entire optical telescope assembly, including a six meter primary, secondary support tower and secondary mirror, will operate at around 40 K.

An example of a current large space structure operating at cryogenic temperatures is the Copernicus OAO-3 (Orbiting Astronomical Observatory) satellite. The satellite consisted of a 80 cm UV telescope which operated at steady-state cryogenic temperatures using a sun shield and heat pipes. No active cooling was used in Copernicus [30]. Also demonstrated on the shuttle was a cryogenic heat pipe (CRYOHP) on STS-53 in December 1992, which operated between 60 to 140 K [31]. More details on cryogenic heat pipes are given in the next section. Because of their flight heritage, cryocoolers and cryogenic heat pipes are promising technologies for the EMFF thermal system.

In this section, examples of a large scale cryogenic system have been shown by JWST and OAO. Consumable-free or passive methods of cooling using sun shields or cryocoolers powered by the Sun have also been presented. Some of the missions have specific orbits, such as JWST, others reside inside the shirtsleeve environment of the space shuttle or ISS. Cooling HTS coils for EMFF combines all of these challenges since a design that is large scale, consumable-free and independent of orbit is needed.

1.3.3 Review of Cryogenic Heat Pipes

A heat pipe is a device used to transport heat from one location to another. Heat pipes work using two phase flow properties of a working fluid and in doing so act like a material with very high thermal conductivity. The length of the pipe is the effective distance that heat is transported. There are two characteristic 'diameters' used to describe the size of a heat pipe in this thesis. For a circular heat pipe in the shape of a coil, its size will be referred to as the coil diameter or simply diameter. Most heat pipes have a circular cross-sectional area. This dimension will be referred to as the pipe diameter or cross-sectional diameter. For a typical heat pipe the pipe length is much larger than the pipe diameter.

The first heat pipes were built at Los Alamos National Laboratory in the 1960s by Grover [32]. Work on cryogenic heat pipes began soon after; one example is a nitrogen heat pipe developed at MIT by Silvares and Cravalho in 1973 [33]. The MIT cryogenic heat pipe used a grooved wick structure constructed from metallic fins and was 12 inches long with a 7/8 inch pipe diameter. It was designed for 309 Watts, but experimentally demonstrated a power capacity of 60 Watts. The first test to demonstrate a cryogenic heat pipe in microgravity was conducted onboard a sounding rocket in 1975 by Harwell [34]. This heat pipe used methane as a working fluid, axial grooves as a wick and was 76 cm long with a 1.58 cm outer pipe diameter. Tests demonstrated operation of the heat pipe during the six minutes of microgravity. Ground heat pipes are one of the earliest examples of large scale heat pipes. During the 1970s, the 'cryo-anchor' program in the Alaskan tundra consisted of heat pipes as large as 18 m in length and 7.5 cm in cross-sectional diameter that were placed in the ground for permafrost preservation [35].

While the concept of using a heat pipe for isothermalization of a large superconducting coil in space is novel, there is heritage for the use of heat pipes in space. Heat pipes have been used within a solar array, connecting opposite faces of the solar array to minimize thermal gradients; one side of the heat pipe located on the cell side facing the Sun, while the other end was on the radiators. Previously it was mentioned that heat pipes were used on OAO in the early 1970s to control thermal gradients of optical surfaces. The highly conductive properties of a heat pipe are used to eliminate structural distortions. Heat pipes have also been proposed as a method for structural isothermalization for the National Space Observatory and the Space Shuttle [35] and to remove heat from infrared detectors and the aperture shroud for satellite infrared systems [36].

There have been additional ground developments related to components of the EMFF thermal system. Daugherty has developed a nitrogen pipe to conductively cool HTS current leads [37]. Prenger used nitrogen heat pipes as a thermal shunt between two stages of a Gifford-McMahon cryocooler [38].

All of the flight cryogenic heat pipes discussed have been either small in cross-sectional diameter, short in length, or both. Based on the size of the EMFF testbed HTS wire stacks, the resulting cross-sectional diameter of a heat pipe containing stacks of HTS wires must be four centimeters or greater. In addition, the heat pipe must be circular to contain the coil. While the coil diameter for the EMFF testbed is approximately 80 cm, flight EMFF coils have been envisioned with diameters of two meters and larger [5]. It is important to note that the length of the heat pipes is determined by the coil's circumference. The heat pipe with the closest scale to this is the CRYOHP onboard the shuttle, which had one to two centimeter cross-sectional diameter heat pipes with effective lengths on the order of 114 cm [31].

There are several challenges to developing cryogenic heat pipes compared to ambient or high temperature heat pipes. In general, the performance of cryogenic working fluids can be limiting because of their low surface tension and heat of vaporization. The working fluid also exhibits high pressures when the pipe is at ambient conditions. This means that wall materials, wall thickness, welding and sealing of cryogenic pipes are very important to avoid leakage and bursting. One alternative to this is to use an excess volume reservoir or a liquid trap at the evaporator [39]. Various lessons learned from previous research have been considered for this thesis. Kreeb tried several mesh types such as open grooves, screen covered grooves and different layers of screen, and determined that screen covered grooves allowed for the most amount of heat transfer [40]. Nitrogen pipes in the past have even used wicks made from a cloth-like material, but usually used a metallic wick [39]. The heat pipe developed in this thesis contains a screen mesh due to ease of manufacturability. Cryogenic working fluids also exhibit small capillary forces, due to low surface tension forces, and therefore horizontal and slightly inclined pipes can be difficult to evaluate since in 1-g it is possible that liquid may not wet the upper parts of the capillary structure [40]. Cryogenic heat pipes also start in a supercritical condition and must be cooled below the critical temperature of the working fluid. Research on the startup conditions of a nitrogen heat pipe has been conducted by Couto [41]. One of the secondary goals of this thesis is to add to the body of work on cryogenic heat pipes.

1.3.4 Applications of HTS

The objective of this thesis, to determine a renewable method of cooling large space structures such as HTS coils, has application beyond use for EMFF. There are four main areas that the thermal system designed can potentially impact. They are in space propulsion, satellite technology, space experiments, and ground HTS applications.

There are two current space propulsion technologies that utilize HTS coils. The Variable Specific Impulse Magnetoplasma Rocket (VASIMR) use HTS coils to act as a magnetic nozzle to confine and channel RF-heated plasma to very high exit velocities [16]. This is a potential propulsion option for interplanetary transport since its high efficiency reduces the amount of propellant required. A concept called Magbeam (Magnetized Beamed Plasma Propulsion) developed by Winglee at the University of Washington uses a series of electromagnetic coils as a magnetic nozzle on electric propulsion systems to focus a plasma stream [42]. This focused plasma is beamed to a recipient spacecraft to transfer power and momentum. It has been proposed by Kwon and Sedwick to reduce the size of the nozzle magnet by using HTS coils [43]. This system is a low-mass, low-power option capable of extending the MagBeam concept to additional applications such as defensive counter-space functions. The HTS coils in both the VASIMR and Magbeam concepts will require a cryogenic control system. A system that is consumable-free, such as the design in this thesis, has the potential to make each concept more efficient in terms of mass and therefore more viable for future space missions.

There are also several other uses for HTS coils on satellites that have been explored. The HTS coils can be used on satellites as torque coils to de-saturate large torques generated by reaction wheels or control moment gyros. For spacecraft requiring large torques, the HTS coils can be a more mass efficient system compared to COTS torque rods or torque coils made from conventional room temperature conductors. The HTS coils could also potentially replace torque rods for geostationary satellites. This is shown in Figure 1.4, which compares the total mass of these options versus the torque for a system in GEO. The torque coils have a one meter radius coil. Details of the analyses are shown in Appendix A. While using these HTS coils may not completely replace control moment gyros, they have the potential to replace torque rods and reaction wheels.

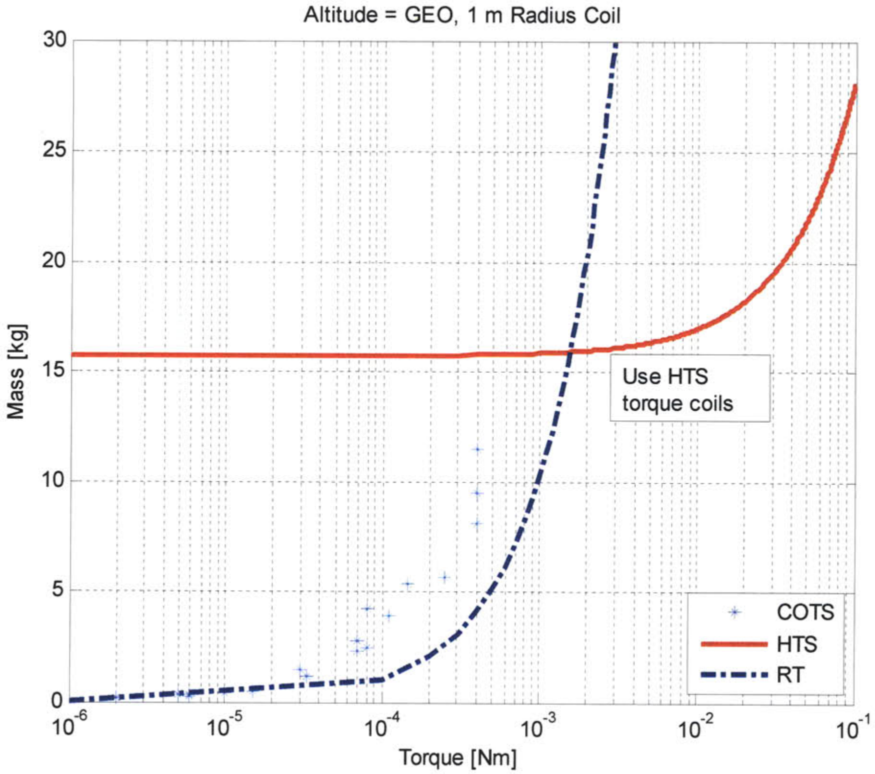

Figure 1.4 Total mass of magnetic torquers vs. Torque in GEO for commercially available torque rods (COTS), and HTS and Room Temperature torque coils.

Hoffman has proposed using superconducting magnets to create a protective magnetic shield for astronaut radiation protection [44]. The results of the study show that using present day HTS, significant radiation shielding is possible with improvement over present passive shielding configurations. However, the cryogenic system necessary required 75 tons of Helium for a three year mission. Clearly, a solution that eliminates consumables would be beneficial for this concept. Another potential application of HTS on satellites can be found on telecommunications satellites [45]. Research by Maignan showed that using HTS for various microwave equipment components improved mass and volume savings, reduced noise, and allowed for device miniaturization. Two proof-of-concept testbeds with pulse tube cryocoolers were built demonstrating that a flight configuration is feasible.

The EMFF HTS thermal system has application in various space experiments. One area is in cooling large space telescope structures. Far Infrared space telescopes operating in the 4-40 K range require cooling for the mirror, detectors, entire structure, and electronics. Proposed missions include the SAFIR mission [46], which has a primary mirror of 10 m diameter, the SPIRIT mission [47], which has two 1 m diameter primary mirrors, and the SPECS mission, which has three 4 m diameter primary mirrors [48]. The SAFIR mission will also need a cryocooler for its secondary mirror assembly and optics train in the instrument cryostat. A current testbed developed by Hoang uses a cryogenic loop heat pipe (C-LHP) [49]. Similar to the heat pipe developed in this thesis, a loop heat pipe has no moving parts to wear out and does not induce unwanted vibrations, two attributes that are favorable for optical components. Heat pipes are virtually maintenance free and reliable for long-term operation. The system tested by Hoang used a small diameter Neon heat pipe with only two loop backs in the C-LHP. Since these space telescope missions are in the far term horizon, there is potential to apply aspects of the EMFF thermal design.

A more recent experiment using superconductors is the AMS-02 experiment, which is to be launched onto the ISS in late 2008. AMS-02 is a particle detector using superconducting magnets and its mission is to search for the presence of dark matter, strange matter, and antimatter [24]. The mission is cooled with liquid Helium and has a three year mission before refilling of the cryogen is needed. The magnet bore is 1.115 m and is designed for very low heat loss. The physical scale of the system is similar to an EMFF spacecraft coil. HTS magnets can also be used for electron cyclotron resonance ion sources [50]. Harrison shows an example of an HTS magnet using cryocooler cooling only. This cryogen-free system is relatively small though, since the size of the HTS "pancake" coils are 16 cm inner diameter and 28.8 outer diameter.

Finally, there is also potential applicability of the EMFF HTS thermal system to the development of cooling large scale HTS wires on the ground. The city of Amsterdam is developing a testbed for using HTS cables for power transmission allowing for the transport of large-scale renewable energy sources such as wind farms or wave energy plants that are geographically dispersed [51]. Their system envisions using kilometer length HTS cables cooled by cryogen stations at the ends of the cable. Cryogen flows through cooling channels in the HTS cables. There is a similar testbed on long HTS cables for power transmission developed by Demko [52] which uses pressurized LN2 for cooling the cable. The system contains a large, main LN2 storage tank, approximately 4,000 L. The HTS cable is wrapped around a center LN2 supply channel. Liquid nitrogen is returned back through the same cable along an outer sleeve channel. A testbed at Oakridge National Laboratory has been testing a five meter HTS transmission cable, which has similar scale to a full flight EMFF coil. It might be possible for the Oakridge testbed to incorporate aspects of the EMFF thermal system into the design of future HTS power cables.

Current HTS power cables have both a rigid and a flexible design. A more viable option for future production is to have HTS power cables that are flexible. Schippl investigated a bendable tube system using stainless steel tubes and multilayer insulation [53]. The use of MLI to reduce heat load is similar to the HTS thermal design in this system. However, Schippl's HTS cables used flowing LN2 to cool the system. Future EMFF designs may require coil sizes that are larger than a launch vehicle shroud, so flexibility of HTS coils may be necessary. One consideration for these systems is to evolve the EMFF design to incorporate a bendable tube system. A more near term application could be for MRI machines. Currently there are MRI machines that are cooled by a cryocooler and use a Neon heat pipe to transfer heat from the HTS to the cryocooler [54]. It may be feasible to integrate the HTS wire with the cryocooled heat pipe similar to the EMFF thermal system.

1.4 Thesis Outline

The research in this thesis develops a flight migratable thermal design to cool large scale HTS coils in space with application to EMFF. The research is presented in a roughly chronological order through the next five chapters. The scale of the thermal problem is introduced in Chapter 2. Requirements on the thermal design are set by determining how many thermal watts are involved. Simple spacecraft thermal models are used to determine the performance of the cryocooler and various types of insulation. Chapter 2 briefly details the thermal design trades and shows that a design using a cryocooler, MLI, and heat pipes can accomplish the research objectives.

While the idealized models in Chapter 2 determine how bulk heat flows, Chapter 3 focuses on a more detailed model for the temperature distribution in the system. The coil temperature distribution is modeled using an analytic model, a finite difference model, and a commercially available thermal modeling code. Model verification is conducted by comparing each of the simulation models with each other and also by experimental verification.

The major contributions of the thesis are developed in Chapters 4 and 5. The research in Chapter 4 develops the design for a straight heat pipe to prove the concept of cooling HTS wires inside the heat pipe. Models for the heat pipe power capacity, temperature distribution, and performance limitations are analyzed. Details of the testbed development give insight into the manufacturing challenges of building a heat pipe with HTS wire enclosed. The results demonstrate the performance of the heat pipe both with and without the HTS.

The research in Chapter 5 builds on the modeling and manufacturing knowledge gained from building a straight pipe and investigates a circular heat pipe. The goal of this chapter is to demonstrate feasibility of the thermal system on a large size coil that is more representative of a flight system. The thesis wraps up with a summary of contributions and recommendations for future work in Chapter 6.

Chapter 2 Thermal Design

One of the first tasks in the design of spacecraft or really any engineering system is to develop and understand the requirements. The goal of this chapter is to understand the thermal requirements necessary for an HTS coil in space. Once the scale of the thermal problem is determined, the details of the design are presented. First, this chapter models the bulk heat flow for a single HTS coil to understand the amount of thermal watts necessary for extraction to determine if one or more cryocoolers meet the requirements. Next, the benefits of operating with more than one cryocooler are investigated. Finally, the EMFF thermal system investigated in the rest of this thesis is presented.

2.1 Bulk Heat Flow for an EMFF Coil

Initial sizing of an EMFF thermal system was conducted by Kwon [5] and forms the basis for the analysis in this section. The first goal is to determine if a passive or active thermal system is required. A passive thermal control system does not require any power to maintain cryogenic temperatures. If a passive system is not able to maintain temperatures below the wire's critical temperature, the amount of heat extraction required by an active thermal control system can be determined. Steady-state analysis is used for the worst-case heating scenario to find the amount of heat into a single coil. Figure 2.1 illustrates using one of the three orthogonal coils from an EMFF vehicle (shown in Figure 1.1) for the analysis along with the cross-sectional area of the HTS wires and the HTS containment system. The coil major radius is R_c, and r_c denotes the radius of a stack or bundle of HTS wires, not necessarily a single HTS wire. The containment system encloses the HTS wire for insulation and has a radius, r_h. The maximum amount of heat absorbed by a single coil occurs when the plane of the coil faces the Sun absorbing solar flux on one side and the opposite side faces the Earth, absorbing solar flux reflected off the Earth and the Earth's infrared emission. In reference to Figure 2.1, this means that the Sun is located out of the page, while the Earth would be in the page.

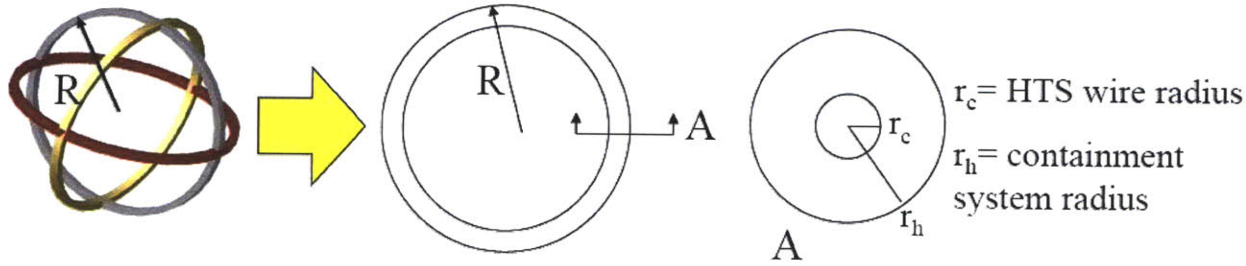

Figure 2.1 Geometry for a single coil in the worst case heating scenario

There is equilibrium between the rate of heat absorbed by the coil, Q_a, the heat rate emitted back into space, Q_e, and the heat rate in the HTS wires, Q_t, by conduction. This is shown in Figure 2.2 and is given by

$$Q_a = Q_e + Q_t \tag{2.1}$$

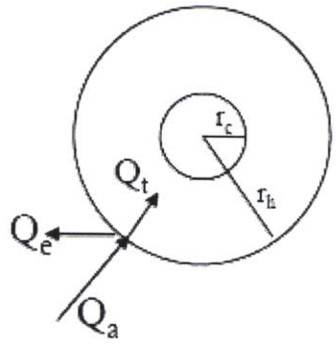

Figure 2.2 Thermal free body diagram for coil cross-section

The power absorbed by the coil is a function of the solar flux and reflected solar energy off the Earth, or albedo, and the Earth emitted IR (infrared) radiation. This is given by

$$\begin{aligned} Q_a &= G_s \alpha A_a + Q_{IR} + Q_{albedo} \\ A_a &= 2r_h \cdot 2\pi R_c = 4\pi R_c r_h \end{aligned} \tag{2.2}$$

The absorbed amount of solar flux, G_s, depends on the area of absorption, A_a, and the absorptivity of the surface, α. The average solar flux in Earth orbit is approximately 1367 W/m^2, however it can be as high as 1418 W/m^2 or as low as 1321 W/m^2 depending on the time of the year [55]. Earth's albedo, Q_{albedo}, and Earth's IR radiation flux, Q_{IR}, are given by

$$\begin{aligned} Q_{IR} &= q_{IR} A_a \varepsilon \sin^2 \rho \\ Q_{albedo} &= G_s a A_c \alpha K_a \sin^2 \rho \end{aligned} \tag{2.3}$$

The Earth's emitted energy flux at the surface, q_{IR}, is 258 W/m^2, the average Earth's albedo, a, is approximately 0.35 [55], and emissivity of the surface is ε. Both ρ and K_a are a function of the altitude, H, and radius of the Earth, R_E, and are given by

$$\begin{aligned} \sin\rho &= \frac{R_E}{H+R_E} \\ K_a &= 0.664 + 0.521\rho - 0.203\rho^2 \end{aligned} \tag{2.4}$$

K_a accounts for the reflection of collimated incoming energy off the spherical Earth while ρ is the angular radius of the Earth.

A common method of insulating spacecraft is to use multilayer insulation (MLI). MLI blankets consist of layers of a low emittance film that is silvered, usually an aluminized film of Mylar, with a low conductance spacer, such as a fiberglass paper, silk netting, Dacron fabric, or other polyester materials [56]. A picture of a typical MLI blanket cross-section is shown in Figure 2.3 [57]. The thermal conductivity is a result of radiation, solid conduction, and gaseous conduction. Solid conduction can be minimized by reducing the contact between layers and gaseous conduction is reduced by operating in a vacuum. To reduce the Mylar layers from touching each other, the Mylar can be crinkled, which is a method used later in this thesis. MLI is not very effective in the presence of gas and the effective thermal conductivity improves as the pressure of the system decreases. The thermal conductivity as a function of pressure is shown in Figure 2.4. MLI is considered highly evacuated once the pressure drops below 10^{-5} Torr. At these pressures gaseous conduction is practically eliminated and radiation is the main method of heat transfer through the blankets.

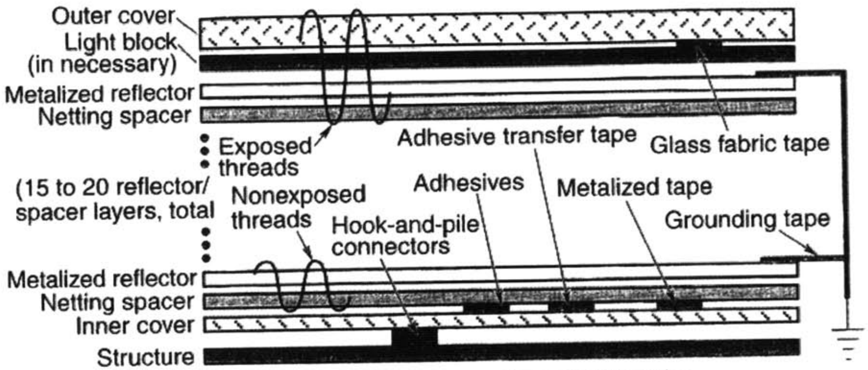

Note: Details and features are shown for illustration and will vary with actual design and installation.

Figure 2.3 Cross-section of a MLI blanket [57].

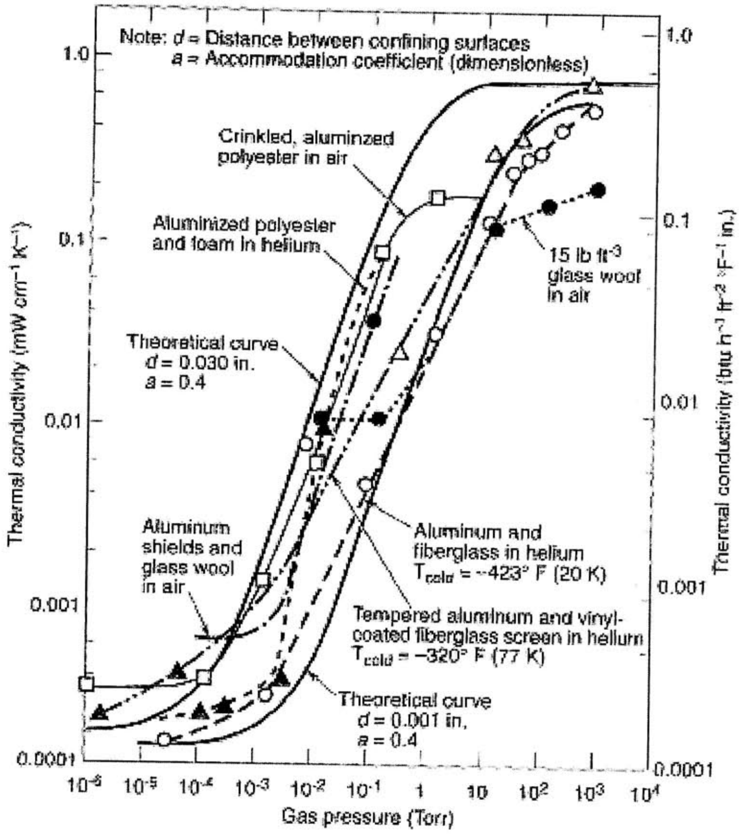

Figure 2.4 Thermal conductivity of MLI versus pressure [57]

There are two methods of modeling MLI that are used. The first method models MLI as a solid insulator with an effective thermal conductivity while the second method models MLI as a series of vacuum gaps. By using two models, a useful bound on the heat flow into the coil can be obtained.

For the first method, MLI is modeled as a solid insulator located between r_h and r_c. As a conservative measure, an upper bound for the MLI thermal conductivity was used, ($k = 4\cdot10^{-4}$ W/m·K = 0.004 mW/cm·K). As a comparison with other solid insulators, foam has an approximate k of 0.2 W/m·K and aerogel has a k of $4\cdot10^{-3}$ W/m·K. MLI is about an order of magnitude improvement over aerogel, which was modeled as an insulation material previously by Kwon [5]. In equilibrium, the absorbed heat is equal to the heat radiated back into the environment plus the heat conducted to the coil and is given by

$$\begin{gathered} Q_a = \sigma\varepsilon(T_h^4 - T_e^4)A_e + \frac{2\pi k \cdot L_c(T_h - T_c)}{\ln\left(r_h / r_c\right)} \\ A_e = 4\pi^2 R_c r_h \qquad L = 2\pi R_c \end{gathered} \tag{2.5}$$

The Stefan-Boltzmann constant is σ ($5.67\cdot10^{-8}$ W·m^{-2}·K^{-4}), the area of emission is A_e, and the circumference of the coil is given by L. The temperature of the environment is T_e and for this analysis the temperature of space is 4 K. The temperature at r_c, is the HTS wire temperature, T_c. The EMFF testbed operates at 77 K and is used as a baseline temperature for operation. If the coil is operating in a different heating environment, such as a vacuum chamber, the temperature of the chamber walls is T_e.

The temperature of the outside of the MLI, T_h, can be solved from Equation (2.5), given the heat rate, Q_a, from Equation (2.2). The result is a quartic equation with a known solution. Once T_h is found, the heat rate into the HTS coil, Q_t, can be determined. The heat rate into the coil as a function of the containment system size is shown in Figure 2.5 for a system in LEO and in Earth trailing orbit. In Earth trailing orbit, it is assumed that the heat from the Earth is negligible so solar flux is the only source of heat. The results show that heat needs to be extracted from the system by an active cooling system and the quantity of heat needed for extraction is on the order of 5 Watts, depending on the amount of insulation used. In LEO, a greater amount of heat needs to be extracted, which is expected because the heating environment is greater than in Earth trailing orbit.

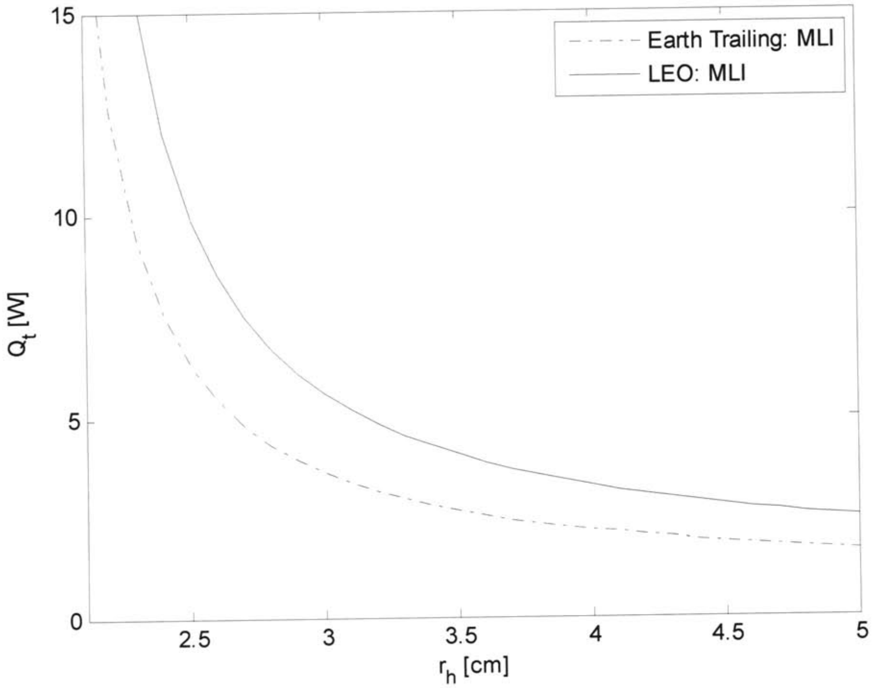

Figure 2.5 MLI as a solid insulator model: Heat flow into the EMFF coils in LEO and Earth trailing orbit

For the analysis in Figure 2.5, a flight sized coil with a radius of 1 meter was used. The HTS wire bundle radius was based on the size of the wire stack for the EMFF testbed. A wire stack that is 4 cm tall holds approximately 100 turns of wire. To model the absorptivity and emissivity of MLI, the material selected at the containment system radius, r_h, is silvered Telfon. For the LEO analysis, an altitude of 400 km was used, which is also the altitude of the International Space Station. The distance to the Sun determines the solar flux and for both the LEO and the Earth trailing orbit system, this distance is 1 AU. A summary of the variables and their quantities is shown in Table 2.1. In conclusion, modeling MLI as a solid conductor results in approximately 5 Watts of heat that are transmitted into the HTS wires when using approximately 1 cm of MLI.

Table 2.1 Variables used in thermal analysis

Variable	Symbol	Quantity
Coil major radius	R_c	1 m
HTS wire bundle radius	r_c	2 cm
MLI thermal conductivity	k	$4\cdot10^{-4}$ W/m-K
Wire temperature	T_c	77 K
Temperature of space environment	T_e	4 K
Emissivity of Silvered Teflon	ε	0.66
Absorptivity of Silvered Teflon	α	0.08
Solar flux	G_s	1367 W/m^2
Earth IR flux	q_{IR}	258 W/m^2
LEO altitude	H	400 km
Earth albedo	a	0.35

It is useful to verify the approximate range of heat flux into the coil using a second method. By doing so, confidence can be gained in understanding the scale of the thermal problem. The second method to determine the heat flux into the HTS system models the MLI as an idealized vacuum gap. Each layer of the MLI is modeled as a non contacting vacuum gap. Radiation is the only method of heat transport into the coil. The heat flow into the coil is given by

$$Q_t = \varepsilon_t \sigma \left(T_h^4 - T_e^4\right) A_c \tag{2.6}$$

Where the effective emissivity, ε_t, for N number of non-contacting layers, is given by

$$\varepsilon_t = \frac{1}{\frac{1}{\varepsilon_c} + \frac{A_c}{A_h}\left(\frac{1}{\varepsilon_h} - 1\right)} \frac{1}{N+1} \tag{2.7}$$

where A_c and A_h are the cross-sectional areas at r_c and r_h respectively [58]. Note that A_h is equal to A_e for an infinitesimally thin vacuum gap material. The heat rate into the coil modeling the MLI as a series of vacuum gaps is shown in Figure 2.6 for both a system in LEO and in Earth trailing orbit. The results also give an approximate range of 5 to 10 Watts necessary for cooling, depending on the number of MLI layers used.

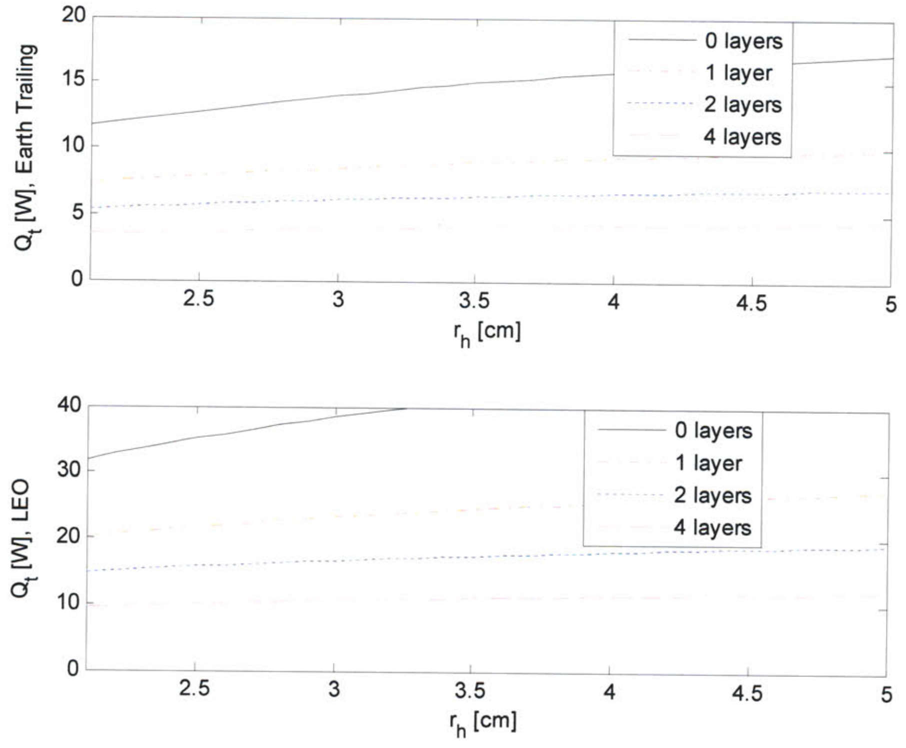

Figure 2.6 Vacuum gap MLI model: Heat flow into an EMFF coil for a various number of vacuum gap layers: Earth Trailing orbit and LEO cases

Since the two methods of modeling MLI are different, it is not surprising that the actual values are different. The important result is that they have the same order of magnitude and this provides a useful bound for the heat flow into the coil. While it may be possible to adjust the MLI design parameters so that the two MLI models match more precisely, the physical implementation of these parameters may not be realistic. One such design parameter is the containment system radius. The trends of each model for varying containment system radii are different. For the solid insulation MLI model, as more insulation is added the heat load is reduced. In practice, MLI does not behave like this. There is a decrease in performance after approximately 20 layers of MLI are used [57]. For the vacuum gap MLI model, as the containment system radius (r_h) increases, the heat load increases because there is a greater area for heat absorption. Note that for a fixed containment system radius, the spacing between vacuum layers decreases as more layers are added. Since the vacuum gap model assumes that neighboring layers do not contact, ideally the heat load can be minimized by having a large amount of vacuum gap layers spaced infinitesimally close together. This minimum heat load system would have a reduced surface area for absorption. In reality, neighboring layers of MLI contact with each other. The methods used in this section are idealized models because no engineering consideration is given for their actual implementation. Again, the main result is that an active cooling system is required to cool an HTS coil and the amount of heat extraction needed is approximately 5 Watts. The goal of this thesis is not to validate MLI but to show the benefits of using MLI for an EMFF thermal system.

Commercially available cryocoolers have the necessary cooling capacity for the EMFF thermal system. The Sunpower cryocoolers have flown in space and have a cooling power as high as 7.5 W at 77 K with an input power of 150 W [59]. They are also a low mass option, approximately 3 kg or less. A summary of Sunpower cryocooler specifications is shown in Table 2.2 along with a picture in Figure 2.7.

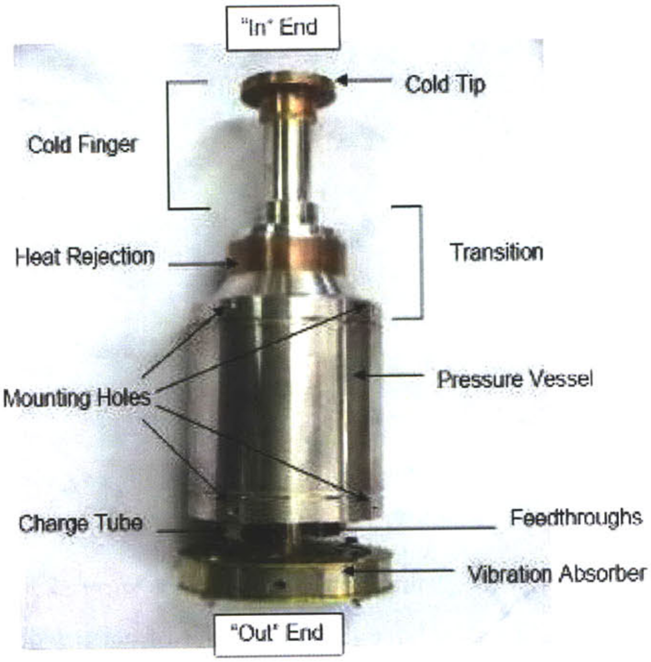

Figure 2.7 Sunpower cryocooler [59]

Table 2.2 Sunpower cryocooler specifications [59]

Model	M77	M87
Cooling Power (W)	4	7.5
Temperature (K)	77	77
Input Power (W)	100	150
Mass (kg)	3	2.7

2.2 Multiple Cryocoolers

The idealized models have shown that the power required for extraction can be accomplished using a single cryocooler. However, it is possible that more than one cryocooler can be used to cool a coil. Additionally, depending on the orbit or insulation materials used, multiple cryocoolers may be necessary. This section uses the idealized model for a vacuum gap from the previous section to determine the merit of using multiple cryocoolers.

The performance of a flight qualified Sunpower M87N Engineering Model #1 cryocooler is shown in Figure 2.8 [29]. There are two important trends used by this analysis that are shown in Figure 2.8a. Given a constant thermal load, the cryocooler input power is lower at warmer cold tip temperatures. For example, at a thermal load of 5 W, it takes 150 W of cryocooler power (blue line) to maintain a cold tip temperature of approximately 62 K, but only 50 W of power (magenta line) for a temperature of approximately 102 K. Another interpretation of this trend is that the ratio of thermal power to electrical power or the efficiency with which thermal power is removed decreases as the applied cold tip temperature decreases.

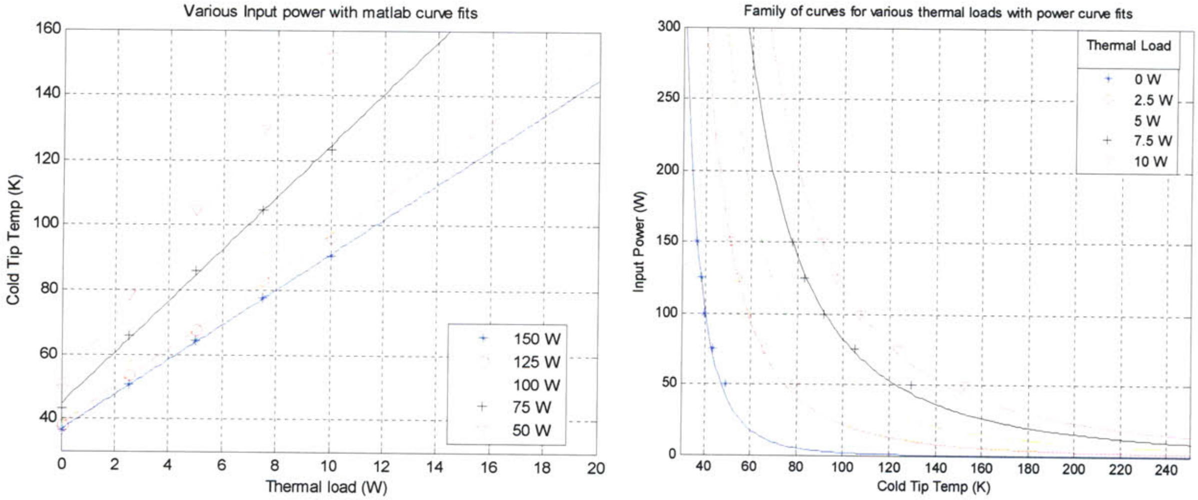

a) Cold tip temperature vs. Thermal load b) Input power vs. Cold tip temperature

Figure 2.8 Cryocooler performance for Sunpower M87N – EM#1

The second trend is that given a constant cold tip temperature, the cryocooler power is less expensive at lower thermal loads. For example, at 77 K, a 7.5 W thermal load takes approximately 150 W of power (blue line with '*' marks), while a 2.5 W thermal load takes approximately 50 W of power (magenta line with '∇' marks). The heat rejection for the cryocooler occurs at 273 K. In order to utilize these two trends, the data from Figure 2.8a is used to describe the input power of the cryocooler as a function of cold tip temperature for various thermal loads. A curve fitting tool using a power law was used in Matlab and the results are shown in Figure 2.8b.

Given the goal of reducing the total power, a simple two cryocooler system with a single vacuum gap is shown in Figure 2.9a. With two cryocoolers, it is possible to implement one cryocooler on the outside surface, the 'hot' side, and a second, inner cryocooler at the coil, the 'cold' side. The outer cryocooler, acting at a higher temperature, reduces the thermal load of inner cryocooler, which is cooling the HTS coil.

The thermal free body diagram for the system is shown in Figure 2.9b. The analysis is similar to the vacuum gap shown in Figure 2.2, except for the addition of the inner cryocooler Q_{cc_c} and the outer cryocooler Q_{cc_h} extracting heat. The equilibrium balance at the containment system outer surface is given by

$$Q_a = Q_e + Q_h + Q_{cc\_h} \tag{2.8}$$

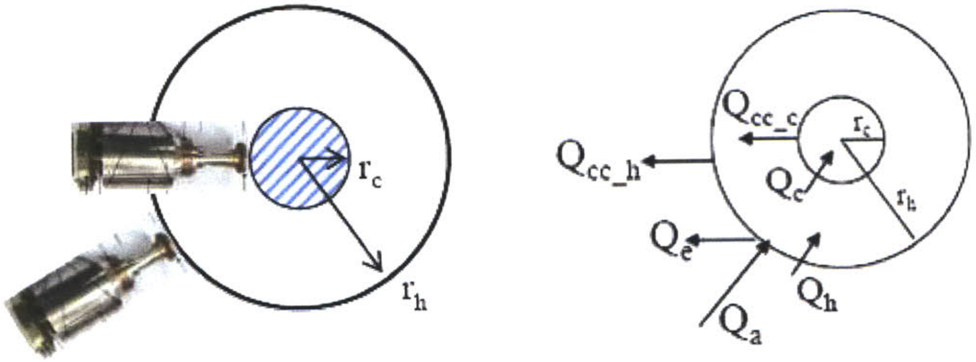

a) b)

Figure 2.9 Setup for multiple cryocoolers (a) and thermal free-body diagram (b)

For simplicity, an Earth trailing orbit case is investigated. The outer surface radiates heat flux back into the space environment and transmits heat flux into the coil. This is given by

$$G_s \alpha A_a = \sigma \varepsilon_t (T_h^4 - T_c^4) A_c + \sigma \varepsilon_h (T_h^4 - T_e^4) A_e + Q_{cc\_h} \tag{2.9}$$

The unknown quantity in Equation (2.9) is the containment system surface temperature, T_h. Equation (2.9) can be rearranged to solve for

$$T_h^4 = \frac{1}{\sigma} \frac{G_s \alpha A_a + \sigma \varepsilon_t T_c^4 A_c + \sigma \varepsilon_h T_e^4 A_e - Q_{cc\_h}}{\varepsilon_t A_c + \varepsilon_h A_e} \tag{2.10}$$

Using T_h, the heat into the coil can be calculated from Equation (2.6). Given the heat flux and temperature at both the inner and outer surfaces, each cryocooler power can be determined from the power fit function in Figure 2.8b. Finally, one can determine the total power required by the cryocoolers. The procedure used is summarized in Figure 2.10.

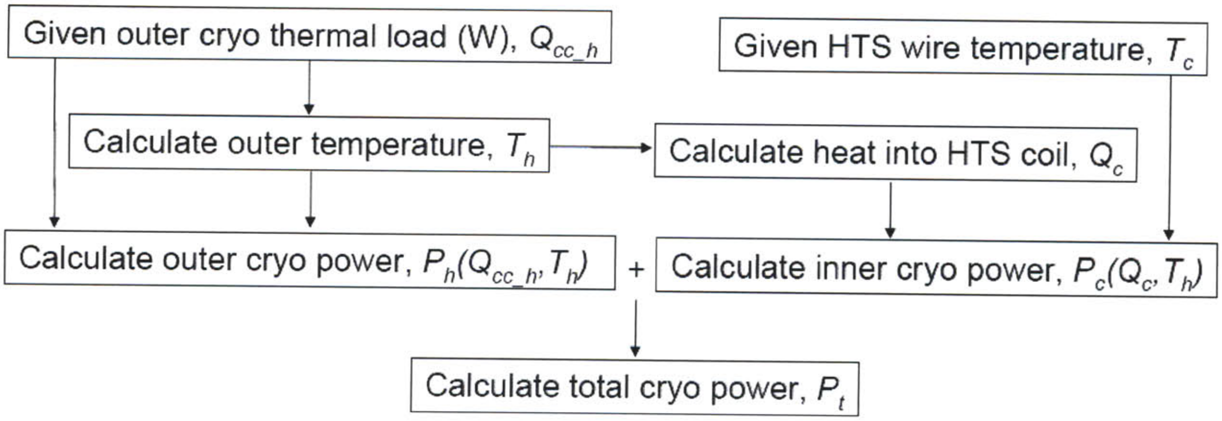

Figure 2.10 Procedure to find total cryocooler power

The thermal environment analyzed the worst case heating from the Sun for a single coil in steady-state. This is for an EMFF system with a one meter radius coil using a single vacuum gap for insulation. The vacuum gap material used was aluminized Kapton, which has an emissivity and absorptivity approximately of 0.1 [60].

The results of the analysis indicate an optimum configuration exists. Figure 2.11 shows that when the outer cryocooler is operating at 65 Watts and extracting 19.5 thermal watts, the total cryocooler power is minimized. The inner cryocooler extracts any remaining thermal watts to maintain the HTS coil temperature at 77 K. A system with a single cryocooler or no outer cryocooler requires approximately 260 W of power, compared to the minimum power system, which requires only 160 Watts. This is a savings of approximately 100 Watts.

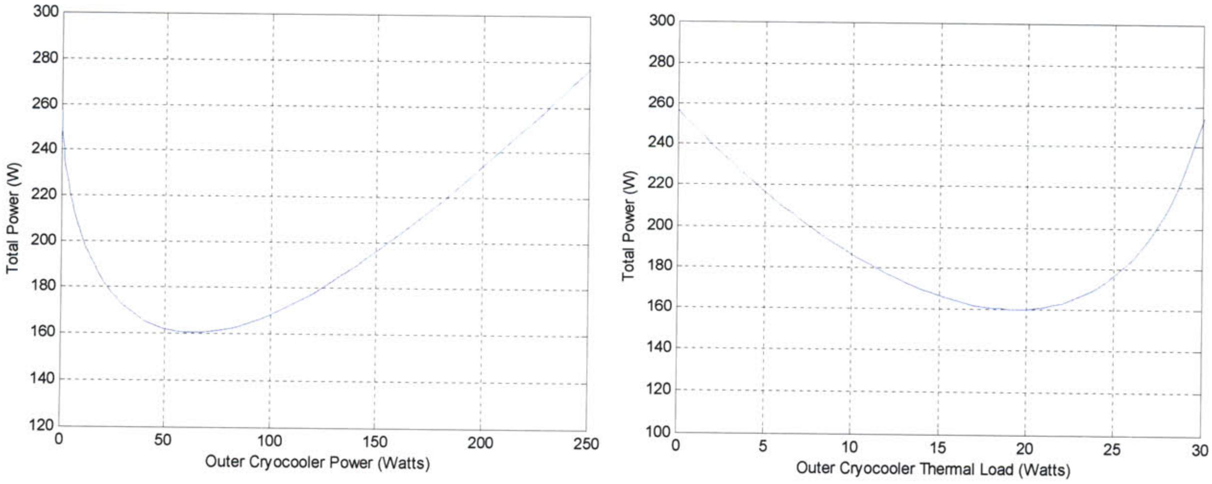

Figure 2.11 Total power requirements using two cryocoolers

Detailed results of the trade study are shown in Figure 2.12. As the outer cryocooler increases its thermal load the temperature of the outer surface decreases and the inner cryocooler thermal load is reduced. A summary of the conditions at the minimum total power consumption point are shown in Table 2.3.

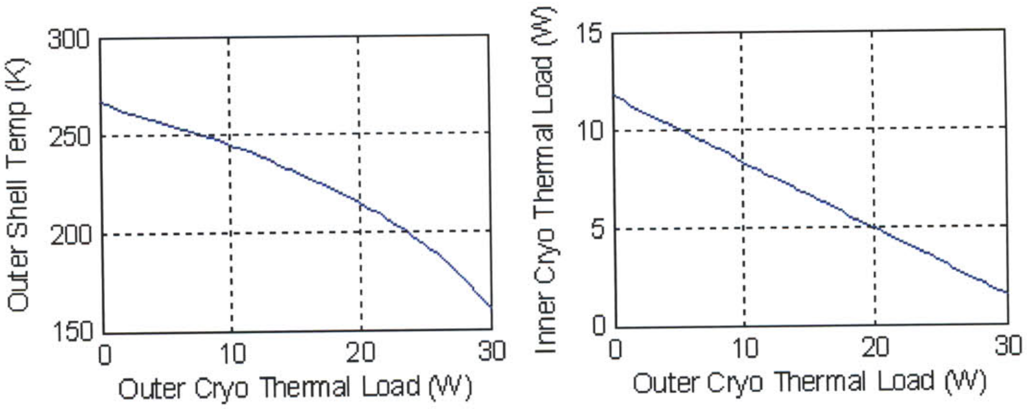

Figure 2.12 Outer temperature and inner cryocooler thermal load versus outer cryocooler thermal load

Table 2.3 Condition at minimum total power condition

Power – Total for both cryocoolers, P_t	160 W
Power – Inner Cryocooler, $P_{cc\ c}$	95 W
Power – Outer Cryocooler, $P_{cc\ h}$	65 W
Temperature – Inner, T_c	77 K
Temperature – Outer, T_h	216 K
Q (thermal) – Inner, Q_c	5.07 W
Q (thermal) – Outer, Q_h	19.5 W

Even though using multiple cryocoolers on a single coil can minimize the total power consumption, this comes at the cost of additional mass. For EMFF, one of the key costs of the thermal system is the extra mass required. An important metric for EMFF is the time-average acceleration, which is the ΔV over the mission lifetime, and not necessarily just the force produced. Operating the HTS wires at colder temperatures allow the wires to carry a larger amount of current which permits higher forces [8]. However, this comes at the cost of a more massive thermal system by using more cryocoolers and also more power required by the cryocoolers and the power subsystem. For a system of two cryocoolers, the minimum total power as a function of the wire temperature is shown in Figure 2.13 and indicates that more cryocooler power is required as the temperature drops.

So far the analyses assume an isothermal coil. As previously stated, the hottest point in the HTS wire determines the maximum amperage. Having a cryocooler at one location has the potential to cause portions of the coil farthest from the cryocooler to be the hottest. Therefore, if multiple cryocoolers are used, it would probably make sense to distribute them evenly along the coil. One of the challenges of realizing multiple cryocoolers and multiple vacuum gaps is the actual engineering implementation of a system. Therefore, the next step is to focus more on the actual temperature distribution within the coil.

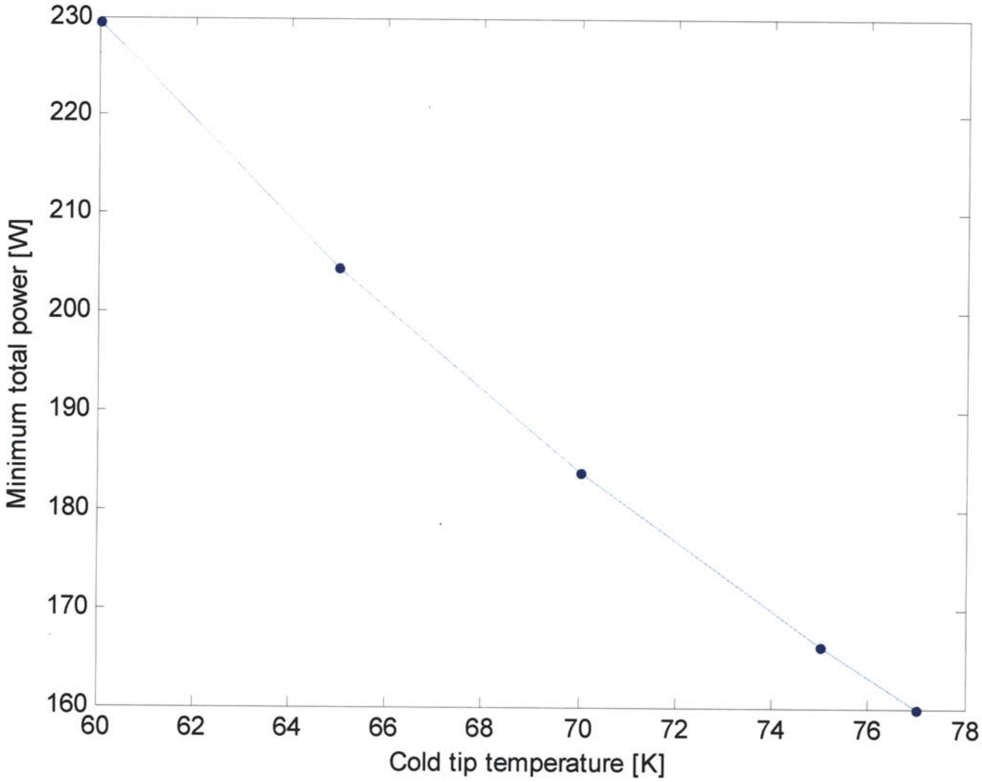

Figure 2.13 Minimum total power for two cryocoolers vs. the cryocooler cold tip temperature

In conclusion, it has been shown using idealized models for bulk heat flow that a system using multiple cryocoolers operating at different locations in the thermal system insulation can be used to reduce the total cryocooler power consumption compared to a single cryocooler system. In addition, more than two cryocoolers can be used on multiple vacuum gap layers to further reduce the total power consumption. This is detailed in Appendix B.

2.3 EMFF Thermal System Design Overview

So far, the bulk heat flow and the method of extracting heat from an HTS coil have been determined. Understanding the engineering details of the design remains. One open issue is how the cryocooler is physically implemented. Also, an important assumption in the previous analyses was that the coil was isothermal. Determining the temperature distribution throughout the coil and understanding if the entire coil remains under the superconducting critical temperature are the next steps.

The first design trade in implementing the HTS coil is to determine if a structure enclosing the wire is required. The MIT-SSL EMFF testbed shown in Figure 1.3b encloses the HTS coil in a copper containment system or copper jacket, which serves as both a structure enclosing the HTS wire and as a dewar for the cryogen. Therefore the testbed copper jacket has both structural and thermal functionality. For a flight system, a Thermally Conductive Jacket (TCJ) is defined as the device which functions as both structure for the coil and as a means for the HTS coil to maintain isothermalization. The design to enclose the HTS wire in the TCJ, similar to the EMFF testbed, will first be examined. There are two options for enclosing the coil to maintain isothermalization. The first is enclosing the wire inside a solid conductor, by which conduction throughout the coil maintains isothermal conditions. The second option is to enclose the coil inside a solid conductor with a working fluid to maintain isothermalization. An example of the second option is a heat pipe. For simplicity, the TCJ will also be referred as a pipe or a heat pipe. The research in this thesis investigates the merits of both options. But first a qualitative discussion about the method for enclosing the wire inside a TCJ is beneficial.

A heat pipe exhibits nearly isothermal conditions throughout its entire length during operation. One of the main advantages for enclosing the wire inside the heat pipe is that the design minimizes temperature gradients within the HTS wire stack. Since the wire stack is inside an isothermal TCJ, the entire stack is also isothermal, assuming minimal internal heat generation. The pipe must be large enough to enclose the entire HTS wire stack. While a pipe with a large cross-sectional diameter has the potential to have a large mass, the advantage of such a system is that the large thermal mass of the TCJ and the HTS together allow for greater thermal stability. In addition, enclosing the HTS wires give the wire stack protection and structural integrity. One of the disadvantages of enclosing the wires is that a method of inserting the wire into the pipe is necessary. Wire leads which feed through the pipe are needed. Sealing the feedthroughs is important for a heat pipe to ensure that no working fluid is lost. These manufacturing issues are addressed in later sections of this thesis.

The alternative design is to have the HTS coil outside of the TCJ, which can be a small diameter heat pipe or solid conductor. In this system the HTS coil is conductively cooled. This is a potentially simpler method of integrating the wires with the TCJ since COTS heat pipes or other available conductors can be used. However, a thermal gradient exists inside the HTS stack because the HTS coil is conductively cooled. The wires in direct contact with the TCJ will be at or close to T_c, while the wires in the stack farthest away will have a higher temperature. Due to a smaller amount of thermal mass this design is inherently less thermally stable than enclosing the wires and given a large unexpected heat load, the wires farthest away from the TCJ could be subject to burnout should the temperature rapidly rise above critical. One possibility to increase the thermal stability is to place additional pipes around the wire stack, but this option would increase the mass of the system. In fact, in the limit where pipes completely surround the HTS wires, the first design option is approached.

An overview of the EMFF cryogenic thermal control system is shown in Figure 2.14. The HTS wires are shown as a block of wire wrapped inside the TCJ. The function of the thermal jacket is to maintain circumferential isothermalization of the HTS coil. Around the thermal jacket is multilayer insulation, which reduces the heat load into the coil. The cryocooler is attached to the thermally conductive jacket and is used for heat extraction.

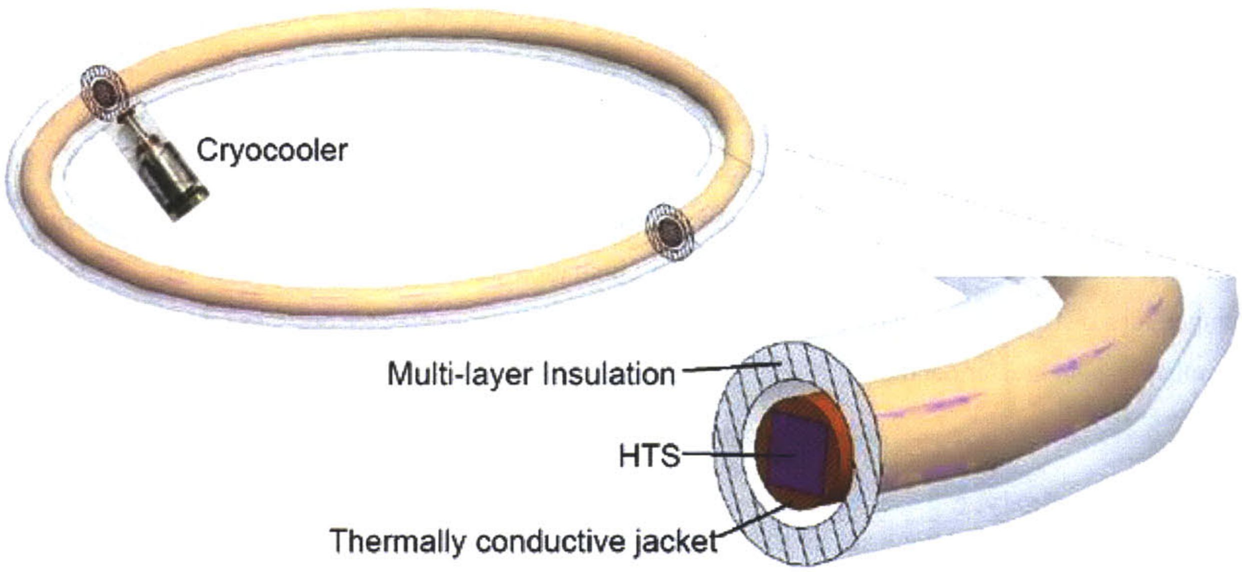

Figure 2.14 Design of EMFF HTS coil thermal system with a single cryocooler

One of the unique aspects of an EMFF heat pipe is that the HTS wire resides inside the vapor space of the pipe. Objects that are cooled by heat pipes are typically external to the heat pipe. In a heat pipe there are typically three regions of operation, called the evaporator, adiabatic, and the condenser region. Passive circulation of a working fluid occurs inside the heat pipe. Heat is absorbed by the pipe in the evaporator, causing the working fluid in the liquid state to evaporate. The working fluid condenses in the condenser, which is where the cryocooler is located. A wicking structure allows for liquid transport back to the evaporator. Commonly the object to be cooled is in direct contact with the evaporator. This also creates a well defined area for the evaporator where a large amount of heat is absorbed by the heat pipe. In contrast to this concentrated area of heat into the pipe, the remaining distance along the heat pipe towards the condenser can be modeled as an adiabatic region. For an EMFF coil in space, the distribution of heat depends on its orientation with the Sun and Earth. The maximum amount of heat the coil absorbs occurs when one side is facing the Sun and the opposite side is facing the Earth. Here, the entire coil is absorbing heat. The EMFF heat pipe must be designed for this scenario when heat is uniformly absorbed across the entire coil. Since the wires are actually not a block (as shown in Figure 2.14), but are individual strands, providing a small gap between each turn would allow vapor circulation at multiple points along the wire stack.

The plan of approach used in this thesis is to utilize three types of models to be confident that the model is accurately capturing all of the physics involved so that is can be used to design a flight-like thermal system. The nature of these models is analytic, discrete, and analog or experimental and is summarized in Table 2.4. For experimental validation it is sufficient to analyze a single HTS coil. The coil shown in Figure 2.14 will be enclosed in a vacuum chamber with cooling provided by liquid nitrogen at a single cross-section since a liquid nitrogen feedthrough system is simpler and more cost effective than a cryocooler. Uniform heating due to radiation from the chamber wall provides the heating environment for the coil. The coil is in contact with a thermal conductor and wrapped in MLI. The first model for the thermally conductive jacket uses a copper pipe as the solid conductor. A more complex design can be analyzed once this simpler system is modeled in simulation and its performance, i.e. the time-varying temperature distribution, is verified experimentally. The following chapter describes the models for the chamber tests in greater detail.

Table 2.4 Plan for current approach

	Analytic	Discrete	Analog
Purpose	Mathematical model of temperature distribution based on first principles	Finite difference model simulates temperature distribution	Experimental verification of analytic and discrete models
Benefits	High fidelity and strong understanding	Ability to add non-uniform parameters and use commercially available codes	Verification of physics modeled by analytic and discrete models, increases TRL of EMFF
Limitations	Nonlinear radiation term makes solution complex	Large models are computationally expensive	Implementing model & environment accurately is challenging
Calibration	Comparison with simpler math models	Comparison with analytic model	Multiple chamber tests, check with predicted results

2.4 Chapter Summary

In this chapter, the EMFF thermal system design has been introduced. Two models for MLI were used to determine that an active cooling system capable of extracting approximately 5 Watts is necessary for operation in both LEO and Earth trailing orbit. This can be accomplished with a single cryocooler.

System trades have been performed to analyze the cost benefits of operating more than one cryocooler. These analyses assumed steady-state bulk heat flow with a uniform temperature and heat flux distribution. It was determined that an operating condition exists using multiple cryocoolers to extract heat at different temperatures that minimizes the total cryocooler power consumption. This is because a cryocooler requires less power when operating at warmer temperatures, given a constant thermal load. Also, given a constant cold tip temperature, a cryocooler requires less power at lower thermal loads. By implementing one cryocooler on the outside of the insulation system, where the thermal load is high, but at a warmer temperature, and implementing one cryocooler right at the coil working at a low temperature and low thermal load, a minimum operating power can be achieved. In this chapter a system of two cryocoolers was analyzed and determined to have a power savings of approximately 100 Watts compared to a single cryocooler system.

The analyses using multiple cryocoolers assumed an isothermal coil. The next step towards a flight design is to understand the temperature distribution away from the cryocooler. For models in the next chapter a single cryocooler is used to determine if the maximum temperature away from the cryocooler is sufficient for operating the HTS wires. Validating the models for a single cryocooler system can then lead to use of multiple cryocoolers, if desired, to minimize power or increase reliability.

The HTS wire stack is located inside a thermally conductive jacket, which provides structure for the wire stack and electrical isolation. Around the thermal jacket is MLI, which provides good insulation from the outside environment reducing the heat load into the coil. The thermally conductive jacket also functions to provide a uniform temperature distribution circumferentially around the coil, to serve as an attachment point for cooling, and as structure for the coil system and spacecraft. Heat is extracted from the coil by a cryocooler. By placing the HTS stack inside the TCJ, thermal gradients within the stack are minimized. Cooling of the superconductor inside of the TCJ is a unique application for heat pipes that will be discussed in later chapters.

Chapter 3 Thermal Modeling

The cryogenic thermal system designed in Chapter 2 is a thermally conductive jacket (TCJ) wrapped around the HTS coil and using a cryocooler for heat removal. Analyses determined that the EMFF thermal system was capable of maintaining temperatures below the superconductor wire critical temperature. Isothermal conditions of the TCJ were used to idealize the coil. This chapter models the temperature distribution around the entire coil by using analytic, discrete, and analog models. A copper pipe is used as the TCJ to determine if a solid conductor with no working fluid is sufficient to maintain isothermalization of the entire coil at cryogenic temperatures.

3.1 Analytic Model

The first step to determine the temperature distribution is to use an analytic math model based on first principles. The goal of the analytic model is to gain a base understanding and first impression of the thermal problem associated with using a solid conductor as the TCJ. The simplest model represents the coil in one dimension as in Figure 3.1. Here the coil is cooled at a single location by the cryocooler. The one dimensional coil can be represented by a line, with the cryocooler at the origin. Given a uniformly distributed heat load the temperature of each half of the coil should be symmetric. To model the temperature the three dimensional steady-state heat diffusion equation is used.

$$\nabla \cdot k\nabla T + \dot{q} = \rho c \frac{\partial T}{\partial t} \tag{3.1}$$

Internal heat generation or the volumetric heat flux is given by $\dot{q}$ [W/m^3]. The product of the density of the material, ρ, and the specific heat capacity, c, yield the volumetric heat capacity, ρc. For a material with constant isotropic thermal conductivity, k, and a thermal diffusivity, α, the heat diffusion equation in steady-state in one dimension becomes

$$\nabla^2 T + \frac{\dot{q}}{k} = \frac{1}{\alpha}\frac{dT}{dt} = 0 \quad \rightarrow \quad \frac{\partial^2 T}{\partial x^2} = -\frac{\dot{q}}{k} \tag{3.2}$$

In Chapter 2 it was determined that a single cryocooler was capable of cooling the coil and the cryocooler thermal load was approximately 5 Watts. The analysis models the cryocooler thermal load of 5 Watts uniformly across the entire one dimensional model.

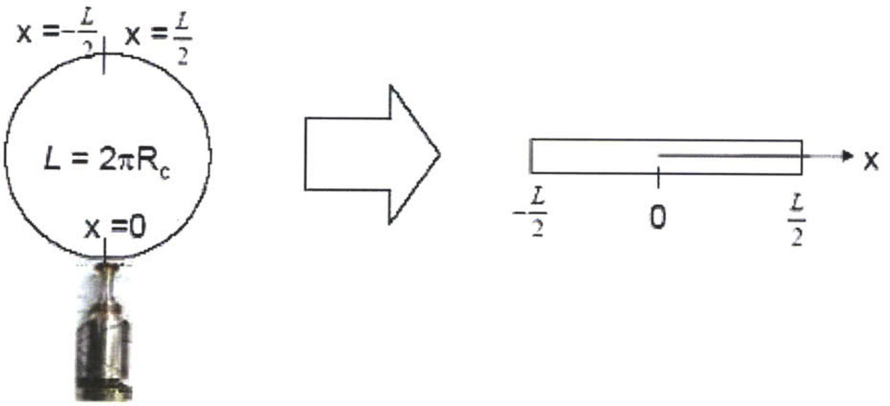

Figure 3.1 Coil geometry for the 1D analytic model with a cryocooler at the origin

The general solution to Equation (3.2) is a second order polynomial with two constants, C_1 and C_2.

$$T = -\frac{\dot{q}}{2K}x^2 + C_1 x + C_2 \tag{3.3}$$

In order to solve for C_1 and C_2, two boundary conditions are necessary. One boundary condition is the temperature set by the cryocooler at the cold finger. This temperature, T_c, occurs at the origin and is 77 K for the model. This is the same temperature for the HTS wire used by the EMFF testbed. The second boundary condition occurs at the ends of the one dimensional model where $x = L/2 = - L/2$. This location may also be referred to as the end of the coil because it is farthest away from the cryocooler. There is symmetry about the origin ($x = 0$) and there is zero spatial gradient at the ends. This means that there is no internal heat generation at the interface so the heat flux is zero at both locations $x = L/2 = - L/2$. Both boundary conditions are summarized in Equation (3.4).

$$\begin{gathered} T(x=0^+) = T(x=0^-) = T_c = 77 \\ \left.\frac{dT}{dx}\right|_{x=-\frac{L}{2}} = \left.\frac{dT}{dx}\right|_{x=\frac{L}{2}} = 0 \end{gathered} \tag{3.4}$$

After applying the boundary conditions, the temperature throughout the coil can be presented by the following piecewise solution.

$$\begin{gathered} T = \frac{\dot{q}}{2k}x(L-x) + T_c \quad , \quad 0 < x < \frac{L}{2} \\ T = -\frac{\dot{q}}{2k}x(L+x) + T_c \ , -\frac{L}{2} < x < 0 \end{gathered} \tag{3.5}$$

Total heat flux into the wire, Q_t, is a function of the volumetric heat flux and the volume of the wires. The wire stack is represented as a circular bundle of wires with radius r_c, and a length of L, which is analogous to the circumference of a coil with radius R_c.

$$Q_t = \dot{q}V = \dot{q}\pi r_c^2 L \tag{3.6}$$

In order to determine the volumetric heat, the analysis assumes that the total heat into the wire is the total heat absorbed by the coil, Q_a. Since the cryocooler is responsible extracting the total heat load, $Q_a = 5$ W.

$$\dot{q} = \frac{Q_a}{\pi r_c^2 L} \tag{3.7}$$

The temperature distribution for the one dimensional analysis is shown for two models in Figure 3.2. For a system without a TCJ, the entire heat load would be carried by the HTS wire stack. Stainless steel is the main structural component of the HTS wires [8]. Within the stainless steel matrix is the Bi-2223 superconducting material. For a wire bundle with a two centimeter radius, the temperature at the hot end of the coil at ±π meters is approximately 285 K, as seen by the dotted blue line in Figure 3.2.

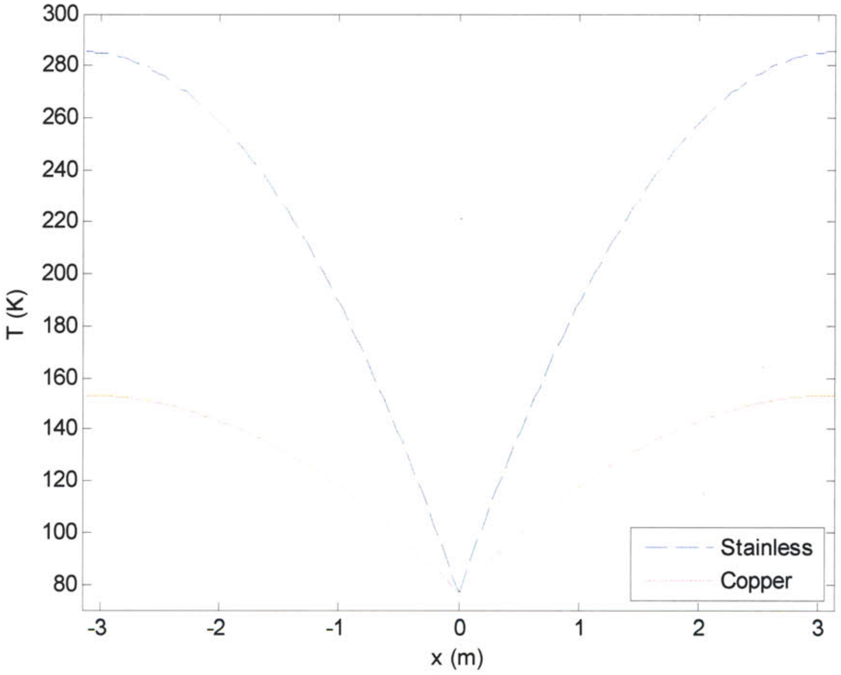

Figure 3.2 Results of 1D analysis showing large temperature rise away from the cryocooler at x = 0

The second system modeled used a copper pipe as the TCJ. In this design, the wire stack resides inside the TCJ as seen by the design in Figure 2.14 in Chapter 2. The copper jacket carries the entire heat load. It is assumed that the HTS wire stack does not generate any internal heat and is thermally isolated from the TCJ. The maximum temperature for the copper jacket system is approximately 153 K. The TCJ has a lower maximum temperature because the thermal conductivity of copper is greater than the stainless steel thermal conductivity. The copper pipe has a wall thickness of one millimeter, which is similar to standard pipes with an approximately four centimeter diameter [61]. The temperature for the copper system could be decreased by using a thicker pipe. The parameters used in the analysis are summarized in Table 3.1.

Table 3.1 Parameters for 1D analysis

Coil radius, R_c	1 m
Wire stack radius, r_c	2 cm
Stainless steel thermal conductivity	15 W/m·K
Copper thermal conductivity	410 W/m·K
Wire temperature, T_c	77 K
Absorbed heat, Q_a	5 W
Copper thickness, t	1 mm

In both designs the entire coil fails to achieve a temperature below 110 K, the critical temperature of the HTS wire. Adding additional cryocoolers or increasing the thermal conductivity are possible solutions however they come with the cost of additional mass and power. But even if the entire wire is below the critical temperature, a large temperature gradient would still exist and the hottest temperature would limit the HTS performance. One of the weaknesses of the 1D analysis is that radiation is not modeled because of its non-linearity. Inside a vacuum chamber, radiation due to the chamber walls is an important source of heating which needs to be modeled. Therefore the analytic model is not applicable to experimental models. Another important assumption is that the analytic model uses the bulk heat flow results from Chapter 2 to find the temperature distribution, not a calculated total applied heat from the environment, such as a solar flux or chamber wall radiation. Therefore, it is assumed that not only is the cryocooler capable of extracting all the absorbed heat, but the insulation system is capable of reducing the thermal load to approximately 5 W. Still the analytic model gave two important results. First that a TCJ is necessary since the HTS wire stack is not capable of maintaining isothermalization by itself. Second, a solid conductor as the TCJ with no working fluid will experience a large thermal gradient from the cryocooler to the opposite end of the coil.

Experimental validation is an important aspect of the research. Even though the heating environment in the vacuum chamber and in space is different, it is important to demonstrate a system that is capable of maintaining the entire coil below critical temperature in the laboratory setting. Therefore, even though the analytic performance indicates that potential solutions exist using a thicker copper jacket with several cryocoolers for a 5 W heat load, this solution will not succeed in environments with a potentially higher heat load, such as the vacuum chamber. However, further investigation is conducted by developing a discrete model for the copper jacket in the vacuum chamber environment. In addition, the temperature data from an experimental test will vary with time, so a time varying discrete model is necessary. The next section investigates the time varying finite difference model for the copper TCJ.

3.2 Finite Difference Model

For simplicity, a one dimensional time explicit finite difference model (FDM) is developed. First, this model is validated by the analytic model using the same conditions from the previous section. After confidence in the FDM is gained, the copper jacket is modeled for comparison to test data acquired in the vacuum chamber.

3.2.1 1D FDM Overview

The steady-state diffusion equation, seen in Equation (3.1), is the starting point for the finite difference model. This time, the model keeps the time varying term. In one dimension the result is

$$\frac{\partial^2 T}{\partial x^2}+\frac{\dot{q}}{k}=\frac{1}{\alpha}\frac{\partial T}{\partial t} \tag{3.8}$$

The geometry for the 1D FDM is slightly changed for easier facilitation of a numerical simulation. The entire coil has the same total circumference L, with an origin '$x = 0$'. However this model for the coil wraps around so that $x = L$ is the same location as $x = 0$. Therefore the cryocooler coldfinger is located at the origin and the end of the coil, which is located π radians away from the cryocooler is $x = L/2$. Therefore the boundary condition are defined as

$$T(x=0)=T(x=L)=T_c=77\text{ K} \tag{3.9}$$

Central differencing Equation (3.8) results in

$$\frac{T_{i-1}^{n}-2T_i^n+T_{i+1}^{n}}{(\Delta x)^2}+\frac{\dot{q}}{k}=\frac{1}{\alpha}\frac{T_i^{n+1}-T_i^n}{\Delta t} \tag{3.10}$$

By rearranging Equation (3.10), the temperature along the jacket, at each finite difference location i, can be determined at every time step, n+1, by

$$T_i^{n+1}=\left(T_{i-1}^{n}-2T_i^n+T_{i+1}^{n}\right)\frac{\alpha\Delta t}{(\Delta x)^2}+\dot{q}\frac{\Delta t}{\rho c}+T_i^n \tag{3.11}$$

A summary of the FDM steps are shown in Figure 3.3. To model the volumetric heating the similar conditions used by the analytic model are used for a copper pipe as the TCJ. This is given by

$$\dot{q}=\frac{Q_a}{2\pi r_c t\cdot L} \tag{3.12}$$

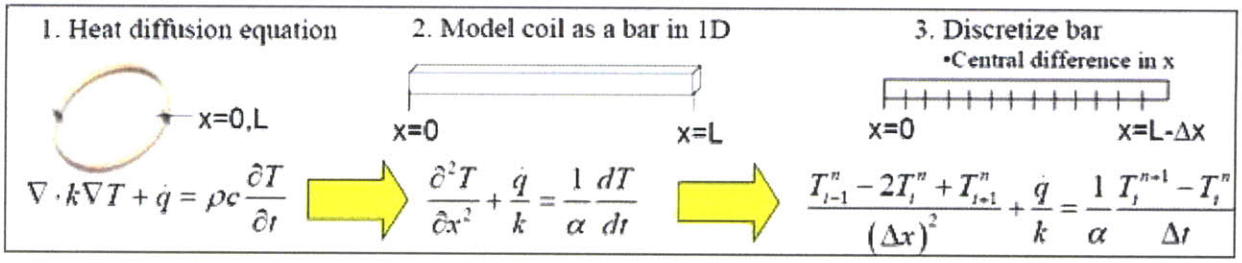

Figure 3.3 Summary of finite differencing procedure for 1D

There is a requirement on the duration of the time step, Δt, to ensure that the finite difference scheme is stable. Discussion of the stability conditions is given by Jaluria [62] and for a 1D time explicit model this is given by

$$\Delta t \leq \frac{1}{2}\frac{(\Delta x)^2}{\alpha} \tag{3.13}$$

Note that the stability depends on the thermal diffusivity, α, and the properties of the grid. A FDM grid that is very coarse (large Δx) will have a larger time step duration than a model that is very fine (small Δx).

Using the same parameters as the analytic model, the results of the 1D FDM are shown by the red dots in Figure 3.4. The steady-state temperature is approached after a large number of iterations; in this example 1,000 iterations were used. Approaching steady-state conditions, the 1D FDM matches well with the steady-state analytic model, shown by the solid blue line in Figure 3.4. Now that the procedure for the 1D FDM is validated, different heating environments can be modeled by changing the volumetric heating term in Equation (3.12). The next subsection models the heat due to radiation from the vacuum chamber.

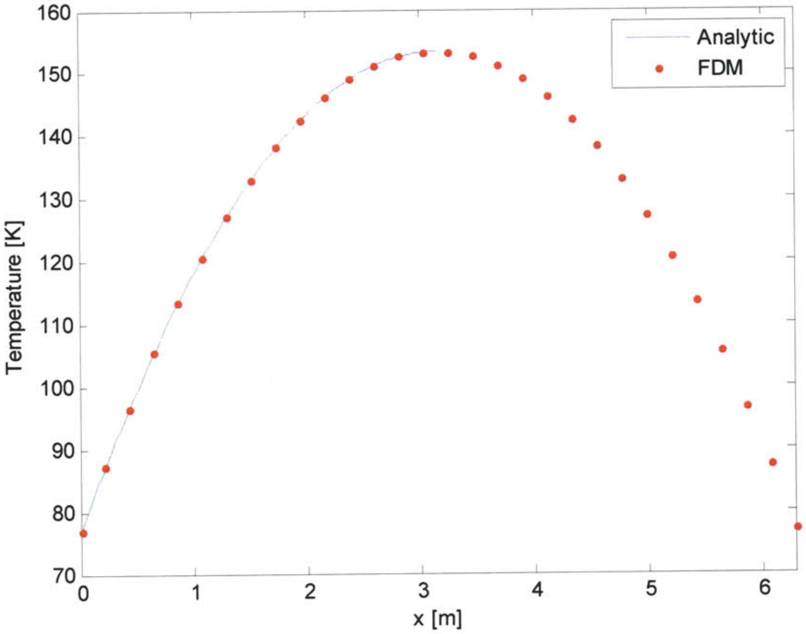

Figure 3.4 Comparing temperature as a function of distance along the TCJ for the 1D FDM and 1D analysis (with no radiation) cases

3.2.2 1D FDM with Radiation

The copper jacket is cooled by a single cryocooler at one location, $x = 0$. In the experiments in this thesis, the function of the cryocooler is mimicked by a liquid nitrogen cooling system, which is discussed in more detail in the next section. The surface area of the jacket that sees the radiation is A_c. The entire length of the jacket absorbs radiative heat flux from the chamber walls. The amount of heat flux is a function of the wall temperature, T_w. The volumetric heating term is given by the following piecewise function as

$$\dot{q} = \begin{cases} \dfrac{q_{cryo}}{\text{Volume Element}} & , x = 0 \\ \dfrac{\varepsilon_t \sigma \left[T_w^4 - \left(T_i^n\right)^4 \right] A_c}{\text{Volume}} & , x > 0 \end{cases} \tag{3.14}$$

The effective emissivity (ε_t) is similar to the effective emissivity used for vacuum gaps from Chapter 2. It is a function of the chamber wall properties (ε_w, A_w) and the pipe properties (ε_c, A_w) and is given by

$$\varepsilon_t = \frac{1}{\dfrac{1}{\varepsilon_c} + \dfrac{A_c}{A_w}\left(\dfrac{1}{\varepsilon_w} - 1\right)} \tag{3.15}$$

The dimensions used in Eqns (3.14) and (3.15) are given by

$$\begin{aligned} &\text{Volume Element} = t \cdot 2\pi r_c \cdot \Delta x \\ &A_c = 2\pi R_c \cdot 2\pi r_c \\ &A_w = 2\pi R_c \cdot 2\pi r_w \\ &\text{Volume} = t \cdot 2\pi R_c \cdot 2\pi r_c \end{aligned} \tag{3.16}$$

The parameters that are known in Equations (3.11) and (3.14) are the material properties, (α, ρ, c), and the size of each finite difference element, such as A_c. The unknown quantity is ε_t because it describes the chamber radiation environment. The effective emissivity of the pipe and chamber walls can be determined using experimental data for the temperature along the coil and ε_t has been found to be approximately 0.2. More details on this result are given later in the chapter. The temperature versus time for the 1D FDM is shown in Figure 3.5a. The model starts out at room temperature. The cold temperature is set to 77 K as defined by the boundary condition in Equation (3.9) and shown by the thick red line in Figure 3.5a. The circumference of the coil is defined as capital 'L', so that $L = 2\pi R_c$. The length to the end of the coil is defined by lowercase 'l' so that $l = L/2 = \pi R_c$. The time varying temperature is shown at various locations throughout the finite differenced coil; the thick solid blue line is at 'l/8', the cyan line is at 'l/4', the dotted black line is at '3l/8', the dash dotted magenta line is at 'l/2', and the dashed black line is at '3l/4'.

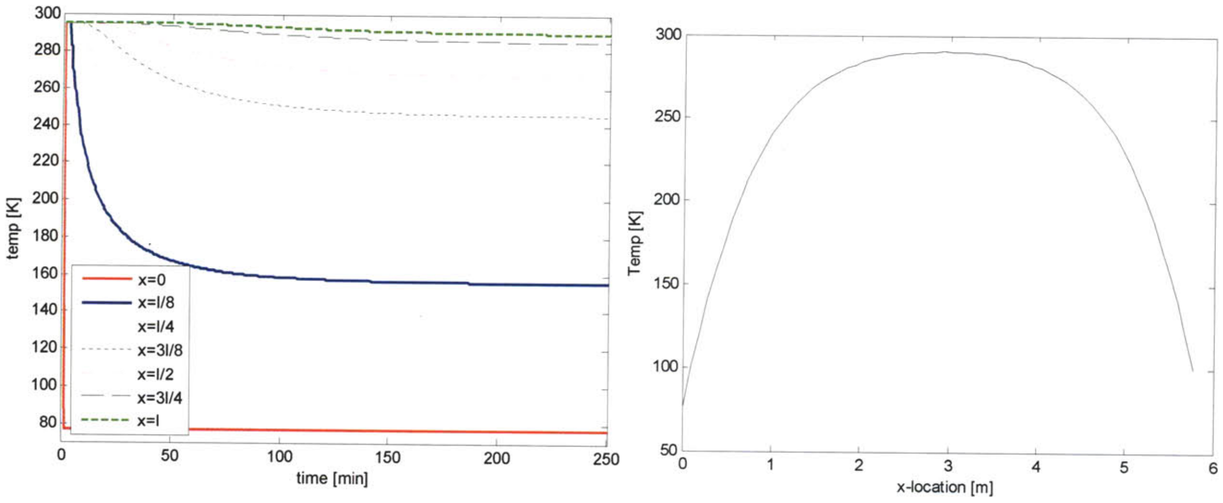

a) Temperature vs. time b) Temperature vs. distance away from cryocooler

Figure 3.5 Temperature distribution in TCJ in vacuum chamber

The temperature as a function of location around the coil at the 250 minute mark is shown in Figure 3.5b. The half length of the coil modeled is $l = 2.93$ m, so the coil radius is slightly less than one meter. The cold temperature is at the origin ($x = 0$), and the hot temperature is located at the coil end ($x = l$), which is 180 degrees around the coil. The shape of the temperature distribution is similar to the analytic model and the previous 1D FDM, however, the heat load is higher. The thermal load as a function of time is shown in Figure 3.6. This represents the amount of heat that a cryocooler would be required to extract in order to maintain T_c. To determine the heat load at $x = 0$, Fourier's law is forward differenced.

$$Q_{cryo} = 2 \cdot k \frac{dT}{dx} A_{element} = 2 \cdot k \frac{T_3 + 4T_2 - 3T_1}{2\Delta x} \cdot \left(2\pi r_c t\right) \tag{3.17}$$

This method and the central differencing in Equation (3.10) have second order accuracy, O $[(\Delta x)^2]$. The factor of 2 in Equation (3.17) is due to the fact that heat is extracted at both sides of the origin, at $x = 0^+$ and $x = 0^-$. At 250 minutes, the maximum temperature at '$x = l$' is 289.7 K and the heat load the cryocooler needs to extract is approximately 26.6 W. This model for the chamber environment is higher than the load for a single cryocooler at 77 K. However, using an insulation system around the copper jacket it is possible to reduce the heat load. This will be examined in the following subsections.

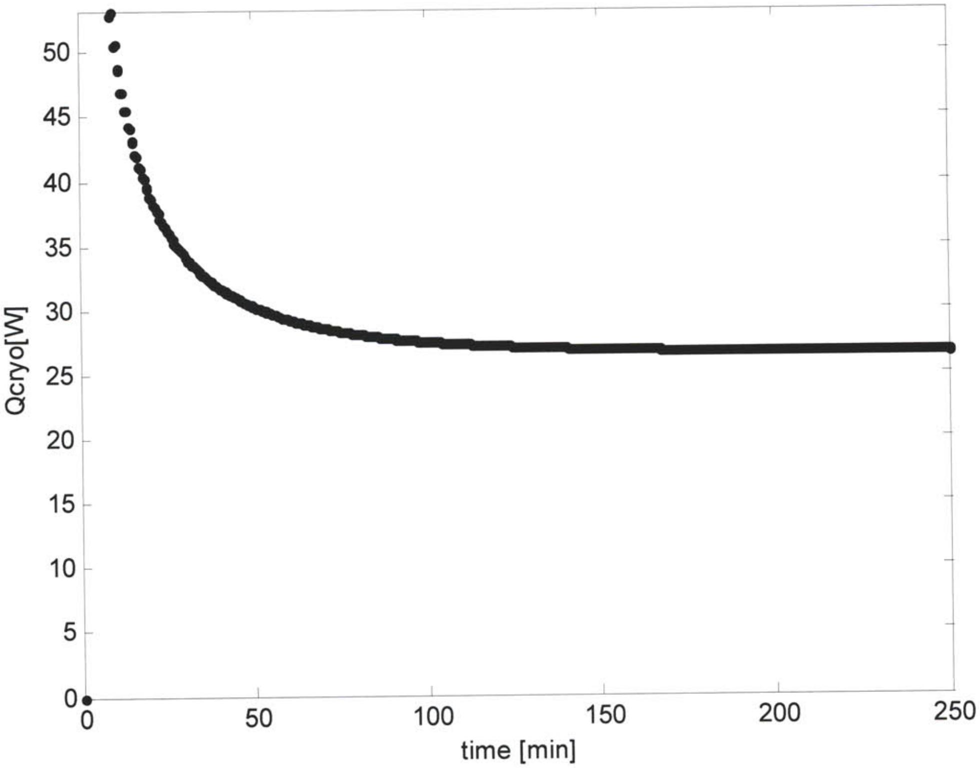

Figure 3.6 Thermal load in TCJ in vacuum chamber as a function of time

The benefit of a simulation model is that different conditions can be predicted without having to physically build them. To determine the performance of the copper solid conductor as the TCJ in space, the volumetric heating term, Equation (3.14) is modified to include the solar flux, G_s, the absorptivity of the material, α_{abs}, and the area of absorption, A_{abs}.

$$\dot{q} = \begin{cases} \dfrac{q_{cryo}}{\text{Volume Element}} & , x = 0 \\ \dfrac{G_s \alpha_{abs} A_{abs} + \varepsilon_t \sigma \left[T_{env}^4 - \left(T_i^n\right)^4 \right] A_c}{\text{Volume}} & , x > 0 \end{cases} \tag{3.18}$$

While this model provides the framework for predicting the performance in space, it is first used to determine the requirements for a 5 W heat load. To achieve this, the overall heat was reduced by approximately 80% from ~25 W in Figure 3.6 to 5 W by adjusting the $G_s \cdot \alpha_{abs}$ term. This assumes that any insulation system used is capable of reducing the heat load by 80%. While this might seem somewhat arbitrary, it is shown in the following section that using MLI in the vacuum chamber has the potential of achieving this.

For the 5 W heat load case, the temperature as a function of time is shown in Figure 3.7a. Here the temperature is shown at the same locations as in Figure 3.5a. All the parameters of the model are identical to the previous 1D FDM, except for the heat loading. Since it takes a longer time to reach an approximate steady-state, the simulation is run for a long time, until 2,000 minutes. The temperature as a function of distance along the coil is shown in Figure 3.7b. In this case the maximum hot end temperature is 148 K. While this is an improvement over the chamber heat loading case, the results indicate that even given a 5 W load, the copper jacket as it is currently designed is insufficient to maintain temperatures below $T_{critical}$ throughout the coil.

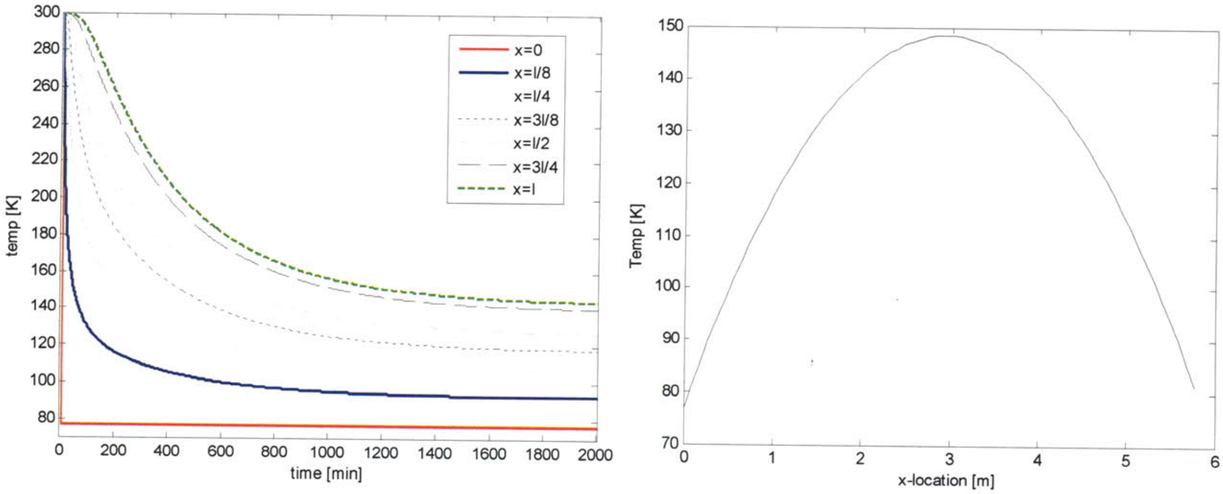

a) Temperature vs. time

b) Temperature vs. distance away from cryocooler

Figure 3.7 Temperature distribution in TCJ in space model

The thermal load for the coil is shown in Figure 3.8. The approximate steady-state heat load after 2,000 minutes is 5.08 W. Again, Fourier's law was used to determine the head load.

One of the challenges in modeling an experiment is determining how much to model. Depending on the chamber pressure, convection can occur by free molecular flow. Also material properties change with temperature. To determine the impact of these effects they were added to the 1D FDM. Details of the models are in Appendix C. In summary, it was found that there is minimal effect from convection and material property changes in the change of temperatures tested in the vacuum chamber. Therefore, for a simple 1D model these effects are ignored.

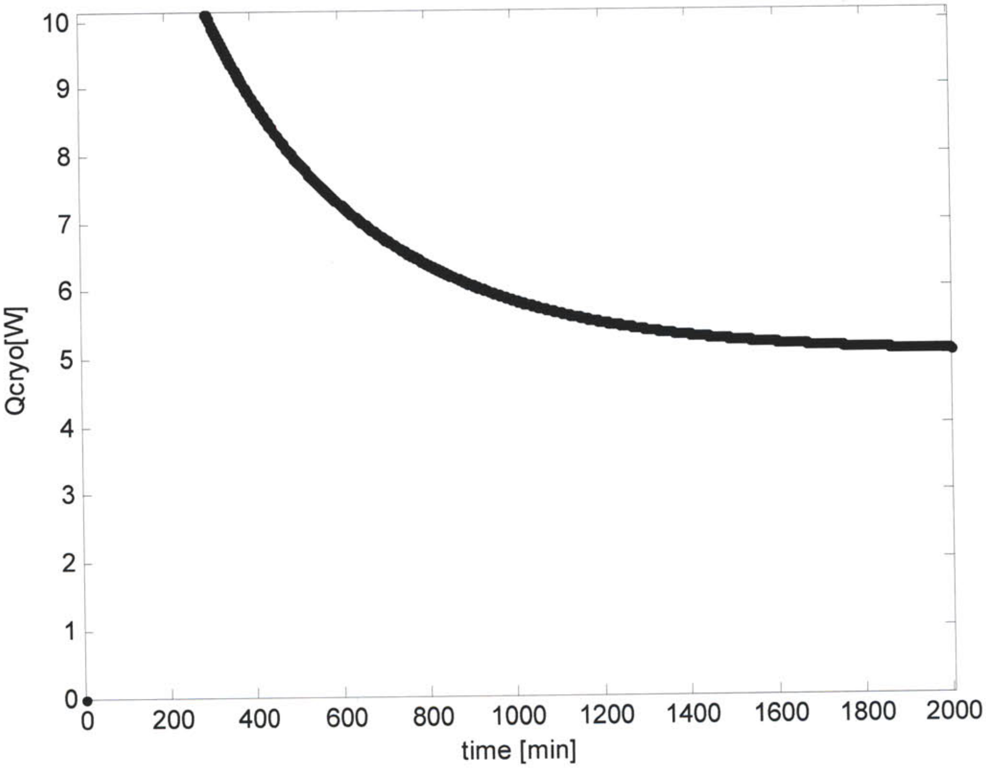

Figure 3.8 Thermal load in TCJ in space model as a function of time

Additionally a 3D FDM complete with a copper jacket and MLI insulation layer is modeled in Appendix C. They are omitted from discussion here because the main goal of the FDM is to provide a quick estimate of the temperature performance of the copper jacket as the TCJ. This can be accomplished easily with the 1D model and discussion is not delayed by details of a more complex model.

3.3 Sinda Model

For comparison with the FDM, a simple 1D model of the copper pipe consisting of 19 nodes was constructed using a commercially available thermal code called Sinda. The Sinda model represents the experimental setup used in the vacuum chamber. Sinda is a general purpose thermal analyzer that was originally developed for aerospace applications to model spacecraft, rockets, and shuttle payloads [63]. Sinda uses lumped parameter representations of a physical system that are governed by diffusion-type equations. A system is divided into a network of thermal mass or thermal capacitance and conductor representations. The 1D Sinda model for the coil is shown in Figure 3.9. The model is limited to 20 nodes since the demonstration version of Sinda was used. The coil is represented by 19 nodes and the 20th node represents the chamber walls. Since the temperature distribution is symmetric for a circular coil, node 1 represents the portion of the coil in direct contact with the cryocooler and node 19 represents the hot end of the coil diametrically opposite the cryocooler at location x = ‘l’.

Each node is given a thermal capacitance, C_{th}, which is a function of the material density (ρ), volume of the node (V), and specific heat of the material represented (c_p). This is given as

$$C_{th} = \rho V c_p \tag{3.19}$$

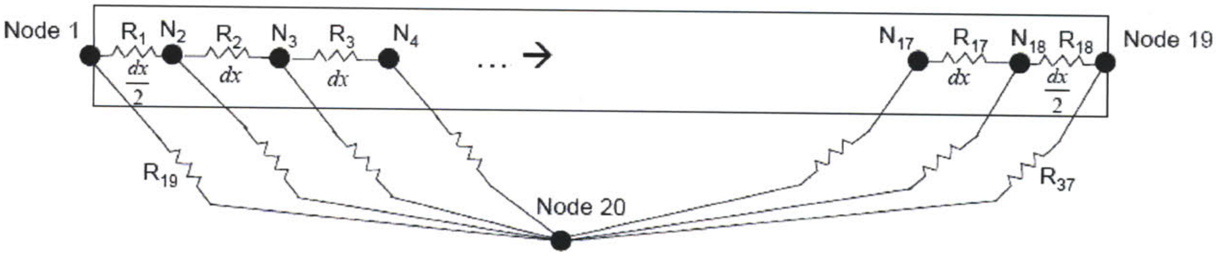

Figure 3.9 Sinda model (1D) for coil

Also initial conditions for each node can be set if necessary. For this model, node 1 is set to T_c = 77 K, the cryocooler cold finger temperature. Also the chamber wall temperature is set by node 20. The thermal relationship between neighboring nodes is described by the thermal resistance. Thermal resistance between nodes on the coil are defined as a function of the area taken up by the node, A_{node}, conductivity, k, and node length L_{node} [64].

$$R = \frac{L_{node}}{k \cdot A_{node}} \rightarrow G = \frac{1}{R} \tag{3.20}$$

The Sinda code uses the thermal conductance, G, which is the inverse of the thermal resistance, R. The relationship between nodes on the coil and the radiation from the walls must also be defined. It is easier to use the conductance for this and is given as

$$G = \sigma \varepsilon A_{node} \tag{3.21}$$

In summary, each node on the coil (nodes 1 through 19) interacts with neighboring nodes given by R_1 through R_{18} and the chamber wall or radiation node (node 20) give by R_{19} through R_{37}. Sinda also allows for heating sources to be defined at nodes; however none are necessary to model the chamber environment since all the heating is from the wall radiation. It is assumed that the wall temperature is constant in time and does not vary spatially.

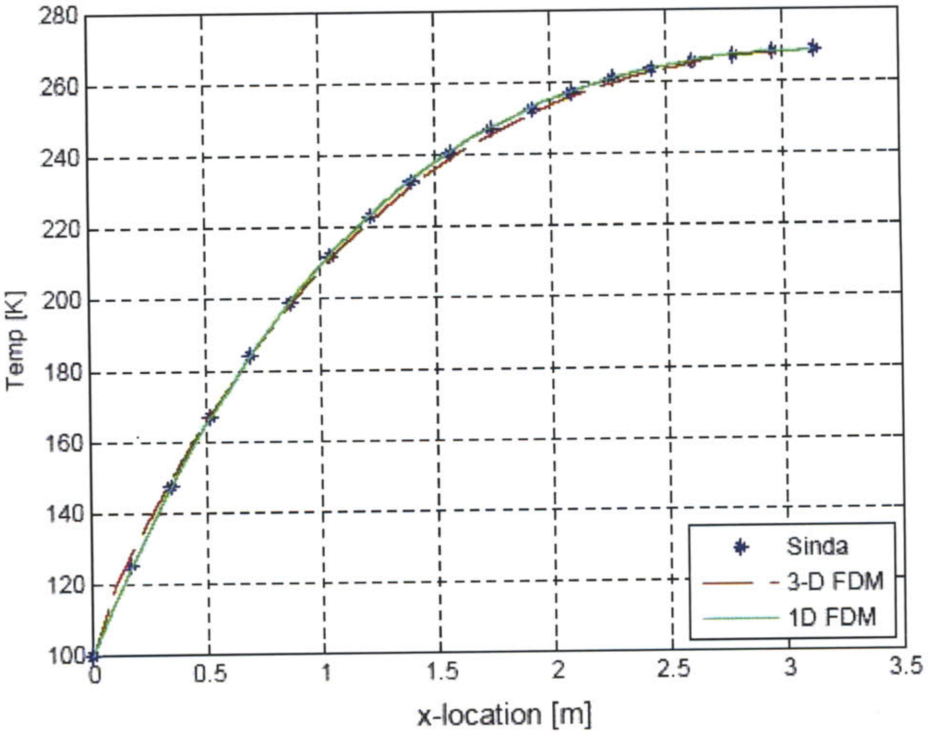

Figure 3.10 Comparison between Sinda and finite difference models showing temperature increase with distance away from the cryocooler (at x = 0)

Comparison between the Sinda model and the FDM is shown by a plot of temperature versus location along half of the coil in Figure 3.10. The steady-state temperature is shown for both the 1D FDM and the 3D FDM, which is detailed in Appendix C. The temperature increases with distance along the coil and the maximum temperature is located opposite the coil, as expected. The models used a coil with a one meter radius and a fixed temperature of 100 K at the cryocooler location. These models are representative of the experimental vacuum chamber discussed in the next section. In conclusion, the finite difference models match well with the Sinda model and have been successfully validated by an analytic model and a commercially available thermal modeling code. Unfortunately, Sinda was not used for any additional modeling due to its high cost and was just used to validate the finite difference models. The next section describes using the FDM to model experimental data.

3.4 Model Verification with Experiment

A toroidal vacuum chamber was designed and built by MIT and Aurora Flight Sciences (formerly Payload Systems Inc.) as a testing facility for the thermal design and is shown with the lid closed in Figure 3.11. The chamber, constructed out of COTS Polyvinyl Chloride (PVC) tubes, has a major radius of one meter, minor radius of 12.5 cm. A Pfeiffer Vacuum Duo 10M rotary vane pump and a Pfeiffer Vacuum TMH 261 turbopump are used to hold a high vacuum (10^{-5} Torr).

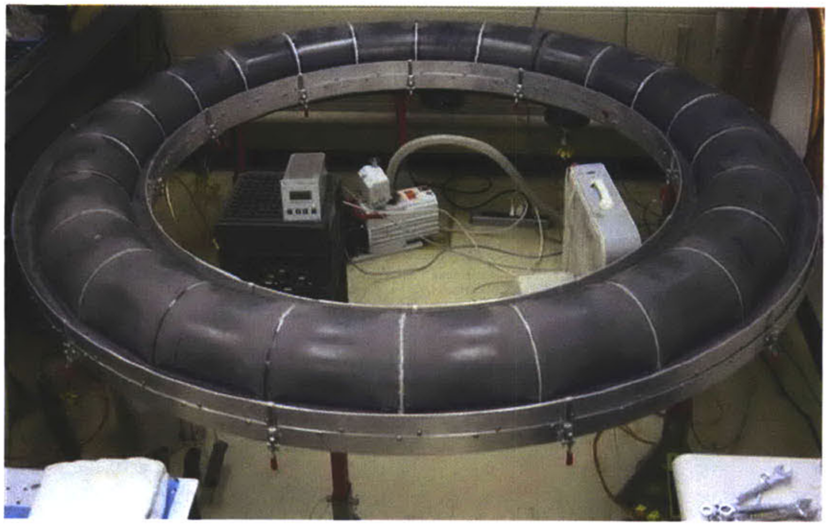

Figure 3.11 Experimental vacuum chamber (closed)

In this initial test, a copper pipe is used as the test article to represent the thermally conductive jacket and is shown in Figure 3.12. A liquid nitrogen feedthrough enters the chamber and wraps around the copper pipe so that conduction with the liquid nitrogen tubing provides cooling for the entire copper pipe and acts as the cryocooler. This cooling system is shown in greater detail in Figure 3.13. Three carbon fiber G10 rods support the copper pipe to keep it centered in the chamber. The G10 has a low thermal conductivity (0.6 W/m·K at 295 K) to minimize heat conduction to the copper from the walls [65]. Ten thermocouples are inside the chamber via two instrumentation feedthroughs. Several experiments have been conducted under repeatable conditions yielding consistent data. A single tank of liquid nitrogen allows for approximately three hours of cooling time.

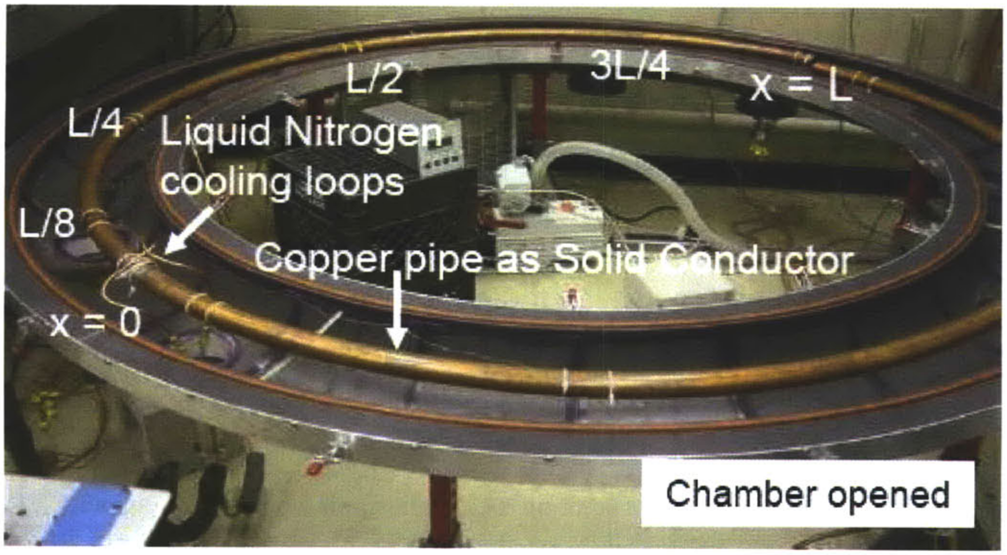

Figure 3.12 Experimental vacuum chamber (opened) with copper thermally conductive jacket

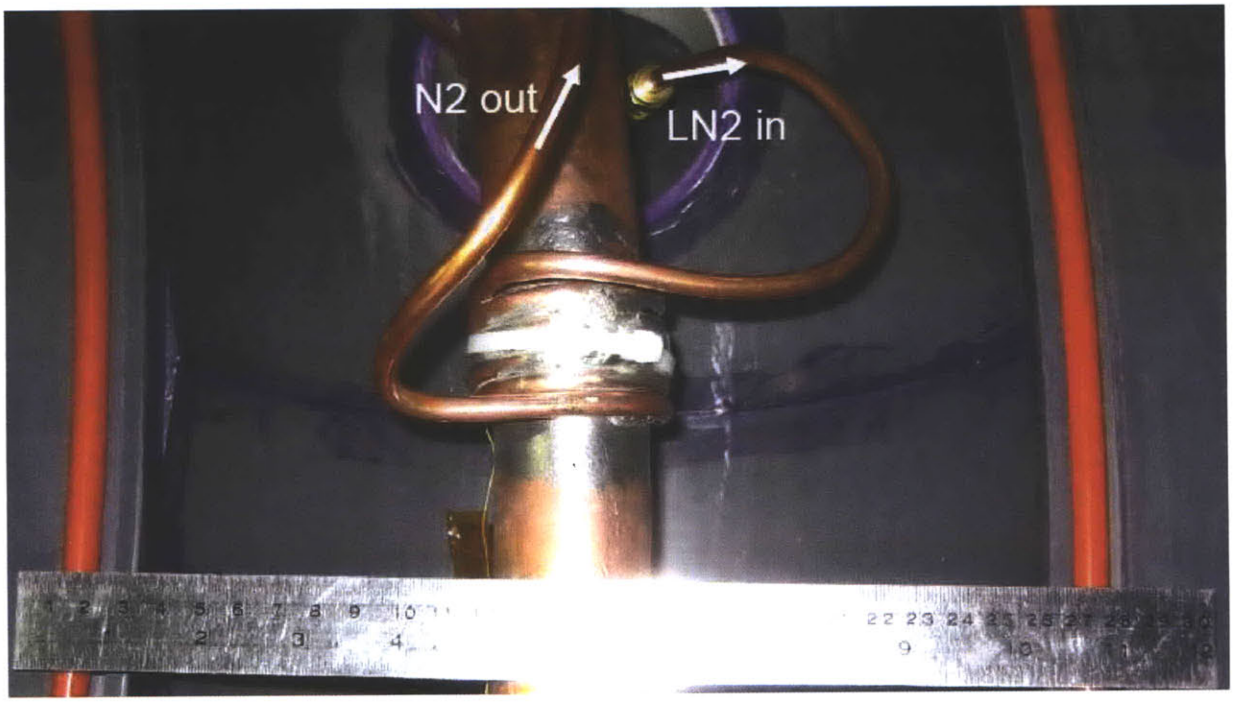

Figure 3.13 Liquid nitrogen cooling loops around copper test article

3.4.1 Copper Pipe Tests

The temperature versus time for a representative experiment is shown in Figure 3.14. Only six of the ten thermocouples are shown in Figure 3.14 for clarity. A thermocouple on the nitrogen cooling loops is labeled 'cryo' and shown by the red dots and a thermocouple right next to the nitrogen cooling loops is labeled 'nextTc', shown by the dashed black line. The remaining thermocouples on the pipe are located at 'l/8' (blue dots), 'l/4' (cyan dots), 'l/2' (magenta dots), and 'l' or 'T-hot' (green dots). There is also a thermocouple located outside the chamber on the outlet of the liquid nitrogen cooling loops, shown by the solid black line in Figure 3.14. Solid lines for the FDM corresponding to each of the thermocouple locations are shown by solid lines of the same color. The FDM uses the temperature data at the cooling loops, 'cryo', as the cold temperature, T_c, for the boundary condition in Equation (3.9) at the origin. There is also a thermocouple mounted on the inside of the chamber wall in the vacuum. This wall temperature data, not shown in Figure 3.14, is used to determine the radiative heat from the wall. The wall temperature at the start of the experiment is the same initial temperature as the copper pipe, which is 297 K. The coldest wall temperature was 296 K measured at the 140 minute mark. Overall, the wall temperature was relatively constant with time. Since the FDM uses the wall temperature measurements, even these small changes are modeled. The properties of the copper pipe in the chamber are the same as in the previous 1D FDM section; the pipe half length, 'l', is 2.92 m and a constant thermal conductivity for copper (410 W/m·K) was used.

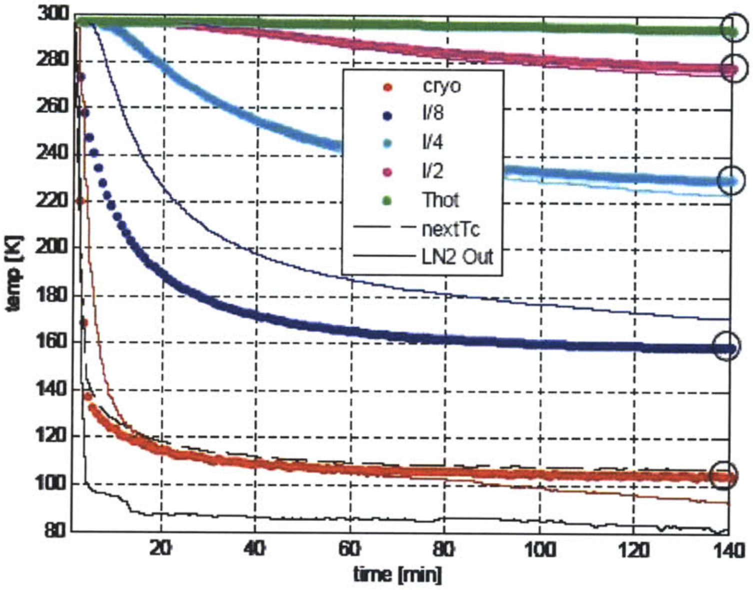

Figure 3.14 Comparing transient temperature of experiment (dots) with FDM (solid lines of same color)

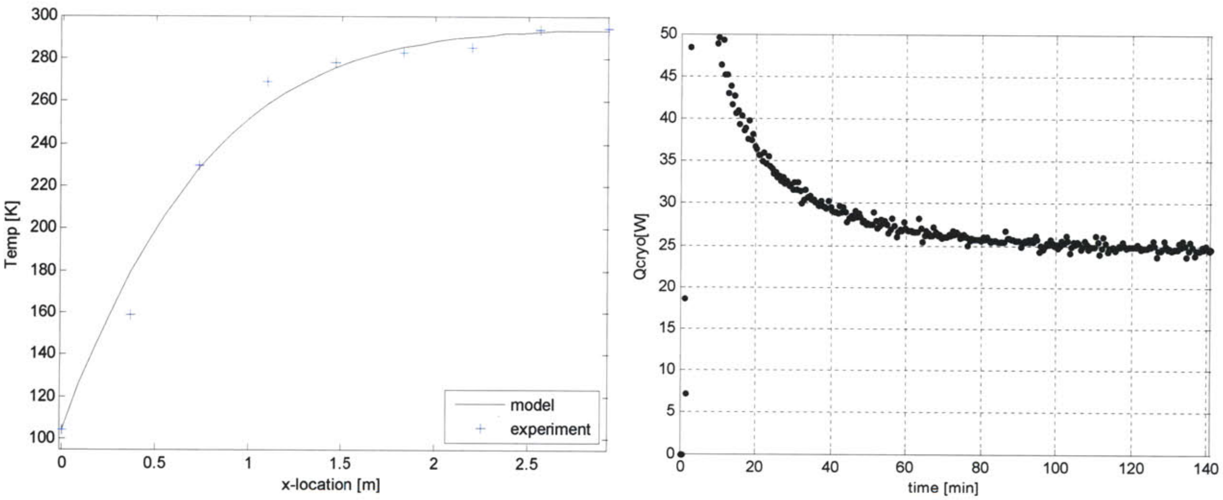

a) Temperature vs. distance from LN2 cooling loops b) Thermal load of TCJ vs. time

Figure 3.15 Temperature and thermal load of TCJ after 140 minutes

The thermocouple measurements in Figure 3.14 at the 140 minute mark are used as an approximate steady-state temperature for comparison with the FDM. These temperatures are circled in Figure 3.14 and are plotted in Figure 3.15a as a function of distance along the coil, shown by the blue '+' marks. All nine thermocouples along the coil are used in Figure 3.15a. The temperature along the coil for the FDM is shown in Figure 3.15a by the solid black line. To determine how much heat a cryocooler is required to extract, the total absorbed heat flux due to the wall radiation on the coil, Equation (3.14) is used. However, this calculation requires the effective emissivity, ε_t, to be known.

Using the steady-state temperature data to find the approximate steady-state heat load, the effective emissivity which minimized the mean square error between the measured data and the finite difference model was determined. In Figure 3.15 this resulted in an effective emissivity of $\varepsilon_t = 0.2$. The thermal load that is extracted by the liquid nitrogen loops is shown in Figure 3.15b and is approximately 25 W after 140 minutes.

Overall, the experimental data had a faster transient cooling rate than predicted by the FDM. Since the purpose of the FDM was to match the experimental data to the steady-state conditions and not the time-varying conditions, discrepancies between the transient temperature and transient model are not critical. The model matched all the experimental data to within 10 K at the end of the data run (approximately 2.5 hours). The time-varying discrepancies between the model and the data are potentially due to the film layer formed in the liquid nitrogen cooling loops which gives unsteady cooling. Also heat introduction from the G10 spacers holding up the copper pipe and any heat through the thermocouple wires were not incorporated in the model.

There are three important results from the experiments with the copper jacket as the TCJ around the HTS wires. First, it was experimentally confirmed that a solid conductor does not allow for isothermalization of the coil. One possible solution is to use multilayer insulation around the copper to reduce the heat load. This will be investigated in the next section.

The second result is that the chamber environment has been modeled and a method of finding the effective emissivity has been determined. This procedure will be used in later chapters to characterize the heating environment of various vacuum chambers for testing the heat pipe.

Additional results from the experiment are the lessons learned from the experimental procedure. It was determined that thermally grounding the thermocouples is critical for obtaining good temperature data. This was done by wrapping the thermocouple wire several times around the copper pipe. Also good contact between the thermocouple bead and the copper pipe is important. The thermocouples used in the experiment were also used by the heat pipe in later chapters, so careful calibration of the thermocouples was carried out. Thermocouples were calibrated by submerging them in ice water and liquid nitrogen.

3.4.2 MLI Tests

Since tests with the copper TCJ indicate that the temperature gradient is too high to support an entire HTS coil at superconducting temperatures, MLI was wrapped around the copper TCJ in order to reduce the heat load. This system is shown in Figure 3.16. Sheets of Mylar that were 56” x 84” were obtained from Edmund Scientific [66]. Approximately five total sheets were used wrap the entire coil. The MLI was crinkled by hand so that conduction between layers was minimized. A single sheet allowed for approximately seven layers, which were loosely wrapped around the copper pipe. Neighboring Mylar sheets were overlapped to avoid any gaps in MLI coverage. The thermocouples from the previous tests were still bonded to the copper pipe and the wire leads were carefully taken out through small gaps in neighboring sheets at one location. Before testing the vacuum chamber was pumped down overnight to allow air between the layers to escape.

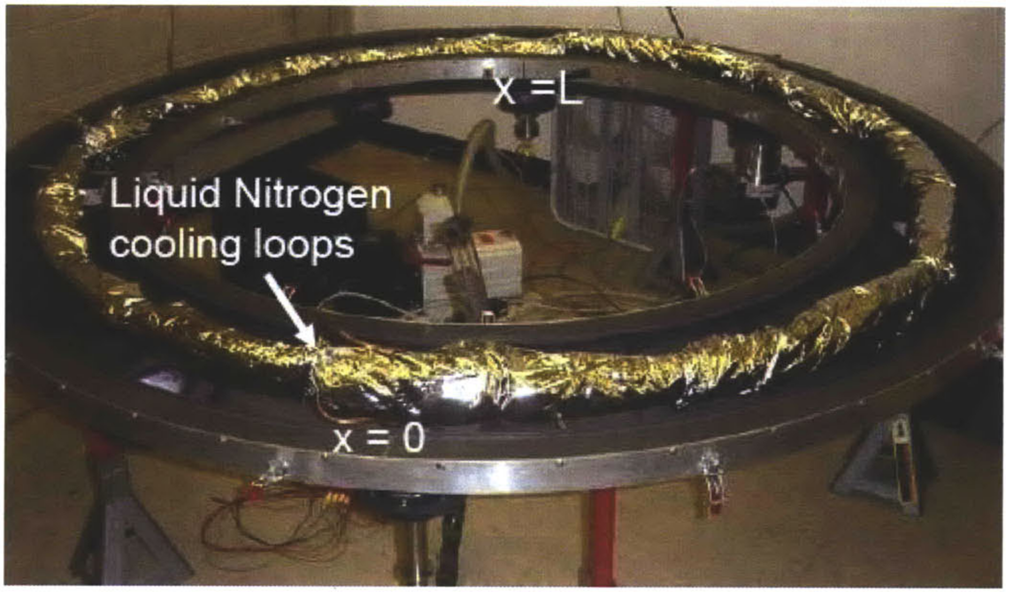

Figure 3.16 Copper jacket wrapped in MLI

Tests with the MLI followed the same procedure as for the copper pipe tests and the results of a representative test are shown in Figure 3.17. The temperature versus time after approximately 550 minutes is shown in Figure 3.17a. Tests with MLI took longer in order to reach an approximate steady-state temperature because the MLI insulates the copper pipe from changes in temperature. The transient temperature data is excluded because the data used to estimate the effect of MLI is the temperature at the end of the test (Figure 3.17a). From the approximate steady-state temperature, the effective emissivity using MLI was determined to be 0.021, which is a reduction of almost one order of magnitude. The MLI also significantly reduced the heat load to approximately 8 W, as seen in Figure 3.17b. Compared to the 25 W heat load without the MLI, this is a reduction of approximately 70%. Earlier simulation models in Section 3.2 assumed an insulation system capable of reducing the heat load on the order of 80% would be beneficial for a flight design. The MLI used in this thesis was close to demonstrating this capability. The 10% difference in heat load between the MLI used in the experiment and the desired MLI performance could be achieved by using more layers of MLI. However, even though the heat load is reduced the temperature is still greater than $T_{critical}$ throughout most of the coil. Therefore, the next step is to investigate the use of a copper pipe as the TCJ with a working fluid to provide isothermalization of the coil.

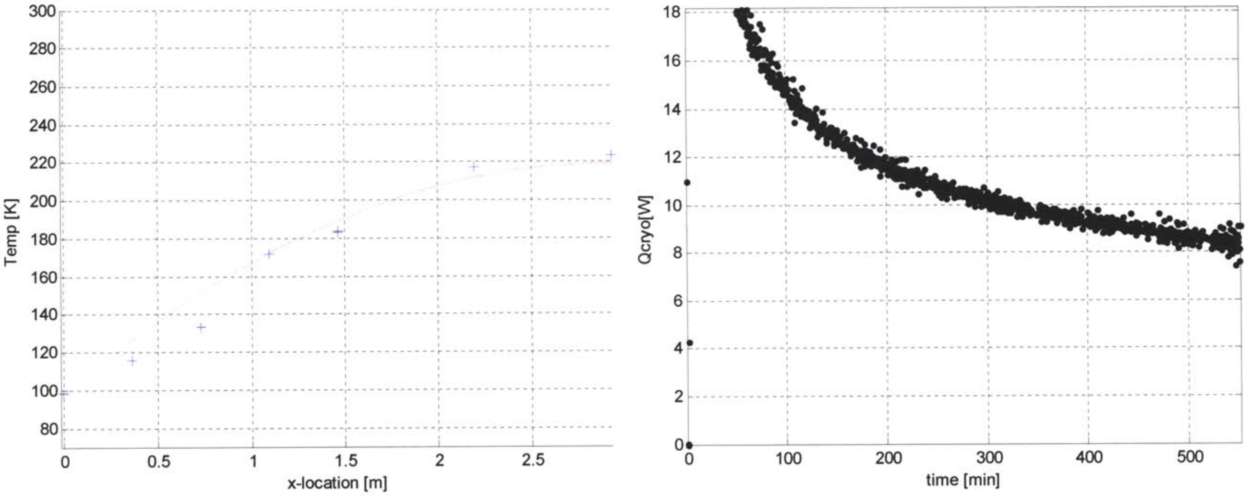

a) Temperature vs. distance from LN2 cooling loops b) Thermal load of TCJ vs. time

Figure 3.17 Temperature and thermal load of TCJ with MLI

3.5 Summary of Modeling

The research in this chapter investigated the use of a copper jacket wrapped around the HTS wires as a means for maintaining the coil below the critical temperature. First, an analytic model was used to determine the general temperature distribution using a single cryocooler. It was determined that a large temperature gradient exists both when the wire bundle is exposed to the entire heat load and also when a copper pipe is used around the wires to carry the heat load. One important use for the analytic model was that it validated the finite difference model. A finite difference model was constructed in order to investigate the temperature as a function of time. This was necessary for comparing temperature data from an experimental test. The FDM and the experiment were used to model the vacuum chamber environment and obtain an effective emissivity of the system. Experimental testing of the copper pipe, both with and without MLI, indicated that a large temperature gradient existed in the chamber environment. In order to obtain a more uniform temperature distribution around the coil, a heat pipe operating at cryogenic temperatures is investigated in Chapter 4.

Chapter 4 HTS Heat Pipe

The design and fabrication of a cryogenic heat pipe for cooling the HTS wires is investigated in this chapter. As a proof-of-concept a straight heat pipe was designed and built. After successful operation of the heat pipe, HTS wires were inserted into the pipe. The results of this test demonstrate the feasibility of operating HTS coils inside a heat pipe vapor space.

This chapter is divided into three main sections; the design of the heat pipe, the implementation of the heat pipe, and the experimental results. For the design of the heat pipe, the heat pipe power capacity, the temperature at the end of the heat pipe and any potential performance limitations are explored. The design of a heat pipe in space and a heat pipe for testing in a ground vacuum chamber are different because they have different heat load requirements. The basic heat pipe theory for power capacity is first applied to a space design. To determine the heat load on the heat pipe from the chamber environment, the finite difference model developed in Chapter 3 was used. The section on implementation of the heat pipe discusses how the HTS wires were inserted. The lessons learned were used to build a large circular heat pipe in Chapter 5. Finally, the experimental results show the heat pipe without the HTS wire reaching saturation condition. The heat pipe with the HTS wires also show that superconductivity was observed when the heat pipe reaches isothermal temperature below $T_{critical}$. The heat pipe was tilted to test the operation of the wick and ensure that pooling of the working fluid at the condenser was not present. Verifying the models with the experimental data ensures that a flight version of the system can be built with confidence.

4.1 Heat Pipe Power Capacity

Heat pipes work by using the two-phase flow properties of a working fluid. There are three operating sections for a heat pipe: the condenser; evaporator; and an adiabatic section. A sketch of a heat pipe is shown in Figure 4.1. Power input (Q_{in}) into the heat pipe causes the working fluid to evaporate in the evaporator. The vapor then flows to the condenser region where it condenses, releasing its heat, and power (Q_{out}) flows out of the heat pipe. Capillary action in the wicking layer, where the liquid resides, pumps the liquid from the condenser to the evaporator. In order for circulation of the liquid and gas in the heat pipe, the capillary pressure drop must overcome the sum of pressure drops in the liquid and vapor phases plus the gravitational head. The standard pressure balance equation for a heat pipe is given by:

$$\Delta P_c = \Delta P_v + \Delta P_l + \Delta P_g \tag{4.1}$$

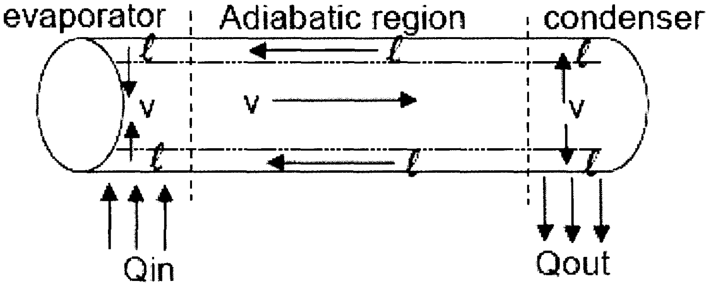

Figure 4.1 Basic operation of a heat pipe

The maximum capillary head, ΔP_c, is given by

$$\Delta P_c = \frac{2\sigma}{r_c}\cos\theta \tag{4.2}$$

where σ is the liquid surface tension. Figure 4.2 illustrates the pore radius, r_c, of the mesh used for the wicking layer and the contact angle, θ, for the liquid with the wick. For a perfectly wetting liquid $\theta = 0°$. Also shown in Figure 4.2 is the pipe diameter, d, and the diameter of the wire mesh, d_w.

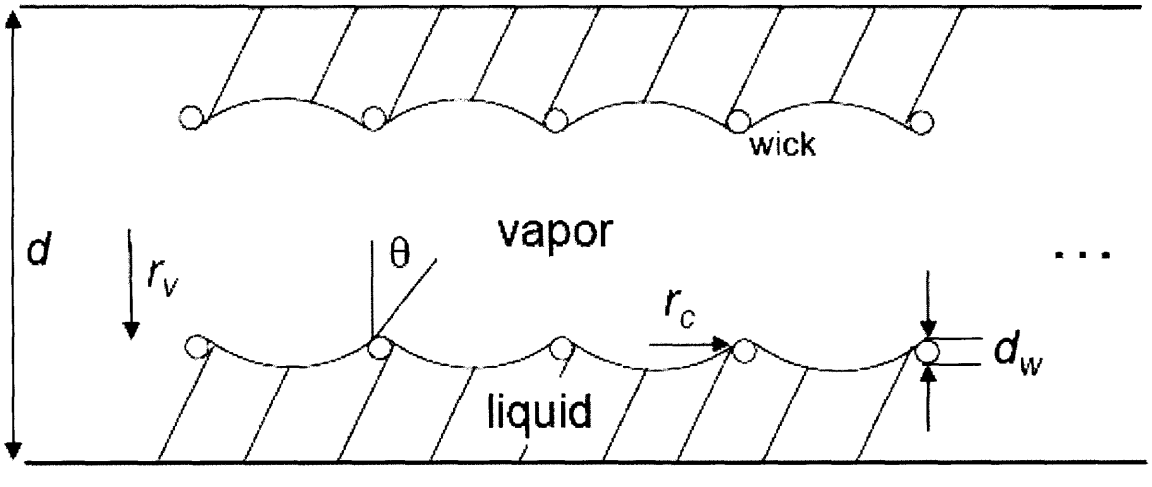

Figure 4.2 Sketch of wick and pore parameters (not to scale)

The liquid pressure drop, ΔP_l, is given by Darcy's law for flow through porous media

$$\Delta P_l = \frac{\mu_l L_{eff} \dot{m}}{\kappa \rho_l A_w} \tag{4.3}$$

where μ_l is the liquid viscosity, ρ_l is the liquid density, $\dot{m}$ is the liquid flow rate, and A_w is the cross-sectional area of the wick. The effective length of the heat pipe, L_{eff}, is the distance from the center of the condenser to the center of the evaporator. The permeability of the wick, κ, is a function of the wick type, wick effective pore radius, permeability, and porosity. Empirical values for κ have been calculated for commercially available wire meshes in Appendix D [67].

The vapor pressure drop, ΔP_v, is given by

$$\Delta P_v = \frac{64}{\mathrm{Re}_{D_h}} \frac{L_{eff}}{D_h}\left(\tfrac{1}{2}\rho_v V_v^2\right); \quad D_h = 4\frac{A_v}{P_w} \tag{4.4}$$

where ρ_v is the liquid density, V_v is the liquid velocity, $\mathrm{Re}_{D_{hv}}$ is the Reynolds number of the vapor. The hydraulic diameter, D_h, is a function of the vapor flow area, A_v, and the wetted perimeter, P_w. The vapor pressure drop is usually much smaller than the liquid pressure drop and for initial calculations can be neglected for cryogenic heat pipes [35]. It is shown in Appendix D that for the straight heat pipe designed in this chapter the capillary pressure drop is five orders of magnitude greater than the vapor pressure drop.

The gravitational pressure head depends on the relative elevations of the evaporator and condenser. This hydraulic pressure difference is given by

$$\Delta P_g = \rho_l g L_{eff} \sin\phi \tag{4.5}$$

where ϕ, the angle made by the heat pipe with the horizontal, is positive when the condenser is lower than the evaporator. For a horizontal heat pipe with a perfectly wetting liquid and ignoring the vapor pressure drop, Equation (4.1) becomes

$$\frac{2\sigma}{r_c} = \frac{\mu_l L_{eff} \dot{m}}{\kappa \rho_l A_w} \tag{4.6}$$

Substituting $\dot{Q}_{\max} = \dot{m}_{\max} h_{fg}$, where h_{fg} is the latent heat of vaporization, and solving for $\dot{Q}_{\max}$, the maximum power capacity of the heat pipe is given by

$$\dot{Q}_{\max} = \frac{2\sigma}{r_c}\frac{\kappa \rho_l A_w h_{fg}}{\mu_l L_{eff} \dot{m}} = 2\left(\frac{\rho_l \sigma h_{fg}}{\mu_l}\right)\left(\frac{A_w}{L_{eff}}\right)\left(\frac{\kappa}{r_c}\right) \tag{4.7}$$

The first quantity in Equation (4.7) is known as the figure of merit, M, for a working fluid. The figure of merit is a function of the fluid properties and varies as a function of temperature. A working fluid has a given range of temperature over which it performs favorably and each fluid has an optimum operating temperature. The higher the merit number, the better the fluid performs. The second quantity in Equation (4.7) contains design parameters of the heat pipe. Characteristics of the wicking structure are in the third quantity. Technically, the wick area is also a function of the number of layers of mesh and wire type used, but the main driving component is the diameter of the pipe. The wick area is given by

$$A_w = 2\pi d d_w N \tag{4.8}$$

where N is the number of layers of screen mesh. The factor of two accounts for overlapping wires in the mesh.

Since a heat pipe is operating at or near the saturation temperature of a working fluid, there are a few suitable options including nitrogen, ammonia, and oxygen. This research uses nitrogen as a working fluid because of its low cost, safety, and ease of handling compared to other possible choices. These reasons are also echoed by Prager [39]. Characteristics of nitrogen can be found in Table 4.1

Table 4.1 Properties of Nitrogen at saturation conditions (77 K, 1 atm)

Property	Symbol	Value
Liquid density	ρ_l	798 kg/m^3
Surface tension	σ	$8.8\cdot10^{-3}$ N/m
Heat of vaporization	h_{fg}	$0.1995\cdot10^{6}$ J/kg
Liquid viscosity	μ_l	$1.51\cdot10^{-4}$ Pa·s
Figure of merit	M	$9.1\cdot10^{9}$ W/m^2

4.1.1 Single mesh number design

The design goal for an EMFF HTS heat pipe operating in space is to have a power capacity of approximately 5 Watts. The dimensions of the heat pipe should be large enough to contain a stack of HTS wire and be long enough to demonstrate that a flight sized coil could be cooled with as few connected heat pipes as possible. Since a cryocooler is used on the condenser end to extract power, the number of heat pipes in the system determines the number of cryocoolers necessary.

In this subsection, the heat pipe designed has the thermal requirements for a flight system (5 Watts), with a size requirement for a ground test. This is to gain insight into a flight design and also to easily migrate a flight design into a testable system. For this reason, a straight heat pipe of one meter in length is selected. This is also applicable for using EMFF on small satellites. As a reference, the length of the copper jacket in the vacuum chamber tested in Chapter 3 is approximately three meters in circumference. The height of a single stack of HTS wires with 33 turns in the EMFF testbed is 1.32 cm. For a 100 turn stack, the total height is 4 cm, which fits within a standard 1.5 inch diameter pipe. The container material is copper, which is chosen since it has a high thermal conductivity and its ease of use simplifies the manufacturing process.

A wicking structure can be as simple as a metallic screen mesh, similar to the mesh material on a screen door. A screen mesh is easy to obtain commercially [68] and is characterized by a mesh number, which is the number of squares per square inch. The pore radius is related to the mesh number by

$$r_c = \frac{1}{2N_{mesh}} \tag{4.9}$$

where N_{mesh} is the mesh number in English units. It is important to convert N to meters in order to obtain r_c in SI units since mesh numbers are commonly given in English units.

Data for a screen wire mesh pore radius and permeability is summarized in Table 4.2. Specifications for #30, #100, and #200 wire meshes were given by the Mills [67] and for the #250 wire mesh by Reay [35]. A plot of the pore radius as a function of wire mesh number is also shown in Figure 4.3. The curve for pore radius shown in Figure 4.3 matches well with the data given by Mills, but is not exactly the same as the data on the #250 mesh for Reay. One of the challenges of heat pipe design is implementing the design based on analysis because commercially available meshes do not always exhibit the same characteristics as theory. For example, for some COTS meshes, the pore radius given by specification sheets is different from the pore radius determined from Equation (4.9). Another example is the wick permeability, which is described in more detail in Appendix D.

Table 4.2 Wire mesh properties

Mesh number [Reference]	Pore radius, r_c [mm]	Permeability, κ [$\cdot 10^{-10}$ m^2]
#30 [Mills]	0.430	25
#100 [Mills]	0.120	1.8
#200 [Mills]	0.063	0.55
#250 [Reay]	0.002	0.302

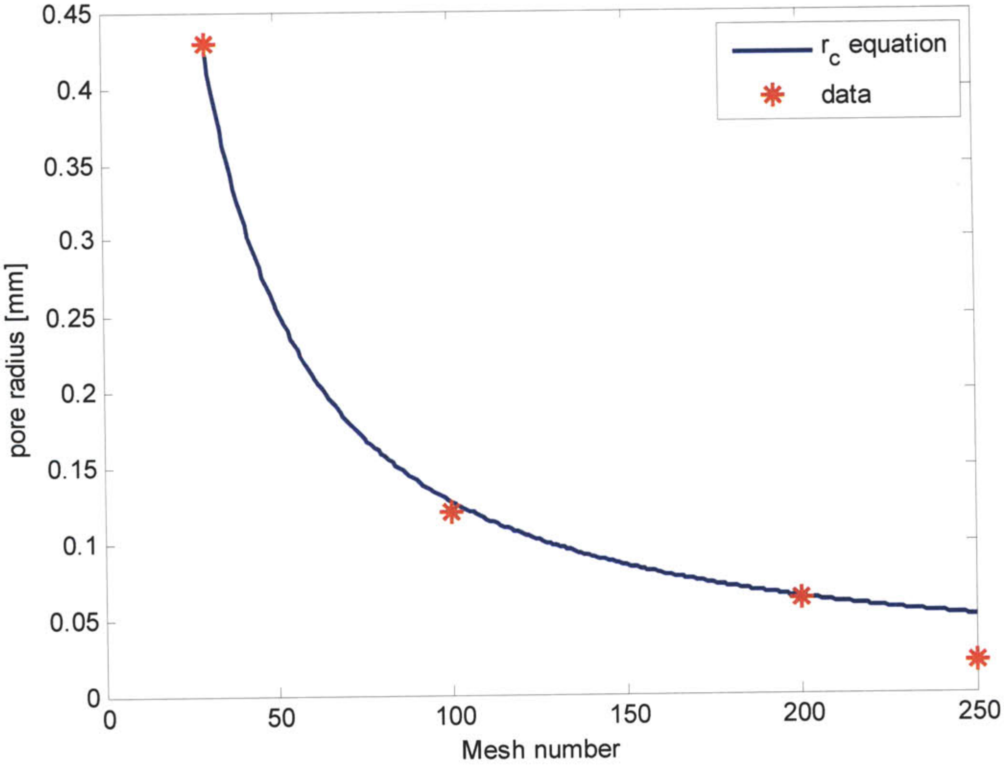

Figure 4.3 Pore radius vs. mesh number

Using data on the screen mesh from Table 4.2, the performance of only the #100 and #250 wire mesh is compared to gain preliminary insight into the heat pipe power capacity. Using Equation (4.7), the power capacity for a #100 and #250 wire mesh as a function of the pipe diameter (*d*) is shown in Figure 4.4. Four layers of the wrapped screen were used. The power increases linearly with pipe diameter. This trend is expected because as the pipe diameter increases the flow area for the liquid also increases which allows for more heat to be pumped through the pipe. The heat capacity also increases with additional layers of screen since the flow area increases. The results in Figure 4.4 indicate that a one meter length pipe with a pipe diameter that can accommodate an HTS stack between 33 turns (d = 1.5 cm) and 100 turns (d = 4.0 cm) has a heat capacity less than 5 Watts. This design does not meet the 5 W power requirements for a flight heat pipe.

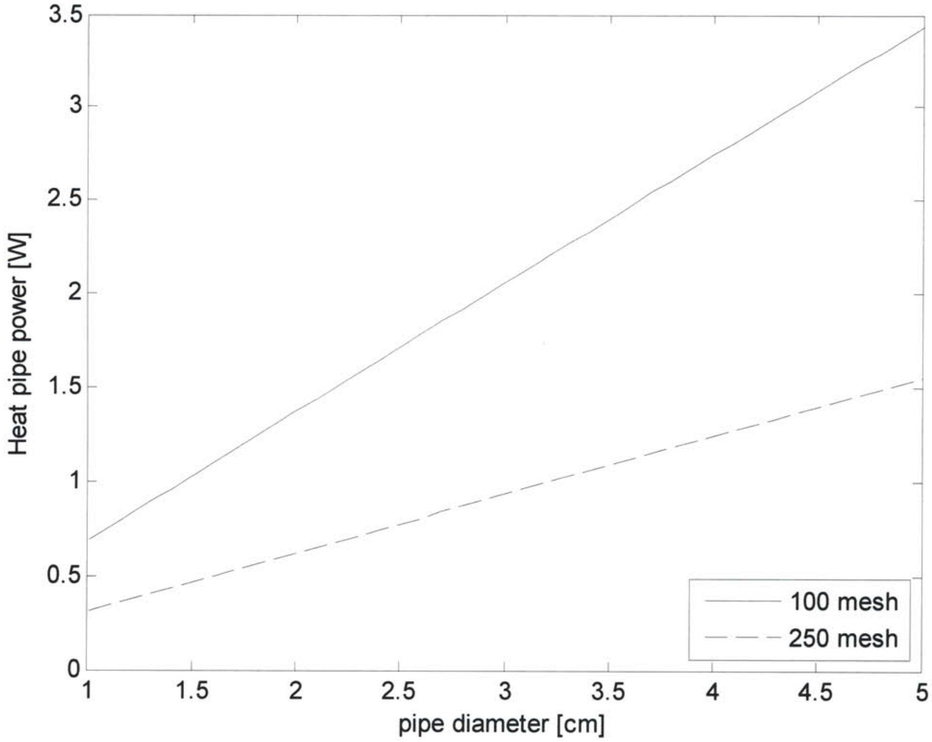

Figure 4.4 Heat pipe power vs. pipe diameter using #100 and #250 wire mesh screens for a 1 m length pipe

Judging from the results of Figure 4.4, one might think that a lower mesh number is favorable; however there is an interesting trade-off that exists for screen meshes. A high permeability, κ, which occurs in lower mesh numbers, allows for liquid to travel from the condenser to the evaporator more easily. However, lower mesh numbers also have a larger pore radius. For high capillary pressure, a smaller pore radius is more favorable. Therefore, the ratio of permeability to pore radius, κ/r_c is a key quantity in Equation (4.7), which varies with mesh number. This ratio is shown in Figure 4.5 as a function of mesh number and indicates that using either a small mesh number screen less than #50 or a large mesh number greater than #250 is favorable. However, using a larger data set for multiple screen mesh numbers is explored in the next subsection.

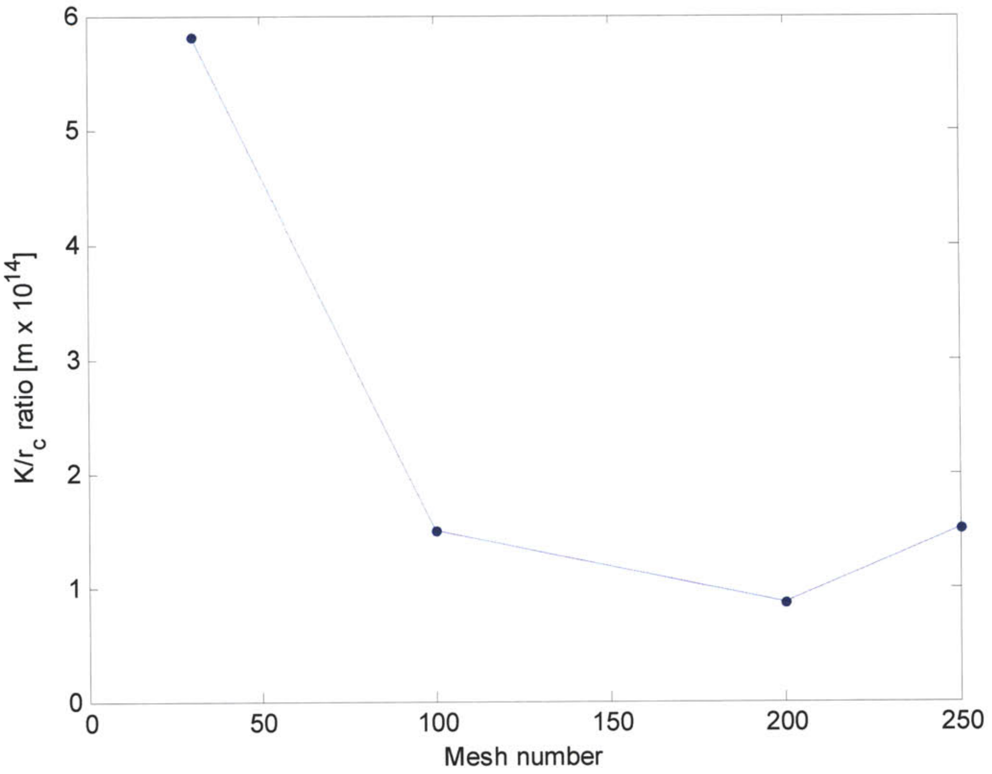

Figure 4.5 Ratio of permeability to pore radius versus mesh number

4.1.2 Multiple mesh number design

In order to maximize the benefits of a small pore radius from fine screen meshes and the high permeability from coarse screen meshes, two different mesh types are investigated. In this example two layers of a #100 mesh screen and two layers of a #250 mesh screen are used. The coarse #100 mesh is located in between the copper wall and the fine #250 mesh as shown in Figure 4.6. The fine mesh acts to hold the liquid in the wick structure and provides the capillary pumping pressure. The coarse mesh allows for the liquid to travel with ease to the evaporator. The results for this design are shown in Figure 4.7. For a 100 turn HTS stack, requiring a 4 cm pipe diameter, the power of the heat pipe is approximately 10 Watts, which meets the requirements for a heat pipe operating in space. This is an improvement of almost an order of magnitude over a design using just a #250 mesh screen with four layers which was analyzed in the previous section.

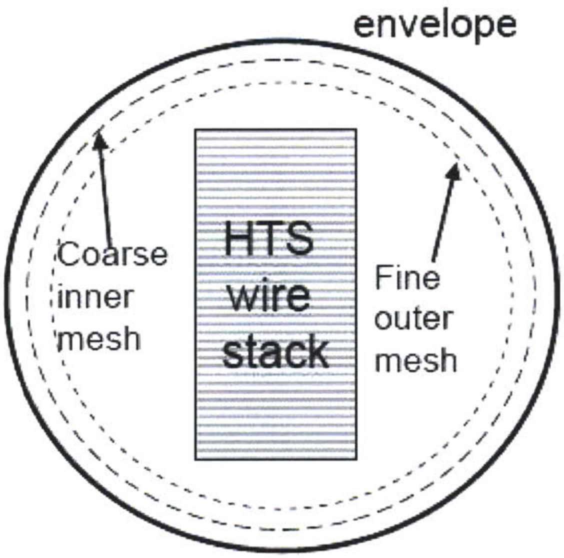

Figure 4.6 HTS wire stack inside a heat pipe

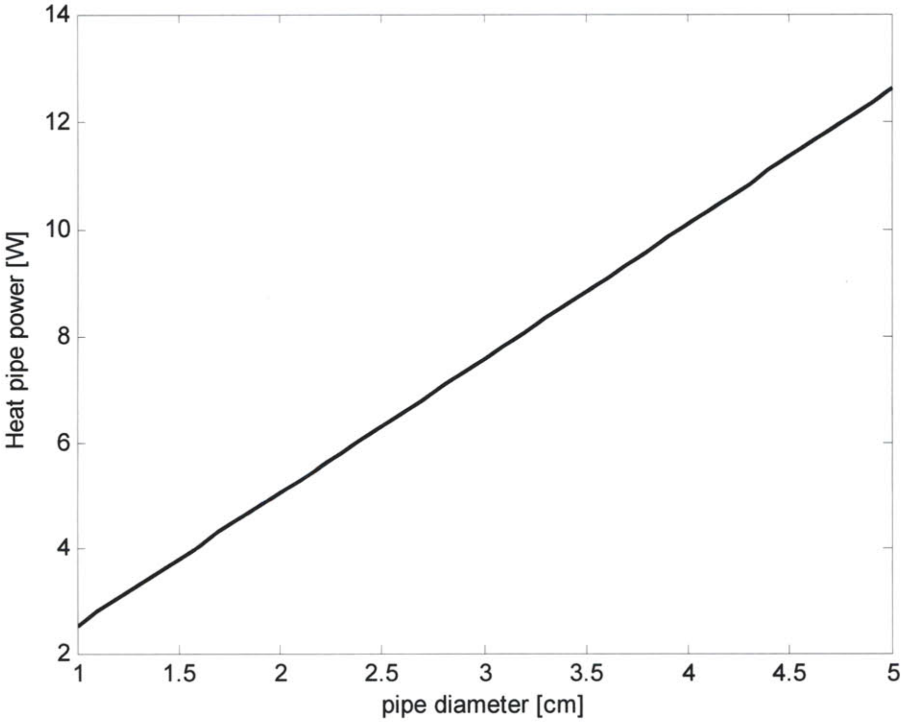

Figure 4.7 Heat pipe design for a #100 inner mesh, #250 outer mesh (2 layers each), 1 m pipe.

Since using a more coarse mesh is favorable, the power for a heat pipe using a #30 mesh inner layer is shown in Figure 4.8 by the red dashed line. A heat pipe with the #30 mesh inner layer shows large improvements over the #100 inner mesh design. Therefore using multiple mesh numbers allows the heat pipe to achieve a performance that meets larger power requirements. Designing for a heat pipe using commercially available screen meshes for ground testing is explored in greater detail in Appendix D.

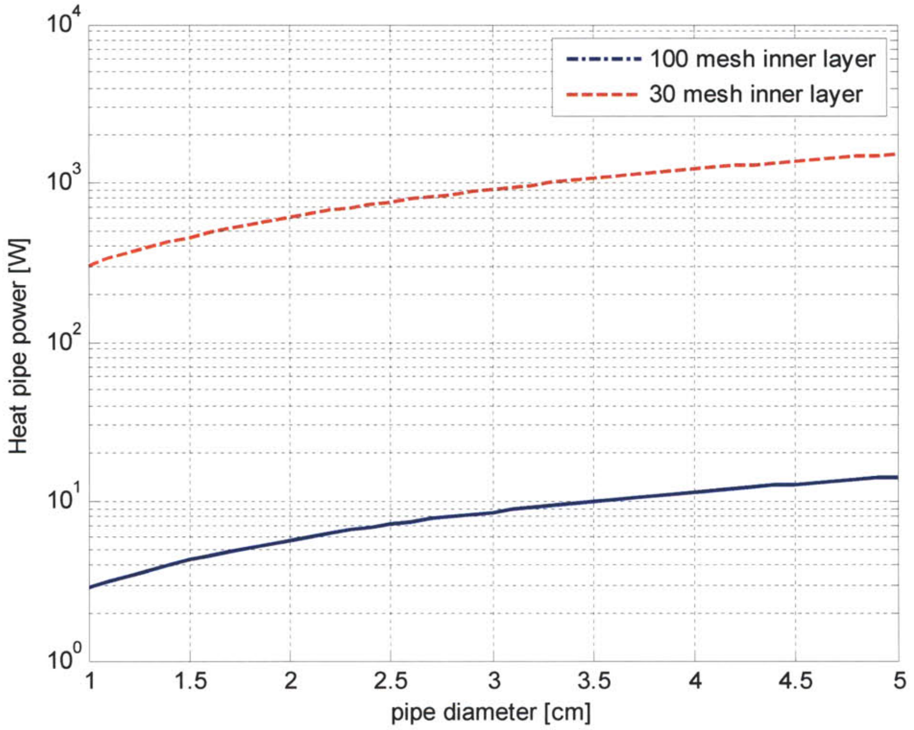

Figure 4.8 Heat pipe designs using 2 layers of either a #30 or #100 inner mesh layer; #250 outer mesh (2 layers)

4.2 Design for a Straight Heat Pipe Inside a Vacuum Chamber

4.2.1 Determining the Heat from the Environment

The first step in designing for the heat pipe is determining the heat from the chamber environment. The heat flux due to radiation sets the minimum power capacity required of the heat pipe. The heat from the chamber is a function of the wall temperature (T_w), effective emissivity (ε_t), and the area of the pipe (A_{pipe}). This is given by

$$Q_{chamber} = \varepsilon_t \sigma \left[T_w^4 - \left(T_{pipe} \right)^4 \right] A_{pipe} \tag{4.10}$$

The unknown quantity in Equation (4.10) is the effective emissivity and to determine ε_t, a heat pipe was tested without any working fluid inside a vacuum chamber. This system is simply a solid conductor, which was modeled by the finite difference method in Chapter 3. The system was cooled down and the experimental temperatures were compared to the FDM. Ten thermocouples were used and were placed in pairs at five different locations, shown in Figure 4.9. The origin or '0' location (red thermocouples) is right next to the reservoir of LN2 used to cool the pipe at a single location. Since this pipe eventually functions as a heat pipe, the LN2 reservoir is also called the condenser. The other thermocouple locations are 10 cm (blue colored), 25 cm (green colored), 50 cm (black colored), and 75 cm (magenta colored) away from the LN2 cooling reservoir. The transient temperature is shown in Figure 4.10a for each thermocouple. The thermocouple measuring the wall temperature is shown in yellow. Changes in the wall temperature as a function of time were very small. At the start of the experiment the wall temperature was 295 K, and the coldest measured wall temperature was 293K and occurred at the end of the test. However, these changes in wall temperature are used by the FDM. The thick colored lines in Figure 4.10a represent the FDM and the color of the FDM line matches the color of each respective thermocouple location.

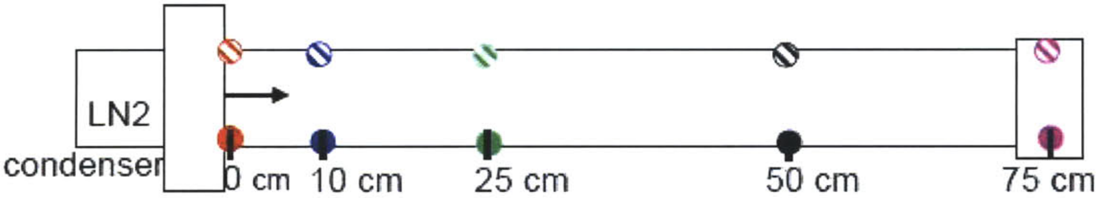

Figure 4.9 Thermocouple locations on pipe

The temperature versus axial distance away from the condenser at the 300 minute mark is shown in Figure 4.10b. The thermocouple temperatures are denoted by '+' marks and the FDM is shown by the solid line. The FDM matched the overall trend in experimental data most closely for $\varepsilon_t = 0.65$. This resulted in

$$Q_{chamber} = 30.4\text{W} \tag{4.11}$$

The paired thermocouples matched well with each other at the '0', '25 cm', and '75 cm' locations. The difference in their temperatures is hard to distinguish from Figure 4.10b because they are less than 1 K. The thermocouples located at '10 cm' and '50 cm' did not match so well, both pairs having approximately a 20 K difference. This is likely because the thermocouple beads were not well bonded with the surface of the pipe. This situation was remedied before testing the heat pipe with working fluid. However the goal of obtaining an estimate for the heat from the chamber environment was still satisfied from the experimental results.

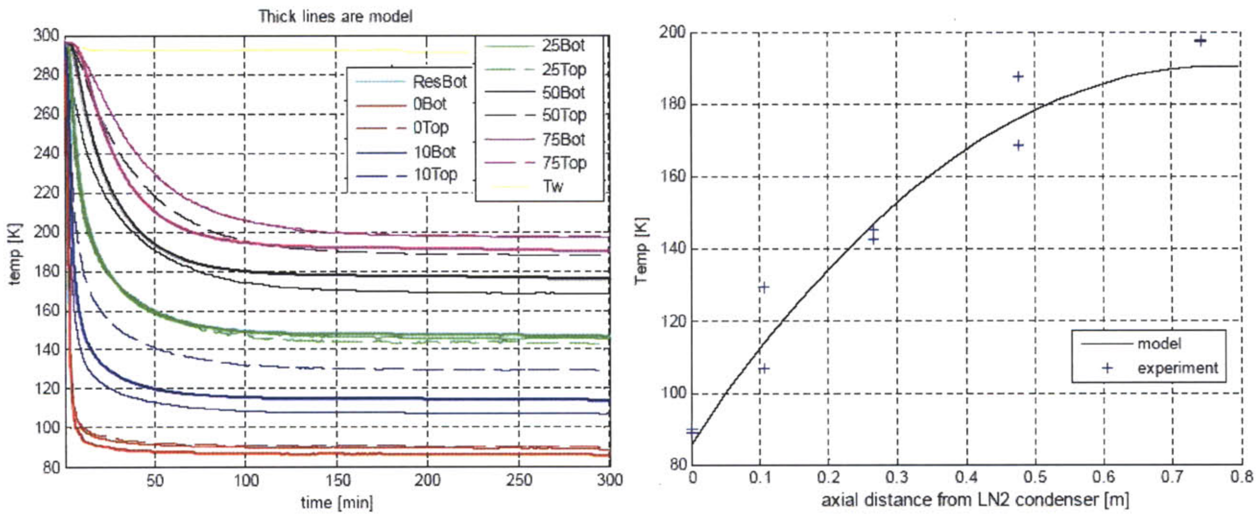

a) Temperature vs. distance from condenser b) Thermal load of pipe vs. time

Figure 4.10 Temperature for heat pipe with no working fluid

4.2.2 Determining the Operational Power Capacity

Now that the minimum requirement of 30 W for the heat pipe power capacity has been established, the design of the different mesh layers of the heat pipe can be considered. To obtain a large power capacity, a coarse inner mesh and a fine outer mesh is used as the wicking structure as shown in Figure 4.6.

In order to test the power capacity of the heat pipe, it is useful to design a system that has greater than the minimum power capacity of 30 W. A 50 W power resistor located at the end of the heat pipe is used to introduce heat into the system, resulting in a maximum power input of approximately 80 W. Using Equation (4.7), a heat pipe with a 4 cm pipe diameter with 2.4 layers of a #50 inner mesh and two layers of a #250 outer mesh results in a power capacity of approximately 63 W. This system exceeds the minimum requirements and has a large enough power capacity beyond 30 W to test with the power resistor. The results of this design are shown in Figure 4.11 and the desired design is circled. Since this design will be fabricated, the parameters for a COTS #250 mesh from TWP were used in the analysis [68]. In addition since a one meter length pipe did not fit into the vacuum chamber, the pipe was cut to a length of 85.5 cm. These parameters are reflected in Figure 4.11. For comparison, the 50 mesh inner layer design is also shown with the #30 mesh and #100 inner mesh designs from Figure 4.11.

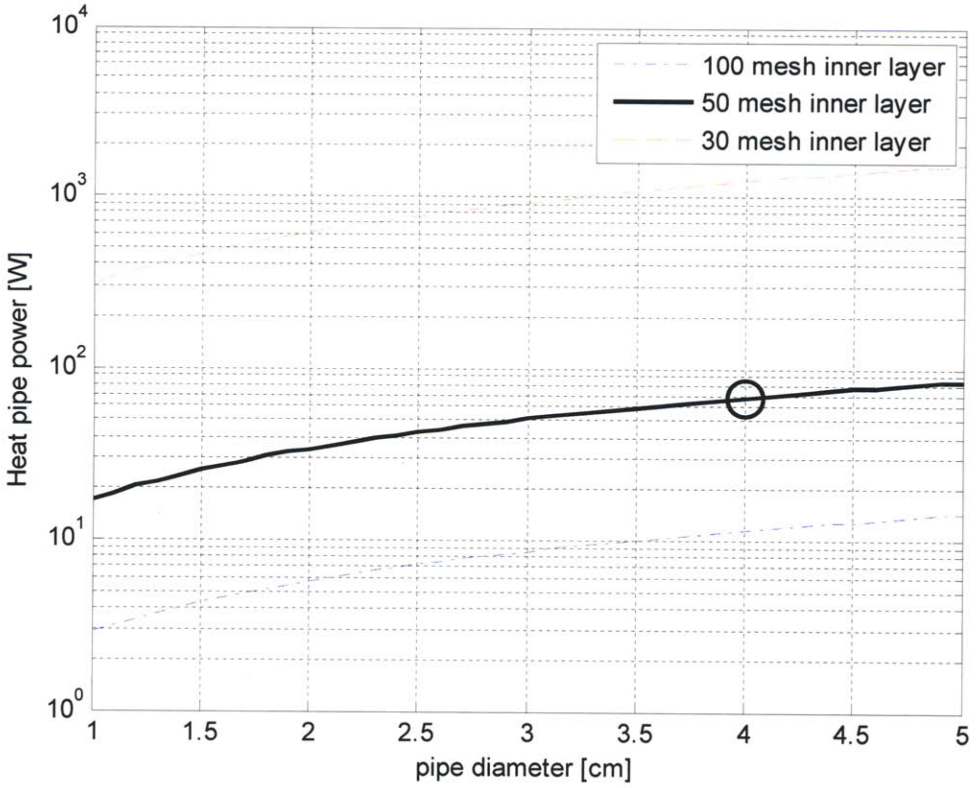

Figure 4.11 Heat pipe design using 2.4 layers of a #30, #50, or #100 inner mesh, 2 layers of a #250 outer mesh

4.2.3 Effect of Angle

Heat pipes are commonly tested at an angle where the evaporator is inclined above the condenser. This test ensures that the wick is working properly and that gravity does not assist the working fluid from traveling to the evaporator. Otherwise this system would be a simple thermosyphon, not a heat pipe. By substituting in the hydraulic pressure from Equation (4.5) into Equation (4.1), the heat pipe power capacity as a function of angle is given by

$$\dot{Q}_{\max} = \left(\frac{\rho_l \sigma h_{fg}}{\mu_l}\right)\left(\frac{A_w \kappa}{L_{eff}}\right)\left(\frac{2}{r_c} - \frac{\rho_l g L_{eff} \sin\phi}{\sigma}\right) \tag{4.12}$$

The heat pipe power versus angle is shown in Figure 4.12. In the experimental testing (Section 4.5) of the heat pipe with the HTS wire the heat pipe is tested at an angle of approximately 0.6 degrees. This results in a power capacity of approximately 50.8 W. The heat pipe power capacity as a function of angle, ϕ, for various lengths of heat pipes is shown in Figure 4.12. The straight heat pipe tested in this research is shown by the circle in Figure 4.12. Figure 4.12 shows that the angle of the pipe has a large effect on the power capacity. A heat pipe at $\phi = 0.6°$ has 12.4 W less than the power at a horizontal inclination. It is important to note that the angle does not affect working fluid mass (Section 4.2.5), only power.

In addition, the effect of the length of the heat pipe is shown in Figure 4.12. Both the vapor pressure drop and liquid pressure drop increase as the length of the heat pipe increases, as seen in Equation (4.3) and (4.4). The capillary pressure is a function of the mesh and working fluid and is not a function of the pipe length. Therefore, a longer heat pipe has a lower power because as the effective length increases, the capillary pressure must overcome a higher liquid and vapor pressure drop. This effect is illustrated in Figure 4.12 and can also be shown in Equation (4.7)

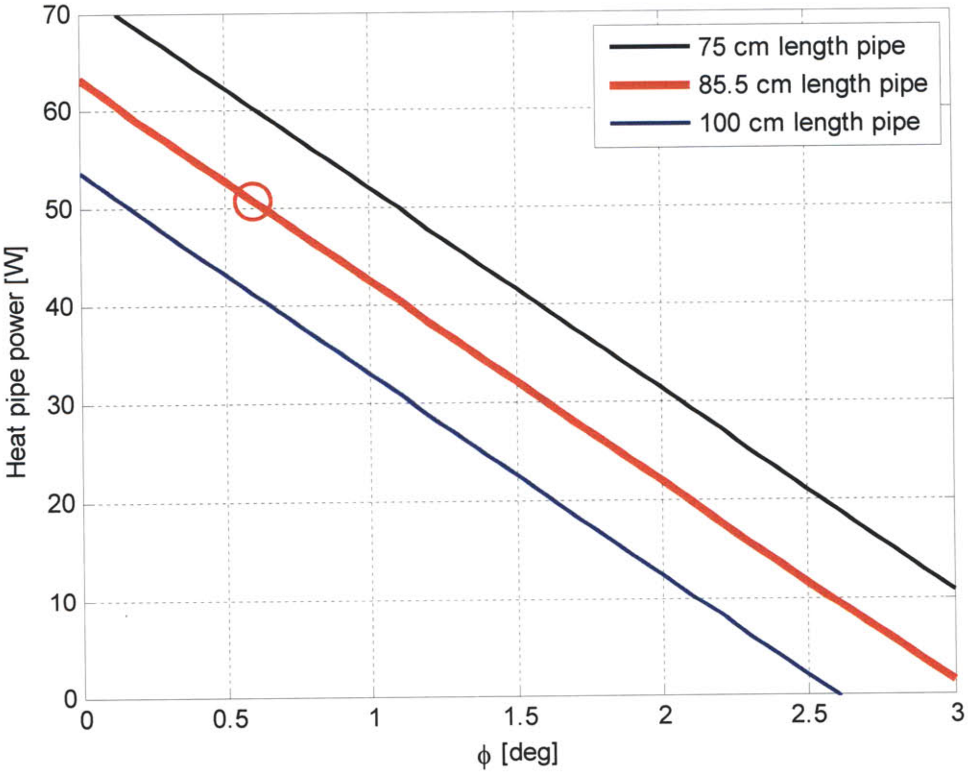

Figure 4.12 Heat pipe power capacity versus angle of evaporator above the condenser for various length pipes

4.2.4 Effects of Uncertainty on the Number of Mesh Layer

While implementing the heat pipe it was difficult to wrap a precise number of layers for both the inner and outer meshes. In general the screen mesh is difficult to handle without bending, wrinkling, or crunching down on the screen. While wrapping it into the pipe, the screen mesh can easily crunch down on itself affecting the number of layers present. The original intent was to have a heat pipe with exactly 2 layers of fine mesh and 2 layers of coarse mesh, however it is likely that this system was built to perfect specifications. In reality approximately 2.4 layers of coarse mesh were likely implemented. Since there is some uncertainty in the effective number of layers in the heat pipe it is useful to understand how this impacts the power capacity. The heat pipe power capacity as a function of the number of coarse mesh layers is shown in Figure 4.13. There is a family of curves for the various number of outer, fine meshes; the blue line is for 2.5 layers, the thick red line is for 2 layers, and the black line is for 1.5 layers. The expected power capacity of the heat pipe is circled and is approximately 50.8 W. Determining this design was an iterative process, using the experimental data from Section 4.5 and the working fluid mass, which is discussed in the next section.

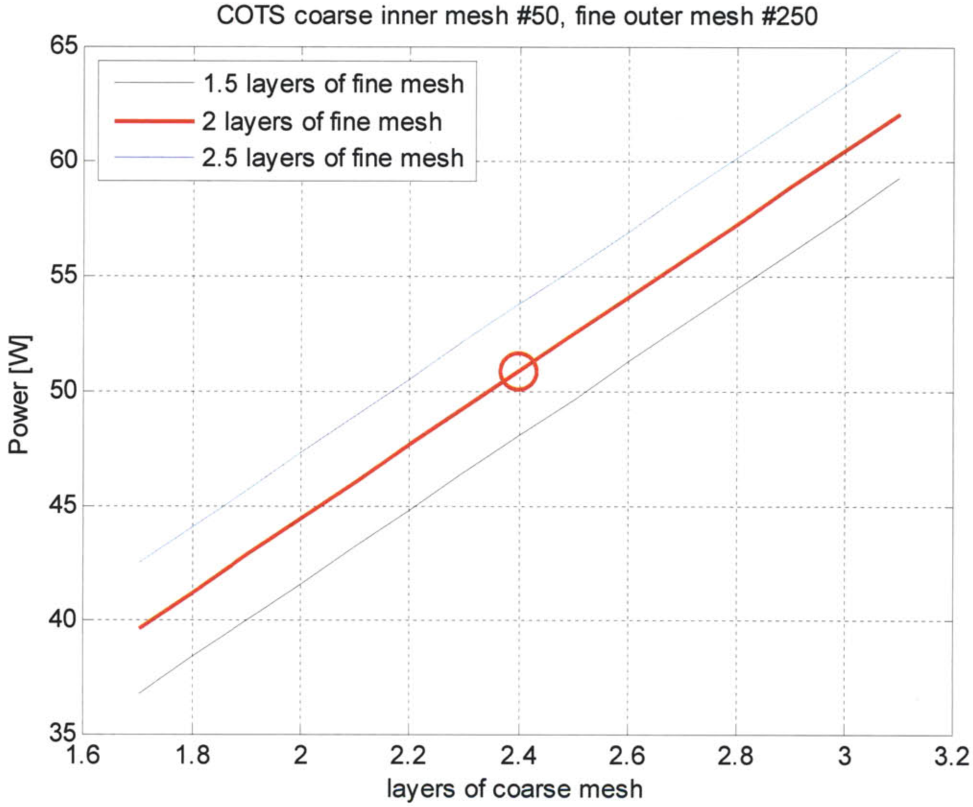

Figure 4.13 Varying the number of coarse mesh (#50) layers with 1.5, 2, and 2.5 layers of fine #250 mesh

4.2.5 Determining the Working Fluid Mass

The model for maximum power capacity of a heat pipe assumes that the wick is fully wetted with working fluid. This is a capillary limited heat pipe meaning that the capillary pressure head drives the limit for power capacity. More discussion on heat pipe limitations is in Section 4.3. Calculation of the working fluid mass accounts for the working fluid in gaseous state in the vapor space and in liquid state in the wick. This is given by

$$M_{LN2} = \rho_v \pi \left(\frac{d_v}{2} \right)^2 L + \rho_l A_w \varepsilon_p L \tag{4.13}$$

The working fluid in the wick assumes that the liquid is only in the coarse mesh structure and accounts for the porosity of the coarse mesh (ε_p). The area of the wick (A_w) is a function of the number of coarse mesh layers and L is the entire length of the pipe. Since it was established in Section 4.2.4 that there is some uncertainty in the effective number of mesh layers, the working fluid mass as a function of number of inner coarse mesh layers with a family of curves for outer fine meshes is shown in Figure 4.14.

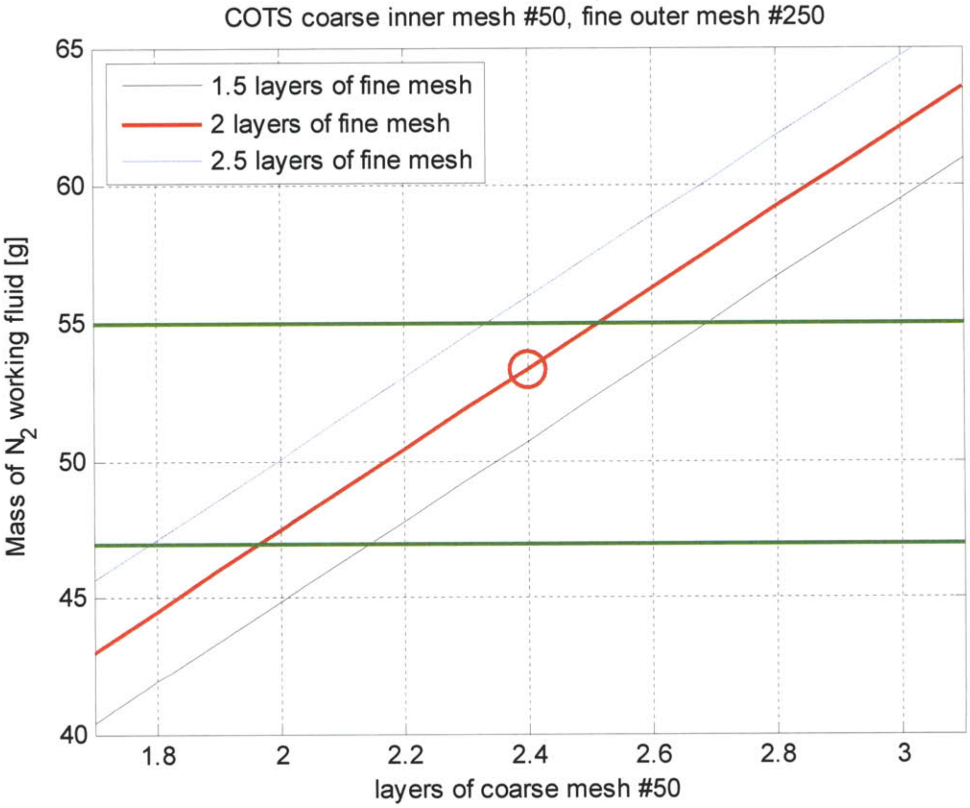

Figure 4.14 Mass of working fluid as a function of inner coarse mesh

There is approximately 53.5 g of working fluid necessary to fully wet the wick. Several experiments were conducted to determine the amount of working fluid necessary for the entire heat pipe to reach saturation. This result is shown in the experimental results in Section 4.5. The working fluid mass is shown in Figure 4.14 by the circle for a heat pipe with 2.4 layers of coarse inner mesh (#50) and 2 layers of fine outer mesh (#250). The two horizontal green lines is the approximate range of working fluid in steady-state that was attained experimentally. The 53.5 g of working fluid is equivalent to approximately 7.8 L of nitrogen gas. The straight heat pipe has approximately 1.07 L of volume. Using a working fluid reservoir tank to contain all the working fluid would require connection with a second pipe over seven times the volume. To simplify the operation of the test, a working fluid reservoir tank was not used and the working fluid was injected at the start of an experimental test. Operating without a working fluid reservoir tank also allows for a reduction in mass and volume of equipment inside the vacuum chamber.

4.2.6 Temperature Model

This section describes a model for the temperature at the end of the heat pipe which will be used as a comparison with the experimental data. Since the performance of the superconducting wire is limited by the section of wire that is hottest, it is important to estimate the temperature of the heat pipe that is farthest away from the condenser. This hot end temperature is T_e, the temperature at the end of the evaporator. A resistive network can be used to model the heat pipe and is shown in Figure 4.15.

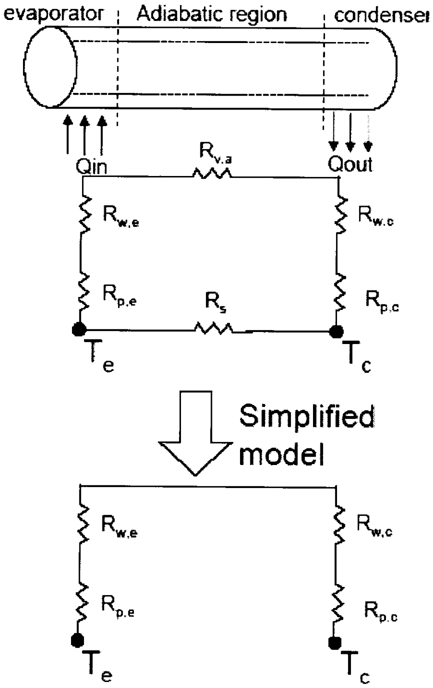

Figure 4.15 Heat pipe modeled as a resistive network

The total temperature drop from the evaporator to the condenser, ΔT, can be solved from

$$Q = \frac{\Delta T}{R_t} \tag{4.14}$$

where R_t is the total thermal resistance of the heat pipe. In terms of the condenser temperature and evaporator temperature, Equation (4.14) can be solved for the evaporator temperature on the pipe as

$$T_e = \frac{Q}{U_{HP,p} A_{cross}} + T_c \tag{4.15}$$

where A_{cross} is the pipe cross-sectional area $\left(\pi r_o^2\right)$ used for the thermal resistances and the sum of the thermal resistances are simplified as

$$U_{HP,p} = \frac{1}{R_{p,c} + R_{w,c} + R_{w,e} + R_{p,e}} \tag{4.16}$$

where $R_{p,c}$ and $R_{p,e}$ are the thermal resistances of the pipe wall in the condenser and evaporator respectively, and $R_{w,c}$ and $R_{w,e}$ are the thermal resistances of the wick in the condenser and evaporator respectively. These quantities are given by

$$\begin{aligned} R_{p,e} &= \frac{r_o t_p}{2L_e k_p} & R_{w,e} &= \frac{r_o^2 t_w}{2L_e r_i k_w} \\ R_{p,c} &= \frac{r_o t_p}{2L_c k_p} & R_{w,c} &= \frac{r_o^2 t_w}{2L_c r_i k_w} \end{aligned} \tag{4.17}$$

where r_o is the pipe outer radius, r_i is the pipe inner radius, t_p is the pipe wall thickness, L_e and L_c are the lengths of the evaporator and condenser, t_w is the wick thickness, k_p is the pipe wall thermal conductivity and k_w is the wick thermal conductivity. The thermal conductivity of a wrapped screen [69] accounts for the liquid conductivity, k_l, the screen conductivity, k_s, and the porosity of the mesh, ε_p, and is given by

$$k_w = k_l \frac{k_l + k_s - \varepsilon_p\left(k_l - k_s\right)}{k_l + k_s + \varepsilon_p\left(k_l - k_s\right)} \tag{4.18}$$

The thermal resistance of the wick is calculated accounting for both the coarse and fine mesh in series. The system shown in Figure 4.15 simplifies the thermal resistance network because the resistance of the vapor space in the adiabatic region, $R_{v,a}$, is several orders of magnitude lower than the wick resistance [35]. Also the axial resistance of the wick and pipe, R_s, was calculated to be approximately three orders of magnitude higher than R_t, the total calculated resistance.

Combining Equations (4.16) through (4.18), the temperature in the evaporator can be found. This model for the hot end temperature will be used to compare with the experimental temperature measured during saturation condition.

4.3 Limitations

There are some limitations to the heat pipe power capacity that are imposed by the working fluid and the design of the overall system. For a low temperature pipe, these limits are not expected to be a problem, however, each are investigated here for completeness.

4.3.1 Entrainment Limit

Entrainment occurs when the vapor in the counter-current near the liquid-vapor interface is able to entrain liquid droplets. Qualitatively, this phenomenon occurs when the vapor is traveling at a fast enough velocity to create waves on the surface of the mesh. High velocity vapor occurs for heat pipes operating at large powers, since fast circulation of the working fluid is required. Thus the entrainment limit puts an upper bound on the power of a heat pipe. The equation for the entrainment limit [35] is given by

$$Q_{ent} = \pi r_v^2 h_{fg} \sqrt{\frac{\rho_v \sigma}{2R_h}} \tag{4.19}$$

where r_v is the radius of the vapor space and is shown in Figure 4.2. The hydraulic radius of the wick surface, R_h, is given by

$$R_h = \frac{2A_{lv}}{P_{pore}} \tag{4.20}$$

and is a function of the area of the individual surface pores of the wick, A_{lv}, and the wetted perimeter of the individual surface pores, P_{pore}. For screen wicks R_h is half of the wire spacing and is equal to r_c. For the straight heat pipe fabricated in this chapter, the entrainment limit is 5.2 kW. Since $Q_{ent} >> Q_{design}$ the entrainment limit is not a concern.

4.3.2 Sonic Limit

The sonic limit is caused by choking at the evaporator exit which limits the vapor flow through the heat pipe, thus putting a limit on the total power of the heat pipe. The power capacity as a function of the Mach number, M, is given by

$$Q_{sonic} = \pi r_v^2 \rho_1 h_{fg} M \sqrt{\gamma R T_1} \tag{4.21}$$

where ρ_1 is the static vapor density, T_1 is the static temperature of the vapor, and R is the gas constant for nitrogen. The relationship between static and stagnation conditions for temperature and pressure is given by

$$\frac{T_o}{T_1} = 1 + \frac{\gamma - 1}{2} M^2 \qquad \frac{\rho_o}{\rho_1} = \frac{1 + \gamma M^2}{1 + \frac{\gamma - 1}{2} M^2} \tag{4.22}$$

Substituting Equation (4.22) into Equation (4.21) for a Mach number equal to one, the sonic limit is

$$Q_{\text{sonic}} = \rho_o A_v h_{fg} \sqrt{\frac{\gamma R T_o}{2(\gamma+1)}} \tag{4.23}$$

For a heat pipe in steady-state operation, T_o is simply the saturation temperature. For the straight heat pipe, the sonic limit is calculated to be 120 kW. Again, the sonic limit is not a concern.

4.3.3 Vapor Core Diameter Limitations

A stack of HTS wires inside the vapor space has a second limitation unique to an EMFF heat pipe. The HTS wire stack reduces the vapor space and could potentially choke the flow. As a conservative estimate, the system is designed so that the vapor Mach number is less than 0.2 for laminar and compressible flow. Accounting for the cross-sectional area taken up by the HTS stack, the area of the vapor space is now given by

$$A_v = \pi \frac{d_v^2}{4} - A_b \tag{4.24}$$

where A_b is the cross-sectional area of the HTS wire stack. In terms of A_b and conservatively assuming a Mach number of 0.2, the maximum heat flow limited by the vapor space blockage is given by

$$Q_{\text{block}} = \rho_o h_{fg} \sqrt{\gamma R T_o} \left(\frac{0.2\sqrt{0.98 + 0.02\gamma}}{1 + 0.04\gamma} \right) \left(\pi \frac{d_v^2}{4} - A_b \right) \tag{4.25}$$

The percentage of vapor space that can be taken up by the block is shown in Figure 4.16. For the heat pipe, the vapor flow blockage does not limit the system performance until the area of the blockage approaches the vapor space area. When the sonic limit is greater than the designed heat capacity, the heat pipe is still capillary limited.

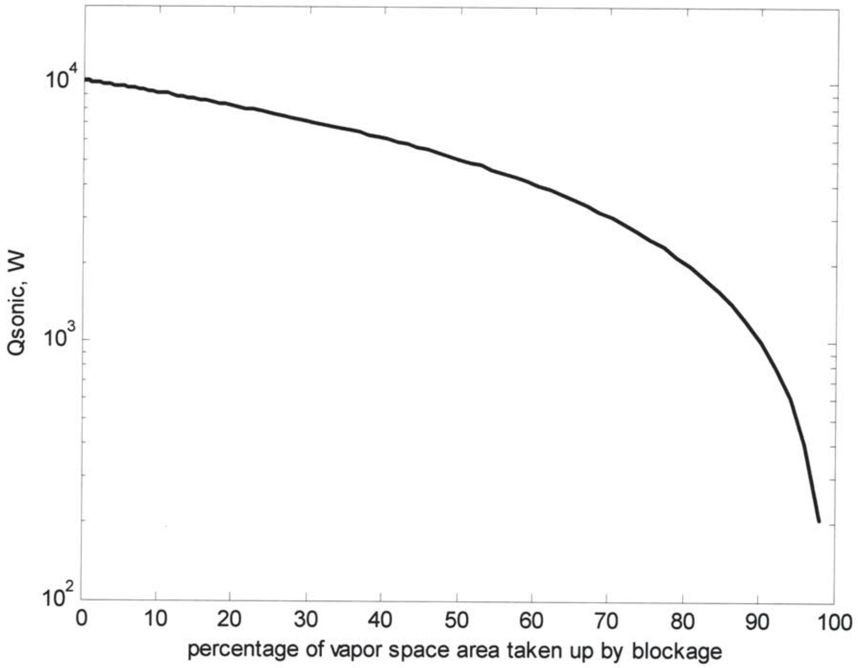

Figure 4.16 Vapor space limitations imposed by HTS stack

4.3.4 Peak Heat Flux

A potential limitation on the performance of the heat pipe is the peak heat flux that the condenser can take away. The liquid nitrogen reservoir is most efficient when the pipe is in complete contact with liquid nitrogen and heat transfer occurs either via convection from the pipe wall to the liquid surface or by nucleate boiling. Given sufficient heat, departure from nucleate boiling occurs. This point is also known as boiling crisis or the burnout point and represents the maximum heat flux the reservoir can handle. Any heat flux beyond the peak heat flux results in a rapid rise in the pipe wall temperature and a decrease in the heat flux the reservoir can take away from the pipe, since film cooling is a less efficient heat transport mechanism [70]. The maximum heat flux is related to the maximum rate at which vapor can leave the wall. This is given by

$$q_{\max} = C_{\max}\rho_v V_{\max} h_{fg} \tag{4.26}$$

where V_{max} is the maximum vapor velocity and C_{max} is a geometry factor. Values for C_{max} depend on L^* and can be found in Mills [71] for various shapes. The dimensionless parameter L^* is given by

$$L^* = \frac{L}{L_c} = \frac{L}{\left(\dfrac{\sigma}{(\rho_l - \rho_v)g}\right)^{1/2}} \tag{4.27}$$

which is the ratio of the condenser length (here denoted simply by L) to the characteristic length, L_c. The characteristic length is a function of the fluid properties, which for the EMFF reservoir is nitrogen. For a condenser length of 17 cm, $C_{max} = 0.12$, which is classified as a large horizontal cylinder.

The mechanism for critical heat flux is that the rate of vapor leaving the heating surface is greater than the rate of liquid reaching the heating surface. To estimate V_{max} the kinetic energy of the vapor can be equated to the work done by the buoyancy force of the liquid and vapor over the characteristic length as

$$\frac{1}{2}\rho_v V_{\max}^2 = g(\rho_l - \rho_v)L_c \tag{4.28}$$

Substituting Equation (4.27) and solving for V_{max} yields

$$V_{\max} \sim \left(\frac{\sigma(\rho_l - \rho_v)g}{\rho_v^2}\right)^{1/4} \tag{4.29}$$

Finally, Equation (4.26) can be solved for the peak heat flux as

$$q_{\max} = C_{\max} h_{fg}\left(\sigma\rho_v^2(\rho_l - \rho_v)g\right)^{1/4} \tag{4.30}$$

The peak heat flux as a function of the condenser length is shown in Figure 4.17. The condenser length of the heat pipe is approximately 6 cm, which yields a peak heat flux of approximately 1500 W. This is well above the intended power capacity of the heat pipe and therefore peak heat flux should not be a limitation.

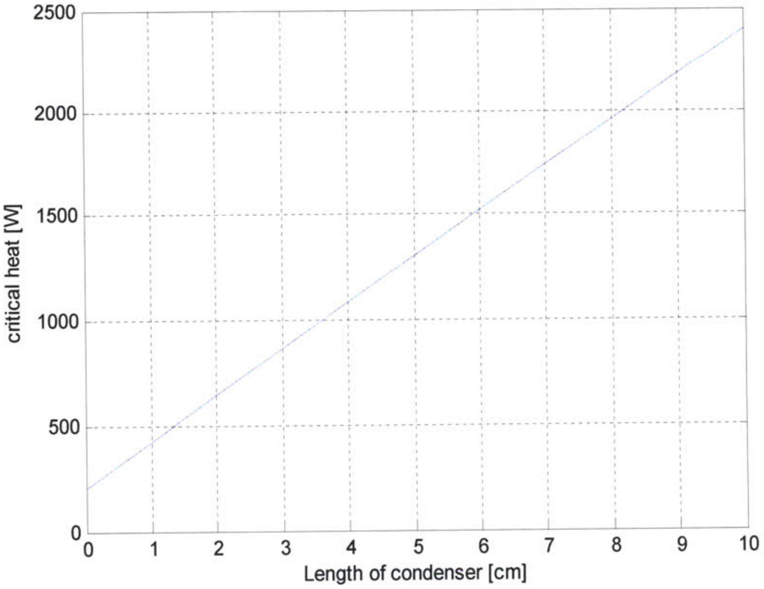

Figure 4.17 Peak heat flux for condenser as a function of condenser length for straight heat pipe

4.4 Testbed Development

A capillary limited heat pipe with a power capacity of 50.8 W was constructed using 2 layers of fine outer #250 mesh and 2.4 layers of coarse inner #50 mesh. A stainless steel screen mesh was used as a wicking structure and nitrogen is the working fluid. Testing for this system with the HTS wires was carried out at a 0.6° angle. The heat pipe was approximately horizontal when testing without the HTS wires. The condenser length was designed to have sufficient area for heat extraction by the liquid nitrogen reservoir. The size is also representative of a cryocooler cold finger. Characteristics of the heat pipe are summarized in Table 4.3.

Table 4.3 Heat pipe design summary

Heat pipe length	85.5 cm
Pipe diameter	4 cm
Wick material	Stainless steel mesh
Inner mesh layers	2.4 layers of #50 mesh
Outer mesh layers	2 layers of #250 mesh
Condenser length	6 cm
Condenser temperature	~77 K (liquid nitrogen)
Working fluid	Nitrogen
Envelope material	Copper
Power capacity	50.8 W

4.4.1 Overview and Setup

The cryogenic heat pipe is tested in a vacuum chamber in order to minimize convective heat exchange and to simulate an environment similar to space where radiation heating is the main heat source absorbed by the pipe. Figure 4.18 shows how the heat pipe is setup inside a vacuum chamber. A liquid nitrogen reservoir inside the chamber provides cooling for the condenser and mimics the function of a cryocooler. This reservoir is completely isolated from the heat pipe. While liquid nitrogen is in direct contact with the heat pipe, it does not enter the sealed pipe. Liquid nitrogen is brought into the reservoir via a vacuum chamber liquid feedthrough and any boiloff or excess liquid nitrogen is brought out of the chamber via a second feedthrough. At the other end of the heat pipe, a resistive heater is used to apply heat to the heat pipe. At this end is also a feed into the heat pipe to inject the working fluid. Using this same feed, the heat pipe is also connected to a pressure relief valve for safety. Multilayer insulation around the heat pipe can be used to create an adiabatic region, however for the experiment setup used, no MLI was applied. In fact, since there is radiation heating along the entire pipe, there is essentially no adiabatic region. Also shown are thermocouples which are applied throughout the heat pipe and on the liquid nitrogen reservoir.

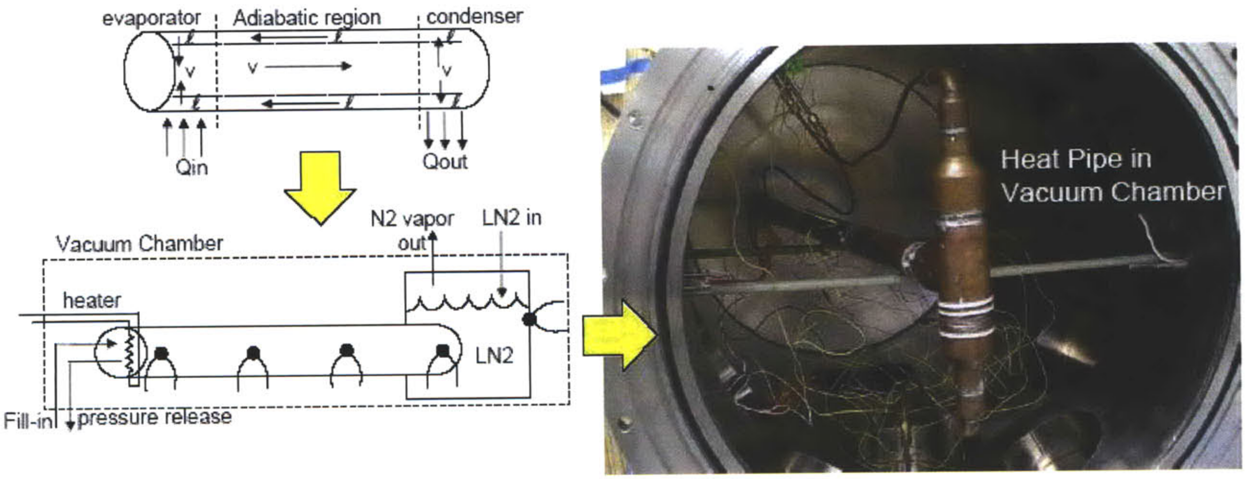

Figure 4.18 Heat pipe setup in vacuum chamber

The heat pipe is also shown in Figure 4.19. This picture shows the liquid nitrogen reservoir before it is soldered onto the heat pipe. The heat pipe condenser is six centimeters long and fits inside the opening for the reservoir which is shown in Figure 4.19. The copper bushing at six cm is then soldered onto the opening in the liquid nitrogen reservoir. There are fourteen thermocouples measuring the temperature of the heat pipe, liquid nitrogen reservoir, and vacuum chamber wall. Two G10 rods are used to support the heat pipe. There is also an electrical feedthrough used to power the resistive heater and to interface with the HTS wire.

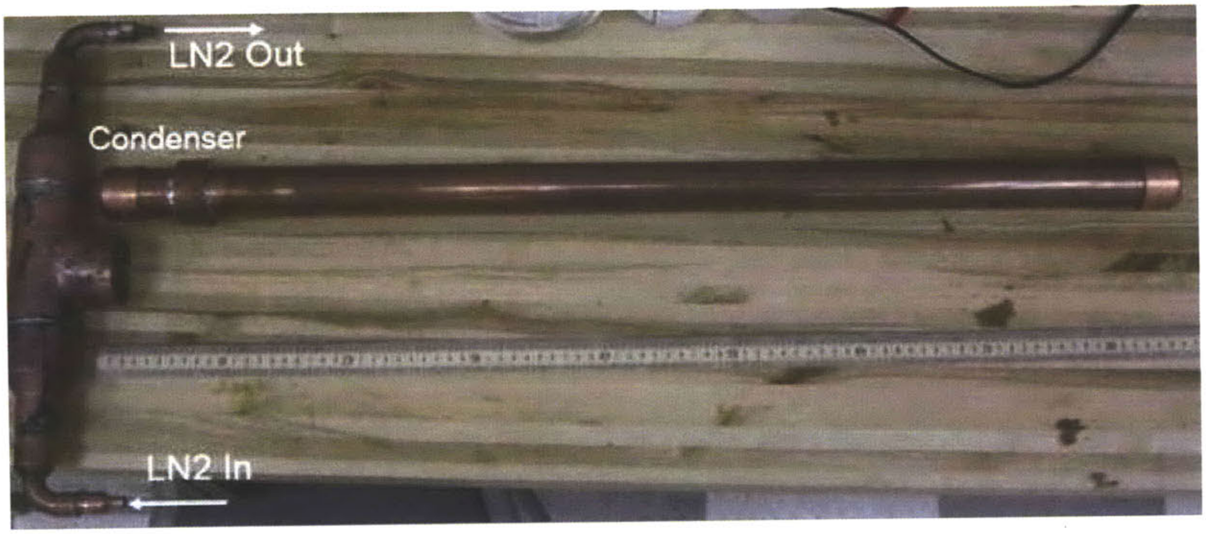

Figure 4.19 Heat pipe and liquid nitrogen reservoir

Figure 4.20 illustrates the devices that are connected to the heat pipe outside of the vacuum chamber. A relief valve and pressure gauge are directly connected to the vapor space of the heat pipe. The cryogenic relief valve is set at 35 psig. Before operating the heat pipe, the vapor space is evacuated using a lab vacuum pump to eliminate any non-condensable gases, which could potentially block the condenser. Nitrogen gas is introduced at approximately 20 psig and is measured using a flowmeter. Calibration of the flowmeter is discussed in Appendix D.

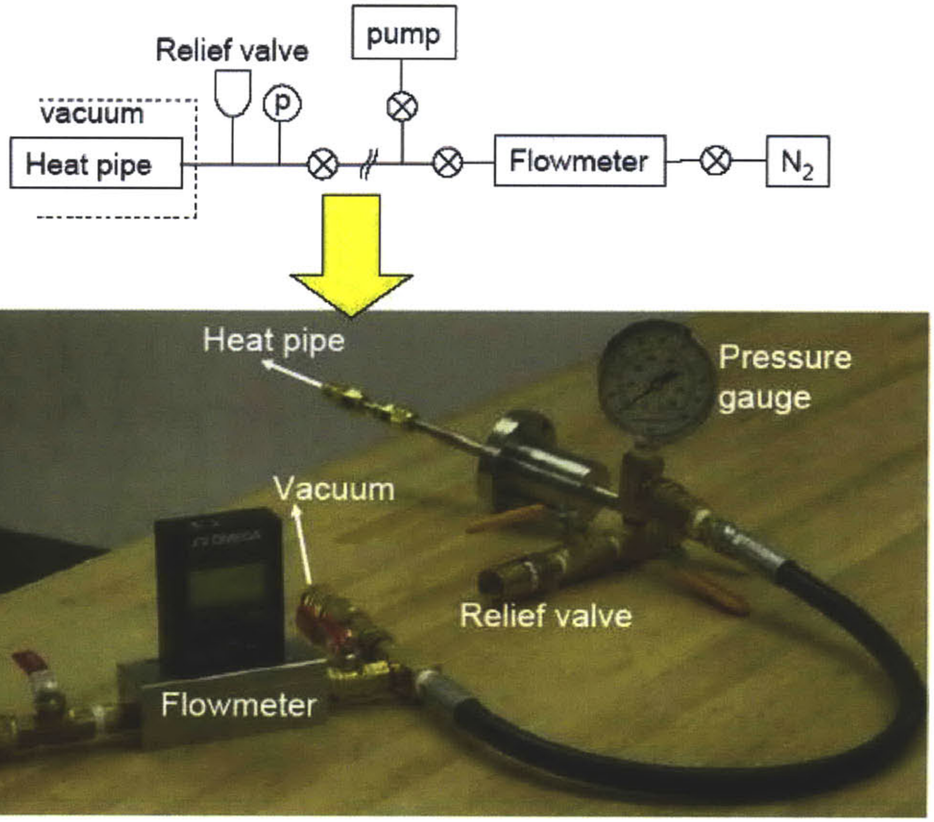

Figure 4.20 Working fluid injection setup

4.4.2 HTS Wire Insertion

Since the straight heat pipe is unable to test a coil of HTS wire, two straight HTS wire segments were inserted into the pipe and connected at one end. Figure 4.21 shows the connectors to the HTS wire on the outside of the sealed pipe. The connectors are 3/16 inch diameter copper rods which connect to the HTS wire on the inside of the pipe. Figure 4.21 also shows the power resistor, which is screwed onto a curved piece of copper, which is soldered onto the heat pipe.

A coil of HTS wire in an EMFF spacecraft contains over a hundred turns of wire. This entire amount of wire must be cooled down before the coils can operate at superconducting levels. In addition, the wire stack could choke the vapor space, if it were sufficiently large. In order to mimic the thermal mass and the potential vapor blocking effect, a circular aluminum block was also inserted into the heat pipe. A groove was machined into the aluminum so that the two HTS wires would be press fit inside the block.

Since the center of the block is likely the last portion of the aluminum to cool down, the HTS wires are placed close to the center. This gives a good indication for how long it might take an entire stack of wires to cool down. The picture of the aluminum block and two HTS wires are shown in Figure 4.22.

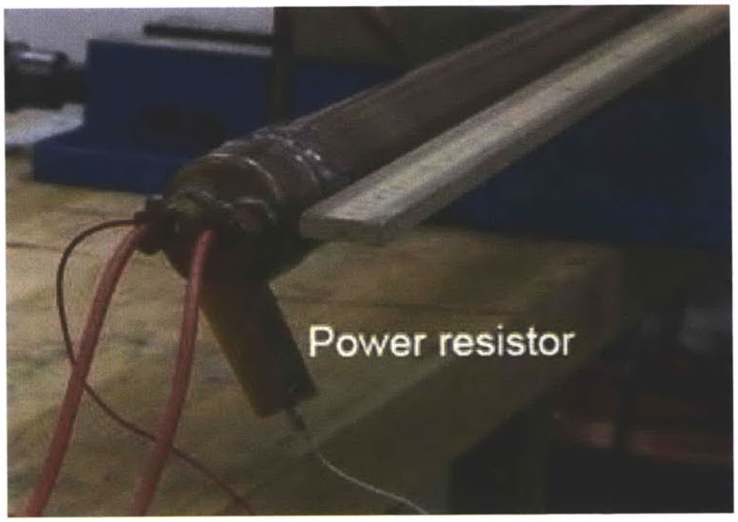

Figure 4.21 Power resistor and HTS wire connectors on the heat pipe

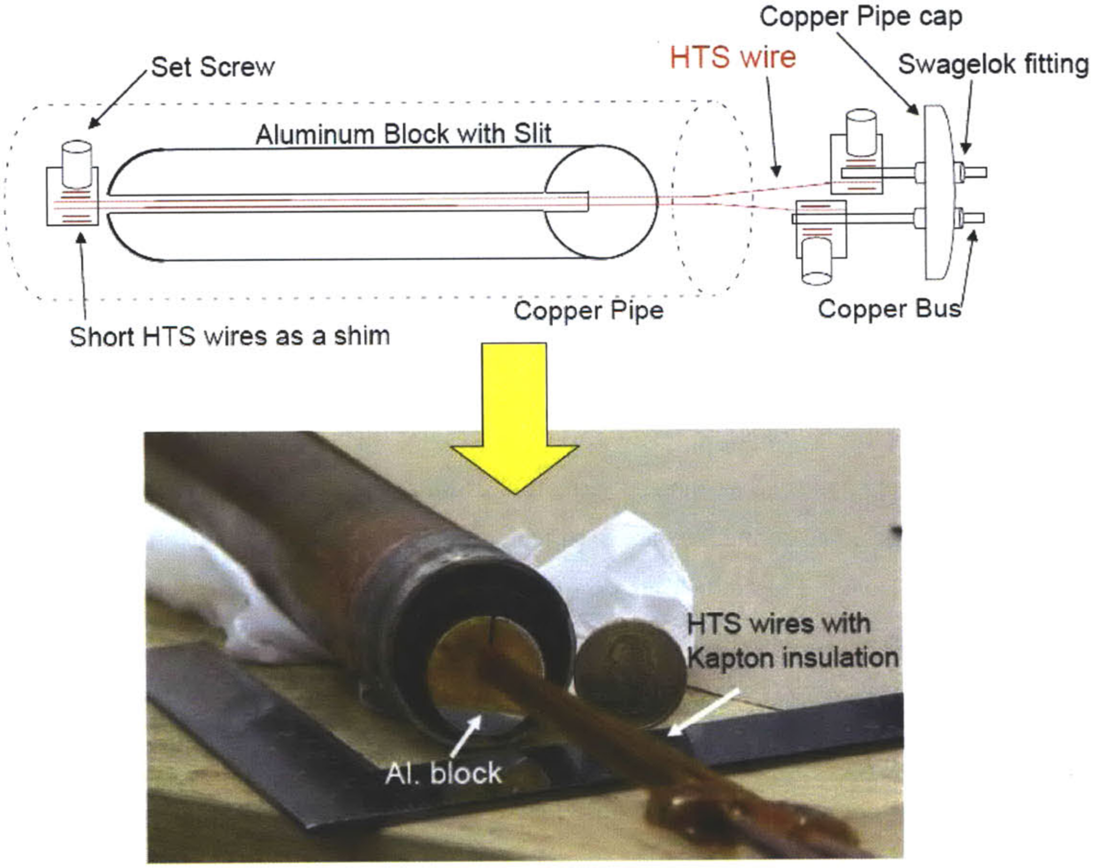

Figure 4.22 Heat pipe with aluminum block and HTS wires

The aluminum block has both a higher conductivity than the HTS wire, whose structure is composed primarily of stainless steel, and a higher specific heat than the HTS. The values for each are given by

$$\begin{aligned} K_{\mathrm{Al}} &= 230 \ {}^{\mathrm{W}}\!/\!_{\mathrm{m \cdot K}} & K_{\mathrm{HTS}} &= 15 \ {}^{\mathrm{W}}\!/\!_{\mathrm{m \cdot K}} \\ C_{\mathrm{Al}} &= 900 \ {}^{\mathrm{J}}\!/\!_{\mathrm{kg \cdot K}} & C_{\mathrm{HTS}} &= 477 \ {}^{\mathrm{J}}\!/\!_{\mathrm{kg \cdot K}} \end{aligned} \tag{4.31}$$

While the system is cooling down, the aluminum block acts to minimize any temperature gradients across the HTS stack, if any existed, since the block transports heat throughout the length of the block faster than the HTS. However, the aluminum block requires more energy to cool than the HTS wires, so the aluminum block will cool more slowly and there will be a slower cooling transient to get below $T_{critical}$.

The thermal resistance of the block (R_b) and the HTS wires (R_{HTS}) are given by

$$R_b = \frac{L_b}{A_b K_b} \qquad R_{HTS} = \frac{L_{HTS}}{N_{turns} \cdot A_{HTS} K_{HTS}} \tag{4.32}$$

As a reference, in order for the thermal resistances to be equivalent, approximately 6,692 turns of HTS wires are necessary. The energy required to cool the system is more important because once the heat pipe is isothermal, temperature gradients should already be minimized in the HTS stack. The simplified steady-flow thermal energy equation can be manipulated to determine the energy required to cool a block of material:

$$Q = \dot{m} C \Delta T = mC \frac{\Delta T}{\Delta t} \rightarrow Q \Delta t [\mathrm{W \cdot s}] = mC \Delta T [\mathrm{J}] \tag{4.33}$$

The energy required to the cool the aluminum block is $1.8 \cdot 10^6$ J, and per unit length this is $2.8 \cdot 10^6$ J/m. For the HTS wire, the energy required per unit length per turn is 988 J/m/turn. For the required energy to cool the aluminum block to equal a stack of HTS wires, 278 turns of wire are necessary. Therefore, the block of aluminum gives a conservative estimate for the transient time to cool a flight-sized stack of HTS wires.

In order to understanding how to connect to an HTS wire inside a pipe a short prototype pipe was built. This system and the lessons learned are discussed in more detail in Appendix D. Inside the pipe, the HTS wires were connected to the copper bus as seen in Figure 4.22. Two holes were cut into a copper pipe cap for two 1/4 inch Swagelok fittings. These fittings were then soldered onto the pipe. The copper bus snugly fits through the Swageloks. In fact, to assist the copper bus through, the openings of the Swageloks were increased by drilling a slightly larger hole. On the outside of the pipe, a Teflon fitting slides over the copper bar to electrically isolate the copper bus from the pipe and Swagelok. By tightening a Swagelok fitting on the outside of the pipe, the system can hold pressure (or a vacuum). Now the HTS wires can be electrically connected to via the copper bus.

There was no additional structural support for the aluminum block inside the copper pipe. For a future flight system, either the HTS wire stack fits tightly into the pipe or some additional supports may be required. One problem that was encountered was that the HTS wires sticking out of the aluminum block bend easily, especially if they were attached to the copper bus, but not yet connected through the copper pipe cap or anything else. In one instance, the HTS wires bent over completely and were damaged. To prevent the HTS wires from bending, additional HTS wires were taped using Kapton to the two wires that were sticking out of the block. These wires also were used as a protective shim by the set screws in the connectors connecting the HTS wires to the copper bus. Since the aluminum block was not tied down while inside the pipe, it was important not to tilt the pipe or turn the pipe upside down.

4.4.3 Heat Pipe Cleaning

Cleanliness of the working gas, pipe envelope, and the wick structure are important since it ensures wetting of the wick and removes particulates which can hinder the capillary action. Solid particulates can block the evaporator and in general plug the wick. Grease or other liquid contaminates affect working fluid wetting abilities and can reduce surface tension and viscosity, resulting in a reduction in the figure of merit for the working fluid. These issues are more critical for high temperature operation, especially for heat pipes using metal liquids, however the following steps were taken for the cryogenic heat pipe to remove particulates, degrease, and deoxidize contaminants [72].

Steps to clean the copper envelope:

1. Soak and rinse the tube with an acetone solution to remove oils and grease.
2. Soak in an acid bath of 50% Phosphoric acid and 50% Nitric acid for 15 minutes. The acid pickle is used to remove oxidation from the copper and also clean it from oils and grease.
3. System is rinsed with water and then air dried.

Steps to clean the stainless steel mesh:

1. Soak and rinse the mesh with an acetone solution to remove oils and grease.
2. Soak in an acid bath of 80% distilled water, 15% Nitric acid, and 5% Hydrochloric acid for 15 minutes.
3. Soak in an acid bath of 85% distilled water and 15% Nitric acid for 15 minutes.
4. System is rinsed with water and then air dried.

To test for good cleanliness and a good wetting surface, a drop of demineralized water is applied to the cleaned surface. If the drop spreads immediate on the copper or is absorbed completely into the wick, the system has been properly cleaned. It is important to note that all cleaning procedures and handling of the heat pipe is conducted with gloves because even grease from hands can contaminate the system. Similar to the theme of cleanliness, a working fluid that is highly pure is important. Low temperature fluids need to avoid the presence of water to prevent any incompatibilities. Finally, before soldering any sections of the pipe, areas to be soldered were cleaned with a metal brush and sandpaper.

4.4.4 Additional Engineering Considerations

There are several additional topics that are important to address for the construction of the heat pipe. One of them is ensuring that the thickness of the pipe walls is sufficient. The maximum stress is the circumferential hoop stress, which is given by

$$\sigma_{\max} = \frac{Pd}{2t} \tag{4.34}$$

For a copper heat pipe, the maximum yield stress σ_{max} is 100 mPa, the wall thickness, t, is approximately 1 mm, and the pipe diameter, d, is approximately 4 cm. This results in a maximum operating pressure which is greater than 1,000 psi and is well above any realistic operating condition. According to the nitrogen saturation table [73] shown in Table 4.4, the pressure of the pipe at 77 K is 23.5 psi and the maximum pressure at 123 K is 418 psi. The relief valve is set at 49 psi (35 psig) and a safe estimate for the integrity of the wrought solder joints is approximately 100 psi [74].

Table 4.4 Nitrogen saturation pressures at various temperatures

Temperature [K]	Pressure
77.4	101.3 kPa = 1 atm = 14.7 psi
80	138 kPa = 1.4 atm = 20 psi
85	228 kPa = 2.3 atm = 33 psi
90	359 kPa = 3.5 atm = 52 psi

One source of heat into the pipe is through the nitrogen gas feedthrough at the evaporator. The feedthrough is a single 1/4 inch outer diameter tube (2nd smallest on Kurt Lesker [75]) with 1/32 inch thick walls and is approximately four inches long (10.16 cm). The feedthrough is made of stainless steel (K_{feed} = 15 W/m·K). The heat into the pipe evaporator from N_2 feedthrough can be approximated by

$$Q = K_{feed}\frac{\Delta T}{l_{feed}}A_{feed} = 15\frac{300-77}{0.1016}\left(0.0008\cdot 2\pi\cdot\frac{0.00635}{2}\right) = 0.525 \text{ W} \tag{4.35}$$

For two pipes this is approximately 1.05 Watts and is small enough to neglect to first order.

During the operation of the heat pipe it is important that the rate at which heat can leave the heat pipe is not limited by the setup. For a large enough heat load, it is possible that the liquid nitrogen reservoir outlet pipe, which carries the boiloff vapor, could become choked, limiting the heat capacity of the system. This problem is similar to the critical heat flux analysis, but more related to how the heat pipe LN2 reservoir is set up. In steady-state the rate at which liquid nitrogen ($\dot{m}$) is consumed by the heat pipe is given as

$$Q[\mathrm{W}] = \dot{m} \cdot h_{fg} \tag{4.36}$$

where $\dot{m}$ can be expressed in terms of the volumetric flow rate, $\dot{V}_l$, as

$$\dot{m} = \rho_l \dot{V}_l \tag{4.37}$$

Substituting into Equation (4.36), another way of expressing the volumetric rate of LN2 consumption is

$$\dot{V}_l = \frac{Q}{\rho_l h_{fg}} \left[\tfrac{m^3}{s}\right] \tag{4.38}$$

Assuming that the entire LN2 in the reservoir is instantaneously turned into nitrogen gas, the mass flow rate is given by

$$\dot{m} = \rho_l \dot{V}_l = \rho_g A v_g \tag{4.39}$$

where A is the area of the reservoir outlet pipe carrying the gas. The limiting diameter of the outlet pipe can be solved for by combining Equations (4.38) and (4.39) and is given by

$$d \geq 2\sqrt{\frac{Q}{\pi h_{fg} \rho_g v_g}} \tag{4.40}$$

The minimum size of the LN2 reservoir outlet pipe as a function of the heat into the system is shown in Figure 4.23. The maximum gas velocity (v_g) of 0.2 Mach was used. The smallest sized pipes used by the LN2 reservoir are 1/4 inch (0.635 cm) inner diameter pipes, which are much larger than the minimum size necessary. Therefore, the setup of the heat pipe does not introduce any limitations on the heat pipe power capacity.

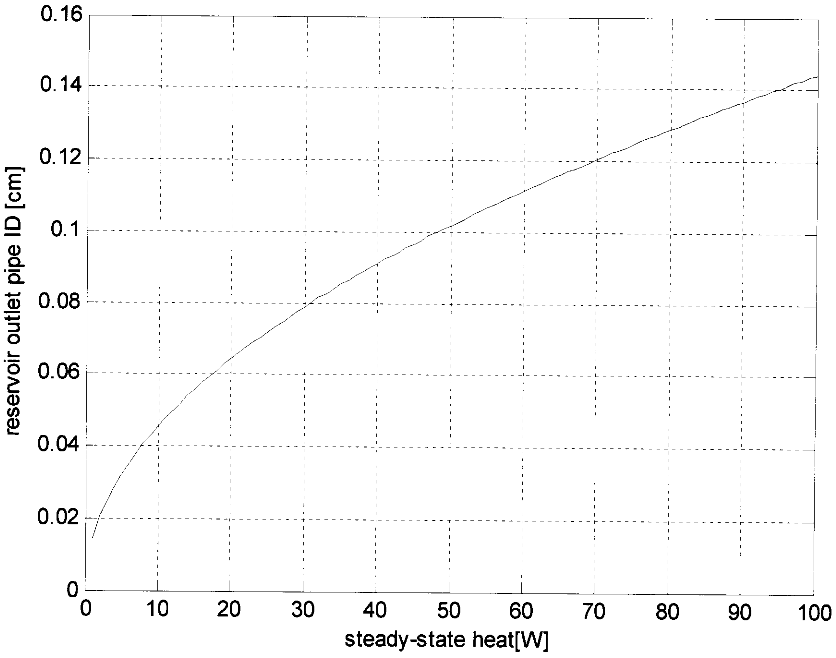

Figure 4.23 Minimum size of LN2 reservoir pipes given the required heat load

One potential issue for a flight heat pipe is the diffusion of working fluid through the pipe walls over time. This is especially true for Helium through materials with an irregular crystalline structure, such as glass, and materials with porous microstructures, such as ceramics. To calculate the rate of gas permeation, the permeation constant of a material is used [78]. Metals do not have a porous microstructure and only gases that are soluble in the metal permeate it. Thus inert gases like Helium will not permeate metals. More importantly nitrogen gas will not diffuse through copper [76].

Outgassing is not a problem for low-temperature heat pipes which are classified as pipes operating less than 400°C. However, for flight-based heat pipes, a bakeout is recommended to prevent any outgassing [77]. Overpressure is a concern for low temperature heat pipes since the pipe must be allowed to rise to room temperature when not in use. Therefore, release mechanisms such as a crimp seal are recommended [78]. This heat pipe system uses a cryogenic relief valve, but for additional safety, after a test, the working fluid is released to the atmosphere by opening the valve that seals the heat pipe.

Some additional engineering considerations for building the system was incorporating bends or U-bends in any cryogenic fluid transfer lines to allow for flexibility to preventing any stress buildup. Before the pipe was tested, the system was pressurized to look for any leaks in the solder joints. Also the liquid nitrogen reservoir was thermally cycled several times. During this, attempts were made to find any leaks in the reservoir. However this task was difficult because the cold copper surface at LN2 temperatures caused air to condense on a bare pipe and drop liquid oxygen. This situation turned out to be dangerous because the oxygen is potentially flammable. The final tests to ensure a leak-free system were to place everything in the vacuum chamber and determine if the pipe and liquid nitrogen reservoir held pressure without changing the vacuum chamber pressure.

4.5 Experimental Results

To test the operation of the heat pipe, the vacuum chamber was evacuated to the base pressure of a roughing pump to about $7{\cdot}10^{-2}$ mbar. During the chamber pumpdown, the heat pipe is connected to a separate lab vacuum supply via the working fluid gas feed to evacuate the system. This minimizes the presence of any non-condensable gases and ensured that nitrogen would be the only working fluid inside the pipe. Once base pressure is achieved and the pipe is evacuated, temperature measurements are started so that the heat pipe is at room temperature. Working fluid is then injected into the heat pipe at ambient conditions. A large tank of industry grade nitrogen at high pressures is the source for the working fluid. To inject working fluid the gas feed valve is opened while the working fluid entering the pipe is measured using a flowmeter. After a gas injection, the gas feed valve is closed. The timer for a test starts when liquid nitrogen first starts to flow into the LN2 reservoir. As the working fluid condenses inside the pipe, the pipe pressure decreases. After a sufficient drop in pipe pressure working fluid is periodically injected.

For the first test without HTS wires, working fluid was injected until saturation was achieved throughout the end of the pipe. For this test the pipe was approximately horizontal and only about 20 g of working fluid was needed in order for the end of the pipe to reach saturation condition. This is less working fluid than the calculated value (53.5 g) from Section 4.2. Therefore, it is likely that the wick is not completely wetted and likely undercharged. However, this partially wetted wick was sufficient to transport heat introduced by the resistor, as will be shown by the test data. Since the heat pipe did reach near isothermalization, further testing to verify the power capacity with a fully wetted wick at tilted conditions was explored while testing the system with an HTS wire.

4.5.1 Test without HTS wires

The heat pipe was first tested without the aluminum block and HTS wire to verify basic operability and to get a first comparison with the power capacity and thermal resistance models. The temperature profile as a function of time for the heat pipe is shown in Figure 4.25 along with the power introduced by the power resistor. Initially the heat pipe is at room temperature. At zero minutes, LN2 is flowed into the liquid nitrogen reservoir. There are five thermocouples pairs located at various distances away from the condenser as shown in Figure 4.24. The first thermocouple pair (magenta) is right next to the condenser, on the opposite side of the copper bushing which is soldered to the reservoir. This location is the '0' origin measuring the axial distance away from the condenser. The other thermocouple pairs are located at

10 cm (blue), 25 cm (green), 50 cm (black), and 75 cm (red) away from the condenser. The power resistor is also shown in Figure 4.24.

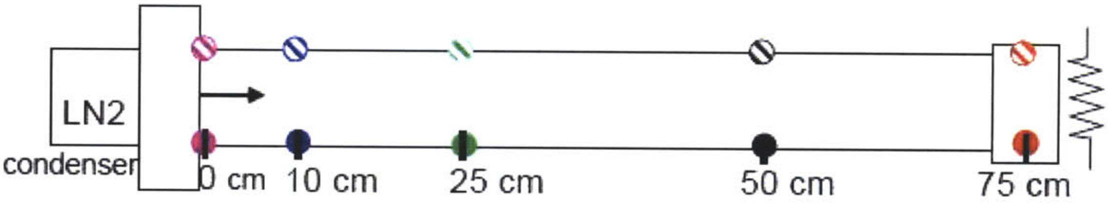

Figure 4.24 Thermocouple locations for test without HTS wire

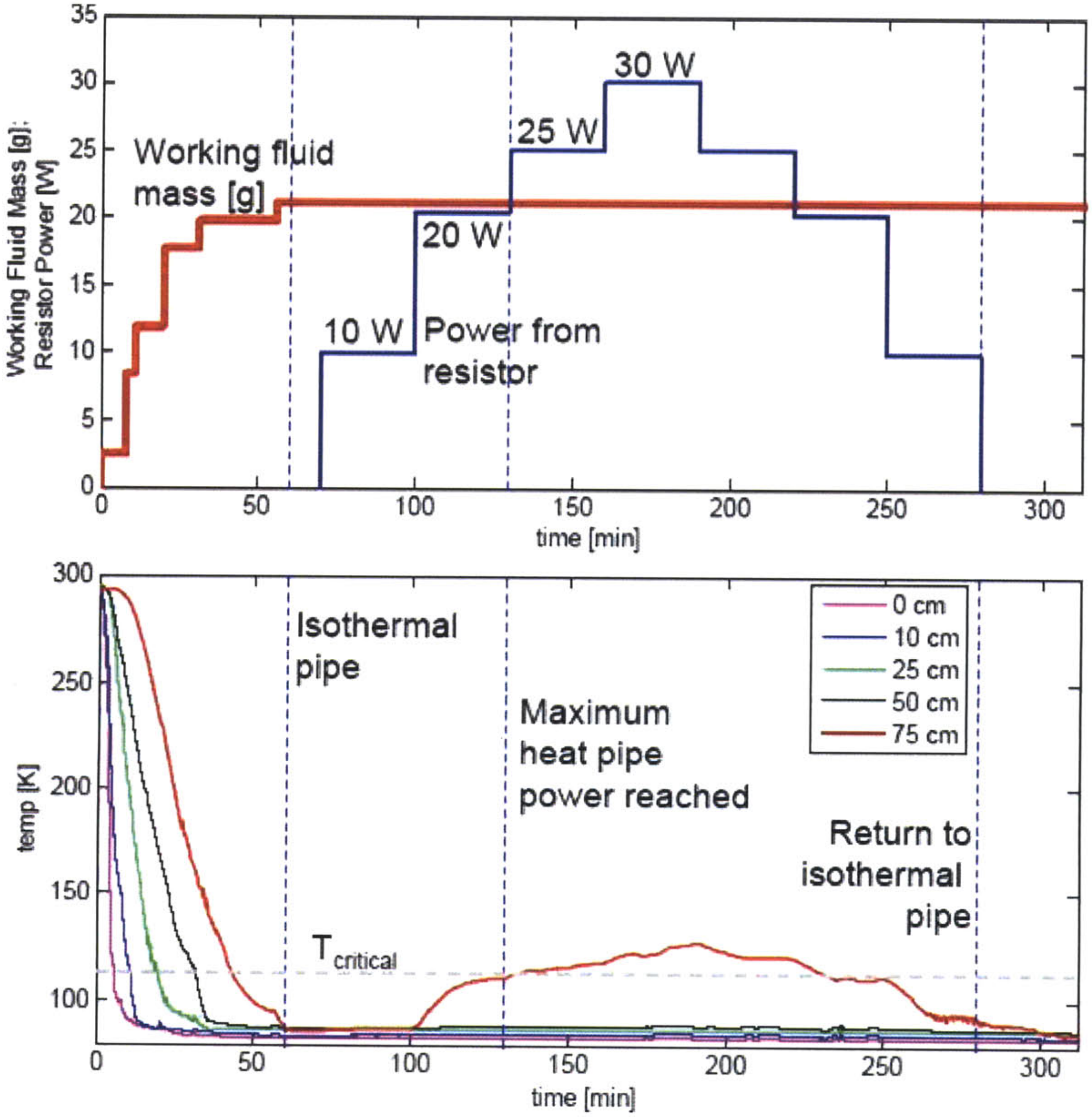

Figure 4.25 Test of heat pipe without HTS wire showing working fluid mass, resistor power and temperature of the pipe as a function of time

Working fluid is added to the heat pipe as the pipe temperature drops. After 20 g were added, the temperature across the pipe is relatively isothermal. For the test shown in Figure 4.25 the heat pipe reaches saturation conditions after approximately 60 minutes. At this time, the temperature of the pipe is relatively isothermal between 84 K and 87 K. To test when dry-out of the wick occurs, heat is added to the system using the power resistor at the end of the pipe starting at the 70 minute mark. The temperature of the heat pipe is allowed to reach an approximate steady-state after 30 minutes at each power level. Steady-state operating conditions were determined when changes in temperature with time less than 1 K were observed. After power was applied, the heat pipe was returned back to steady-state saturation conditions. For each of the thermocouple pairs at each location in Figure 4.24, only the bottom thermocouple measurement was plotted in Figure 4.25 because the same temperature was measured by each thermocouple pair.

The temperature as a function of axial distance along the length of the pipe with the condenser located at the origin is shown in Figure 4.26. The temperatures shown are at an approximate steady-state after 30 minutes of applied power. The temperature for no applied power (0 W, shown in green), is the temperature distribution for the heat pipe carrying heat only from the environment, which is approximately 30 W. The heat pipe is relatively isothermal for this case. It is also isothermal for the case when 10 W is applied, which means the heat pipe is carrying 40 W total. The temperature profile seen in Figure 4.26 is similar to temperature profiles in Silvares and Cravalho for a 12 inch long nitrogen pipe with finned metallic wick structure [33].

Dryout of the wick occurs when there is a large increase in temperature beyond the saturation conditions. Dryout indicates that the maximum heat pipe power capacity has been exceeded. From Figure 4.26, dryout of the wick occurs somewhere between 10 and 20 Watts of applied power from the resistor. Since power coming into the pipe from the chamber radiation environment is approximately 30 Watts the measured total power capacity is approximately 40 to 50 Watts. This is close to the designed power capacity of approximately 50 Watts. These differences can come from how dry-out is interpreted from the temperature data.

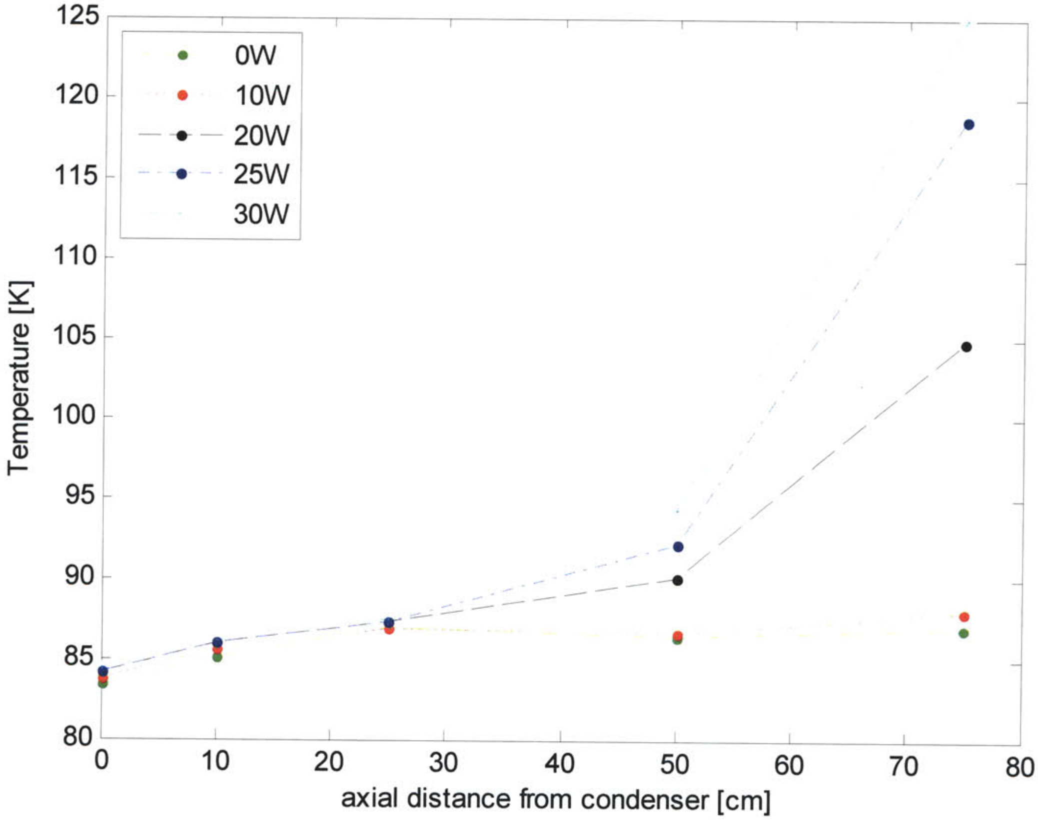

Figure 4.26 Temperature vs. axial distance from the condenser for various values of applied power

Using the temperature data from Figure 4.25 at various amounts of applied power, a comparison of the evaporator temperature (thermocouple at 75 cm) as a function of total power into the pipe is shown in Figure 4.27. The temperature at the end of the evaporator in the thermal resistive network from Section 4.2 is shown by the black line. A finite difference model is also shown by the cyan line and the experimental data is shown by the blue line with data points marked by "x's". The FDM uses an effective thermal conductivity for the heat pipe based on the temperature data at saturation. Using the experimental data, the heat pipe operating at saturation condition, with no applied power, has a calculated effective thermal conductivity of 24 kW/m·K, which is approximately 59 times the thermal conductivity of copper. This calculation used a condenser temperature of 82.55 K and a temperature for the end of the evaporator of 87 K located 75 cm away.

Figure 4.27 can also be used to bound the heat pipe power capacity. But first it is important to understand relevant uses for the resistive network model and the FDM. The resistive network model only accounts for the heat pipe in steady-state operation. Dry-out is not captured by the model. Similarly the FDM does not account for dryout conditions; it also assumes the pipe is always at saturation. Therefore, any region of temperature greater than the models indicates the occurrence of dryout. Therefore, from Figure 4.27, dryout occurs approximately between 45 to 50 W, which is where there is a large rise in temperature compared to the models. This result correlates well with the power capacity deduced from Figure 4.26. Again, it is important to note that this is a result for a horizontal pipe where the wick is not fully wet, so it is expected that the power capacity is less than the designed power of 50 W. These models will be revisited later in this chapter.

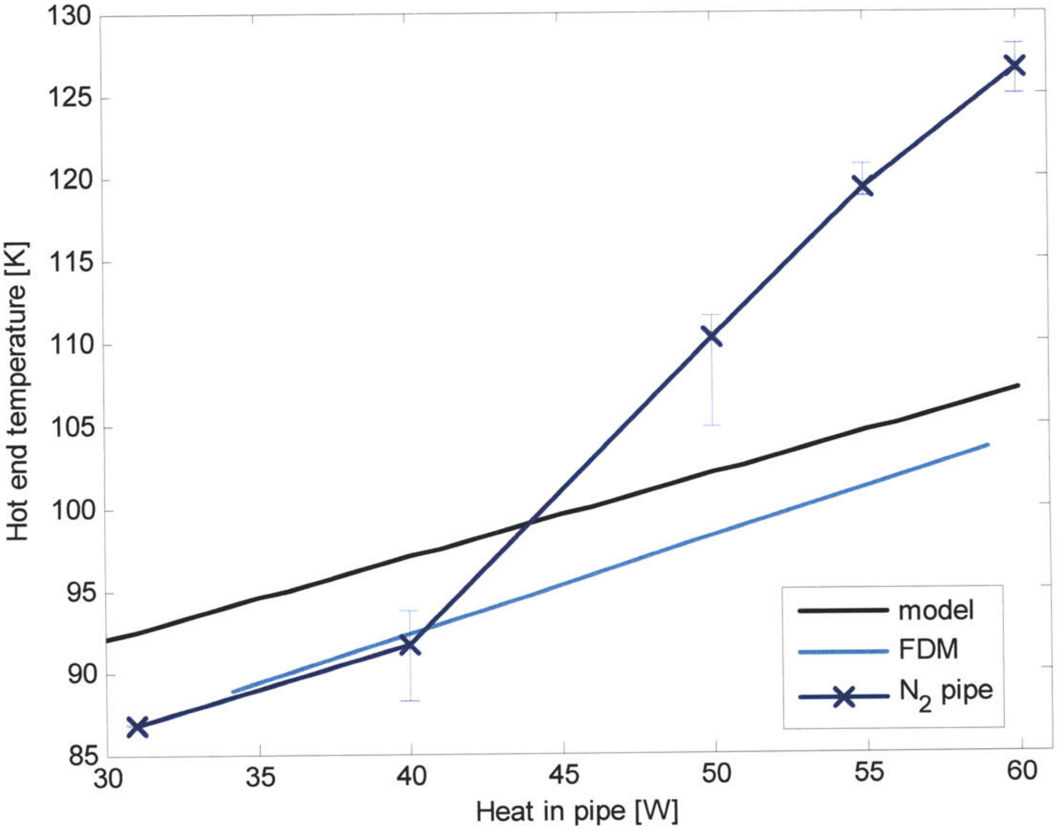

Figure 4.27 Temperature at end vs. total power input

4.5.2 Test with HTS Wires

After verifying operation of the cryogenic heat pipe, the HTS wire and aluminum block were inserted and tested. An additional thermocouple pair was added to the heat pipe and some of the thermocouples were moved to have greater concentration at the hot end, farthest away from the condenser. The thermocouple locations are shown in Figure 4.28. In addition, the resistor was moved to accommodate the HTS connectors.

The results of a test with HTS wire are shown in Figure 4.29. The middle plot shows temperature for the heat pipe as a function of time. The thermocouples are located at 0 cm, 25 cm, 50 cm, 65 cm, 70 cm, and

75 cm away from the condenser. For simplicity, the bottom thermocouples are shown since at each pair, similar temperatures were observed.

The top plot in Figure 4.29 shows the cumulative working fluid mass in the pipe as a function of time in red. The same procedure of filling the heat pipe was used with working fluid injected at periodic intervals. Working fluid was injected during the first 60 minutes approximately every six to eight minutes. With the HTS wire tests, it was noticed that the heat pipe took a longer time to cool down and working fluid needed to be injected at more intervals. The steady-state working fluid mass needed to fully wet the wick is approximately 53.5 g as was shown in Figure 4.14. During testing it was observed that the heat pipe was leaking some working fluid into the vacuum chamber at a rate of approximately 2.45 g every 10 minutes. To compensate for this, additional working fluid was injected occasionally. An example of this is seen by additions to the working fluid cumulative mass at approximately 81 and 92 minutes into testing. After a test is conducted the working fluid is evacuated from the heat pipe and measured. For the test shown in Figure 4.29, working fluid was evacuated at 220 minutes. The top plot in Figure 4.29 accounts for the leak rate after post-processing. This is why the graph for working fluid mass looks like a stair case plot with decreasing amounts of working fluid after an injection. Every jump in the stair case indicates when working fluid was injected. Once the wick is saturated at approximately 60 minutes, working fluid is injected to compensate for the leak rate and to keep approximately 53.5 g of steady-state working fluid.

The top plot of Figure 4.29 also shows input from the power resistor in blue. The bottom plot of Figure 4.29 shows the resistance of the HTS wire as a function of time. This aspect of the test will be discussed in Section 4.5.3.

The test shown in Figure 4.29 achieved saturation conditions throughout the heat pipe at approximately 65 minutes as shown by the dotted blue vertical lines. Saturation occurs when the wick is fully wetted with around 53.5 g.

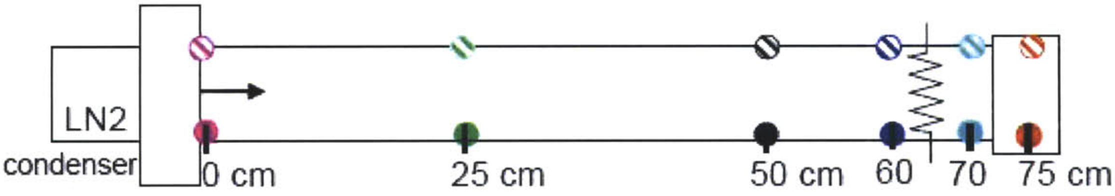

Figure 4.28 Thermocouple locations for tests with HTS wire

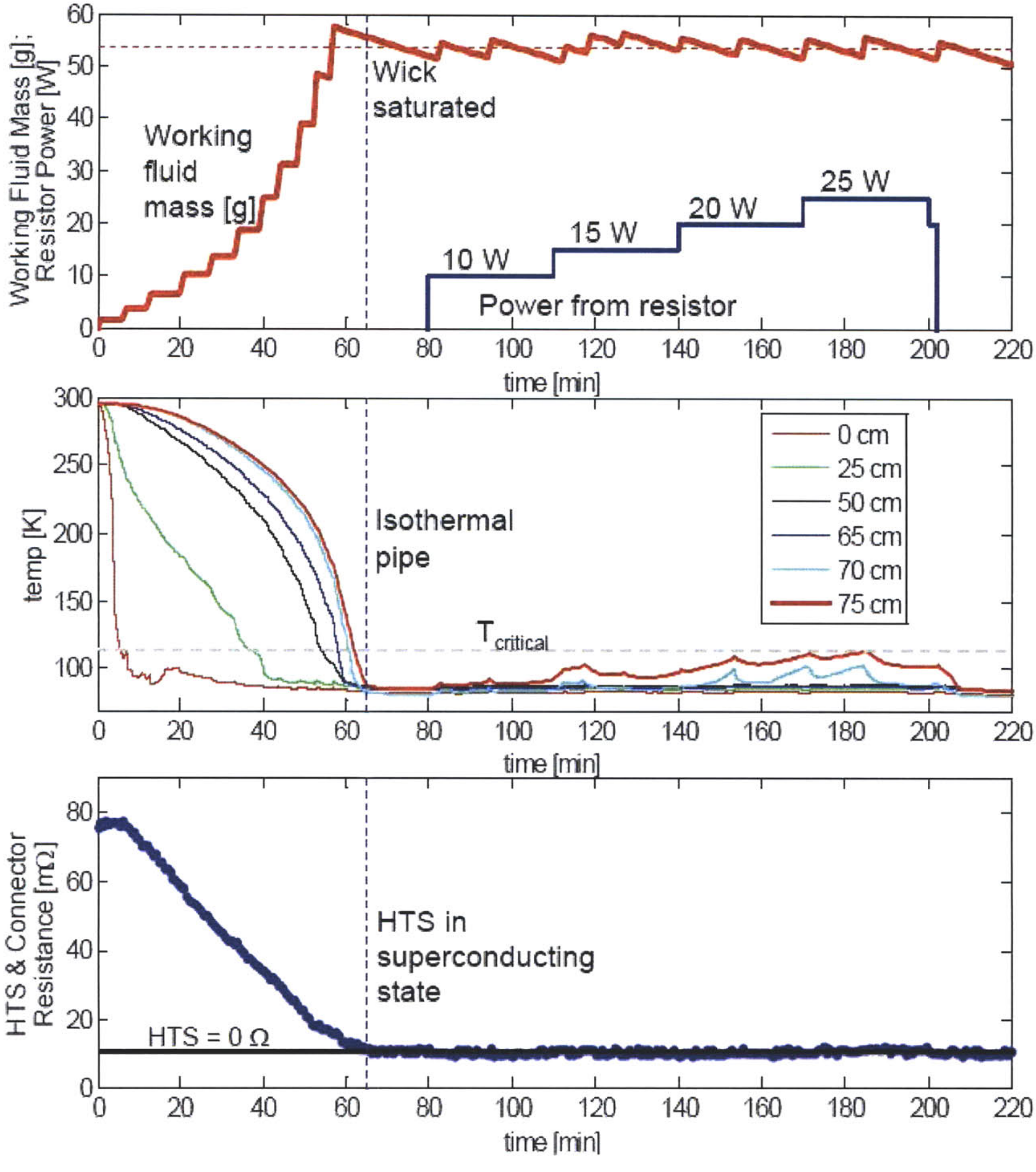

Figure 4.29 Test of heat pipe with HTS wire

The pressure in the pipe is shown in the top plot of Figure 4.30. During steady-state operation (between 65 minutes and 220 minutes) the pipe pressure is between 20 to 25 psi. The pipe pressure fluctuates every time working fluid is injected. The pressure of the nitrogen pipe corresponds to a temperature of approximately 80 to 82 K according to the nitrogen saturation properties (Table 4.4). This corresponds with the approximate temperatures measured throughout the pipe seen in Figure 4.29.

The pressure of the vacuum chamber is also shown in the bottom plot of Figure 4.30. The chamber pressure rises as the pipe temperature drops because of the coefficient of thermal expansion mismatch at the HTS connectors. The CTE mismatch is discussed later in this section. The vacuum pressure during testing is approximately one millibar, which is a sufficient vacuum to minimize any convective heat transfer.

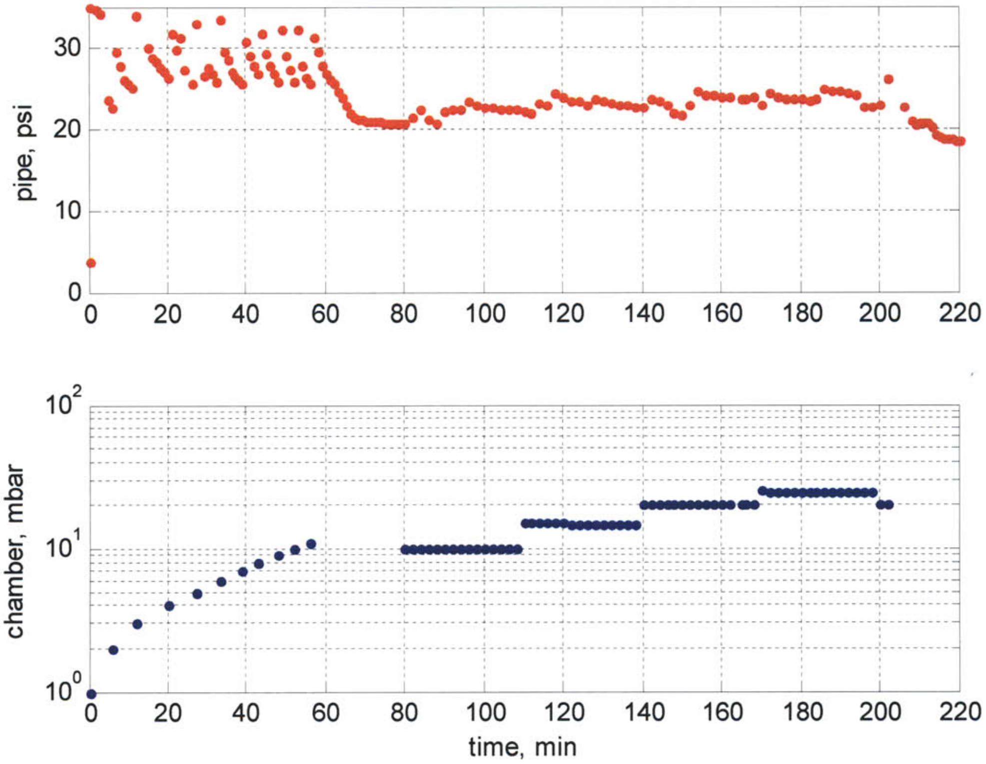

Figure 4.30 Pressure in the heat pipe (top) and the vacuum chamber (bottom) during testing

After 25 minutes of steady-state operation at saturation condition, the power resistor was turned on to 10 Watts, as shown by the blue curve in on top plot of Figure 4.29. For this test, a maximum of 25 Watts was applied before dry-out occurred. This is slightly greater than the same conditions that dryout occurred in the pipe without the aluminum block and HTS wire. The temperature as a function of axial distance away from the condenser is shown in Figure 4.31 for various amounts of total power carried by the heat pipe. There is a large rise in temperature at the end of the heat pipe between 45 W to 50 W of total power. This is one indication that dryout occurs in range of 45 W to 55 W.

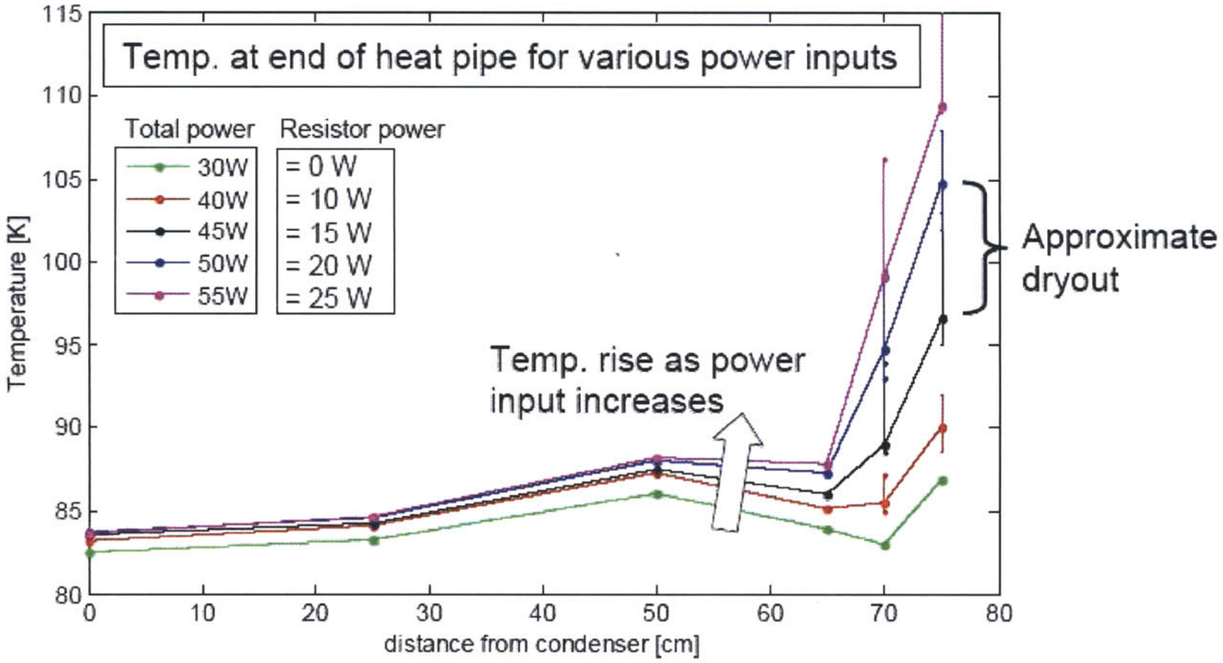

Figure 4.31 Temperature vs. axial distance from the condenser for various amounts of total power

The second method of examining for dryout conditions is to compare the difference between the experimentally measured temperature at the end of the evaporator with the evaporator temperature from the resistive network model. This difference shown in Figure 4.32 and is normalized by the model temperature. The HTS test data exhibits a large rise in temperature beyond the temperature models at around 45 to 50 W. This result is similar to the test without the HTS wires and aluminum block, which is also shown in Figure 4.33. The exhibited power capacity of approximately 50 W was closely predicted by the model, as was shown in Figure 4.13. Now that the power capacity can be accurately predicted the performance of the HTS wires is described in the next subsection. It is important to note that the test with the HTS wires used a fully wetted wick and was tested at a 0.6° angle while the test without the HTS wires tested a horizontal heat pipe with an under-saturated wick.

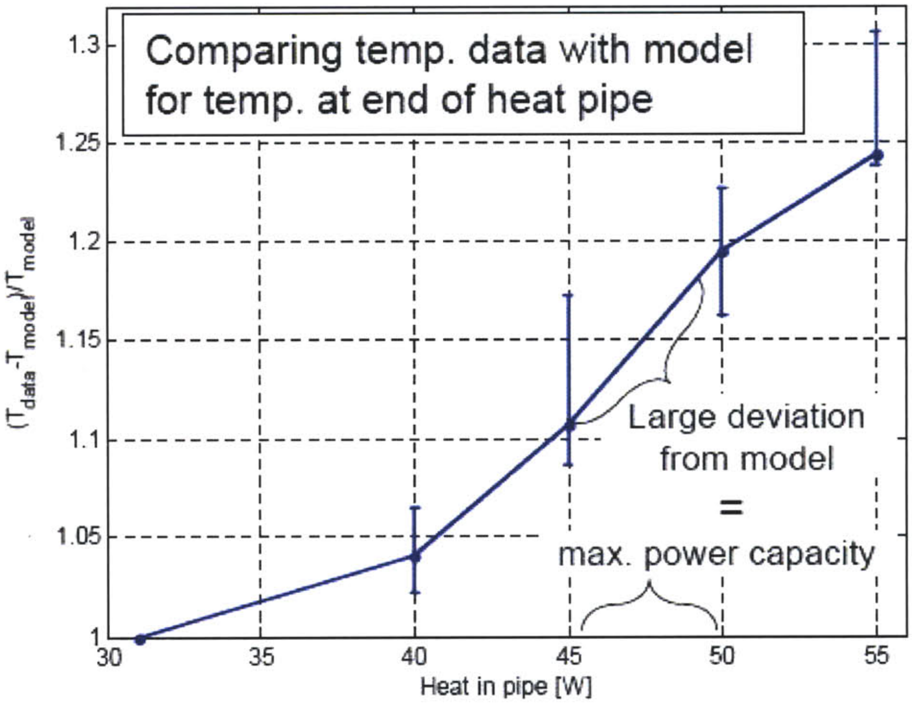

Figure 4.32 Normalized difference in experimental and modeled evaporator temperature for test with HTS

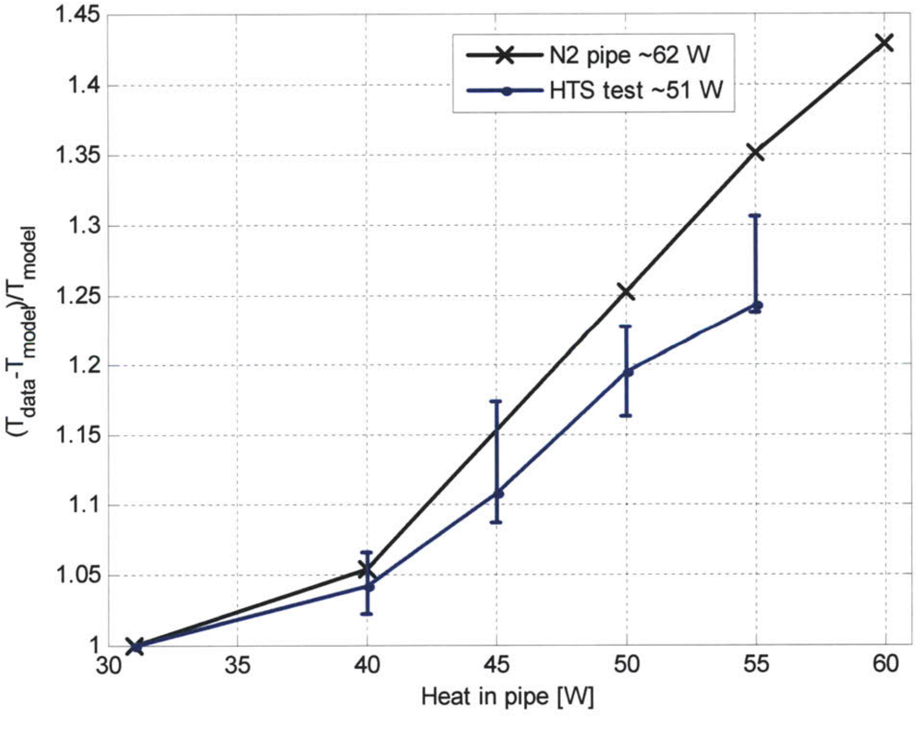

Figure 4.33 Normalized difference in experimental and modeled evaporator temperature for tests with and without HTS

4.5.3 Measuring the state of the HTS

A Wheatstone bridge is used to determine the drop in resistance for the HTS wire during heat pipe operation and is shown in Figure 4.34. One leg of the Wheatstone bridge is the superconducting wire, while the other three legs are known resistances. The voltage of the bridge is given by

$$V_g = \left(\frac{R_x}{R_3 + R_x} - \frac{R_2}{R_1 + R_2} \right) V_d \tag{4.41}$$

where R_x is the superconductor, and the values for R_1, R_2, and R_3 are shown in Figure 4.34. To determine the resistance of the superconductor, Equation (4.41) is solved for R_x and is given by

$$R_x = \frac{R_3\left(R_2 + \frac{V_g}{V_d}\left(R_1 + R_2\right)\right)}{R_1 - \frac{V_g}{V_d}\left(R_1 + R_2\right)} \tag{4.42}$$

In order to determine the change in resistance for the HTS from non-superconducting to superconducting state, a 21 cm diameter, 21 turn coil was dunked into liquid nitrogen. Its change in resistance was measured, and the resistance per meter was found to be approximately 40 mΩ/m. The length of the HTS wire in the heat pipe is approximately 1.64 meters long, so the expected drop in resistance is approximately 65 mΩ.

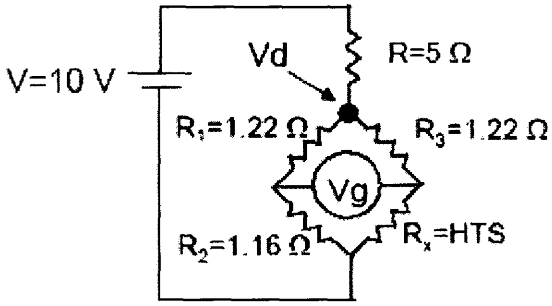

Figure 4.34 Wheatstone bridge circuit

The resistance measured by the Wheatstone bridge includes the connectors and wiring, which are non-superconducting and will always have a finite resistance. This includes the vacuum chamber electrical feedthrough, the copper connector, and wiring used between each of these. The estimated total resistance of the connection is approximately 10 mΩ and the components are summarized in Table 4.5.

Table 4.5 Non-superconducting resistances measured by Wheatstone bridge

Wire type	Length	Resistance
Copper wire – 12 gauge Deans wire	~83 cm x 2 = 4 ft	8.7 mΩ
Copper bus – 3/16" diameter	9 cm + 7 cm	0.3 mΩ
Feedthrough, ¼" stainless steel	10 cm x 2	1.0 mΩ
	Total	10.0 mΩ

The drop in resistance is shown by the bottom plot in Figure 4.29. The thick solid black line shows the approximate baseline resistance of the wire connections that are non-superconducting. At approximately 65 minutes, when the heat pipe is at saturation conditions, the entire HTS wire is in a superconducting state. There is a drop in resistance of approximately 70 mΩ. The estimated resistance drop if the HTS were replaced by a conductor, such as silver, is approximately 19 mΩ [79]. In fact, this drop in resistance is consistent to the change in resistance noticed in the first 20 minutes of a test. It appears that the superconductor is also operating at superconducting levels even when dryout occurs (between ~140 min. and ~200 min.). From Figure 4.29, temperatures measured on the outside of the heat pipe are above the critical temperature (110 K), however it is likely that the current Wheatstone bridge is not sensitive enough to detect small portions of change in superconductor resistance which occur on the order of a few centimeters of the HTS wire at the end of the heat pipe evaporator. The overall results of testing shows that the HTS wire can be cooled in the vapor space of a cryogenic heat pipe.

4.5.4 Experimental Results of HTS Carrying Current

Operation of the HTS wires was also tested by carrying current through the wires. The purpose of this test was to demonstrate the operation of the HTS wires using a current source. The previous measurement of the HTS wires using the Wheatstone bridge was considered a voltage source test. The HTS wire carried 10 A during the entire test, which is shown in Figure 4.35. The voltage of the HTS wires was measured and the resistance of the HTS wires was calculated from the current and voltage data. The resistance of the HTS wires is shown in the bottom plot in Figure 4.35. Once saturation of the heat pipe is achieved resistance of the HTS wires drops to 10 mΩ, which is the same resistance of the non-superconducting connectors used in the previous test. Once the heat pipe is at saturation condition, the HTS wires remain in a superconducting state.

The middle plot shows the temperature versus time and the top plot shows the cumulative working fluid mass in red. In addition, the approximate additional power carried by the heat pipe is shown by the blue line. At time = 0, the HTS wires is carrying 10 A at 1 V, and introducing 10 W into the heat pipe vapor space. However, as the HTS wires cool, its resistance drops, and therefore the power also decreases. At approximately the 90 minute mark, a resistor is turned on to 5 W. This is insufficient additional power to cause a large change in temperature. The HTS wire and power resistor system were configured so that no additional power could be introduced to test for dryout.

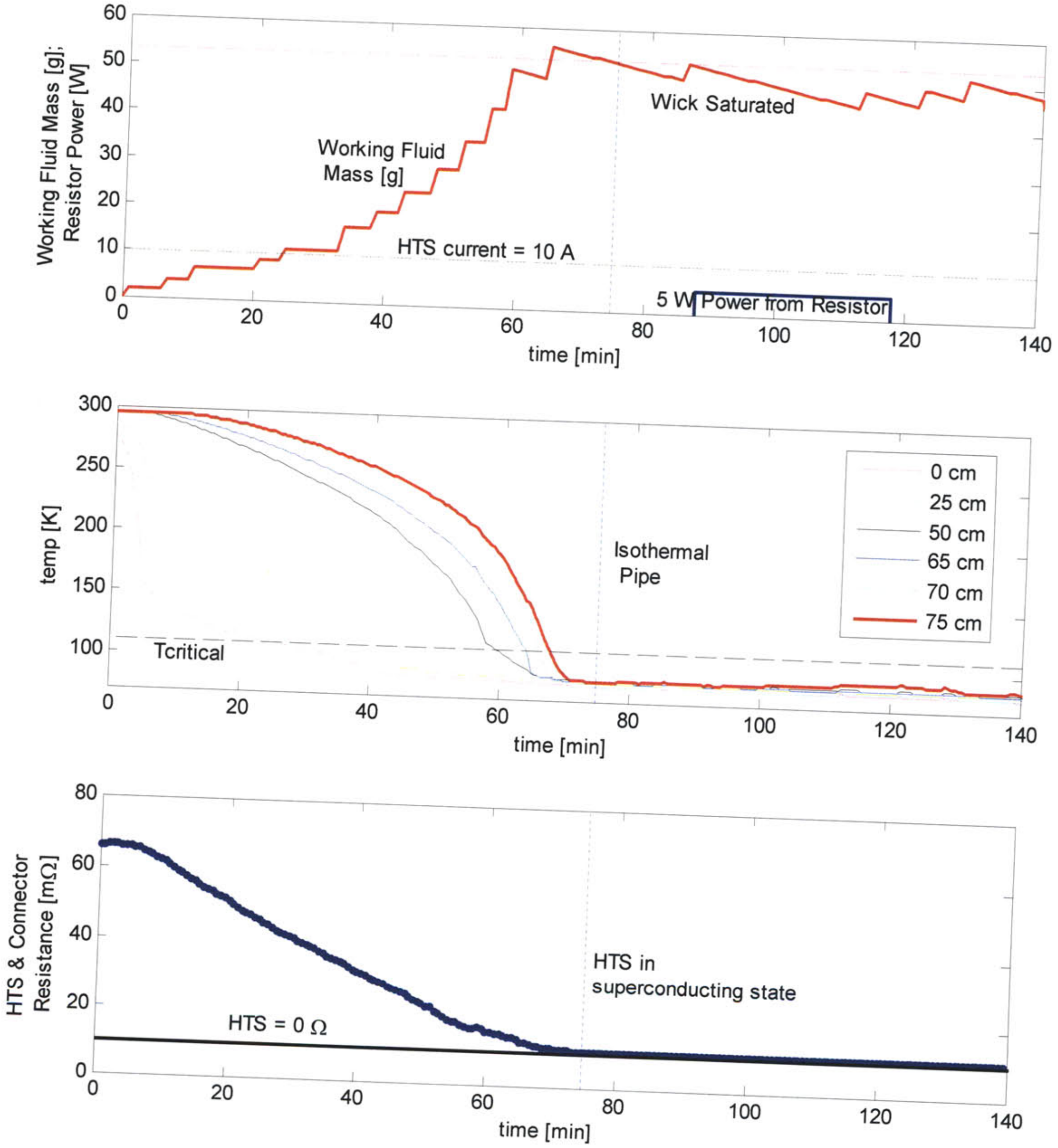

Figure 4.35 Experimental results for a heat pipe with HTS carrying current

Saturation condition for the test occurred at approximately 75 minutes and is shown by the vertical dotted blue lines in Figure 4.35. The approximately steady-state mass is between 48 and 53 g, which is the range predicted by analysis in Figure 4.14. It took approximately 10 minutes longer to achieve saturation condition. This is likely because the addition of heat via the HTS wires during injection of the working fluid slowed the cooling of the aluminum block inside of the pipe. However, past tests without any heat introduced during working fluid injection have experienced a variation in the time to achieve saturation on the order of five to ten minutes. This depended on the frequency of working fluid injection.

In summary, the results of testing the HTS wires with current provided a second method of demonstrating operation of the HTS wires inside the vapor space of a heat pipe.

4.6 Analysis of Testing

4.6.1 Heat Pipe Leaking

Leaking in the heat pipe is likely due to the coefficient of thermal expansion mismatch at the Teflon – copper interface in the HTS connectors. In Figure 4.36, the working fluid mass is shown during a test. The blue line corresponds to the cumulative mass in the pipe without calculating for any leaks. The red line is the cumulative mass accounting for leaking and is the same line that was shown in the top plot of Figure 4.29. The test shown in Figure 4.29 ends at the 220 minute mark and the working fluid is vented, as shown by the decrease in working fluid mass between minute 220 to minute 250. The leak in the heat pipe accounts for the difference in final working fluid mass seen in Figure 4.36 at the 250 minute mark. The leak rate is approximately 0.245 g/min assuming that the leaking occurs at approximately 50 minutes.

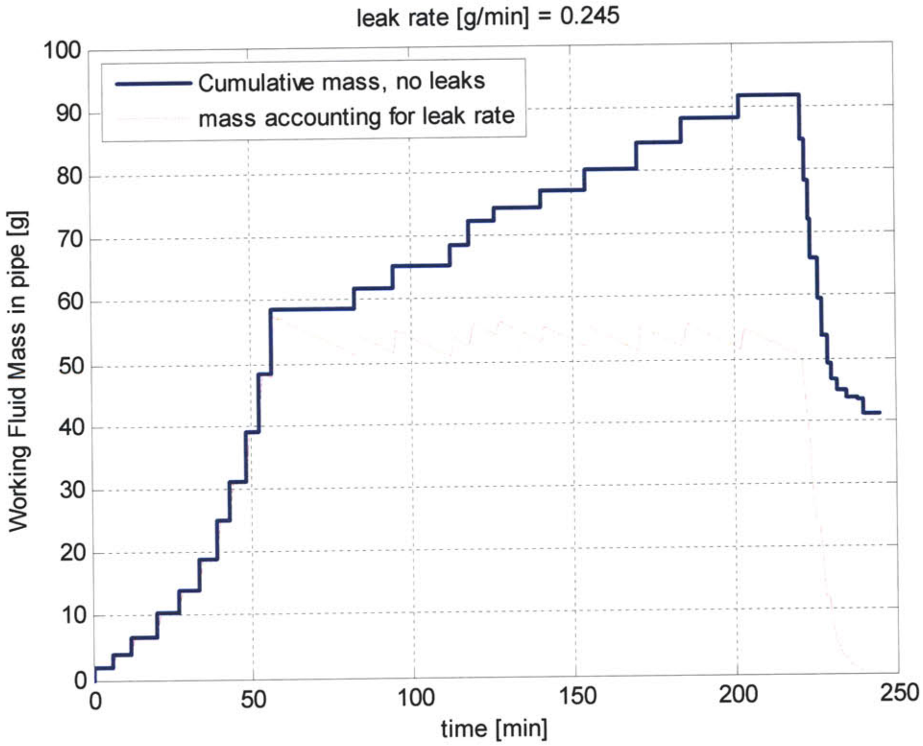

Figure 4.36 Working fluid mass during a test comparing total measured mass and post-processed mass accounting for leaking

An approximate size of any hole or gap created by the thermal coefficient mismatch can be determined using a simple one dimensional model for the change in length, δ, for each material

$$\delta = \alpha_{\exp}\Delta TD \qquad \begin{aligned} \alpha_{Cu} &= 20\cdot 10^{6}\,/^{\circ}\,\mathrm{C} \\ \alpha_{PTFE} &= (70-120)\cdot 10^{6}\,/^{\circ}\,\mathrm{C} \end{aligned} \tag{1.43}$$

given the coefficient of thermal expansion ($\alpha_{\exp}$) for each material, the change in temperature ($\Delta T = 300 - 70 = 223$), and the approximate length (*D*). There is a range of $\alpha_{\exp}$ for the Teflon or PTFE (Polytetrafluoroethylene) [80]. The Teflon shrinks more than the copper bus or the fittings so the problem could be between the brass ferule used by the Swagelok and the Teflon at the 1/4 inch interface. The length *D* used by the 1D model is a circumference distance so the change is length is actually a circumferential δ. Since the length is really 2πr, and using the 1/4 inch interface ($r \sim 6.35\cdot 10^{-3}$ m), the change in length for each material is given by

$$\begin{aligned} \delta_{Cu} &= 178\mu\mathrm{m} \\ \delta_{PTFE} &= 623\mu\mathrm{m} - 1.1\mathrm{mm} \end{aligned} \tag{4.44}$$

The circumferential δ's calculated in Equation (4.44) can be used to calculated δ_{radius} in Figure 4.37, which is an approximate radial change in distance for each materials. The gap size is then the difference in δ_{radius}.

$$\text{gap size} = \delta_{PTFE-radius} - \delta_{Cu-radius} \tag{4.45}$$

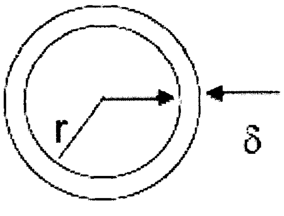

Figure 4.37 Geometry of gap size due to thermal coefficient mismatch

For each material the change in radius, δ_{radius}, is calculated to be

$$\begin{aligned} \left(2\pi\left(\mathrm{r}+\frac{\delta_{Cu-radius}}{2}\right)\right) &= C - 178\mu\mathrm{m} \rightarrow \delta_{Cu-radius} = 57\mu\mathrm{m} \\ \left(2\pi\left(\mathrm{r}+\frac{\delta_{PTFE-radius}}{2}\right)\right) &= C - \delta_{PTFE} \rightarrow \delta_{PTFE-radius} = 198 - 350\mu\mathrm{m} \end{aligned} \tag{4.46}$$

This results in a gap size that is between 150 to 300 μm and this gap is continuous around the circumference.

In order to verify this result, there is a second method of determining the hole size. This calculation uses the mass flow rate of a gas at choked conditions

$$\frac{\dot{m}}{A_{hole}}=\frac{P_o}{\sqrt{RT_o}}\sqrt{\gamma}\left(\frac{2}{\gamma+1}\right)^{\gamma+1/2(\gamma-1)} \qquad A_{hole}=\frac{\pi}{4}d_{hole}^{\;2} \tag{4.47}$$

Using the conditions of the test, the pipe pressure, P_o is approximately 24 psi ($1.65\cdot10^5$ Pa), the gas constant for Nitrogen is 297 J/kg-K, and the pipe temperature T_o is approximately 100 K. During testing, the system has been observed to lose as much as 3.1 grams every 10 minutes, which yields a mass flow rate, $\dot{m}$, that is approximately $5\cdot10^{-6}$ kg/s. Substituting these values into Equation (4.47), the approximate hole size is 100 μm. This is close to the same hole size calculated using the thermal coefficient mismatch. In conclusion, the CTE mismatch appears to cause a leak rate in the HTS connectors with a gap size on the order of 100 μm.

For a future flight version, it is necessary to redesign the HTS connectors to prevent any leaking. Creating leak tight electrical feedthroughs has been discussed by Richardson [81]. There are various types of epoxy that are useful for electrical feedthroughs and as a structural member. One example is Stycast 1266 from Emerson and Cuming [82] that can be applied at room temperature and provide electrical insulation. One topic for future HTS connectors is to either use a custom design feedthrough with leak tight epoxies or to use commercially available HTS leads.

4.6.2 Verifying Operation at an Angle

One of the reasons for testing the heat pipe at an angle is to ensure that the wick is working properly and that no flooding of the condenser with working fluid occurs. To model the pooling of working fluid the pipe can be approximated as a rectangular box with the same volume as the pipe. The box has a length *L* and side *s* and is shown in Figure 4.38. The volume, V_p, for the entire pipe as modeled by the box and as a pipe with radius *r* is given by

$$V_p=\pi r^2 L=s^2 L \tag{4.48}$$

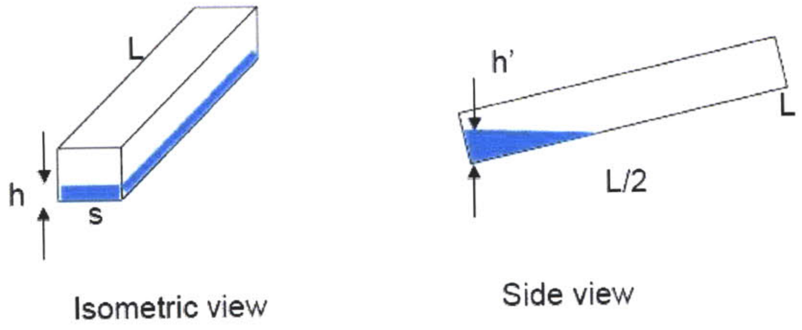

Figure 4.38 Geometry of a 'pipe' at an angle showing the liquid level if pooling occurs

Let *h* be the height of the liquid in the box that runs the entire length, as shown in Figure 4.38. The volume of liquid in the system is given by

$$V_l = \frac{m}{\rho} = h \cdot s \cdot L \tag{4.49}$$

Now the height of the liquid in the pipe can be solved from Equation (4.49)

$$h = \frac{m}{\rho} \frac{1}{Lr\sqrt{\pi}} \tag{4.50}$$

To determine the height of the liquid for a pipe at an angle, let the entire volume of liquid be contained to half of the pipe length at *L*/2. Now the liquid has a height $h^{'}$ as shown in the side view in Figure 4.38. The side view of this geometry has an area

$$A_{side} \sim \frac{1}{2} h^{'} \frac{L}{2} \tag{4.51}$$

Setting this area equal to the side view area for a non tilted pipe (*h*·*L*), the height, $h^{'}$', can be solved to be

$$h^{'} = 4h = 4\frac{m}{\rho} \frac{1}{Lr\sqrt{\pi}} \tag{4.52}$$

The angle of the heat pipe during the tests is approximately 0.6°. At this angle, the bottom of the pipe at *L*/2 (half way) is approximately 4.55 mm above the condenser, and the bottom of the pipe at the end of the pipe (*L*) is approximately 9 mm above the condenser. For the working fluid to pool in the entire half-length of the pipe 53 g of working fluid are required. However, if pooling occurred, the near isothermal behavior of the heat pipe that was observed would not have been exhibited. The height of the liquid level given other amounts of working fluid is shown in Table 4.6. Even if additional amounts of working fluid were injected, the potential height of any pooling liquid does not pool to the elevated end of the pipe.

This shows confidence that the wicking structure is working properly and that the working fluid does not appear to pool at the bottom of the pipe.

Table 4.6 Height of liquid level given mass of working fluid

m [g]	h' [mm]
46.6	4
53	4.55
65	5.3
85	6.9

4.6.3 Performance of Heat Pipe with only a Coarse Mesh

Another interesting analysis is to verify the operation of the heat pipe if only a coarse mesh were present. This would mean that the fine mesh does not function to provide capillary pressure. The power capacity as a function of layers of a coarse #50 mesh is shown in Figure 4.39. The results use the same configuration of the heat pipe tested with only the fine mesh removed. Using only a coarse mesh, the heat pipe power capacity is drastically reduced, as heat pipe power is less than one Watt. This system would not be able to carry any power in the experimental test. Clearly, the fine mesh is important in providing the capillary pressure that allows for a large power capacity.

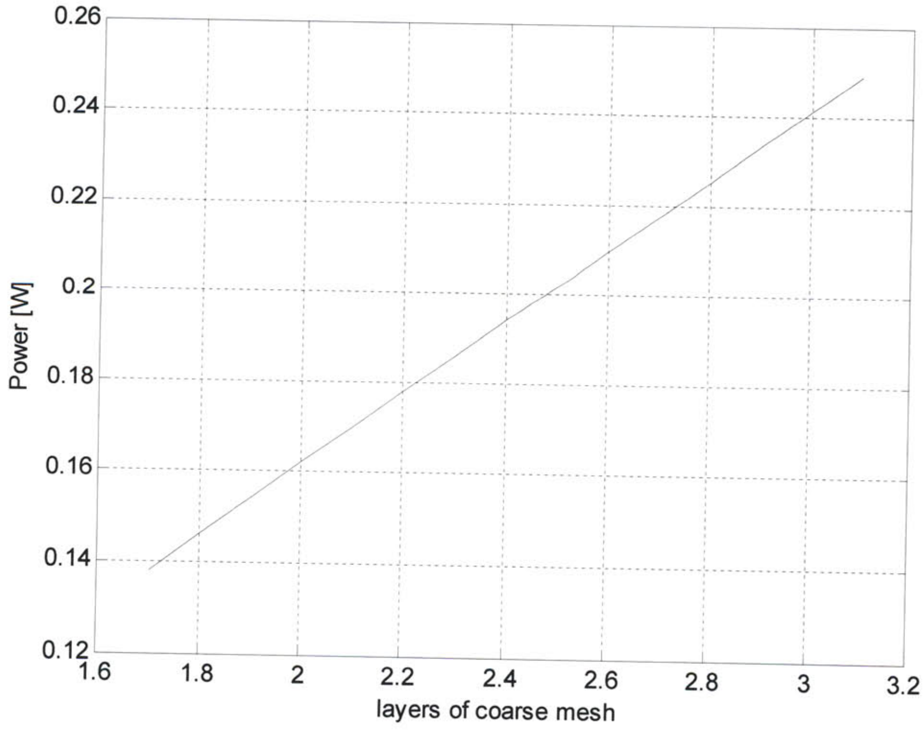

Figure 4.39 Heat pipe power capacity for a system with only coarse mesh

4.6.4 Maximum Current during Test

The performance of the HTS wire is affected by the operating temperature and the local magnetic field. These effects are shown in Figure 4.40. The magnetic field effects are described by Kwon [5] and also discussed in Appendix D. This section concentrates on the effect of the temperature on the current that the HTS wire can carry. Given a magnetic field, the critical current density of the HTS wire, I_c, increases as the wire operating temperature is reduced. In Figure 4.40a, the dependent variable (y-axis) shows the ratio of in I_c over the I_c at 77 K. This ratio, I_c/I_c(77 K), increases as the temperature decreases. For example, given zero magnetic field in Figure 4.40a, the ratio at 77 K is one (as expected), while the ratio is approximately 5.3 at 20 K, meaning the HTS wires can hold 5.3 times more current at 20 K compared to at 77 K.

Commercially available cryocoolers can operate at temperatures below 77 K enabling the HTS wire to hold more current. However, the cryocooler requires additional electrical power to operate at colder temperatures. The temperature range of the heat pipe is between the working fluid triple point and the critical point. For nitrogen this temperature range is between 63 K and 126 K.

Since the heat pipe in this chapter operates at temperature greater than 77 K, the system does not offer an improvement in I_c. In fact, assuming that there is a reduction in I_c for warmer operating temperatures, operating the HTS wires in the current heat pipe may reduce the maximum current. The different amount of heat carried by the heat pipe changes the temperature at the end of the pipe, as seen by tests with a power resistor turned on. Since the current in the HTS wire is limited by the hottest portion, these temperature fluctuations may affect the maximum operating current.

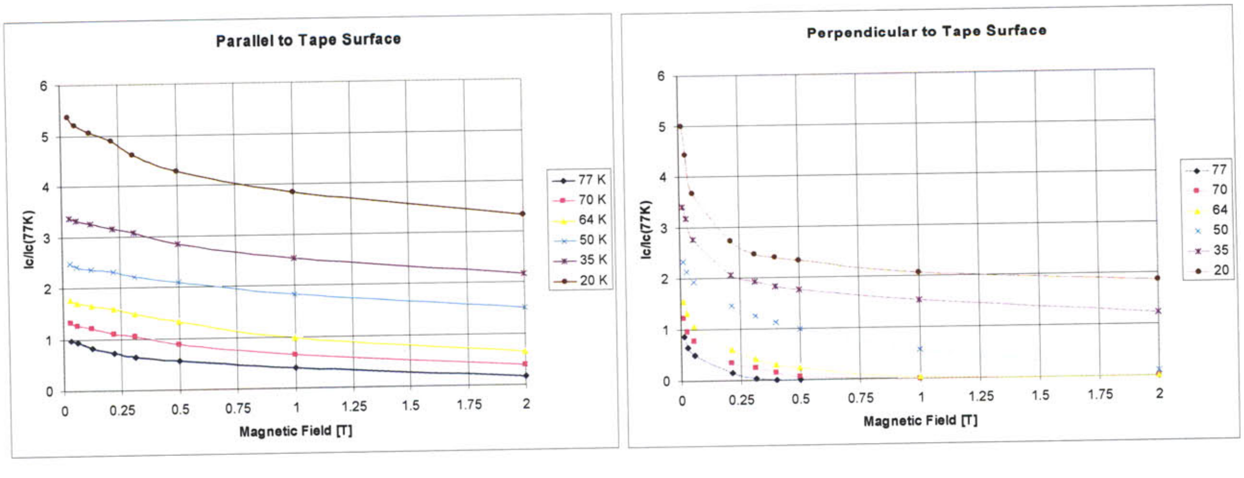

a) b)

Figure 4.40 Variation of HTS critical current density with temperature and magnetic field parallel (a) and perpendicular (b) to the HTS wire [8]

To model the effect of warmer temperatures on I_c, the $I_c/I_c(77\text{ K})$ from Figure 4.40a with no magnetic field is fit to an exponential curve in Figure 4.41 and is shown by

$$\frac{I_c}{I_c(77\text{K})} = 9.6391 \cdot e^{(0.0277 \cdot T)} \tag{4.53}$$

where T is the operating temperature. Using the data available, the exponential curve fit was used to determine I_c for temperatures greater than 77 K. The exponential fit puts the $I_c/I_c(77) = 1$ point at 81 K. In general, it is close to the experimental data and provided a better fit than using a power function or a polynomial fit.

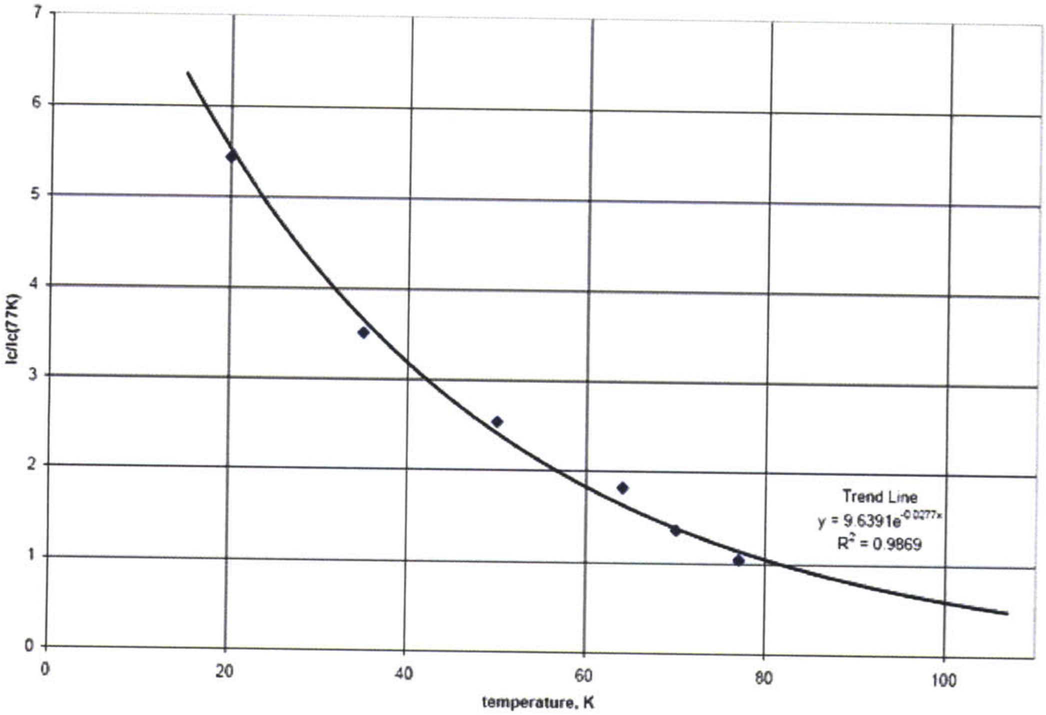

Figure 4.41 Variation of HTS critical current density with temperature, no self field

Using Equation (4.53), the maximum current allowed by the HTS wires for a representative test shown in Figure 4.42a was calculated and is shown in Figure 4.42b. One of the parameters for the current model was that if the temperature during a test was greater than $T_{critical}$ (110 K), the HTS current was set to a non-superconducting level of 10 A. The $T_{critical}$ boundary is shown by the thick black solid line in Figure 4.42a. The analysis assumed that the current is 'on' during the start of the heat pipe test. For the HTS wire, the specifications for the COTS HTS wire used by the EMFF testbed were used. This wire had a maximum I_c equal to 13,300 A/cm^2. The cross-sectional area of the wire is 0.01161 cm^2, which yields a maximum current of 154 A.

One of the interesting aspects of this analysis is that the temperature during the test rises above $T_{critical}$, approximately between the 140 and 160 minute marks. Therefore, the HTS wire reverts to a non-superconducting state. However, when saturation condition is re-achieved at approximately 160 minutes, the HTS wire is back to a superconducting level of current. Understanding how the HTS wires react during changes in temperature in flight is critical knowledge for the control system. This type of analysis is recommended for a flight system.

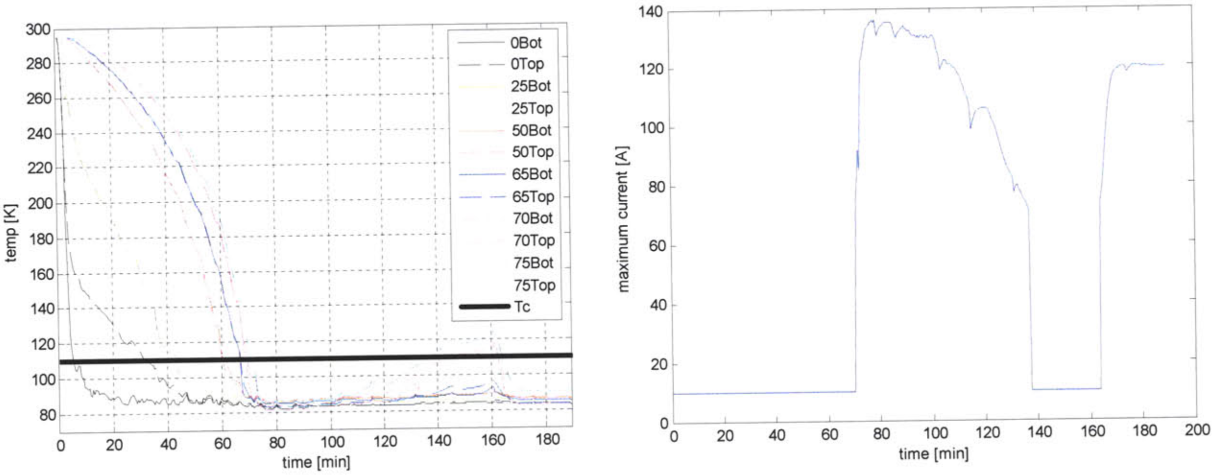

a) b)

Figure 4.42 Temperature vs. time for a test with HTS wire (a) and corresponding theoretical maximum current vs. time (b)

4.7 Summary of Straight Heat Pipe

As a proof of concept for the EMFF heat pipe, a straight 85.5 cm heat pipe was built and tested. The pipe envelope was made of copper and used a stainless steel mesh wick. Nitrogen was the working fluid. The heating environment of the vacuum chamber set the minimum power requirements for the heat pipe. By matching a finite difference model with experimental data, it was found that there was approximately 30 W of heat due to radiation from the chamber walls. The heat pipe was designed to have a larger power capacity to allow for testing at an angle. The design of the wick used 2 layers of a fine #250 mesh and 2.4 layers of a coarse #50 layer mesh and had a power capacity of approximately 50 W.

Inside the heat pipe were two HTS wires. To model the effects of a large stack of HTS wires, an aluminum block was also placed inside the straight heat pipe. The aluminum had a circular cross-sectional area and the two HTS wires were press fit into a groove that was cut along the entire length. The HTS wires with aluminum block served to model the effects of cooling a large stack of wires by blocking the vapor space. It was observed that it took longer to cool the system down with the aluminum block and HTS wires than without them. The aluminum block was designed so that the sonic limit was not approached, and the heat pipe power observed validated that vapor flow blockage did not occur.

Experimental results demonstrated the HTS wires reaching a superconducting state once the entire pipe reached saturation conditions. A test using a Wheatstone bridge to measure the resistance of the HTS wire system and a test where the HTS wire carried current were conducted. Both demonstrated the operation of the HTS wires once temperatures below the HTS critical temperature was reached throughout the pipe. A resistor at the end opposite from the condenser was used to input additional heat into the pipe to test the power capacity of the pipe and induced dryout when the maximum power capacity was reached. The observed power capacity was between 45 and 50 W. The heat pipe model was successfully validated to within ten percent and is used to design a circular heat pipe. In conclusion, the heat pipe designed meets the goals for a proof-of-concept testbed by demonstrating the feasibility of operating HTS wires in the vapor space of a heat pipe.

Chapter 5 Circular Heat Pipe

To bring the state of the EMFF thermal system closer to flight, a circular heat pipe has been designed and tested in this chapter. One of the differences of the circular heat pipe is that the system really functions as two heat pipes that share a common condenser and are connected at the far ends of the evaporator. Each heat pipe is half of the coil. They also share the same vapor space since the HTS wire is continuous inside the heat pipe. For simplicity, the entire coil will be referred to as simply a heat pipe; however it is important to note that the entire heat load that the coil must carry is actually split between the two pipes. Therefore, if the entire coil must carry 100 W, then half of the coil is simply designed to carry 50 W.

This chapter has similar structure to Chapter 4. First the design of the heat pipe is discussed. Then details of the implementation are presented. Finally, the experimental testing of the circular heat pipe will demonstrate the feasibility of operating large scale HTS coils for EMFF.

5.1 Modeling the Circular Heat Pipe

5.1.1 Performance without the Working Fluid

The first step to designing the circular heat pipe is determining the power requirements. Since the pipe is tested inside a vacuum chamber, the heat due to radiation from the chamber walls must be determined. This is done by using a finite difference model of the heat pipe and chamber environment and correlating it with temperature data. The experimental measurements are for a heat pipe without working fluid inside the chamber. The heat pipe without working fluid acts just like the copper jacket that was modeled and tested in Chapter 3. The same procedure outlined in Figure 3.3 for the 1D FDM is used to model the coil as a solid conductor in order to determine $Q_{chamber}$.

Using data for the temperature along the coil, ε_t, the effective emissivity of the pipe and chamber walls can be determined. Figure 5.1 illustrates the temperature distribution of the coil as a function of axial distance away from the pipe condenser. Again, it is important to note that no working fluid is inside the heat pipe, the condenser was only used to model a cryocooler cooling the pipe at a single location. Figure 5.1 shows the finite difference model for an effective emissivity of 0.2 (blue dotted line), 0.3 (red solid line), and 0.4 (black dashed line). The temperature is measured at various locations, approximately every 36 cm, and is indicated by '+' marks. The system tested is shown in Figure 5.4 and is the fully constructed heat pipe without working fluid. The results show there is an effective emissivity of approximately $\varepsilon_t = 0.3$. Now the heat into an operating heat pipe can be determined using the radiation equation (Equation (4.10)) assuming that the entire pipe is at or near saturation conditions. The heat due to the chamber environment is found to be approximately 96 W and is the minimum power capacity that the heat pipe is required to carry.

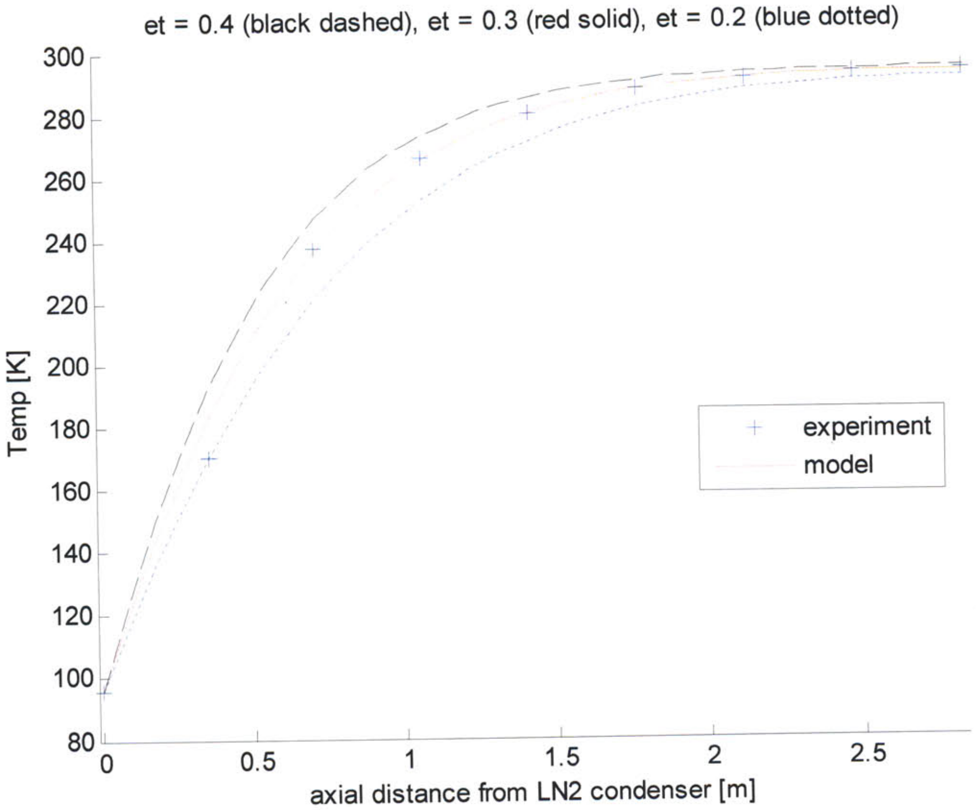

Figure 5.1 Temperature vs. distance away from the condenser for heat pipe without working fluid

5.1.2 Performance with Working Fluid

Given the heat from the environment, a requirement on the minimum heat pipe power capacity, Q_{max}, in Equation (4.7) is known. Since nitrogen has been selected as the working fluid, the merit number, M, is known. The effective length of the heat pipe is determined by the desired size of the EMFF coil. Flight sized EMFF coils for a large mission, such as NASA's Terrestrial Planet Finder Interferometer could on the order of two meters in diameter [5]. Since the heat pipe length is really half of the coil, a heat pipe with a length of 2.84 m was built. This is the distance from the end of the condenser to the halfway point of the coil and does not include the condenser length. Manufacturability of the condenser resulted in a condenser of approximately 17 cm. The total length of the heat pipe plus condenser results in a system with a major diameter close to two meters. The diameter of the pipe's cross-section affects the area of the wick, A_w in Equation (4.8). The pipe diameter was sized so that approximately 100 turns of HTS wire could reside inside the pipe, assuming minimal area was taken up by a wicking structure. This is the same diameter as the straight heat pipe from Chapter 4 and is 4 cm.

The wick characteristics are the next parameters to determine in order to find the maximum heat pipe power capacity. Using a fine outer mesh with mesh number 250 and a coarse mesh with mesh number 40, the heat pipe power as a function of the number of mesh layers, for both inner and outer mesh, are shown in Figure 5.2. The reason for showing the effects of a various number of mesh layers is that implementation of the heat pipe can cause some uncertainty in the effective number of mesh layers present. The heat pipe was designed for a power capacity of approximately 100 W. This corresponds to a heat pipe with approximately 2.5 layers of fine mesh and 2.6 layers of coarse mesh and is shown by the red circle in Figure 5.2. Also, the results in Figure 5.2 are for a heat pipe where the condenser is located approximately 0.3 degrees above the evaporator. The heat pipe power capacity is sensitive to the angle of the heat pipe, as seen in Equation (4.12). While the heat pipe was implemented to be as level as possible, a slight tilt in the heat pipe during experimentation was observed.

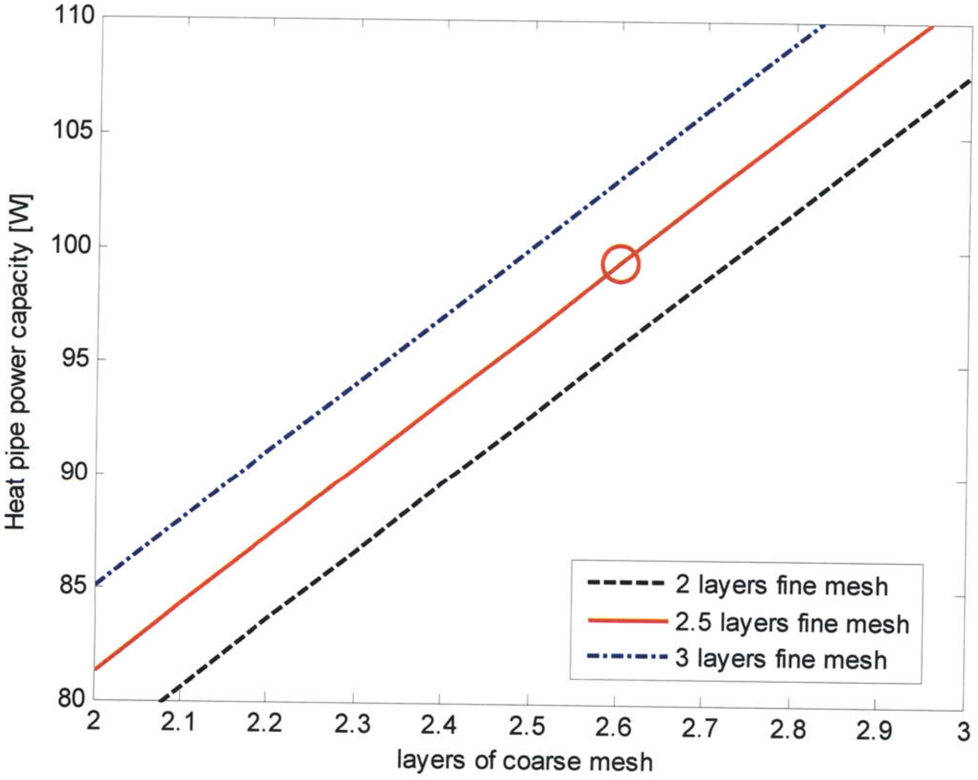

Figure 5.2 Heat pipe power capacity of various numbers of inner mesh and outer mesh layers

The amount of working fluid in the coarse mesh was calculated and depends on the porosity, ε_p, of the wick. The mesh number 40 has a ε_p of 0.54 according to the mesh manufacturer, TWP Inc. [68].

However, the working fluid mass varies largely for even small changes in ε_p. Figure 5.3 shows the working fluid for $\varepsilon_p = 0.54$ (black dashed line), $\varepsilon_p = 0.50$ (blue dashed-dot line), $\varepsilon_p = 0.46$ (red solid line). The working fluid mass calculated accounted for only the working fluid mass present in the wick. According to several experimental tests, wick saturation occurred at approximately 210 g of working fluid. Therefore, it is likely that the wick porosity is $\varepsilon_p = 0.46$ as shown by the red circle in Figure 5.3.

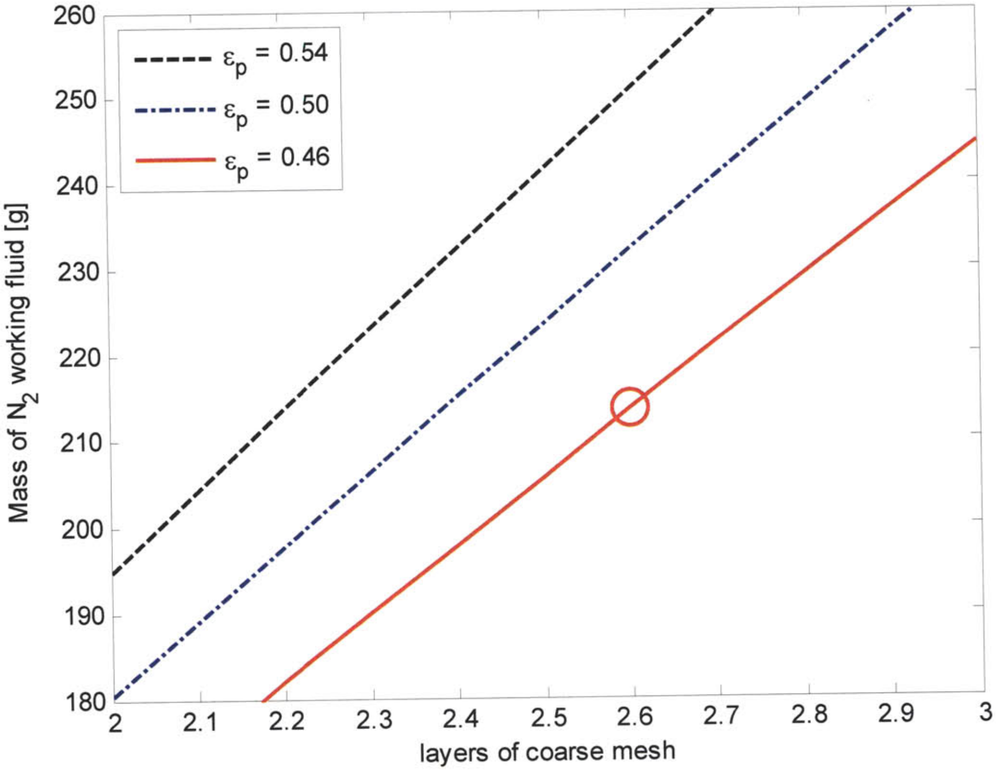

Figure 5.3 Working fluid mass

A summary of the circular heat pipe characteristics is shown in Table 5.1. Overall, the design of the circular heat pipe was intended to be based on the straight heat pipe as closely as possible. This way the manufacturing and testing procedures remained similar. Also, confidence in the models gained from testing the straight heat pipe could be applied to the circular heat pipe. The resistive network model for the temperature at the end of the heat pipe from Chapter 4 was applied to the circular heat pipe and is shown later in Section 5.3 to compare with the experimental data.

Table 5.1 Summary of EMFF circular heat pipe

Heat pipe length	2.84 m
Pipe diameter	4 cm
Wick material	Stainless steel mesh
Inner mesh layers	2.5 layers of #40 mesh
Outer mesh layers	2.6 layers of #250 mesh
Condenser length	17 cm
Condenser temperature	~77 K (liquid nitrogen)
Working fluid	Nitrogen
Envelope material	Copper
Approx. power capacity	100 W

5.2 Testbed Development

Lessons learned from construction of the straight heat pipe were used in construction of the circular heat pipe. This includes methods for wrapping the screen mesh, integration of the HTS wires, and the testing procedures for injecting the working fluid. The differences in constructing a circular heat pipe are that the screen mesh was inserted into a curved section of pipe and the large scale of the circular heat pipe meant individual curved pieces of the pipe envelope had to be cut and then resoldered together. Documentation of these efforts is intended to help bring the technology readiness level of the EMFF coil closer to a brassboard state.

Experimental testing of the heat pipe occurs inside a toroidal vacuum chamber which is shown in Figure 5.4 with the top off. The white arrows in Figure 5.4 indicate the thermocouples on the heat pipe. They are equally distributed throughout the pipe every 'L/8', where 'L' is the distance from the condenser to the end of the evaporator. There are feedthroughs for liquid nitrogen and nitrogen gas, and two thermocouple feedthroughs. The heat pipe is supported by three G10 rods, which minimize heat conduction between the pipe and the chamber walls.

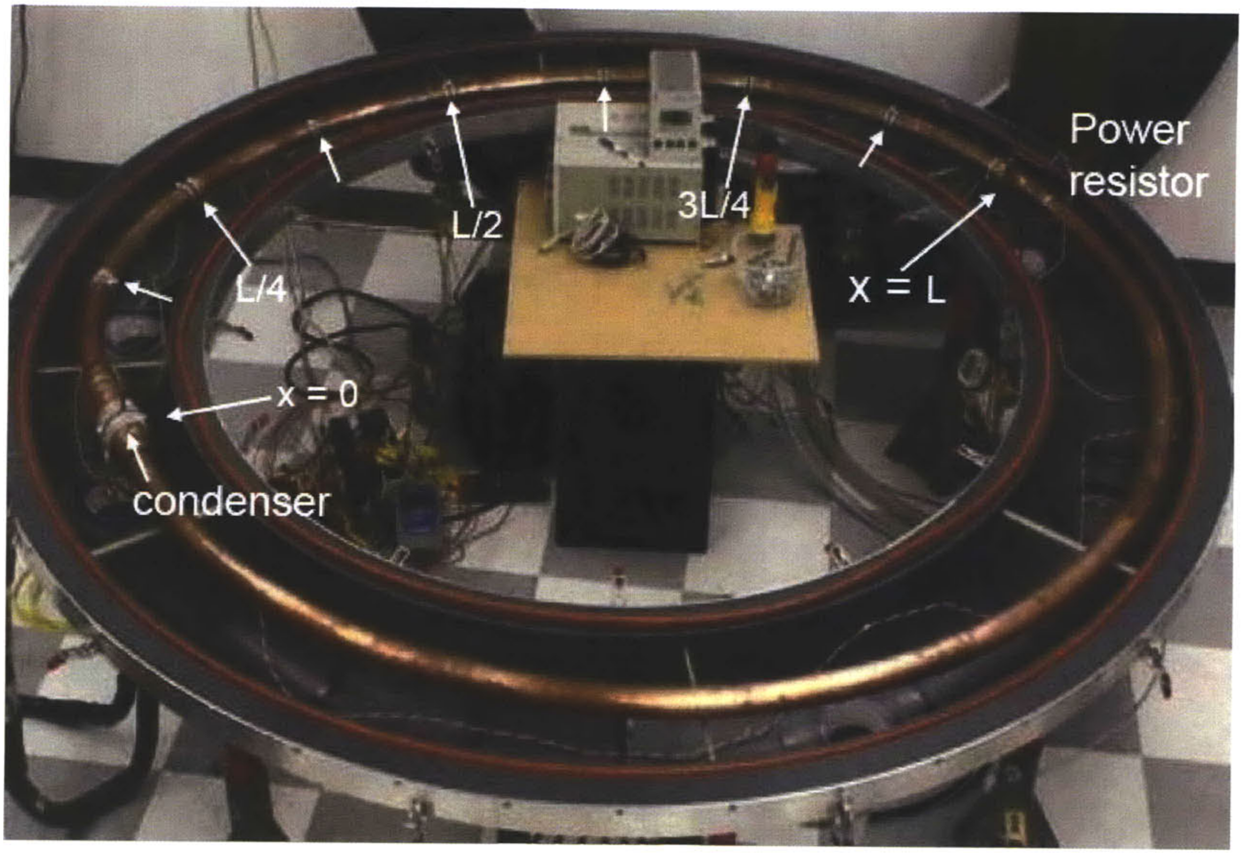

Figure 5.4 Toroidal vacuum chamber with heat pipe

5.2.1 Heat Pipe Construction

Prior to inserting the screen, both the pipe and the screen were cleaned in multiple acid baths to eliminate any contaminants, grease, and oxidation. The procedure for screen and pipe cleaning are outlined in Section 4.4.3. An HTS wire was not inserted into the circular heat pipe since cooling of HTS wires was already validated in the straight heat pipe tests. In the straight heat pipe system, the electrical feedthroughs connecting the HTS wire caused the heat pipe to leak. To minimize complications caused by leaking working fluid, the HTS wire was not inserted. The goal to demonstrate the ability to cool large scale HTS coils can still be achieved with this circular EMFF heat pipe.

One of the main challenges to constructing the circular heat pipe was inserting the screen mesh. In order for the screen mesh to maintain good capillary pressure throughout the entire length of the pipe (half of the coil), a continuous piece of mesh is desired. The mesh required a length around three meters to account for margin; however the mesh was manufactured in smaller lengths. To create a longer continuous piece, the mesh was overlapped and soldered together. To minimize interference with the working fluid (both the capillary pressure and the liquid transport), the mesh was overlapped by only 2 to 3 mm, and each overlap contained only four solder joints, each with an area less than 10 mm^2.

A second challenge faced during construction was that the mesh is not very rigid, and tends to crumple or fold on itself easily when pushed into a pipe. To help mitigate the situation, the heat pipe was cut into eight separate sections so that each section was approximately 75 cm long. Instead of pushing the screen through half of the coil, the screen only needed to be pushed through a single section. When the screen appeared through the end of a pipe section, the screen was pulled through so that there was enough screen for the neighboring pipe sections. This procedure is sketched in Figure 5.5. When the screen was inserted into each half of the circular pipe, all the sections were soldered together. The ends of the screens for each half of the pipe are located at the middle of the condenser, and where the two halves meet at the end of the evaporator, 180 degrees away from the condenser.

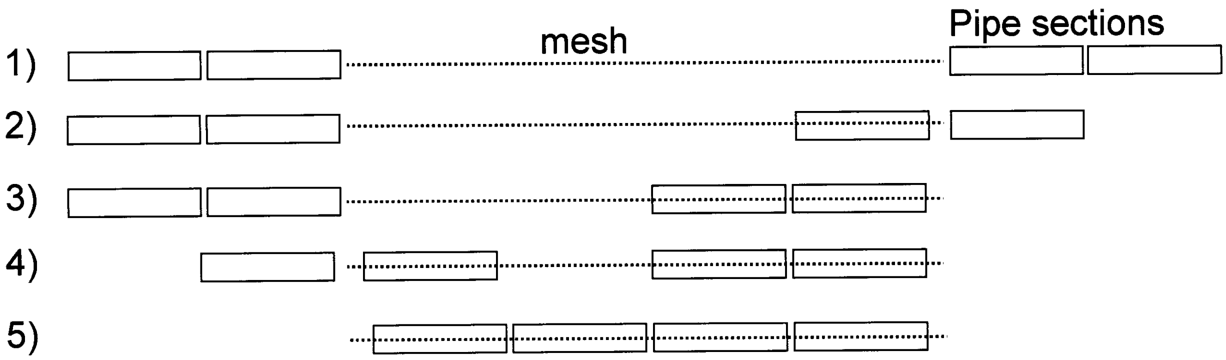

Figure 5.5 Procedure to insert mesh into pipe sections

5.2.2 Liquid Nitrogen Reservoir and Working Fluid System

A liquid nitrogen reservoir was built to extract heat from the system in place of a cryocooler. This system is shown in Figure 5.6. The liquid nitrogen in the reservoir is isolated from the inside of the pipe and is in direct contact with outside of the pipe forming a condenser with a length of approximately 17 cm. The reservoir was constructed by soldering wrought solder fittings onto a copper bushing. One end of the bushing is in contact with liquid nitrogen while the opposite end serves as the end of the condenser. Liquid nitrogen enters the bottom of the reservoir while nitrogen gas due to boiloff escapes out of the top of the reservoir. Thermocouples are located at the top, middle, and bottom of the LN2 reservoir to help monitor the liquid level.

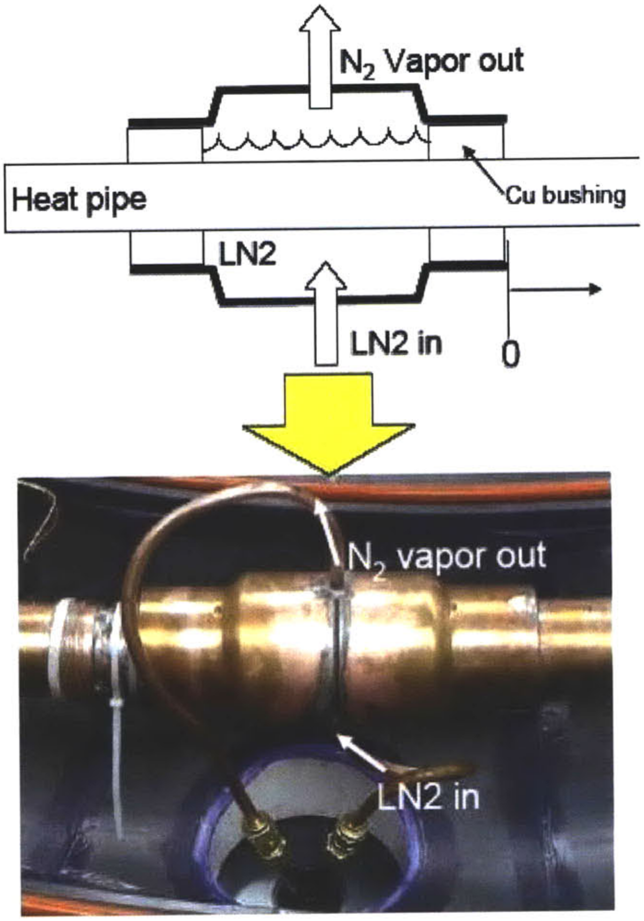

Figure 5.6 Liquid nitrogen reservoir for circular heat pipe

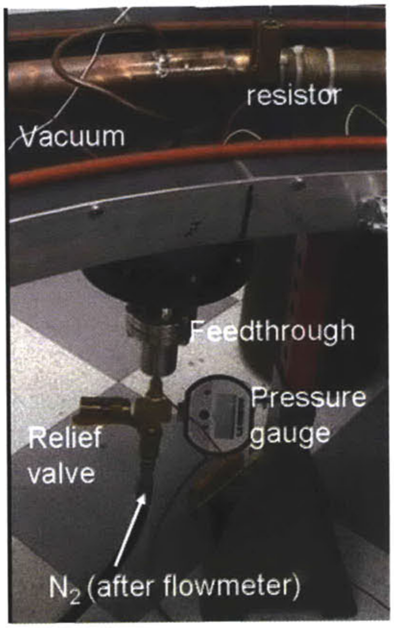

Figure 5.7 Working fluid fill system for circular heat pipe

The working fluid injection system is shown in Figure 5.7. It is similar to the working fluid injection system used in the straight heat pipe as shown in Figure 4.20. Nitrogen gas from a gas tank is measured by a flowmeter (not pictured in Figure 5.7) and then enters the vacuum chamber via a gas feedthrough. The working fluid enters the pipe at the end of the evaporator, at location 'L'. Also connected to the heat pipe are a relief valve and a digital pressure gauge. A power resistor is located at 'L' and is used to test the power capacity of the heat pipe.

5.3 Experimental Results

The testing procedure for the circular heat pipe was similar to the testing procedure for the straight heat pipe. Testing of the EMFF heat pipe begins by flowing liquid nitrogen into the LN2 reservoir. This begins at time = 0 minutes. Initially the pipe is filled with nitrogen gas at approximately 40 psi. As the pipe starts to cool, pressure inside the pipe decreases. After about ten minutes the LN2 reservoir is full and the working fluid begins to rapidly condense inside the pipe in the region surrounding the condenser. As the pipe pressure continues to drop, and condensation occurs, working fluid is injected periodically, approximately every five minutes. Working fluid is injected at pressures between 40 and 45 psi depending on how much fluid resides in the wick.

The bottom plot in Figure 5.8 illustrates the temperature of the pipe as a function of time. There are thirteen thermocouples located inside the chamber. Three are located on the LN2 reservoir, nine are located on the pipe, and one thermocouple measures the chamber wall temperature inside the vacuum. The first thermocouple is located right next to the copper bushing on the pipe and is the 'x = 0' location (see Figure 5.6). This is shown by the magenta line in Figure 5.8. The length of half of the pipe is 'L', and each of the remaining thermocouples is spaced at distances 'L/8' apart, which is approximately 36 cm. This is the same thermocouple configuration from Figure 5.4. Only the thermocouples located every quarter of the pipe half length are shown in Figure 5.8 for clarity. These are at 'L/4' (green line), 'L/2' (black line), '3L/4' (blue line), and 'L' (red line).

The cumulative amount of working fluid in the pipe is shown in the top plot in Figure 5.8. Analysis from Section 5.1 and previous tests were conducted to determine the amount of working fluid to wet the entire length of the wick. After approximately 120 minutes the wick is wetted and approximately 210 g of working fluid have been injected. Once there is sufficient working fluid in the pipe, the liquid is slowly transported throughout the entire wick and saturation conditions exist throughout the pipe. This occurs around 150 minutes into the test.

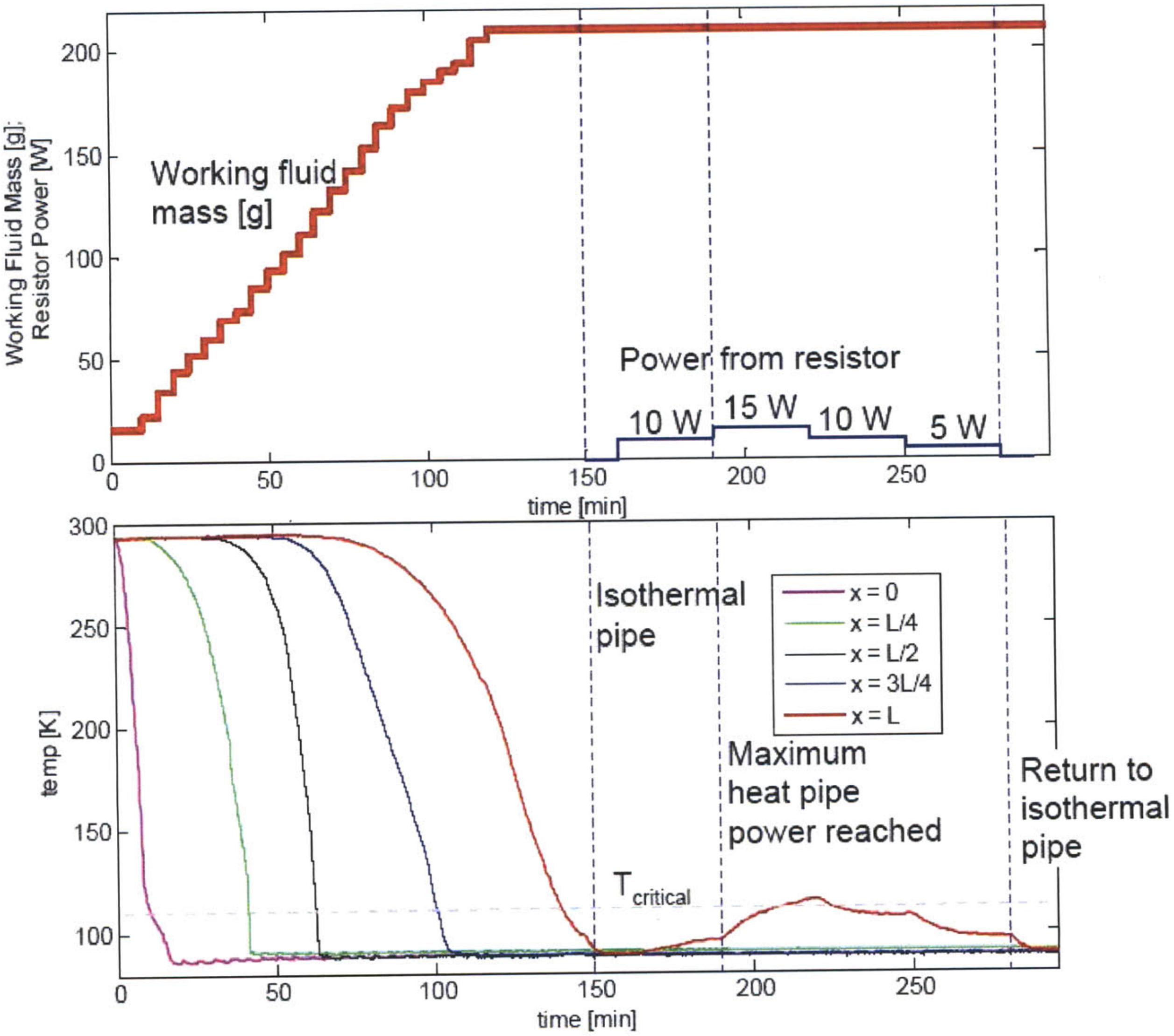

Figure 5.8 Testing a circular EMFF heat pipe showing working fluid mass, resistor power and temperature

To test the heat pipe power capacity and to determine dryout conditions a resistor at location 'L', next to the 'x = L' thermocouple and gas feed, is used as a heating source (Figure 5.7). The power profile for the resistor is shown in the top plot of Figure 5.8. Note that there is also approximately 96 W into the heat pipe due to radiation from the chamber walls.

The pressure in the pipe and in the vacuum chamber is shown in Figure 5.9. Once the heat pipe has reached saturation at 150 minutes, the pipe pressure is relatively steady at 42 psi. The pressure seen is consistent with the pressure and temperature for nitrogen at saturation (see Table 4.4). A pressure of 42 psi corresponds to a temperature of approximately 88 K. The vacuum chamber pressure operates between 4 to 6 mbar during testing. The toroidal chamber itself had some leaks in it, independent of the heat pipe. However, operating at these pressures provides a sufficient vacuum for testing.

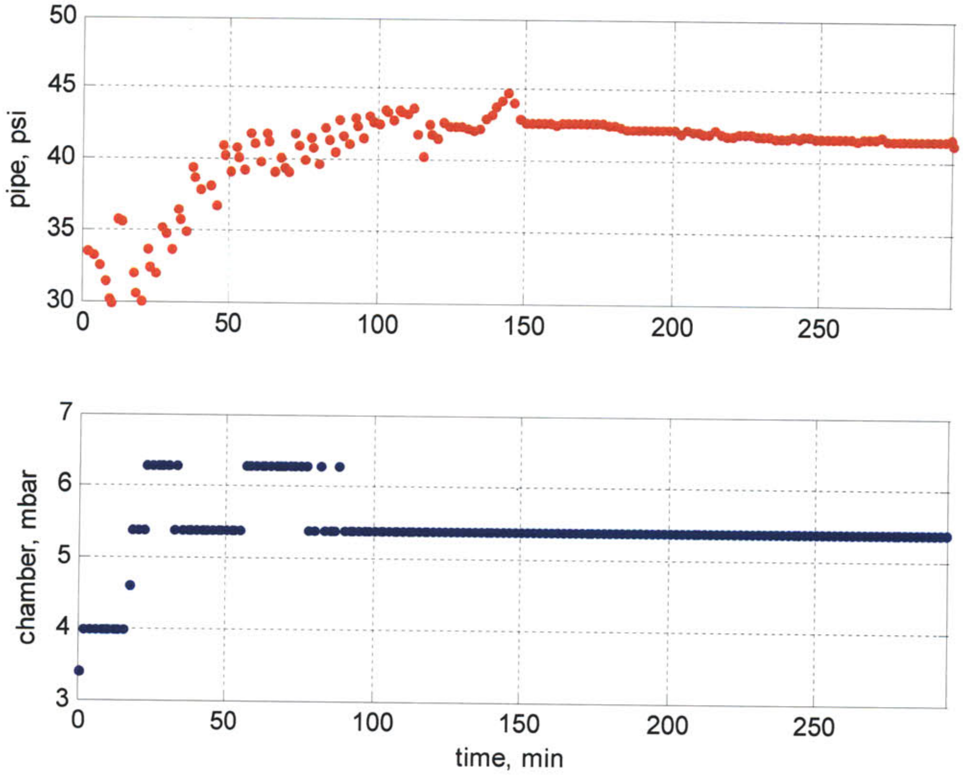

Figure 5.9 Pressure in heat pipe (top) and vacuum chamber (bottom) during testing

Introducing additional heat into the system elevates the temperature at the end of the evaporator. This is seen in Figure 5.8 by the increased temperature as the thermocouple at the evaporator end ('L') rises at around the 180 minute mark. When the heat pipe is carrying a total of 111 W, the temperature rises above the wire critical temperature (110 K). For each resistor power level, the power applied was held until an approximate steady-state condition was observed by the 'L' thermocouple

After power is removed, the heat pipe returns back to saturation conditions throughout the pipe at around 290 minutes into the test. After the test, the heat pipe is vented and the working fluid exiting the pipe is also measured by the flowmeter to double check the working mass present. This test measured a vented mass of 205.4 g, which has a 1.6% difference with the injected mass and correlates to the accuracy of the flowmeter, which is discussed in Appendix D. No significant amounts of working fluid are observed to be leaked during testing of the circular heat pipe.

5.3.1 Model Comparison

The temperature around the heat pipe at various power levels is also shown in Figure 5.10. The approximate steady-state temperature at each applied power level (0, 5, 10, 15 W) used by the resistor was used to generate Figure 5.10. Dryout of the wick occurs when there is a large increase in temperature beyond the saturation conditions and indicates the maximum heat pipe power capacity has been exceeded. From Figure 5.10, dryout occurs in the region of large temperature increase when the resistor is set to generate 10 W, meaning the heat pipe is carrying approximately 106 W total.

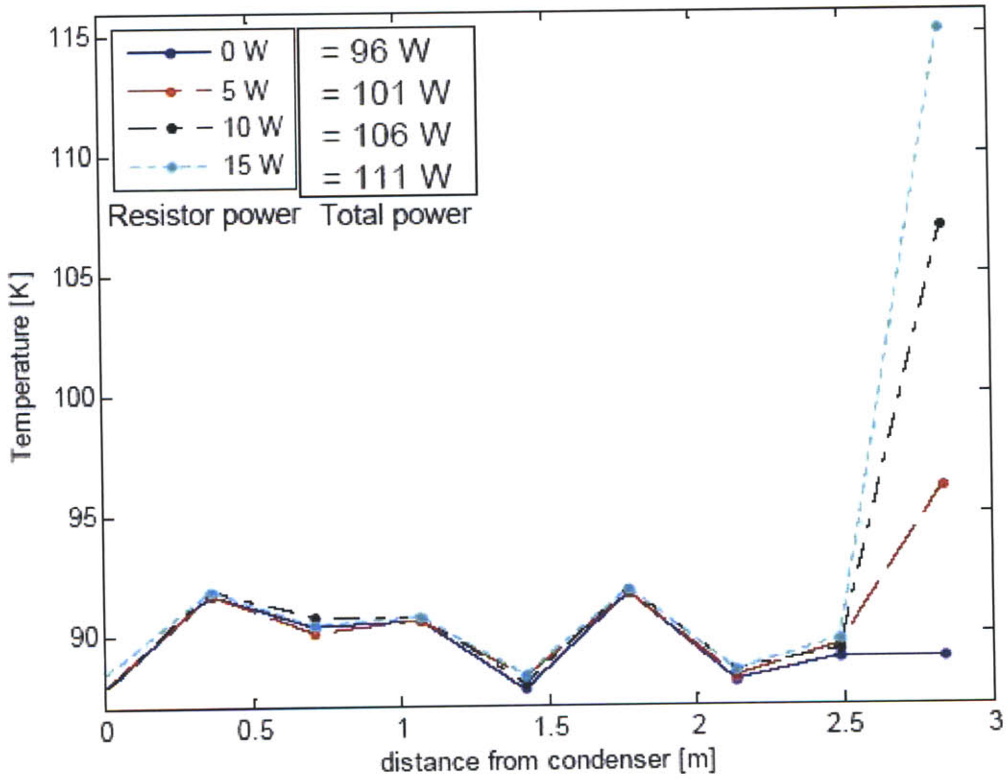

Figure 5.10 Temperature around heat pipe for various amounts of power from resistor

A second method of verifying the heat pipe power capacity is by examining the normalized difference between the experimentally measured temperature at the end of the evaporator with that modeled by the resistive network as a function of the total heat the pipe is carrying. This is shown in Figure 5.11. Two tests are shown, marked red +'s and blue x's, where the results of the first test (red +'s) were shown in Figure 5.8. The important comparison to make is that the resistive network model only models a pipe in saturation conditions, and not when dryout occurs. The indicator for when dryout occurs is by looking for a large deviation between the experiment and the model. This occurs at approximately 106 W. This is similar to the dryout estimate of 106 W from Figure 5.10. The experimental results of the heat pipe show a heat pipe power capacity that is close to the desired design of approximately 100 W, and is approximately 6 percent accurate. The overall results show that cooling of large scale HTS coils can be achieved using a cryogenic heat pipe for isothermalization.

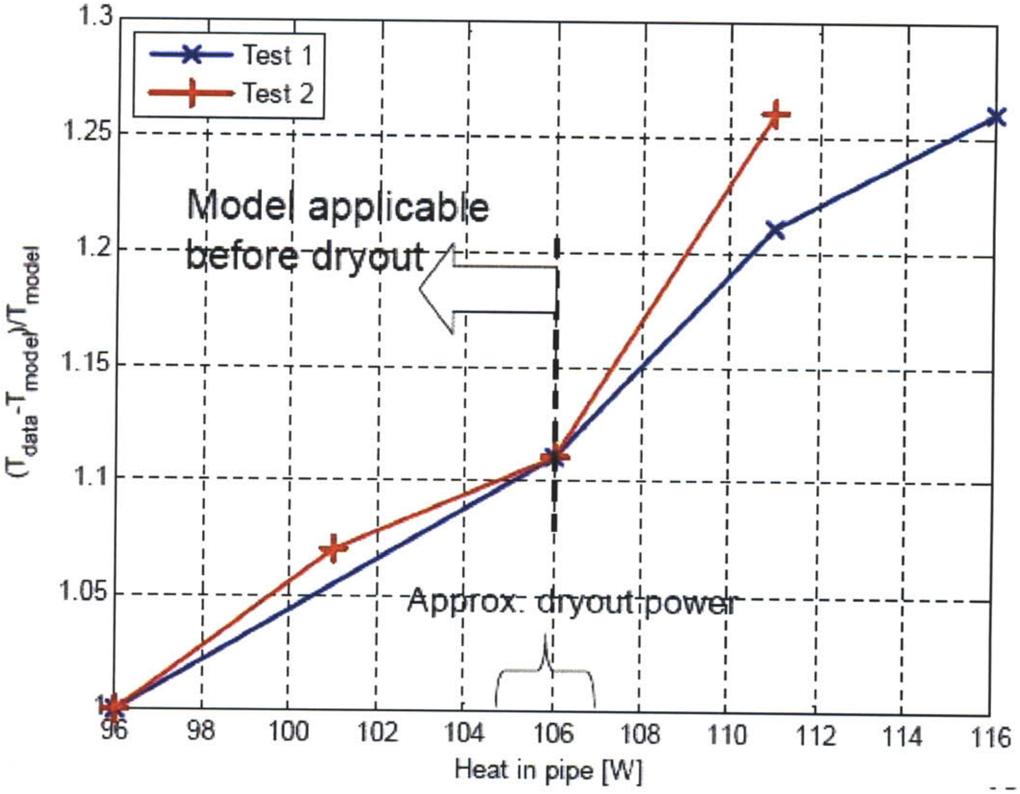

Figure 5.11 Comparing normalized difference between experimental data and resistive network model for temperature at the end of the evaporator

5.3.2 Tests with Additional Working Fluid

A third test with the circular heat pipe was conducted that injected more working fluid in order to over-saturate the wick. A working fluid mass of 220 g was injected, which is approximately a 5% increase in working fluid. Dryout conditions were also tested using the power resistor, and the data, normalized with the model, versus total heat pipe power is shown in Figure 5.12 by the green circles and is called Test #3.

According to Figure 5.12 the power capacity of Test #3 is approximately 116 W to 121 W, which corresponds to between 20 W and 25 W of applied power from the resistor. It is interesting to observe that the heat pipe remains relatively isothermal when 15 W and 20 W are applied by the resistor (111 W and 116 W total). These results indicate that over-saturating the wick can lead to an increase in power capacity. In this case, over-saturating the wick by 5% led to approximately a 12% increase in power capacity. However, in general a heat pipe does not operate with an oversaturated wick because the pressure at ambient is potentially very large. This results in thicker walls and heavier heat pipes. For a flight heat pipe, minimizing the mass is important.

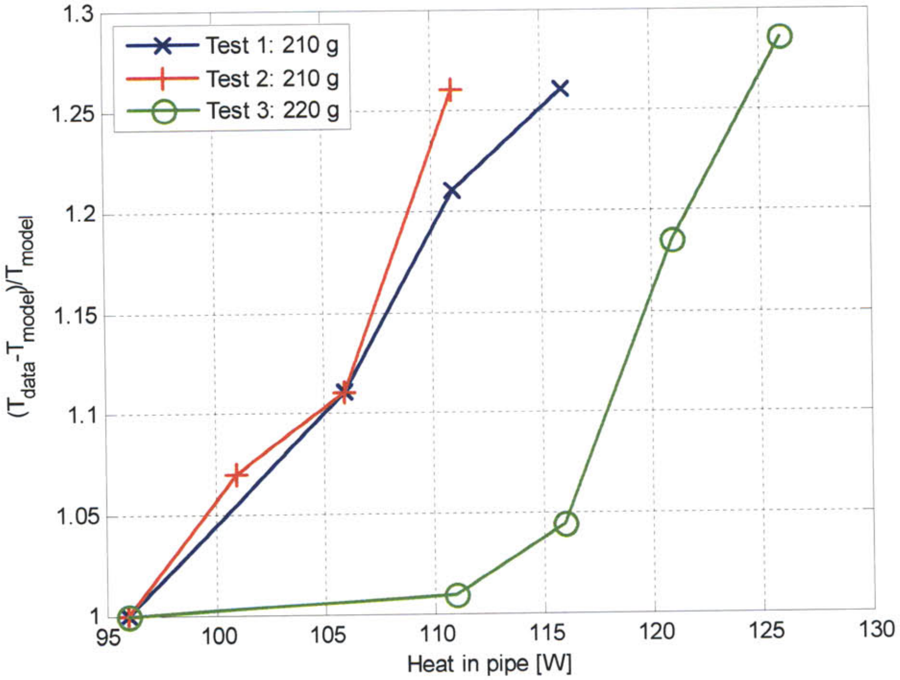

Figure 5.12 Temperature vs. heat pipe power

5.4 Summary of Thesis Experiments

The research in this thesis has examined the performance of a thermally conductive jacket (TCJ) as a means of isothermalization for a large scale HTS coil for EMFF. In Chapter 3 the use of a solid conductor or copper jacket, both with and without MLI was examined. The copper jacket is essentially a heat pipe without working fluid. The research in this chapter has examined the use of a heat pipe with working fluid. A summary of the experimental results as a function of time for all three circular thermally conductive jacket systems is shown in Figure 5.13. The performance of the heat pipe without working fluid is shown by the dotted lines, the heat pipe without working fluid, but with MLI is shown by the dashed lines and the heat pipe with working fluid is shown by the solid lines. For each of the systems temperature data at locations ‘x = 0’ (black colored), ‘x = L/8’ (magenta colored), ‘x = L /4’ (red colored), ‘x = L /2’ (blue colored), and ‘x = L’ (green colored) are given.

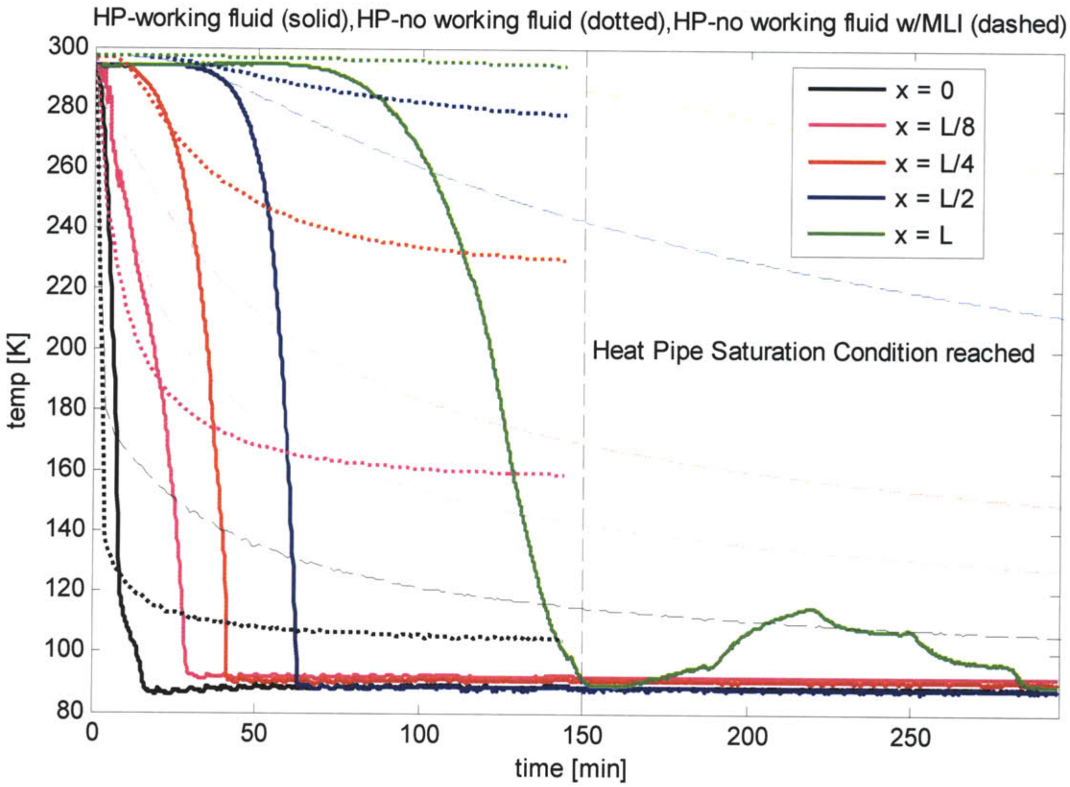

Figure 5.13 Transient temperatures for Heat pipe with working fluid, HP without working fluid, and HP without working fluid with MLI

The effectiveness of operating with a working fluid is clearly seen in Figure 5.13. The system tested in Chapter 5 was the only TCJ that was capable of reaching temperatures below $T_{critical}$. Using the experimental data, a conservative estimate for the effective thermal conductivity of the heat pipe with working fluid is 214 kW/m·K. This is a 523 times improvement over solid copper, which is the heat pipe without working fluid. This calculation uses an evaporator temperature of 91.7 K at 1.75 m away from a condenser with a temperature of 87.925 m. The effective thermal conductivity is much higher if a temperature of 89.02 K at 2.93 m away from the condenser was used.

One of the difficulties in comparing the transient temperature data is that not all three tests lasted for the same duration. The test for the heat pipe without working fluid and no MLI (dotted) lasted for only 145 minutes while the other two tests lasted beyond 295 minutes. The heat pipe with working fluid used a resistor to change the heat carried, while the other two tests did not. Another aspect that is different is that the condenser or liquid nitrogen reservoir for the tests without working fluid was built differently from the heat pipe with working fluid. Cooling for the copper jacket systems was composed of loops of copper tubing with liquid nitrogen flowing inside. These loops of copper tubing were in direct contact with the copper jacket. This cooling system had much less thermal mass than the liquid nitrogen system used in this chapter for the heat pipe with working fluid. Therefore, the tests without working fluid were able to lower their temperature more rapidly at locations 'x = 0' and 'x = L/8' compared to the heat pipe with working fluid (solid lines). However, once enough working fluid is injected and starts to circulate, the temperature of the heat pipe drops significantly and reaches near isothermal conditions once the wick is saturated. The two systems without the working fluid are unable to match these conditions.

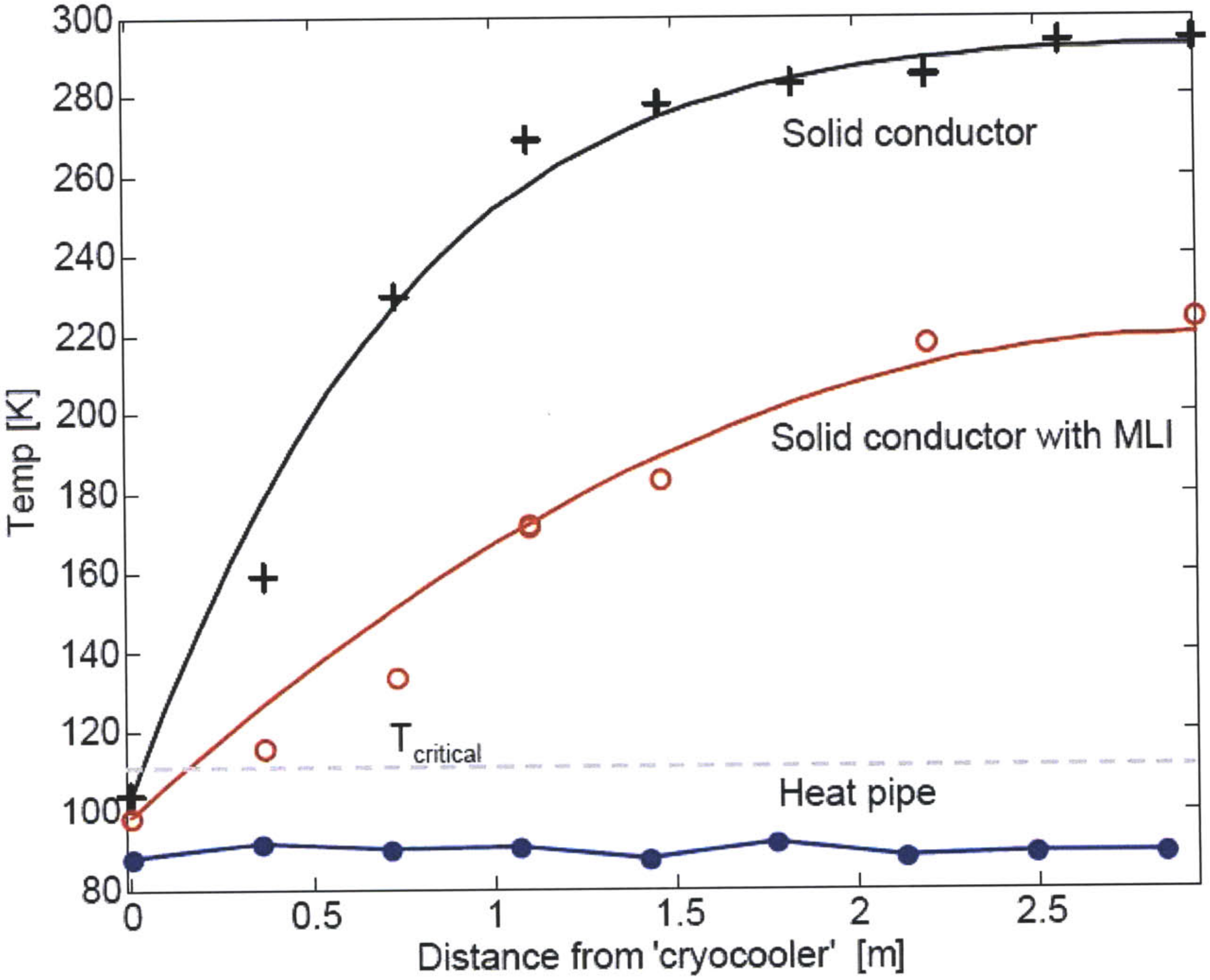

Figure 5.14 Temperature vs. axial distance from the condenser for heat pipe, heat pipe without working fluid and heat pipe without working fluid with MLI

Using the approximate steady-state temperature for all three TCJ systems shown in Figure 5.13, the temperature as a function of axial distance along the length of the pipe away from the condenser is shown in Figure 5.14. The heat pipe without the working fluid and no MLI is shown in black, the heat pipe without working fluid with MLI is shown in red and the heat pipe with working fluid is shown in blue. For the two TCJ systems without working fluid the finite difference model is shown along with the experimental data. The heat pipe with working fluid does not have an associated model for axial temperature distribution since isothermal conditions are assumed throughout the heat pipe when it is operating at saturation conditions. It should be noted that for the system with MLI, the approximate steady-state experimental data was taken at 550 minutes, which is not shown in Figure 5.13.

There are two conclusions that are summarized in Figure 5.14. First, the benefits of operating with a working fluid are shown by comparing the heat pipe without working fluid (black) and with working fluid (blue). Both systems were operated in the toroidal vacuum chamber, and saw relatively similar heat loads. The heat load carried by the heat pipe was higher due to a difference in the effective emissivity. However the copper TCJ has a large temperature gradient while the heat pipe with working fluid is able to achieve isothermal conditions below $T_{critical}$.

Second, the benefits of operating with insulation are shown by comparing the copper TCJ system with and without MLI (black and red, respectively). In Chapter 3 it was discussed that MLI is able to reduce the heat load by approximately 70%. While the temperature gradient is lower for the MLI case it is still not sufficient for operating the HTS. One item for future testing would be to consider using additional MLI to determine how much more the heat load can be reduced. Operating in a thermal vacuum chamber may allow for further reduction of the heat load and simulation of space heating conditions.

Chapter 6 Conclusions

6.1 Thesis Summary

The core hypothesis of this thesis is that a consumable-free method for maintaining cryogenic temperatures for large scale HTS coils exists using a cryogenic heat pipe, by which isothermalization of the coil is maintained by locating the HTS wire inside the vapor space of the heat pipe. To achieve this objective the following steps were taken:

- Model development of consumable-free designs, including a copper pipe as a solid conductor, a system with MLI, and a heat pipe
- Experimental testing of a solid conductor, both with and without MLI
- Experimental testing of a heat pipe to verify the hypothesis, including:
  - Testing a straight heat pipe to verify modeling and manufacturing processes
  - Testing a straight heat pipe with HTS to verify the ability to cool HTS
  - Testing a circular heat pipe to verify the ability to cool a large scale HTS coil

The following is a chapter-by-chapter summary of these steps taken to achieve the thesis objective.

The concept of Electromagnetic Formation Flight was introduced in Chapter 1. EMFF is a unique and promising propellant-less propulsion system for future formation flying satellites. To implement EMFF, a cryogenic thermal control system is required to cool the high temperature superconducting coils. A thermal system that is also consumable-free consists of a cryocooler to extract heat and a cryogenic heat pipe to maintain isothermalization of the coils. One of the benefits of these technologies is that both have flight heritage. Application of the HTS thermal control system beyond EMFF was also discussed in Chapter 1. Some possibilities include alternative space propulsion, torque coils, space experiments, and ground power transmission.

The scale of the thermal problem was introduced in Chapter 2 using a simplified model for the coil with insulation. An active cooling system was necessary to extract the five to ten watt thermal load in LEO. System trades were also performed to explore the benefits of using multiple cryocoolers on a single coil. Conditions exist for two cryocoolers that allow for a reduction in total cryocooler power. The EMFF thermal system was formally introduced in Chapter 2. A thermally conductive jacket surrounds the HTS coil to provide isothermalization and structure for the wire stack. The benefit of enclosing the wire is that thermal gradients across the HTS wire stack can be minimized if the thermal jacket is isothermal. Investigating the performance of a copper pipe acting as a solid conductor for the thermally conductive jacket occurred in Chapter 3.

Analytic and discrete models for the copper pipe were discussed in Chapter 3. The finite difference model was validated by analysis and a Sinda model. In addition, experimental testing of the copper jacket inside a toroidal vacuum chamber was conducted to validate the finite difference model. A solid conductor was unable to achieve the low temperatures necessary for the HTS coil. Therefore, use of a cryogenic heat pipe was investigated. One useful result of the modeling was that the finite difference models were applied to characterize the vacuum chamber environments used for heat pipe testing.

In Chapter 4, a straight cryogenic heat pipe was designed and built to demonstrate the ability to cool HTS wire. The superconducting wire resides inside the vapor space of the heat pipe. This is a unique application of heat pipes because typically a heat pipe cools an object that is external to the pipe. The heat pipe was made of copper, and used multiple layers of stainless steel mesh as the wicking structure. Nitrogen was the working fluid. First, the heat pipe was tested without an HTS wire inside to verify the heat pipe power capacity. Manufacturing lessons learned in constructing the heat pipe were also used in building a circular heat pipe in Chapter 5. To test the heat capacity of the system, power was introduced by a resistive heater, which was located farthest away from the condenser. Dryout conditions were observed and the heat pipe returned to saturation conditions after the applied heat was turned off. Once performance of the straight heat pipe was validated, HTS wire was inserted into the straight heat pipe. Experimental tests show that the HTS wire reached a superconducting state when the heat pipe reached saturation condition.

To demonstrate the feasibility of cooling large scale EMFF coils a circular cryogenic heat pipe was designed and built in Chapter 5. The circular heat pipe had a two meter major diameter and was tested inside a toroidal vacuum chamber. The design was based on the straight heat pipe from Chapter 4. Experimental results show the entire coil reaching saturation condition after sufficient working fluid was injected into the heat pipe.

6.2 Thesis Contributions

This thesis demonstrates the first operation of a cryogenic heat pipe for cooling HTS wire inside a heat pipe vapor space. This system has demonstrated the feasibility of operating HTS coils in space without using consumables. The operation of this system is not constrained by any specific orbit. In addition, the models for temperature distribution can be used for a future flight EMFF thermal system.

6.3 Future Work

In order to bring EMFF closer to flight there are four main topics that would benefit from future work. They include testing in a thermal vacuum chamber, integration of the power and thermal systems, more efficient manufacturing techniques, and use of cryocoolers for multiple coils. These items are discussed in an approximate chronological order that research should be conducted.

One of the first future steps is to test the EMFF thermal system in a thermal vacuum chamber. This system can use multiple radiative heating sources to mimic the effect of the Sun and Earth for a satellite in low Earth orbit. This initial test could use the current circular heat pipe with MLI in a thermal vacuum chamber with the walls at liquid Helium temperature. However, a redesigned circular heat pipe that has a power capacity closer to a flight system has more relevance. In addition, this system should have HTS wire integrated inside of it and use a cryocooler, if available.

While aspects of the present EMFF power system design may be sufficient for eventual flight migration, there are benefits with integrating the power and thermal systems more closely. This research can be done in parallel with the thermal vacuum tests. The power dissipated by the HTS coils is lost through mosfets used in the power system's H-bridge design. Mosfets exhibit a reduction in resistance as their operating temperature is lowered. Currently the operating temperature for the EMFF testbed power system is ambient room temperature. However, if the power system were operating at lower temperatures or even the cryogenic temperatures of the HTS coil system the reduction in mosfet resistance could decrease the power consumed by the coils. Therefore, potential benefits exist for integrating the power and thermal system. A related area for future work is the design of the leads used by the HTS coils. In any superconducting magnet system, the non-superconducting leads present an additional heat load on the cryogenic system due to ohmic heating. A future flight version of the HTS coils can either use COTS HTS leads or design a custom HTS lead. However, research must be conducted to ensure that the parasitic heat load is minimized and the system can be integrated into a heat pipe without leading to leaks. Integration of HTS wires and a power system to drive large amounts of current is the next manufacturing challenge for the circular heat pipe.

The third step to bringing EMFF closer to flight is considering the manufacturing of the heat pipe and the wire stack design. Winding up to one hundred turns of HTS wire inside the heat pipe, while also dealing with the wick requires careful planning regarding the order of construction. Manufacturing of the wicking structure, perhaps using sintered metal fibers, is one possible alternative structure that should be explored. Also, the heat pipe mass for a flight system can be greatly reduced by using a pipe envelope with a thinner wall. Therefore, design of a flight heat pipe wick with both pipe performance and HTS integration must be carefully considered. One possibility is to re-examine the stack configuration. The

EMFF testbed uses three connected stacks of HTS wire that are side by side. One problem with the configuration of the stacks is that the local magnetic field, as seen by each individual wire, acts to reduce the critical current carrying ability of the wire. Preliminary research outlined in Appendix E has determined that it is possible to improve the HTS coil stack performance though more unique coil stack configurations.

Finally, integration of a cryocooler and use of multiple coils with heat pipes should be explored in order to bring the EMFF thermal system closer to flight. Testing in a thermal vacuum chamber of at least two separate EMFF coils, each with a complete thermal system should be conducted to determine the forces and torques achievable during realistic flight conditions. The heat pipe should be initially sealed to determine the startup conditions needed to use the coils. After testing of two separate coils, the use of two testbed vehicles with multiple coils should be considered in the thermal vacuum chamber. The testbed can either use a single cryocooler for each coil or one shared among the coils on each vehicle. This system would demonstrate in a relevant operating environment high confidence in bringing EMFF satellites to flight.

Appendix A HTS Torque Coils

This section summarizes the trade between HTS torque coils, room temperature (RT) copper torque coils and commercially available torque rods. Torque, T, is equal to the magnetic dipole, μ, cross the Earth's magnetic field, B. The Earth's magnetic field at an altitude of 400 km (LEO) is approximately $3\cdot 10^{-5}$ Tesla and is approximately 10^{-6} Tesla in GEO [55]. Examining the maximum torque,

$$T = \mu \times B \to \mu B = niAB = ni\pi R_c^{\ 2} B \tag{A.1}$$

Here, the number of turns is n, the current is i, and the coil radius is R_c. Using the HTS wire critical current density, I_c, and the HTS coil density, ρ_c, and HTS wire cross-sectional area, A_c,

$$\begin{aligned} i &= I_c A_c \\ M_c &= 2n\pi R_c A_c \rho_c \end{aligned} \tag{A.2}$$

the coil mass as a function of the torque is

$$M_c = \frac{2T}{\left(\frac{I_c}{\rho_c} \right) R_c B} \tag{A.3}$$

The analysis used a one meter radius coil. The total mass for the magnetic torquer using the HTS coil is

$$M_t = M_c + M_{thermal} + M_{SA} \tag{A.4}$$

where $M_{thermal}$ is 3 kg (Sunpower cryocooler mass [29]) and the solar array mass is

$$M_{sa} = \frac{(I_c A_c)^2 R + P_{thermal}}{P_s} \tag{A.5}$$

where the cryocooler power $P_{thermal}$ is 150 W, the solar array specific power P_s is 25 W/kg, and the resistance in the HTS coil is based on the resistance in the EMFF testbed, R is 0.01 Ω. The total mass for the magnetic torquer using the copper coil is

$$M_t = M_c + M_{SA} \tag{A.6}$$

The solar array mass is

$$M_{sa} = \frac{i^2 R}{P_s} = \frac{I_c^{\,2} p_c M_c}{\rho_c P_s} \tag{A.7}$$

where the power, $P = i^2 R$ comes from

$$(i^2)(R) = \left(I_c^{\,2} A_c^{\,2}\right)\left(\frac{p_c l_c}{A_c}\right) = \left(I_c^{\,2} A_c^{\,2}\right)\left(\frac{p_c 2\pi R_c n}{A_c}\right) = \left(I_c^{\,2} A_c^{\,2}\right)\left(\frac{p_c 2\pi R_c}{A_c}\frac{M_c}{2\pi R_c A_c \rho_c}\right) = \frac{I_c^{\,2} p_c M_c}{\rho_c} \tag{A.8}$$

where p_c is the resistivity of copper ($1.673\cdot10^{-8}$ Ohm·m), the critical amperage density for copper is $500\cdot10^4$ A/m^2, and the density of copper is 8920 kg/m^3. COTS torque rods were built by Microcosm [83]. The total mass of the torque rods include the torque rod and the solar array mass. Figure A.1a shows the total mass of COTS torque rods and both HTS and copper coils versus torque for a satellite in LEO. For one meter radius coils, the use of room temperature (RT) torque coils is more mass efficient than both HTS coils and COTS torque rods. More importantly, RT coils are more mass efficient that HTS coils.

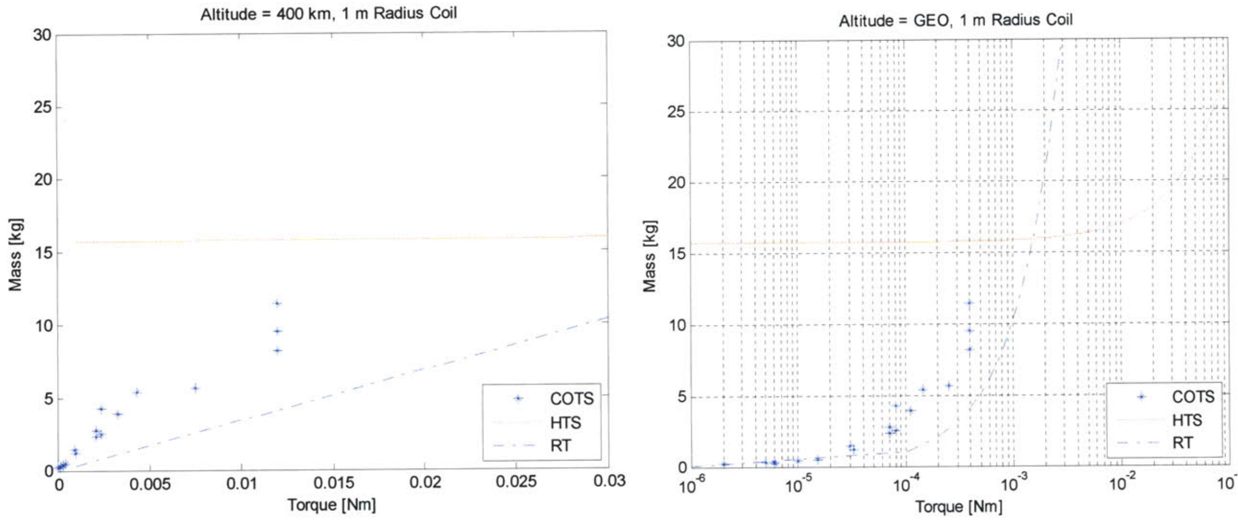

a) b)

Figure A.1 Total mass of magnetic torquer versus torque, for HTS and room temperature copper coils, 1 m radius, and COTS torque rods for a satellite in LEO (a), in GEO (b)

A mass comparison of the magnetic torquers in GEO is shown in Figure 1.4 and again in Figure A.1.b. HTS coils in GEO are the most mass efficient option for higher torque systems. A breakdown of the coil and solar array mass for each system is shown in Figure A.2. The solar array mass of the HTS system is constant because the resistance in the system is not a function of the mass of the coil. However for the RT coils, the mass of the coil affects the total resistance and thus the solar array mass.

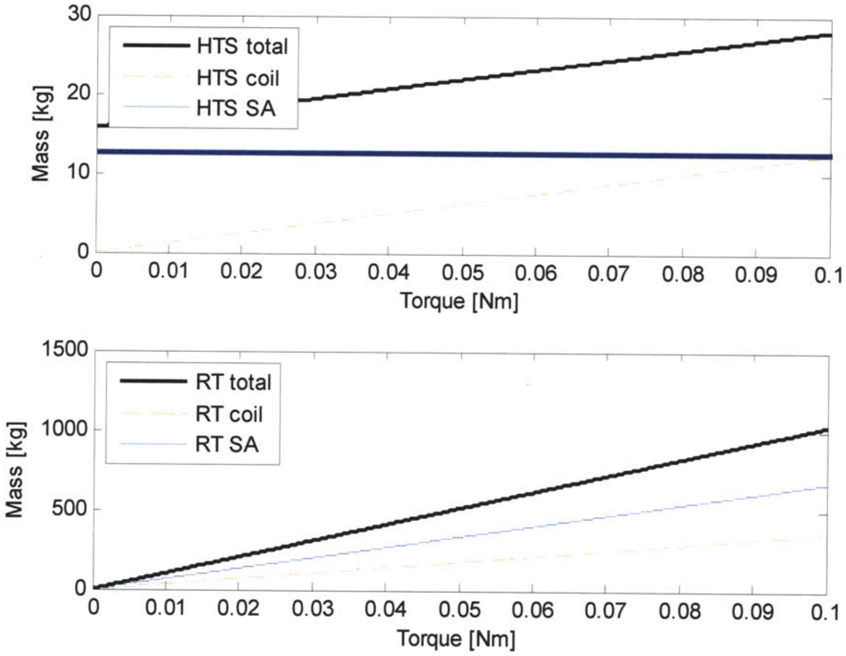

Figure A.2 Component masses for the HTS and RT torque coils.

Appendix B Additional Thermal Design

B.1 Multiple Cryocoolers

In Chapter 2 it was determined that there is an optimum configuration with respect to the total cryocooler power when using two cryocoolers, located at different regions of a vacuum gap insulation, to cool a single coil. This section expands on that concept using multiple cryocoolers on multiple vacuum gap layers. Figure B.1 shows the thermal free body diagram for the cross-section of multiple vacuum gaps. The notation is modified to allow for easier understanding using multiple layers. The outermost layer is labeled '1', which is the same outer layer that is labeled '*h*' in Chapter 2. The coil layer is denoted by '*c*', which is the same as Chapter 2. Here, there are additional vacuum gap layers, labeled by their subscript. *N* is the total number of gap layers. At the outer layer, the thermal balance is the same as seen in Chapter 2, the heat flux from the Sun is either reradiated to space or transmitted to the coil. The heat flux transmitted is the same through the various layers.

$$\begin{aligned} Q_{sun} &= Q_e + Q_t \\ Q_{sun} - Q_e &= Q_t = Q_1 = Q_2 = Q_i \end{aligned} \tag{B.1}$$

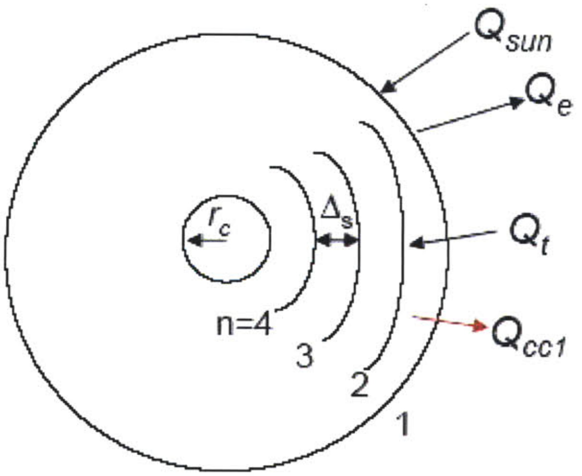

Figure B.1 Thermal free body diagram for multiple vacuum gaps with multiple cryocoolers

Substituting in the heat flux from the Sun and the heat flux reradiated into space this can be expressed for the i^{th} layer as

$$G_s\alpha_1 A_{sun} - \varepsilon_1 A_1 \sigma\left(T_1^4 - T_s^4\right) = \frac{A_2\sigma\left(T_1^4 - T_2^4\right)}{\frac{1}{\varepsilon_1} + \frac{A_2}{A_1}\left(\frac{1}{\varepsilon_2} - 1\right)} = \frac{A_{i+1}\sigma\left(T_i^4 - T_{i+1}^4\right)}{\frac{1}{\varepsilon_{i+1}} + \frac{A_{i+1}}{A_i}\left(\frac{1}{\varepsilon_i} - 1\right)} \tag{B.2}$$

The subscript denotes the vacuum gap layer where the absorption area, A_{sun}, and the area of the i^{th} layer is given by

$$\begin{aligned} A_{sun} &= 4\pi R_c r_1 \\ A_i &= 4\pi^2 R_c r_i \end{aligned} \tag{B.3}$$

Equation (B.2) is rearranged to include known heating terms on the right hand side and unknown temperature on the left hand side.

$$\frac{A_{i+1}\sigma\left(T_i^4 - T_{i+1}^4\right)}{\frac{1}{\varepsilon_{i+1}} + \frac{A_{i+1}}{A_i}\left(\frac{1}{\varepsilon_i} - 1\right)} + \varepsilon_1 A_1 \sigma T_1^4 = G_s \alpha_1 A_{sun} + \varepsilon_1 A_1 \sigma T_s^4 \tag{B.4}$$

For the i^{th} layer, a simplified way of describing Equation (B.4) is

$$q_i T_i^4 + c T_1^4 = Q \tag{B.5}$$

where the coefficients q_i and c are defined as

$$q_i = \frac{A_{i+1}\sigma}{\frac{1}{\varepsilon_{i+1}} + \frac{A_{i+1}}{A_i}\left(\frac{1}{\varepsilon_i} - 1\right)} \qquad c = \varepsilon_1 A_1 \sigma \tag{B.6}$$

In Equation (B.5) the Q term is a known quantity; however the temperature at each layer and the temperature at the outer layer are unknown quantities. The only given is the coil temperature, T_c. At each vacuum gap layer, the thermal balance seen in Equation (B.1) can be rearranged into the form seen in Equation (B.5), with the unknown variables on the left hand side. In order to solve for the temperature at each layer, the set of unknown temperatures can be rearranged into $Ax = b$ form:

$$\begin{bmatrix} q_1 + c & -q_1 & 0 & \cdots & 0 \\ c & q_2 & -q_2 & 0 & \vdots \\ c & 0 & q_3 & \ddots & \\ \vdots & \vdots & & \ddots & -q_{n-1} \\ c & 0 & \cdots & 0 & q_n \end{bmatrix} \begin{bmatrix} T_1^4 \\ T_2^4 \\ T_3^4 \\ \vdots \\ T_1^4 \end{bmatrix} = \begin{bmatrix} Q \\ Q \\ Q \\ \vdots \\ Q + q_n T_c^4 \end{bmatrix} \tag{B.7}$$

A cryocooler located at layer 1, the outermost layer, is shown by the red arrow for Q_{cc1} in Figure B.1. The thermal balance for this system is given by

$$Q_{sun} - Q_e = Q_1 + Q_{cc_1} \tag{B.8}$$

For the i^{th} layer the thermal balance is

$$Q_{sun} - Q_e = Q_i - \left(\sum_{j=1}^{N-1} Q_{cc_j} \right) + Q_{cc_i} \tag{B.9}$$

With a cryocooler at each layer, the b vector is modified to include the amount of each extracted by the i^{th} cryocooler, Q_{cc_i}. This is shown by

$$\begin{bmatrix} q_1 + c & -q_1 & 0 & \cdots & 0 \\ c & q_2 & -q_2 & 0 & \vdots \\ c & 0 & q_3 & \ddots & \\ \vdots & \vdots & & \ddots & -q_{n-1} \\ c & 0 & \cdots & 0 & q_n \end{bmatrix} \begin{bmatrix} T_1^4 \\ T_2^4 \\ T_3^4 \\ \vdots \\ T_1^4 \end{bmatrix} = \begin{bmatrix} Q \\ Q \\ Q \\ \vdots \\ Q + q_n T_c^4 \end{bmatrix} + \begin{bmatrix} Q_{cc_1} \\ Q_{cc_2} \\ Q_{cc_3} \\ \vdots \\ Q_{cc_n} \end{bmatrix} - \begin{bmatrix} 0 \\ Q_{cc_1} \\ Q_{cc_1} + Q_{cc_2} \\ \vdots \\ \sum_{j=1}^{N-1} Q_{cc_j} \end{bmatrix} \tag{B.10}$$

Now the temperature can be solved for a system with multiple cryocoolers given the thermal load of each cryocooler. In the design space, the thermal load of a cryocooler can be arbitrarily set. The cryocooler located at the coil is responsible for extracting the necessary amount of heat flux in order to bring the coil to T_c. For a system with ten cryocoolers, each extracting 0.5 W, the total cryocooler power is 23 W.

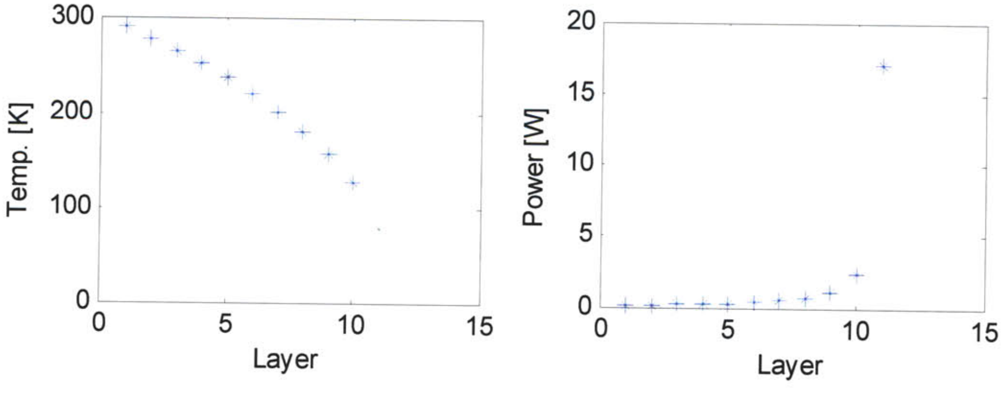

Figure B.2 Results for a uniformly cooled system

The results are shown in Figure B.2. The parameters of the analysis are same as those used in Chapter 2. This is a reduction in power compared to a system using a single cryocooler or two cryocoolers. Shown in Figure B.2 is the temperature and the cryocooler power at each layer. The outermost layer is layer '0' while the coil layer is layer '11'. For a uniformly cooled system the innermost cryocooler, located at the coil, uses the most amount of power.

To further explore the trade space, a system with cooling close to the coil is investigated in Figure B.3. Here the amount of thermal watts extracted by the coil is defined as

$$Q_{1\text{-}10} = [0\ 0\ 0\ 0\ 0\ 0\ 1\ 2\ 3\ 4] \tag{B.11}$$

where cryocooler '10' is located right next to the coil on the 10th layer and is extracting four thermal watts. Cryocooler 7 is located on the 7th layer away from the outside and is extracting one thermal watt. Layers 1 through 6 have no cryocooler. In this case, the total required power by the cryocoolers is 42 Watts, which is an increase compared to the uniformly cooled case. But this system only has four cryocoolers, compared to the ten cryocoolers in the uniformly cooled case.

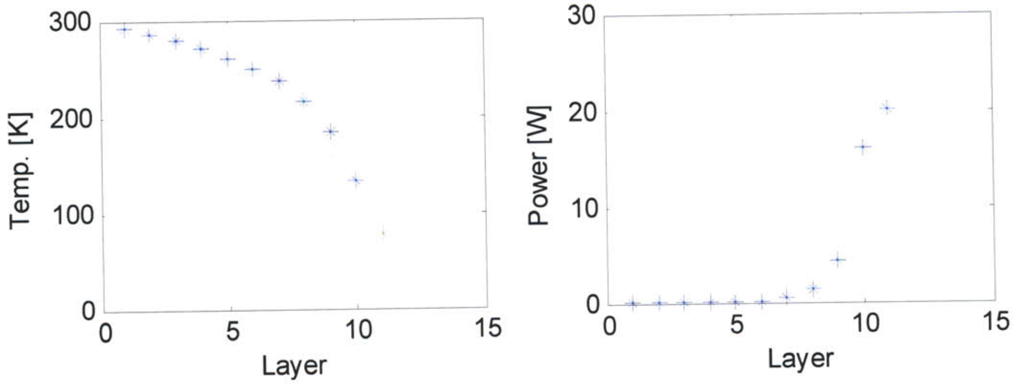

Figure B.3 Results with cooling located close to the coil

The final case is a system with cooling close to the outer surface is shown in Figure B.4. The amount of thermal watts extracted by the coil described in similar fashion to Equation (B.11) and for this case is defined as

$$Q_{1\text{-}10} = [3\ 2\ 1\ 0\ 0\ 0\ 0\ 0\ 0\ 0] \tag{B.12}$$

The total cryocooler power is 30 W and uses only three cryocoolers. This result is somewhere in between the uniform cooling and the cooling close to the coil case. In reality, the design space has numerous possibilities. The work in this section has not explored the entire trade space, but merely showed a few examples. This section has set up a framework for trade space exploration that can be pursued as future work, if implementation of multiple cryocoolers is a realistic possibility. Similar to the challenge of implementing two cryocoolers, the engineering details of using multiple cryocoolers needs to be addressed, in addition to the mass implications. However, there is a possibility of power reduction by using more than one or two cryocoolers on the system.

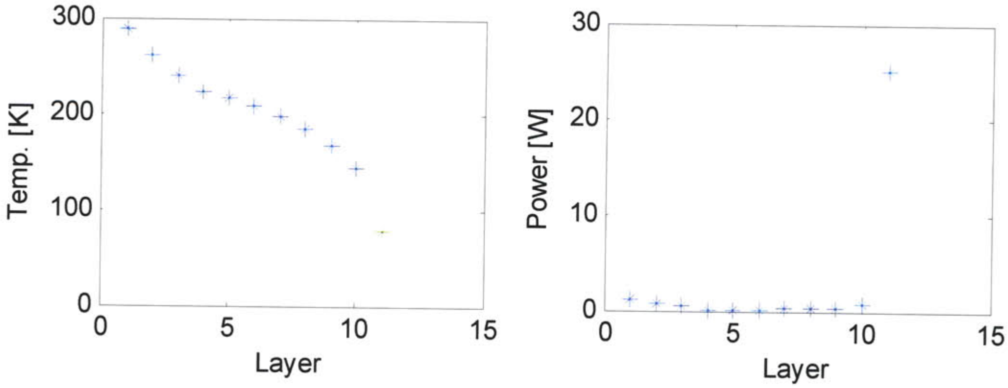

Figure B.4 Results with cooling located close to the outer layer

B.2 Radiator Design

A simple steady-state analysis to determine the approximate size of the radiator needed to reject heat from a single cryocooler is useful for the flight design of EMFF. The heat that is emitted by radiation, Q_e, is given by

$$Q_e = \varepsilon \sigma T_{rej}^{\ 4} A_{rad} \tag{B.13}$$

where A_{rad} is the area of the radiator and T_{rej} is the temperature of heat rejection by the radiator. Assuming that the cryocooler needs to reject 5 Watts from the coil and 150 Watts of electrical power and the rejection temperature of the cryocooler is 300 K, the area for an ideal black body radiator is

$$A_{rad} = \frac{Q_e}{\varepsilon \sigma T_{rej}^{\ 4}} = \frac{155}{(1)\sigma 300^4} = 0.3375 \text{ m}^2 \tag{B.14}$$

This yields a square radiator with 58 cm sides. Overall, the size of the radiator does not seem to be a major obstacle. The radiator could be connected to the end of the cryocooler by a heat pipe so that heat is radiated in a direction away from the coils. One of the challenges in designing the radiator is to make sure that heat from the radiator that is not re-absorbed by the coils.

B.3 Mass of multiple cryocooler system

This section compares the mass of two heat pipe systems; a heat pipe containing all the working fluid inside of it; and a heat pipe with a gas reservoir. The wall thickness of the heat pipe without the gas reservoir must be large enough to contain the high pressure of the gas at ambient room temperature conditions, such as before launch. For the heat pipe with a gas reservoir, a spherical gas reservoir is connected to the heat pipe and sized so that the volume of the reservoir is large enough to hold any working fluid gas that might expand as the temperature rises.

The goal of designing a heat pipe that holds the pressure at ambient conditions (300 K) is to determine the necessary wall thickness to maintain structural integrity if the cryocooler fails. First, the maximum pressure for the pipe operation, $P_{\max}$, must be determined. This depends on the amount of working fluid present in the pipe. Assuming that 210 g of working fluid is needed, such as the design for the circular heat pipe in Chapter 5, this means that 160 L of N_2 gas will result in a pressure of 294 psi or 2.02 MPa at room temperature.

Next, to find the minimum pipe wall thickness (*t*), given the maximum possible pressure, $P_{\max}$, and assuming the pipe cross-sectional diameter (*d*) is 2 cm, same as testbed heat pipes, Equation (B.15) is used.

$$\sigma_{\max} = \frac{P_{\max} d}{2t} \rightarrow t = \frac{P_{\max} \cdot r}{\sigma_{\max}} \tag{B.15}$$

Using the calculated value for the wall thickness and assuming negligible mass for the mess, the mass of the heat pipe, m_{HP}, is given by

$$m_{HP} = \rho t(\pi d)(2\pi R_c) \tag{B.16}$$

A summary of the heat pipe mass using aluminum, copper, and stainless steel is shown in Table B.1. for a one meter coil.

Table B.1 Mass of heat pipe for a 1 m coil

Material	σ_{max} [MPa]	t [mm]	m_{HP} [kg]
Aluminum	20	20	43
Copper	100	0.4	2.8
Stainless steel	500	0.1	0.5

In the case where two cryocoolers are used, the 2nd stage, or outer stage is located on the outside of the vacuum gap at a hotter temperature. This 2nd stage can be implemented as a heat pipe to provide isothermalization of the outer layer. Assuming it has similar pressure requirements as the nitrogen pipe, which is the inside stage, the mass of the 2nd stage heat pipe is given by

$$m_{HP\_2^{nd}stage} = \rho t\left(2\pi\left(\frac{d}{2} + 2mm\right)\right)(2\pi R_c) \tag{B.17}$$

In this case, let the gap between the 1st and 2nd stage ($r_h - r_c$) be 2 mm. There are a large range of working fluids that exist for a 2nd stage heat pipe operating at a higher temperature than nitrogen at saturation conditions. Ammonium and methanol are two possible working fluids.

The total mass for the single stage heat pipe system is

$$M_{t\_\text{singlestage}} = m_{HP} + m_{cryo} + m_{coil} \tag{B.18}$$

where m_{cryo} = 2.7 kg for a single COTS cryocooler. The mass of the coil, m_{coil}, is given by

$$m_{coil} = N_{turns} \rho_{HTS} A_c 2\pi R_c \tag{B.19}$$

where N_{turns} = 100, A_c = 0.27 mm x 4.3 mm for COTS HTS wire.

For a second stage system the total mass is given by

$$M_{t\_\text{2stages}} = M_{t\_\text{singlestage}} + m_{cryo} + m_{HP\_2^{nd}\,stage} \tag{B.20}$$

Keep in mind the additional cryocooler associated with the 2nd stage. The mass of the thermal system (coil, heat pipe and cryocooler) using a single stage and two stages are shown in Figure B.5. Since using aluminum results in very large heat pipe masses, it is not shown. The heat pipe made of stainless steel is the least massive material choice. For a one meter radius coil, using stainless steel and a single stage, the ratio of the heat pipe mass (0.505 kg) to coil mass (5.836 kg) is 0.0866. Note that the cryocooler adds a constant 2.7 kg to the thermal related masses (cryocooler plus heat pipe).

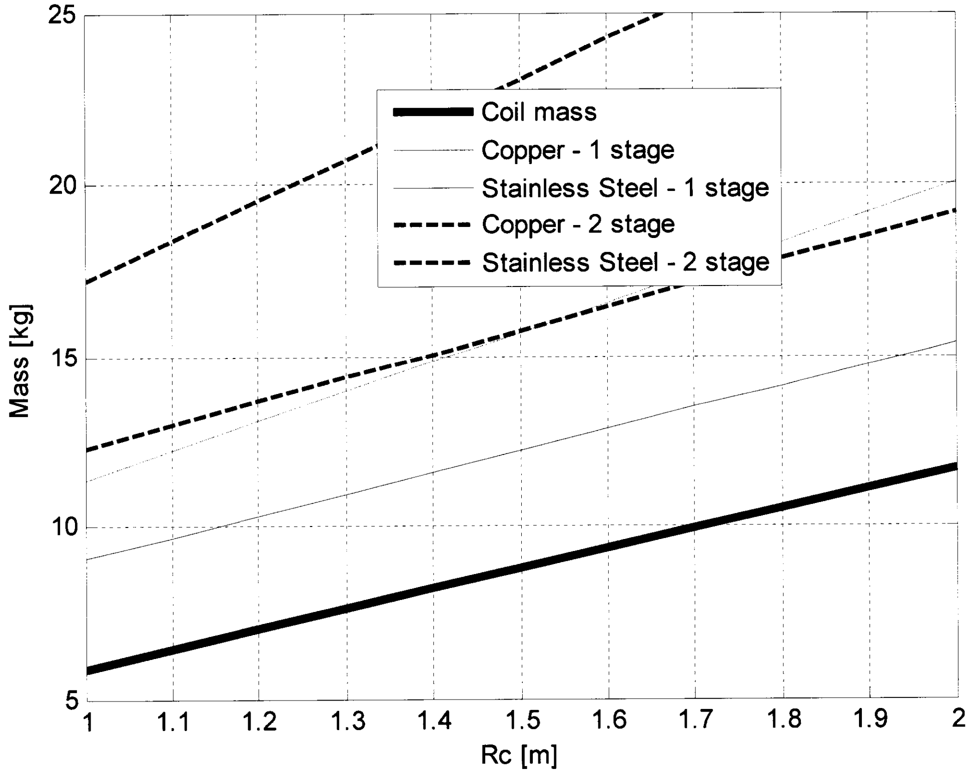

Figure B.5 Mass of thermal system for a single stage and two stage system

For the heat pipe with a gas reservoir, both the reservoir and heat pipe are sized for a lower maximum pressure. If the pressure rises above the maximum pressure in the heat pipe, the working fluid expands into a gas reservoir. Given the low pressure conditions at 90 K, which yield a pressure of 52 psi or 357 kPa, the wall thickness is determined from Equation (B.15). Next, the volume of gas, V_{gas}, is determined in the case where all the working fluid in the wick is turned into gas. Based on the EMFF heat pipe wick characteristics A_w and ε_p from Chapter 5, the working fluid mass, $m_{w.f.}$, and volume of gas are given by

$$m_{w.f.} = \rho_l \left(A_w \varepsilon_p\right)\left(2\pi R_c\right) = \rho_g V_{gas} \tag{B.21}$$

$$V_{gas} = \frac{\rho_l}{\rho_g}\left(A_w \varepsilon_p\right)\left(2\pi R_c\right) \tag{B.22}$$

If gas reservoir were designed to be a pipe with the same cross-sectional diameter as the heat pipe, then the volume of the gas reservoir is approximately six times the volume of the heat pipe. If the gas reservoir were designed to be a spherical shape, with same thickness t as the heat pipe, and made of the same material, the size and mass of the sphere are given by

$$r^3_{sphere} = \frac{\rho_l}{\rho_g}\left(A_w \varepsilon_p\right)\left(2\pi R_c\right)\left(\frac{3}{4\pi}\right) \tag{B.23}$$

$$m_{sphere} = \rho_{sphere} t \left(4\pi r_{sphere}^2\right) \tag{B.24}$$

The mass of the gas reservoir for a one meter coil is summarized in Table B.2. The analysis used a safety factor of 5 for the stainless steel system to allow for a more realistic wall thickness. As a reference, the HTS wire thickness is 0.27 mm. The radius of sphere for a one meter coil is 23 cm. The mass of a gas reservoir system is shown in Figure B.6.

Table B.2 Mass of gas reservoir for a 1 m coil

Material	t [mm]	m_{sphere} [kg]	m_{HP} [kg]
Aluminum	3.6	6.25	7.653
Copper	0.14	0.83	0.508
Stainless steel	0.1	0.15	0.454

For a single stage case, comparing the system with and without the gas reservoir is shown in Figure B.7. The system without the gas reservoir is least massive using stainless steel as a material. A simple heat pipe containing all the working fluid is also beneficial because there is not large space taken up by a gas reservoir.

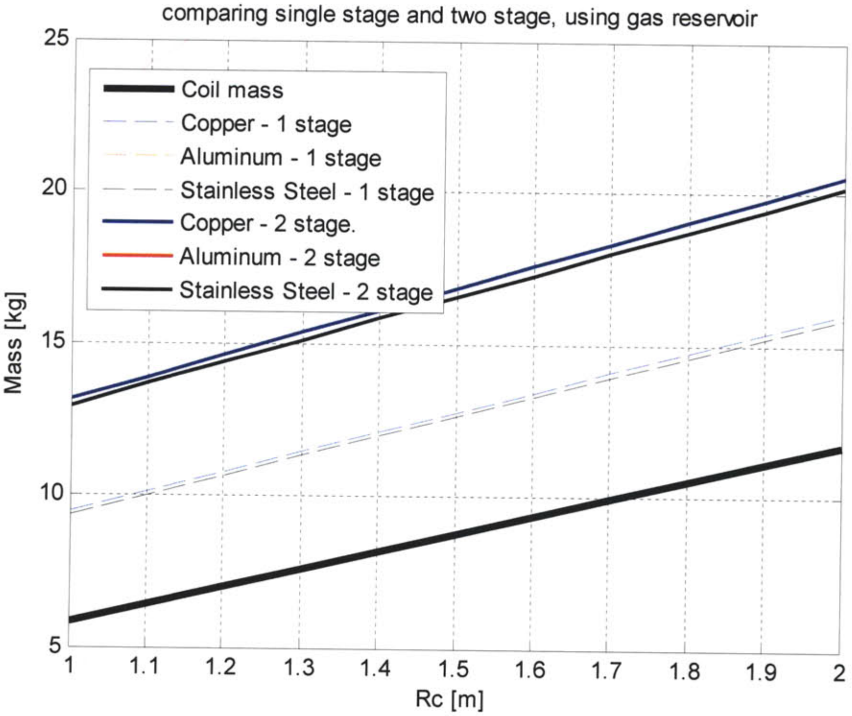

Figure B.6 Mass of a system using a gas reservoir

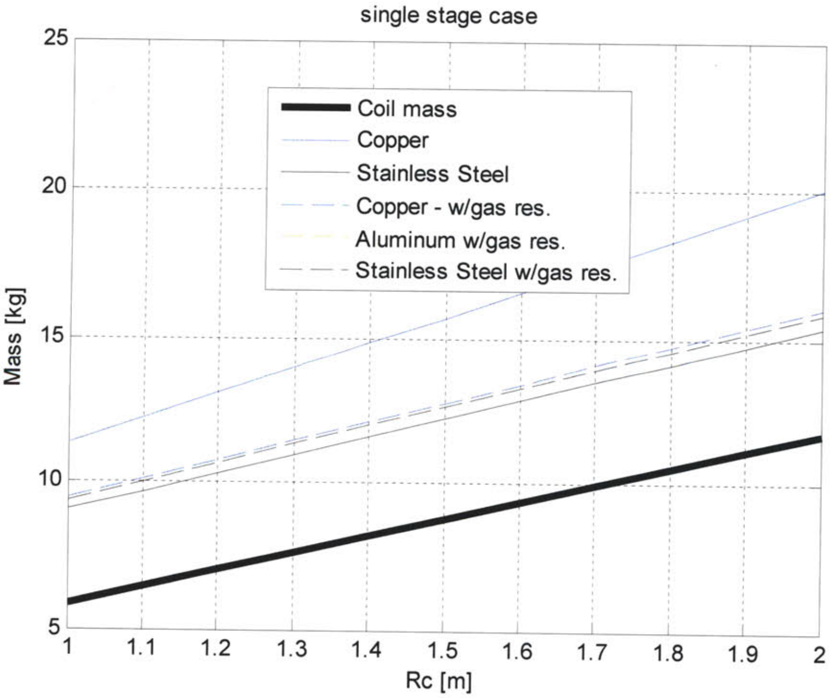

Figure B.7 Mass of a single stage thermal system

Appendix C Additional Thermal Modeling

C.1 1D FDM Additions

There are two additions discussed in this section that can help improve the fidelity of the 1D FDM. They are accounting for the convection that occurs inside the vacuum chamber and accounting for the change in material properties as a function of temperature. The standard equation for the heat flux due to convection is given by

$$q_{convection} = h\left(T_{body} - T_{\infty}\right) \tag{C.1}$$

In the case of the vacuum chamber model, the body temperature, T_{body}, is the temperature of the copper jacket (T_{copper}) and T_{∞} is the air temperature in the vacuum, which is essentially the same as the wall temperature (T_w). For natural convection, the convection coefficient is typically between 5-30 W/m^2·K and for forced convection the range of h is 10-250 W/m^2·K [84]. In a vacuum, convection can function a little differently depending on the pressure. The regime of flow can be determined by the Knudsen number, which is defined as

$$Kn = \frac{\lambda}{L_e} \tag{C.2}$$

where, L_e is the characteristic dimension, and λ is the mean free path. The three vacuum flow regimes are as follows:

Continuum flow: $Kn < 0.01$

Mixed flow: $0.01 < Kn < 0.30$

Free-molecular flow: $Kn > 0.30$

In the vacuum chamber, L_e is the distance between the copper jacket and the chamber wall, so L_e = 9 cm. The mean free path, λ is defined as

$$\lambda = \frac{RT}{\sqrt{2}\pi d^2 N_A P} \tag{C.3}$$

where R is the universal gas constant, T is the temperature of the vacuum, N_A is Avogadro's number, d is the diameter of the gas particles and P is the vacuum pressure. Using gas particles with a three angstrom diameter and a vacuum pressure of $3.4\cdot10^{-5}$ mbar, the mean free path is approximately 2.7 m. This yields a Knudsen number of approximately 30, which is well in the free-molecular flow case. In addition, if $\lambda \gg L_e$, then convection does not occur. To model the free molecular flow between two surfaces, the heat flux is given as [56]

$$q\left[{}^{w}\!/_{m^2}\right] = F_a G\cdot P\left(T_2 - T_1\right) = h_{eff}\left(T_{CU} - T_w\right) \tag{C.4}$$

Where the accommodation factor, F_a, accounts for gas interactions, and G is given by

$$G = \frac{\gamma+1}{\gamma-1}\left(\frac{R}{8\pi T}\right)^{1/2} \tag{C.5}$$

For a system with a pressure of $3.4\cdot10^{-5}$ mbar, the effective conduction coefficient is

$$h_{eff} \cong 0.0038 \tag{C.6}$$

Therefore, the free-molecular flow is a very low-order effect in the vacuum chamber and is essentially negligible.

The second addition to the 1D FDM is accounting for the variation in the thermal diffusivity, α, and the volumetric heat capacity, ρc_p, as a function of temperature for the copper jacket. This is seen in Figure C.1 where the volumetric heat capacity at 90 K is reduced to approximately 65% of the room temperature value and in Figure C.2 where the thermal diffusivity at 90 K is approximately 180% larger than the room temperature value. Using this coarse set of data for both α and ρc_p, curve fits were developed so that each quantity can be modeled as a function of temperature. Now for the 1D explicit FDM, at each time step and at each location along the copper pipe, the temperature can be solved for using $\alpha(T)$ and $\rho c_p(T)$. It is important to note that the variation in α also can affect the stability of the explicit scheme because the change in timestep, Δt, is a function of α.

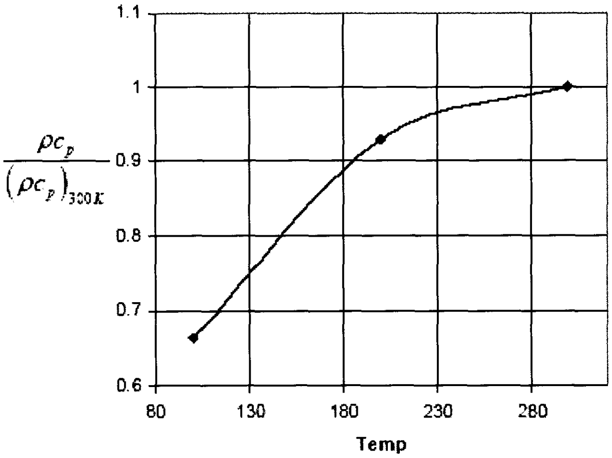

Figure C.1 Volumetric heat capacity vs. temperature relative to room temperature values

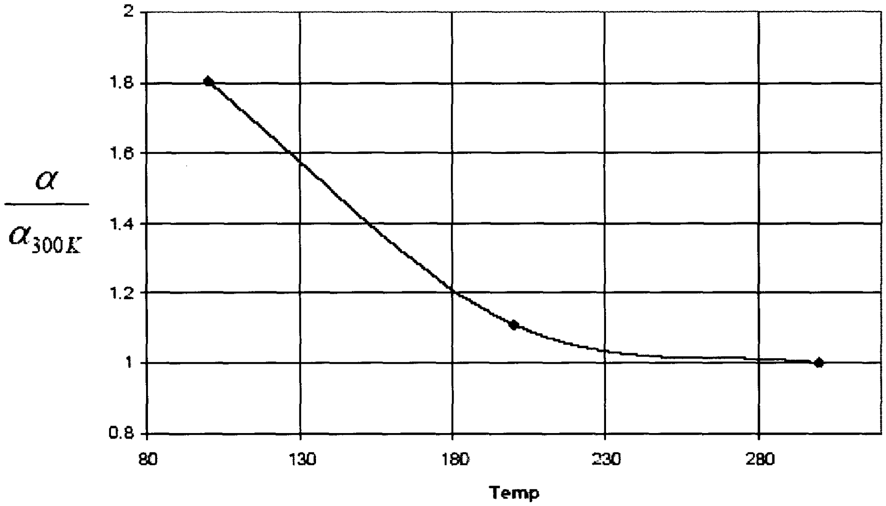

Figure C.2 Thermal diffusivity vs. temperature relative to room temperature values

C.2 1D Implicit FDM

One final 1D FDM scheme was investigated for completeness. An implicit scheme allows all the temperatures at a given time step to be solved for simultaneously. Starting with the steady-state heat diffusion equation, the 1D model is central differenced so that all the temperatures on the left hand side are determined at the n+1 time step as follows.

$$\nabla^2 T + \frac{\dot{q}}{k} = \frac{1}{\alpha}\frac{dT}{dt} \quad \rightarrow \quad \frac{T_{i-1}^{n+1} - 2T_i^{n+1} + T_{i+1}^{n+1}}{(\Delta z)^2} + \frac{\dot{q}}{k} = \frac{1}{\alpha}\frac{T_i^{n+1} - T_i^n}{\Delta t} \tag{C.7}$$

The temperatures at time step n are known quantities and Equation (C.7) can be rearranged so that all the unknown temperatures at time n+1 are arranged on the left hand side.

$$cT_{i-1}^{n+1} - (1+2c)T_i^{n+1} + cT_{i+1}^{n+1} = -T_i^n + \frac{\dot{q}}{k}\alpha\Delta t \tag{C.8}$$

Here the coefficient $c = \frac{\alpha\Delta t}{(\Delta z)^2}$. Similar to the 1D explicit FDM, boundary conditions are set at the cryocooler location and are defined as

$$\left.\begin{array}{l} T(z=0) = T_1 \\ T(z=L) = T_m \end{array}\right\} = T_c = 77 \tag{C.9}$$

Equation (C.8) can be put into $Ax = b$ form where the x-vector contains the unknown temperatures at the next time step. This is shown as

$$\begin{bmatrix} -(1+2c) & c & 0 & 0 & \cdots & 0 \\ c & -(1+2c) & c & 0 & \cdots & 0 \\ & & & & & \\ \cdots & c & -(1+2c) & c & \cdots & \\ & & & & & \\ 0 & \cdots & & 0 & c & -(1+2c) \end{bmatrix} \begin{bmatrix} T_2^{n+1} \\ T_3^{n+1} \\ \vdots \\ T_i^{n+1} \\ \vdots \\ T_{m-1}^{n+1} \end{bmatrix} = \begin{bmatrix} -T_2^n - cT_1 \\ -T_1^n \\ \vdots \\ -T_i^n \\ \vdots \\ -T_{m-1}^n - cT_m \end{bmatrix} - \tfrac{\dot{q}}{k}\alpha\Delta t \tag{C.10}$$

Now the temperature can be solved for by $x = A^{-1}b$. A time dependent scheme does not affect the A matrix and therefore does not affect the matrix inversion calculation. One of the benefits of the implicit scheme is that there is no stability requirement on the time step. The implicit scheme can become computationally expensive for a large number of points because the A-matrix becomes large. A time-independent implicit scheme can be implemented by making the right hand side of Equation (C.7) go to zero. Now the steady-state temperature can be solved for with a single calculation. This implicit scheme is benchmarked with the analytic model using the same conditions. The result is shown in Figure C.3. Since the analytic model also was validated with the explicit model (not shown for clarity), all three models match. The explicit scheme was used in this thesis because it was the fastest scheme to implement and the time-varying explicit scheme was useful for comparing with the transient experimental data. A comparison of the speed of each scheme is shown in Table C.1. For the cases run, the maximum temperature was 123.2963 K. For the time dependent schemes, the explicit FDM ran faster than the implicit FDM.

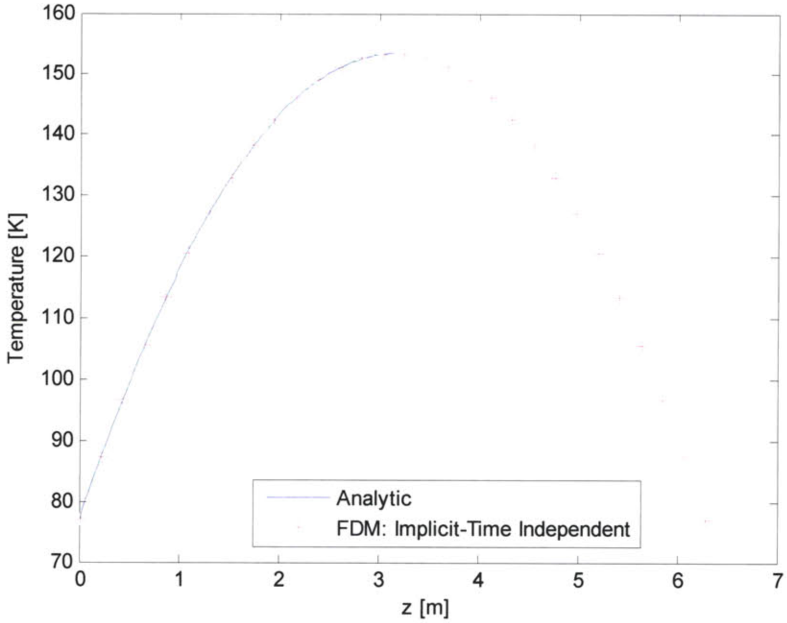

Figure C.3 Temperature distribution for the implicit FDM

Table C.1 Computational time comparison between different modeling schemes

Model	# iterations	Max temp [K]	Computation time [s]
Analytic	N/A	123.2963	0.001
FDM - Explicit	10000	123.2412	31.205
FDM – Explicit	1000	120.7072	0.107
FDM - Implicit	10000	123.2412	46.892
FDM - Implicit	1000	120.6853	1.862
FDM – Implicit, time independent	1	123.2412	0.019

C.3 3D FDM

A discrete model of the thermal system that finite differences the coil in three dimensions has also been investigated. A time-varying implicit model has been constructed for the thermally conductive jacket. The anisotropic property of the MLI has also been modeled. There is a thermal conductivity perpendicular to the radiation shields, K_r, which acts through the MLI layers, and a thermal conductivity parallel to the radiation shields, K_θ, acting along a MLI layer. The heat diffusion equation is used as a starting point and is finite differenced so that the temperature at each node can be solved by Gaussian Elimination. The governing equation for temperature distribution in the thermal system is the heat diffusion equation with no assumptions on k is given by

$$\nabla \cdot k\nabla T + \dot{q} = \rho c \frac{\partial T}{\partial t} \tag{C.11}$$

The coil is finite differenced in the radial (r), circumferential (z), and theta (θ) directions and shown in Figure C.4. The temperature at the (r, z, θ) coordinate is represented by subscript indices (m, n, p), so that the temperature $T_{m,n,p}$ maps to $T_{r,z,\theta}$. A superscript on the temperature indicates the time. The radius, r, is divided into M total layers and layer I is located at the interface of the copper and MLI. The length, or circumferential length, z, is divided in N parts and the discretization in the theta direction has P total parts. The total number of nodes in the coil is $M{\cdot}N{\cdot}P$. This can lead to a large, but sparse matrix. For example, using 10 discrete points for r, z, and θ leads to a 1000 x 1000 matrix.

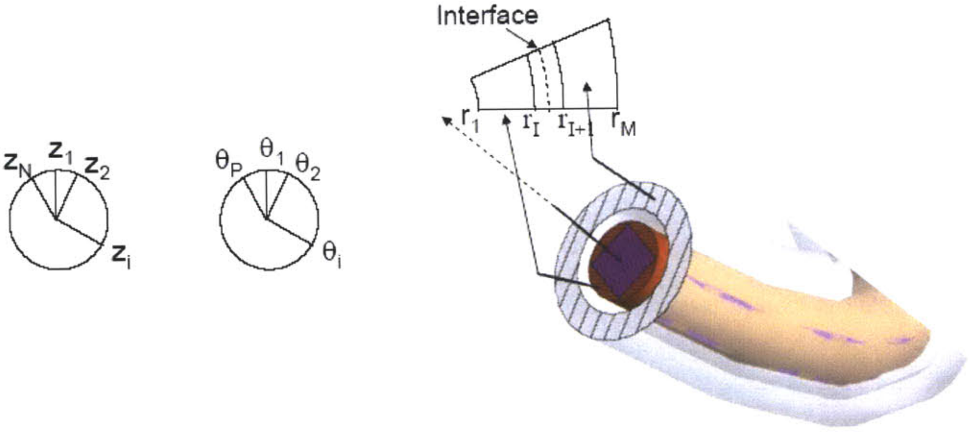

Figure C.4 Finite difference regions for 3D FDM

The coil is divided into five regions for the finite difference model, which are shown in Equation (C.12).

$$\begin{bmatrix} \text{Inner Boundary Condition, CVA} \\ \text{Copper Interior, } K\nabla^2 T \\ \text{Cu Interface Layer, CVA} \\ \text{MLI Interface Layer, CVA} \\ \text{MLI Interior, } \nabla\cdot K\nabla T \\ \text{Outer Boundary Condition, CVA} \end{bmatrix} \begin{bmatrix} T^{h+1}_{1,[1...N],[1...P]} \\ \vdots \\ T^{h+1}_{I,[1...N],[1...P]} \\ T^{h+1}_{J,[1...N],[1...P]} \\ \vdots \\ T^{h+1}_{M,[1...N],[1...P]} \end{bmatrix} = \begin{bmatrix} aT_{1,[1...N],[1...P]} \\ 0 \\ \vdots \\ \vdots \\ 0 \\ aT_{M,[1...N],[1...P]} + b\cdot q \end{bmatrix} \tag{C.12}$$

The inner layer of the copper ($r = 1$) and the outer layer of the MLI ($r = M$) are boundary condition layers which use the control volume approach (CVA). The governing equation for the interior layer of the copper and MLI is Laplace's equation with isotropic thermal conductivity for the copper and anisotropic thermal conductivity for the MLI. At the interface layers I and J, Laplace's equation is still the governing equation however a thermal resistive network model for the anisotropic conductivities is used. The following subsections describe how to obtain the necessary components in Equation (C.12).

C.3.1 Copper Interior

Since the copper jacket has a toroidal configuration with a large major radius, the Laplacian in cylindrical coordinates is used

$$\frac{\partial^2 T}{\partial r^2}+\frac{1}{r}\frac{\partial T}{\partial r}+\frac{1}{r^2}\frac{\partial^2 T}{\partial \theta^2}+\frac{\partial^2 T}{\partial z^2}=\frac{\rho C}{K_{Cu}}\frac{dT}{dt} \tag{C.13}$$

The interior layers use a spatial central difference and a forward difference in time. Finite differencing Equation (C.13) yields

$$\begin{gathered}\frac{T^{h+1}_{m-1,n,p}-2T^{h+1}_{m,n,p}+T^{h+1}_{m+1,n,p}}{\left(\Delta r_i\right)^2}+\frac{1}{r_m}\frac{T^{h+1}_{m+1,n,p}-T^{h+1}_{m-1,n,p}}{2\Delta r_i}+\\ \frac{1}{r_m^2}\frac{T^{h+1}_{m,n,p-1}-2T^{h+1}_{m,n,p}+T^{h+1}_{m,n,p+1}}{\left(\Delta\theta\right)^2}+\frac{T^{h+1}_{m,n-1,p}-2T^{h+1}_{m,n,p}+T^{h+1}_{m,n+1,p}}{\left(\Delta z\right)^2}=\frac{\rho C}{K_{Cu}}\frac{T^{h+1}_{m,n,p}-T^{h}_{m,n,p}}{\Delta t}\end{gathered} \tag{C.14}$$

Solving for the temperature at the (*m*,*n*,*p*) row yields

$$\begin{gathered}T^{h+1}_{m,n,p}\left(-\frac{\rho C}{K_{Cu}\Delta t}-\frac{2}{\left(\Delta r_i\right)^2}-\frac{2}{r_m^2\left(\Delta\theta\right)^2}-\frac{2}{\left(\Delta z\right)^2}\right)+T^{h+1}_{m-1,n,p}\left(\frac{1}{\left(\Delta r_i\right)^2}-\frac{1}{2r_m\Delta r_i}\right)+\\ T^{h+1}_{m+1,n,p}\left(\frac{1}{\left(\Delta r_i\right)^2}+\frac{1}{2r_m\Delta r_i}\right)+\frac{T^{h+1}_{m,n,p-1}}{r_m^2\left(\Delta\theta\right)^2}+\frac{T^{h+1}_{m,n,p+1}}{r_m^2\left(\Delta\theta\right)^2}+\frac{T^{h+1}_{m,n-1,p}}{\left(\Delta z\right)^2}+\frac{T^{h+1}_{m,n+1,p}}{\left(\Delta z\right)^2}=-\frac{\rho C}{K_{Cu}\Delta t}T^{h}_{m,n,p}\end{gathered} \tag{C.15}$$

The next step is to express Eq (C.15) using non-dimensional parameters

$$\begin{gathered}T=\overline{T}\cdot T_D \quad K=\overline{K}\cdot K_D\\ r=\overline{r}\cdot r_D \quad z=\overline{z}\cdot z_D\end{gathered} \tag{C.16}$$

$$\begin{gathered}\overline{T}^{h+1}_{m,n,p}\left(-\frac{\rho C}{\overline{K}_{Cu}K_D\Delta t}-\frac{2}{\left(\Delta\overline{r}_i\right)^2}-\frac{2}{\overline{r}_m^2\left(\Delta\theta\right)^2}-\frac{2}{\left(\Delta\overline{z}\right)^2}\right)+\overline{T}^{h+1}_{m-1,n,p}\left(\frac{1}{\left(\Delta\overline{r}_i\right)^2}-\frac{1}{2\overline{r}_m\Delta\overline{r}_i}\right)+\\ \overline{T}^{h+1}_{m+1,n,p}\left(\frac{1}{\left(\Delta\overline{r}_i\right)^2}+\frac{1}{2\overline{r}_m\Delta\overline{r}_i}\right)+\frac{\overline{T}^{h+1}_{m,n,p-1}}{\overline{r}_m^2\left(\Delta\theta\right)^2}+\frac{\overline{T}^{h+1}_{m,n,p+1}}{\overline{r}_m^2\left(\Delta\theta\right)^2}+\frac{\overline{T}^{h+1}_{m,n-1,p}}{\left(\Delta\overline{z}\right)^2}+\frac{\overline{T}^{h+1}_{m,n+1,p}}{\left(\Delta\overline{z}\right)^2}=-\frac{\rho C}{\overline{K}_{Cu}\Delta t}\frac{r_D^2}{K_D}\overline{T}^{h}_{m,n,p}\end{gathered} \tag{C.17}$$

Note that in the Matlab code Eq (C.17) is rewritten as

$$\begin{gathered}\overline{T}^{h+1}_{m,n,p}\left(-\alpha-\frac{2\overline{K}_{Cu}}{\left(\Delta\overline{r}_i\right)^2}-\frac{2\overline{K}_{Cu}}{\overline{r}_m^2\left(\Delta\theta\right)^2}-\frac{2\overline{K}_{Cu}}{\left(\Delta\overline{z}\right)^2}\right)+\overline{T}^{h+1}_{m-1,n,p}\overline{K}_{Cu}\left(\frac{1}{\left(\Delta\overline{r}_i\right)^2}-\frac{1}{2\overline{r}_m\Delta\overline{r}_i}\right)+\\ \overline{T}^{h+1}_{m+1,n,p}\overline{K}_{Cu}\left(\frac{1}{\left(\Delta\overline{r}_i\right)^2}+\frac{1}{2\overline{r}_m\Delta\overline{r}_i}\right)+\overline{K}_{Cu}\frac{\overline{T}^{h+1}_{m,n,p-1}}{\overline{r}_m^2\left(\Delta\theta\right)^2}+\overline{K}_{Cu}\frac{\overline{T}^{h+1}_{m,n,p+1}}{\overline{r}_m^2\left(\Delta\theta\right)^2}+\overline{K}_{Cu}\frac{\overline{T}^{h+1}_{m,n-1,p}}{\left(\Delta\overline{z}\right)^2}+\overline{K}_{Cu}\frac{\overline{T}^{h+1}_{m,n+1,p}}{\left(\Delta\overline{z}\right)^2}=-\alpha_{Cu}\overline{T}^{h}_{m,n,p}\end{gathered} \tag{C.18}$$

The right hand side is simplified to be $-\alpha_{Cu}\overline{T}^{h}_{m,n,p}$ where

$$\alpha_{Cu} = \frac{\rho C}{\Delta t}\frac{r_D^2}{K_D} \tag{C.19}$$

The form in Equation (C.18) can be put into Equation (C.12) in order to solve for the temperature of the system.

C.3.2 MLI Interior

The thermal conductivity of the MLI in the through direction, perpendicular to the shields is K_r, while the thermal conductivity parallel to the shields is K_θ. For a biaxial media, where the thermal conductivity can be described as

$$\overline{\overline{K}} = \begin{bmatrix} K_r & 0 & 0 \\ 0 & K_\theta & 0 \\ 0 & 0 & K_\theta \end{bmatrix} \tag{C.20}$$

The Laplacian for an anisotropic K is

$$\nabla\cdot\left(\overline{\overline{K}}\nabla T\right) = K_r\left(\frac{1}{r}\frac{\partial T}{\partial r}+\frac{\partial^2 T}{\partial r^2}\right)+K_\theta\left(\frac{1}{r^2}\frac{\partial^2 T}{\partial \theta^2}+\frac{\partial^2 T}{\partial z^2}\right) \tag{C.21}$$

Thus central differencing the heat diffusion equation follows a similar pattern to Equation (C.13)

$$\begin{aligned} &K_r\frac{T^{h+1}_{m-1,n,p}-2T^{h+1}_{m,n,p}+T^{h+1}_{m+1,n,p}}{(\Delta r_o)^2}+\frac{K_r}{r_m}\frac{T^{h+1}_{m+1,n,p}-T^{h+1}_{m-1,n,p}}{2\Delta r_o}+ \\ &\frac{K_\theta}{r_m^2}\frac{T^{h+1}_{m,n,p-1}-2T^{h+1}_{m,n,p}+T^{h+1}_{m,n,p+1}}{(\Delta\theta)^2}+K_\theta\frac{T^{h+1}_{m,n-1,p}-2T^{h+1}_{m,n,p}+T^{h+1}_{m,n+1,p}}{(\Delta z)^2}=(\rho C)_{MLI}\frac{T^{h+1}_{m,n,p}-T^{h}_{m,n,p}}{\Delta t} \end{aligned} \tag{C.22}$$

Rearranging to get an expression of the temperature in row (m,n,p) of the MLI

$$\begin{aligned} &T^{h+1}_{m,n,p}\left(-\frac{(\rho C)_{MLI}}{\Delta t}-\frac{2K_r}{(\Delta r_o)^2}-\frac{2K_\theta}{r_m^2(\Delta\theta)^2}-\frac{2K_\theta}{(\Delta z)^2}\right)+T^{h+1}_{m-1,n,p}\left(\frac{K_r}{(\Delta r_o)^2}-\frac{K_r}{2r_m\Delta r_o}\right)+ \\ &T^{h+1}_{m+1,n,p}\left(\frac{K_r}{(\Delta r_o)^2}+\frac{K_r}{2r_m\Delta r_o}\right)+K_\theta\frac{T^{h+1}_{m,n,p-1}}{r_m^2(\Delta\theta)^2}+K_\theta\frac{T^{h+1}_{m,n,p+1}}{r_m^2(\Delta\theta)^2}+K_\theta\frac{T^{h+1}_{m,n-1,p}}{(\Delta z)^2}+K_\theta\frac{T^{h+1}_{m,n+1,p}}{(\Delta z)^2}=-\frac{(\rho C)_{MLI}}{\Delta t}\cdot T^{h}_{m,n,p} \end{aligned} \tag{C.23}$$

Nondimensionalizing yields

$$\begin{aligned}&\overline{T}^{h+1}_{m,n,p}\left(-\frac{(\rho C)_{MLI}}{\Delta t}\frac{r_D^2}{K_D}-\frac{2\overline{K}_r}{(\Delta\overline{r}_o)^2}-\frac{2\overline{K}_\theta}{\overline{r}_m^2(\Delta\theta)^2}-\frac{2\overline{K}_\theta}{(\Delta\overline{z})^2}\right)+\overline{T}^{h+1}_{m-1,n,p}\left(\frac{\overline{K}_r}{(\Delta\overline{r}_o)^2}-\frac{\overline{K}_r}{2\overline{r}_m\Delta\overline{r}_o}\right)+\\&\overline{T}^{h+1}_{m+1,n,p}\left(\frac{\overline{K}_r}{(\Delta\overline{r}_o)^2}+\frac{\overline{K}_r}{2\overline{r}_m\Delta\overline{r}_o}\right)+\overline{K}_\theta\frac{\overline{T}^{h+1}_{m,n,p-1}}{\overline{r}_m^2(\Delta\theta)^2}+\overline{K}_\theta\frac{\overline{T}^{h+1}_{m,n,p+1}}{\overline{r}_m^2(\Delta\theta)^2}+\overline{K}_\theta\frac{\overline{T}^{h+1}_{m,n-1,p}}{(\Delta\overline{z})^2}+\overline{K}_\theta\frac{\overline{T}^{h+1}_{m,n+1,p}}{(\Delta\overline{z})^2}=-\frac{(\rho C)_{MLI}}{\Delta t}\frac{r_D^2}{K_D}\cdot\overline{T}^h_{m,n,p}\end{aligned}\tag{C.24}$$

The right hand side is simplified to $-\alpha_{MLI}\overline{T}^h_{m,n,p}$ where

$$\alpha_{MLI}=\frac{r_D^2}{K_D}\frac{(\rho C)_{MLI}}{\Delta t}\tag{C.25}$$

Equation (C.24) can be put into the $Ax=b$ form in order to determine the temperature of the copper and MLI toroidal system.

C.3.3 Boundary Conditions

The control volume approach is used as the boundary condition on the inner copper layer and the outer MLI layer. The control volume approach uses an energy balance for a finite region around each node. It accounts for conduction in and out of the control volume along with energy storage and generation. An alternative way of setting the boundary conditions is to use a finite difference equation for the heat conduction across a boundary. This does not account for the energy storage and heat generation terms, however in the limit that the infinitesimal region approaches zero, for example, if $\Delta r \rightarrow 0$, then these terms drop out. In general, the control volume approach is more accurate than the differential approach [62]. A slice of a finite difference element is shown in Figure C.5.

Using first order finite difference derivatives for the conduction out of a node in the outer MLI layer, the CVA is written as

$$\begin{aligned}&K_\theta\left(\frac{T^{h+1}_{M,n,p}-T^{h+1}_{M,n,p-1}}{r_o\Delta\theta}\right)\Delta z\frac{\Delta r_o}{2}+K_\theta\left(\frac{T^{h+1}_{M,n,p}-T^{h+1}_{M,n,p+1}}{r_o\Delta\theta}\right)\Delta z\frac{\Delta r_o}{2}+K_\theta\left(\frac{T^{h+1}_{M,n,p}-T^{h+1}_{M,n-1,p}}{\Delta z}\right)r_o\Delta\theta\frac{\Delta r_o}{2}+\\&K_\theta\left(\frac{T^{h+1}_{M,n,p}-T^{h+1}_{M,n+1,p}}{\Delta z}\right)r_o\Delta\theta\frac{\Delta r_o}{2}+K_r\left(\frac{T^{h+1}_{M,n,p}-T^{h+1}_{M-1,n,p}}{\Delta r_o}\right)\left(r_o-\frac{\Delta r_o}{2}\right)\Delta\theta\Delta z+\\&(\rho C)_{MLI}\frac{T^{h+1}_{M,n,p}-T^{h}_{M,n,p}}{\Delta t}\Delta z\frac{\Delta r_o}{2}r_o\Delta\theta=q_A\cdot r_o\Delta\theta\Delta z\end{aligned}\tag{C.26}$$

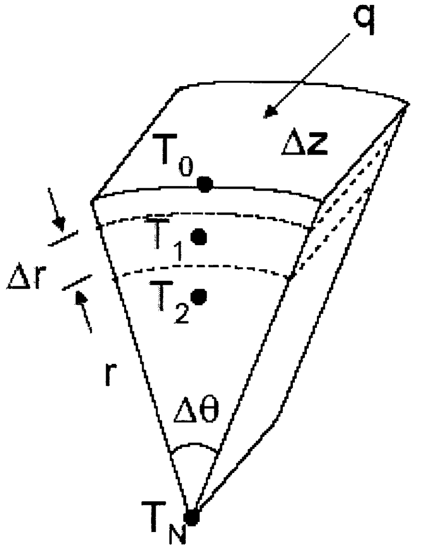

Figure C.5 Slice of a finite difference element

It is important to note that since the radial length of each control volume is $\Delta r/2$ instead of Δr the exact volume is given by

$$V=\int_0^{\Delta z}\int_0^{\Delta\theta}\int_{r_o-\frac{\Delta r_o}{2}}^{r_o} r\,dr\,d\phi\,dz=\Delta\theta\Delta z\left[\frac{r^2}{2}\right]_{r_o-\frac{\Delta r_o}{2}}^{r_o}$$
$$V=\Delta\theta\Delta z\left[\frac{r_o^2}{2}-\frac{\left(r_o-\frac{\Delta r_o}{2}\right)^2}{2}\right]=\Delta\theta\Delta z\left[\frac{r_o\Delta r_o}{2}-\frac{\left(\Delta r_o\right)^2}{2}\right] \tag{C.27}$$

This also means that the area terms in the z-direction are $\Delta\theta\left[\frac{r_o\Delta r_o}{2}-\frac{\left(\Delta r_o\right)^2}{2}\right]$ instead of $\frac{r_o\Delta\theta\Delta r_o}{2}$.

Rearranging to get an expression for each row (M,n,p)

$$\begin{gathered}T_{M,n,p}^{h+1}\left(K_\theta\frac{\Delta r_o\Delta z}{r_o\Delta\theta}+K_\theta\frac{\Delta r_o\cdot r_o\Delta\theta}{\Delta z}+K_r\frac{\left(r_o-\frac{\Delta r_o}{2}\right)\Delta\theta\Delta z}{\Delta r}+\frac{\left(\rho C\right)_{MLI}}{\Delta t}\frac{\Delta z\cdot r_o\Delta\theta\Delta r}{2}\right)+\\ T_{M-1,n,p}^{h+1}\left(-K_r\frac{\left(r_o-\frac{\Delta r_o}{2}\right)\Delta\theta\Delta z}{\Delta r}\right)+T_{M,n,p-1}^{h+1}\left(-K_\theta\frac{\Delta r_o\Delta z}{2r_o\Delta\theta}\right)+T_{M,n,p+1}^{h+1}\left(-K_\theta\frac{\Delta r_o\Delta z}{2r_o\Delta\theta}\right)+\\ T_{M,n-1,p}^{h+1}\left(-K_\theta\frac{\Delta r_o\cdot r_o\Delta\theta}{2\Delta z}\right)+T_{M,n+1,p}^{h+1}\left(-K_\theta\frac{\Delta r_o\cdot r_o\Delta\theta}{2\Delta z}\right)=q_A\cdot r_o\Delta\theta\Delta z+\frac{\left(\rho C\right)_{MLI}}{\Delta t}\frac{\Delta z\Delta r_o\cdot r_o\Delta\theta}{2}T_{M,n,p}^{h}\end{gathered} \tag{C.28}$$

Nondimensionalizing each side,

$$LHS = \frac{T_D K_D r_D \cdot \cancel{r_D}}{\cancel{r_D}} \left[\begin{array}{l} \overline{T}_{M,n,p}^{h+1} \left(\overline{K}_\theta \frac{\Delta\overline{r}\,\Delta\overline{z}_o}{\overline{r}_o \Delta\theta} + \overline{K}_\theta \frac{\Delta\overline{r} \cdot \overline{r}_o \Delta\theta_o}{\Delta\overline{z}} + \overline{K}_r \frac{\left(\overline{r}_o - \frac{\Delta\overline{r}_o}{2}\right)\Delta\theta\Delta\overline{z}}{\Delta\overline{r}} + \frac{(\rho C)_{MLI}}{\Delta t} \frac{\Delta\overline{z} \cdot \overline{r}_o \Delta\theta\Delta\overline{r}_o}{2} r_D^2 \right) \\ +\overline{T}_{M-1,n,p}^{h+1} \left(-\overline{K}_r \frac{\left(\overline{r}_o - \frac{\Delta\overline{r}_o}{2}\right)\Delta\theta\Delta\overline{z}}{\Delta\overline{r}_o} \right) + \overline{T}_{M,n,p-1}^{h+1} \left(-\overline{K}_\theta \frac{\Delta\overline{r}_o \Delta\overline{z}}{2\overline{r}_o \Delta\theta} \right) + \\ \overline{T}_{M,n,p+1}^{h+1} \left(-\overline{K}_\theta \frac{\Delta\overline{r}_o \Delta\overline{z}}{2\overline{r}_o \Delta\theta} \right) + \overline{T}_{M,n-1,p}^{h+1} \left(-\overline{K}_\theta \frac{\Delta\overline{r}_o \cdot \overline{r}_o \Delta\theta}{2\Delta\overline{z}} \right) + \overline{T}_{M,n+1,p}^{h+1} \left(-\overline{K}_\theta \frac{\Delta\overline{r}_o \cdot \overline{r}_o \Delta\theta_o}{2\Delta\overline{z}} \right) \end{array} \right]$$

$$RHS = r_o \Delta\theta\Delta z \cdot \varepsilon\sigma \left(T_{envo}^4 - \left(T_{M,n,p}^h\right)^4 \right) + \frac{(\rho C)_{MLI}}{\Delta t} \frac{\Delta z \cdot r_o \Delta\theta\Delta r_o}{2} T_{M,n,p}^h \tag{C.29}$$

$$RHS = \overline{r}_o \Delta\theta\Delta\overline{z} \cdot \varepsilon\sigma \left(\overline{T}_{envo}^4 - \left(\overline{T}_{M,n,p}^h\right)^4 \right) \cdot T_D^4 r_D^2 + \frac{(\rho C)_{MLI}}{\Delta t} \frac{\Delta\overline{z} \cdot \overline{r}_o \Delta\theta\Delta\overline{r}_o}{2} \overline{T}_{M,n,p}^h \cdot T_D r_D^3$$

In summary, the control volume approach for the outer boundary is implemented as the following

$$[A]\left[\overline{T}^{h+1}\right] = \overline{r}_o \Delta\theta\Delta\overline{z} \cdot \varepsilon\sigma \left(\overline{T}_{envo}^4 - \left(\overline{T}_{M,n,p}^h\right)^4 \right) \frac{T_D^3 r_D}{K_D} + \alpha_{MLI} \frac{\Delta\overline{z} \cdot \overline{r}_o \Delta\theta\Delta\overline{r}_o}{2} \overline{T}_{M,n,p}^h \tag{C.30}$$

For the inner copper boundary, the approach is similar except that there is no q_A term since there is no heat addition.

$$\begin{array}{l} K_{Cu} \left(\frac{T_{1,n,p}^{h+1} - T_{1,n,p-1}^{h+1}}{r_i \Delta\theta} \right) \Delta z \frac{\Delta r_i}{2} + K_{Cu} \left(\frac{T_{1,n,p}^{h+1} - T_{1,n,p+1}^{h+1}}{r_i \Delta\theta} \right) \Delta z \frac{\Delta r_i}{2} + K_{Cu} \left(\frac{T_{1,n,p}^{h+1} - T_{1,n-1,p}^{h+1}}{\Delta z} \right) r_i \Delta\theta \frac{\Delta r_i}{2} + \\ K_{Cu} \left(\frac{T_{1,n,p}^{h+1} - T_{1,n+1,p}^{h+1}}{\Delta z} \right) r_i \Delta\theta \frac{\Delta r_i}{2} + K_{Cu} \left(\frac{T_{1,n,p}^{h+1} - T_{2,n,p}^{h+1}}{\Delta r_i} \right) \left(r_i + \frac{\Delta r_i}{2} \right) \Delta\theta\Delta z + \rho C \frac{T_{1,n,p}^{h+1} - T_{1,n,p}^h}{\Delta t} \Delta z \frac{\Delta r_i}{2} r_i \Delta\theta = 0 \end{array} \tag{C.31}$$

Again, note that the volume term is actually $\Delta\theta\Delta z \left[\frac{r_i \Delta r_i}{2} - \frac{(\Delta r_i)^2}{2} \right]$ and the area term in the z-direction is $\Delta\theta \left[\frac{r_i \Delta r_i}{2} - \frac{(\Delta r_i)^2}{2} \right]$. Rearranging to get an expression for each row $(1,n,p)$

$$\begin{array}{l} T_{1,n,p}^{h+1} \left(\frac{\Delta r_i \Delta z}{r_i \Delta\theta} + \frac{\Delta r_i \cdot r_i \Delta\theta}{\Delta z} + \frac{\left(r_i + \frac{\Delta r_i}{2}\right)\Delta\theta\Delta z}{\Delta r} + \frac{\rho C}{K_{Cu} \Delta t} \frac{\Delta z \cdot r_i \Delta\theta\Delta r_i}{2} \right) + \\ T_{2,n,p}^{h+1} \left(-\frac{\left(r_i + \frac{\Delta r_i}{2}\right)\Delta\theta\Delta z}{\Delta r_i} \right) + T_{1,n,p-1}^{h+1} \left(-\frac{\Delta r_i \Delta z}{2 r_i \Delta\theta} \right) + T_{1,n,p+1}^{h+1} \left(-\frac{\Delta r_i \Delta z}{2 r_i \Delta\theta} \right) + \\ T_{1,n-1,p}^{h+1} \left(-\frac{\Delta r_i \cdot r_i \Delta\theta}{2\Delta z} \right) + T_{1,n+1,p}^{h+1} \left(-\frac{\Delta r_i \cdot r_i \Delta\theta}{2\Delta z} \right) = \frac{\rho C}{K_{Cu} \Delta t} \frac{\Delta z \Delta r_i \cdot r_i \Delta\theta}{2} T_{1,n,p}^h \end{array} \tag{C.32}$$

Nondimensionalizing each side,

$$LHS = \frac{T_D r_D \cdot \cancel{K_D}}{\cancel{K_D}} \left[\begin{array}{l} \overline{T}^{h+1}_{1,n,p} \left(\frac{\Delta\overline{r}_i \Delta\overline{z}_o}{\overline{r}_i \Delta\theta} + \frac{\Delta\overline{r}_i \cdot \overline{r}_i \Delta\theta_o}{\Delta\overline{z}} + \frac{\left(\overline{r}_i + \frac{\Delta\overline{r}_i}{2}\right)\Delta\theta\Delta\overline{z}}{\Delta\overline{r}_i} + \frac{\rho C}{\overline{K}_{Cu}\Delta t} \frac{\Delta\overline{z} \cdot \overline{r}_i \Delta\theta\Delta\overline{r}_i}{2} \frac{r_D^2}{K_D} \right) \\ + \overline{T}^{h+1}_{2,n,p} \left(- \frac{\left(\overline{r}_i + \frac{\Delta\overline{r}_i}{2}\right)\Delta\theta\Delta\overline{z}}{\Delta\overline{r}_i} \right) + \overline{T}^{h+1}_{2,n,p-1} \left(- \frac{\Delta\overline{r}_i \Delta\overline{z}}{2\overline{r}_i \Delta\theta} \right) + \\ \overline{T}^{h+1}_{2,n,p+1} \left(- \frac{\Delta\overline{r}_i \Delta\overline{z}}{2\overline{r}_i \Delta\theta} \right) + \overline{T}^{h+1}_{2,n-1,p} \left(- \frac{\Delta\overline{r}_i \cdot \overline{r}_i \Delta\theta}{2\Delta\overline{z}} \right) + \overline{T}^{h+1}_{2,n+1,p} \left(- \frac{\Delta\overline{r}_i \cdot \overline{r}_i \Delta\theta_o}{2\Delta\overline{z}} \right) \end{array} \right] \tag{C.33}$$

$$RHS = \frac{\rho C}{\overline{K}_{Cu}\Delta t} \frac{\Delta\overline{z} \cdot \overline{r}_i \Delta\theta\Delta\overline{r}_i}{2} \overline{T}^{h}_{1,n,p} \cdot \frac{T_D r_D^3}{K_D}$$

The CVA for the inner boundary is actually implemented in Matlab code as

$$LHS = \left[\begin{array}{l} \overline{T}^{h+1}_{1,n,p} \left(\overline{K}_{Cu} \frac{\Delta\overline{r}_i \Delta\overline{z}_o}{\overline{r}_i \Delta\theta} + \overline{K}_{Cu} \frac{\Delta\overline{r}_i \cdot \overline{r}_i \Delta\theta_o}{\Delta\overline{z}} + \overline{K}_{Cu} \frac{\left(\overline{r}_i + \frac{\Delta\overline{r}_i}{2}\right)\Delta\theta\Delta\overline{z}}{\Delta\overline{r}_i} + \alpha \frac{\Delta\overline{z} \cdot \overline{r}_i \Delta\theta\Delta\overline{r}_i}{2} \right) \\ + \overline{T}^{h+1}_{2,n,p} \left(-\overline{K}_{Cu} \frac{\left(\overline{r}_i + \frac{\Delta\overline{r}_i}{2}\right)\Delta\theta\Delta\overline{z}}{\Delta\overline{r}_i} \right) + \overline{T}^{h+1}_{1,n,p-1} \left(-\overline{K}_{Cu} \frac{\Delta\overline{r}_i \Delta\overline{z}}{2\overline{r}_i \Delta\theta} \right) + \\ \overline{T}^{h+1}_{1,n,p+1} \left(-\overline{K}_{Cu} \frac{\Delta\overline{r}_i \Delta\overline{z}}{2\overline{r}_i \Delta\theta} \right) + \overline{T}^{h+1}_{1,n-1,p} \left(-\overline{K}_{Cu} \frac{\Delta\overline{r}_i \cdot \overline{r}_i \Delta\theta}{2\Delta\overline{z}} \right) + \overline{T}^{h+1}_{1,n+1,p} \left(-\overline{K}_{Cu} \frac{\Delta\overline{r}_i \cdot \overline{r}_i \Delta\theta_o}{2\Delta\overline{z}} \right) \end{array} \right] \tag{C.34}$$

$$RHS = \left(\frac{\rho C}{\Delta t} \frac{r_D^2}{K_D} \right) \frac{\Delta\overline{z} \cdot \overline{r}_i \Delta\theta\Delta\overline{r}_i}{2} \overline{T}^{h}_{1,n,p} = \alpha \frac{\Delta\overline{z} \cdot \overline{r}_i \Delta\theta\Delta\overline{r}_i}{2} \overline{T}^{h}_{1,n,p}$$

An alternative method for the inner boundary was to forward difference in the *r*-direction, which is more akin to the differential approach. Using 2nd order forward difference in *r* and 2nd order central difference in *z* and *θ*, Laplace's equation with heat capacitance is

$$\begin{array}{l} \frac{2T^{h+1}_{1,n,p} - 5T^{h+1}_{2,n,p} + 4T^{h+1}_{3,n,p} - T^{h+1}_{4,n,p}}{(\Delta r_i)^2} + \frac{1}{r_i} \frac{-3T^{h+1}_{1,n,p} + 4T^{h+1}_{2,n,p} - T^{h+1}_{3,n,p}}{2\Delta r_i} + \\ \frac{1}{r_i^2} \frac{T^{h+1}_{1,n,p-1} - 2T^{h+1}_{1,n,p} + T^{h+1}_{1,n,p+1}}{(\Delta\theta)^2} + \frac{T^{h+1}_{1,n-1,p} - 2T^{h+1}_{1,n,p} + T^{h+1}_{1,n+1,p}}{(\Delta z)^2} + \frac{\rho C}{K_{Cu}} \frac{T^{h+1}_{1,n,p} - T^{h}_{1,n,p}}{\Delta t} = 0 \end{array} \tag{C.35}$$

Non-dimensionalizing and rewriting the expression for each row (*1,n,p*),

$$\begin{gathered}
\overline{T}_{1,n,p}^{h+1}\left(\frac{2}{\left(\Delta\overline{r}_i\right)^2}-\frac{3}{2\overline{r}_i\Delta\overline{r}_i}-\frac{2}{\overline{r}_i^{\,2}\left(\Delta\theta\right)^2}-\frac{2}{\left(\Delta\overline{z}\right)^2}+\frac{\rho C}{\overline{K}_{Cu}\Delta t}\cdot\frac{r_D^2}{K_D}\right)+\overline{T}_{2,n,p}^{h+1}\left(\frac{-5}{\left(\Delta\overline{r}_i\right)^2}+\frac{2}{2\overline{r}_i\Delta\overline{r}_i}\right)+\\
\overline{T}_{3,n,p}^{h+1}\left(\frac{4}{\left(\Delta\overline{r}_i\right)^2}-\frac{1}{2\overline{r}_i\Delta\overline{r}_i}\right)+\overline{T}_{4,n,p}^{h+1}\left(-\frac{1}{\left(\Delta\overline{r}_i\right)^2}\right)+\overline{T}_{1,n,p-1}^{h+1}\left(\frac{1}{\overline{r}_i^{\,2}\left(\Delta\theta\right)^2}\right)+\overline{T}_{1,n,p+1}^{h+1}\left(\frac{1}{\overline{r}_i^{\,2}\left(\Delta\theta\right)^2}\right)+\\
\overline{T}_{1,n-1,p}^{h+1}\left(\frac{1}{\left(\Delta\overline{z}\right)^2}\right)+\overline{T}_{1,n+1,p}^{h+1}\left(\frac{1}{\left(\Delta\overline{z}\right)^2}\right)=-\frac{\rho C}{\overline{K}_{Cu}\Delta t}\overline{T}_{1,n,p}^{h}\cdot\frac{r_D^2}{K_D}\\
\overline{T}_{1,n,p}^{h+1}\left(\frac{2K_{Cu}}{\left(\Delta\overline{r}_i\right)^2}-\frac{3K_{Cu}}{2\overline{r}_i\Delta\overline{r}_i}-\frac{2K_{Cu}}{\overline{r}_i^{\,2}\left(\Delta\theta\right)^2}-\frac{2K_{Cu}}{\left(\Delta\overline{z}\right)^2}+\alpha\right)+\overline{T}_{2,n,p}^{h+1}K_{Cu}\left(\frac{-5}{\left(\Delta\overline{r}_i\right)^2}+\frac{2}{2\overline{r}_i\Delta\overline{r}_i}\right)+\\
\overline{T}_{3,n,p}^{h+1}K_{Cu}\left(\frac{4}{\left(\Delta\overline{r}_i\right)^2}-\frac{1}{2\overline{r}_i\Delta\overline{r}_i}\right)+\overline{T}_{4,n,p}^{h+1}\left(-\frac{K_{Cu}}{\left(\Delta\overline{r}_i\right)^2}\right)+\overline{T}_{1,n,p-1}^{h+1}\left(\frac{K_{Cu}}{\overline{r}_i^{\,2}\left(\Delta\theta\right)^2}\right)+\overline{T}_{1,n,p+1}^{h+1}\left(\frac{K_{Cu}}{\overline{r}_i^{\,2}\left(\Delta\theta\right)^2}\right)+\\
\overline{T}_{1,n-1,p}^{h+1}\left(\frac{K_{Cu}}{\left(\Delta\overline{z}\right)^2}\right)+\overline{T}_{1,n+1,p}^{h+1}\left(\frac{K_{Cu}}{\left(\Delta\overline{z}\right)^2}\right)=\alpha\overline{T}_{1,n,p}^{h}
\end{gathered}\tag{C.36}$$

Now that the boundary conditions have been described so that they can be put into the $Ax = b$ form, the final piece is the interface layers.

C.3.4 Interface Layers

At the interface between the copper and the MLI, $\nabla^2 T$ using a constant thermal conductivity K is not applicable since there are two different materials at the boundary. Forward differencing at r_{I+1}, then backward differencing at r_I leaves the copper and MLI layers uncoupled, so this is also not a solution. As a solution, thermal resistances are used to create an "interface layer." The thermal resistance in series, R_s, models the interface between the copper and the MLI in the radial direction

$$R_s = R_{Cu} + R_{MLI,\theta}\tag{C.37}$$

This thermal resistance is dominated by the MLI. The thermal resistance in parallel, R_p, models the interface between the copper and MLI along the shields in the z and θ directions.

$$\frac{1}{R_p}=\frac{1}{R_{Cu}}+\frac{1}{R_{MLI,r}}\tag{C.38}$$

This thermal resistance is dominated by the copper. The procedure for creating the A matrix remains the same as for the MLI interfaces however with a different thermal conductivity. Since this basic procedure has been reviewed earlier it is omitted here for brevity.

The final modification to the $Ax = b$ form is to add a term for the cryocooler. The cryocooler temperature, for example at $T(I,1,1)$ is a known temperature and can be removed from the T-vector and the corresponding rows and columns of the A matrix and b-vector. Now the temperature for the copper-MLI system can be solved for. Earlier in Chapter 3 it was shown that the 3D FDM matches with the 1D FDM. While further validation for the FDM is recommended for future work, the framework for the system has been laid out in this Appendix. Since the 1D FDM was a sufficient tool for this thesis, the author anticipates that the analysis for the 3D FDM can be used in a future multilayer finite differencing scheme.

C.4 3D Analytic Model

A 3-D analytic model in cylindrical coordinates (r, θ, z) has been developed for the temperature distribution for the coil system. Both the thermally conductive jacket and the MLI are modeled forming a two-layer model for a coil with length, l. The function for the temperature distribution has the following form consisting of Bessel functions (I_n, K_n) and sinusoids:

$$\begin{aligned} T(r,\theta,z) = {} & \sum_{m=1}^{\infty}\sum_{n=1}^{\infty}\left(A_{mn} I_n\left(\tfrac{m\pi}{l} r\right) + B_{mn} K_n\left(\tfrac{m\pi}{l} r\right)\right)\cos n\theta \cos(\tfrac{m\pi}{l} z) \\ & + \sum_{m=1}^{\infty}\left(C_m I_n\left(\tfrac{m\pi}{l} r\right) + D_m K_n\left(\tfrac{m\pi}{l} r\right)\right)\cos(\tfrac{m\pi}{l} z) \\ & + \sum_{n=1}^{\infty}\left(E_n r^n + F_n r^{-n}\right)\cos n\theta + G \log r + H \end{aligned} \tag{C.39}$$

where the constants (A through H) are solved for by applying orthogonality and the boundary conditions. Some references that were useful in the analysis includes work by Hildebrand [85], Ozisik [86], and Carslaw [87]. The boundary condition given at the outer MLI layer is a linearized form of the radiation from the chamber wall and from the coil itself radiating outwards. At the inner copper layer, the cryocooler was modeled to extract heat from a small segment of the coil. The analytic model determined that MLI is a promising insulation material. It also showed that a simple conductor may not be sufficient as the thermal jacket around the HTS, because it exhibits a large temperature spread away from the cryocooler. Placing multiple cryocoolers along the coil is a possible solution, but comes with mass and power penalties. The limitations of the analytic model were that it contained a linearized radiation approximation and did not model the anisotropic properties of the MLI. For these properties, the finite difference model was used.

C.5 Minimum Mean Square Error

In order to match the finite difference model with the experimental data to determine ε_t, the minimum Mean Square Error (MSE) is calculated. For n number of data points, this is given by

$$\mathrm{MSE} = \frac{1}{n}\sum_{i=1}^{n}\left(T_{\mathrm{model},i} - T_{\mathrm{data},i}\right)^2 \qquad \text{(C.40)}$$

A summary of the MSE calculations for the copper TCJ without MLI examined in Chapter 3 are shown in Table C.2. In this case, an ε_t = 0.2 was the minimum MSE case and was used by the FDM.

Table C.2 ε_t and MSE for the copper TCJ without MLI

ε_t	MSE
0.15	88.7
0.17	69.6
0.18	64.6
0.19	62.2
0.20	62.1
0.21	64
0.22	67.6
0.23	72.8
0.25	87

In the case for the copper TCJ with MLI, there were a few modifications to the MSE calculation in order to obtain an ε_t = 0.021 to avoid biasing the results from duplicate temperature measurements or outlier data. Therefore, the temperature data at x = 0.73 m away from the condenser was excluded from the MSE calculation. The duplicate thermocouple measurements at x = 1.1 m and x = 1.47 m away from the condenser were averaged together to use as a single measurement in the MSE calculation.

For the straight heat pipe, the minimum MSE approximate was not considered. Future work should consider running the straight heat pipe without working fluid to obtain a more accurate model for ε_t. For example if ε_t = 0.57, the heat from the chamber absorbed by an isothermal pipe at 80 K is 26.7 W. While very small differences in ε_t may not change, a 12% change, such as a previous example, could lead to a 14% change in heat from the chamber walls.

MSE calculations for circular heat pipe are summarized in Table C.3. Here, the resulting ε_t was 0.28, which is close to the ε_t of 0.3 which was used in Chapter 5.

Table C.3 ε_t and MSE for the circular heat pipe

ε_t	MSE
0.27	15.1
0.28	15
0.29	16.1
0.30	18.3

Appendix D Heat Pipe

D.1 Vapor Pressure Calculation

The vapor pressure drop, ΔP_v, for laminar flow with full pressure recovery is given by [35]

$$\Delta P_v = \frac{8\mu_v L_{eff} Q_{\max}}{\rho \pi r_v^4 h_{fg}} \tag{D.1}$$

For the straight heat pipe fabricated in Chapter 4, the vapor pressure was ignored and the capillary pressure had to overcome the liquid pressure and gravitational head. The ratio between the liquid pressure and the capillary pressure is

$$\frac{\Delta P_l}{\Delta P_c} \simeq 0.8 \tag{D.2}$$

The capillary pressure is slightly greater than the liquid pressure and both quantities are approximately the same order of magnitude. However when comparing the vapor pressure with the capillary pressure, the vapor pressure is approximately five orders of magnitude less than the capillary pressure. The ratio between the vapor pressure and capillary pressure was determined to be

$$\frac{\Delta P_v}{\Delta P_c} \simeq 10^{-5} \tag{D.3}$$

Therefore, it is justified to ignore the vapor pressure drop when calculating the heat pipe power capacity.

D.2 Viscous Limit

The viscous limit occurs when viscous forces in the vapor flow dominate the vapor flow down the pipe. When this occurs, the pressure gradients within the vapor region are insufficient to generate vapor flow. The viscous limit is most often observed at low temperatures in cryogenic heat pipes, heat pipes with extremely long condensers, or during startup of heat pipes [72]. The expression for the viscous limit is given by

$$Q_{vis} = \frac{A_v r_v^2 h_{fg} \rho_v P_v}{16\mu_v L_{eff}} \tag{D.4}$$

where A_v is the cross-sectional area of the vapor space and P_v and ρ_v refer to the vapor pressure and vapor density at the evaporator end of the heat pipe. Assuming that the vapor properties are relatively constant throughout the length of the pipe, Q_{vis} for the straight heat pipe in Chapter 4 is approximately 10^9 W. This is much greater than the capillary limit and is not a concern for the design. A general criterion for avoiding the viscous limit given by Peterson [72] is

$$\frac{\Delta P_v}{P_v} < 0.1 \tag{D.5}$$

For the straight heat pipe the ratio of vapor pressure drop to vapor pressure is on the order of 10^{-8} and is significantly lower than the criterion in Equation (D.5).

D.3 Using COTS Screen Meshes

Since the wire mesh used to construct the heat pipe is obtained through a commercial vender it is useful to obtain information on the mesh characteristics from them. The goal of the exercise of investigating COTS meshes was to ascertain if they exhibited the same characteristics as those given by Mills and Reay from Table 4.2. Using data on a stainless steel mesh from TWP Inc [68], Figure D.1 shows the pore radius as a function of mesh number for the COTS mesh from TWP Inc, along with the mesh from Table 4.2. The line for the pore radius was generated from Equation (4.9). It is important to note that for some mesh numbers there are multiple types of screen available. Some have difference pore size and wire diameter.

The equation for permeability, κ, is given by

$$\kappa = \frac{d_w^2 \varepsilon^3}{122\left(1-\varepsilon_{void}\right)^2}; \qquad \varepsilon_{void} = 1 - \frac{1.05\pi N d_w}{4} \tag{D.6}$$

where ε_{void} is the void fraction of the mesh. For the COTS meshes, Figure D.2 shows ε_{void} and κ as a function of mesh number. The three red circles in the permeability plot are data from Mills in Table 4.2 and show that it correlates well with the COTS meshes.

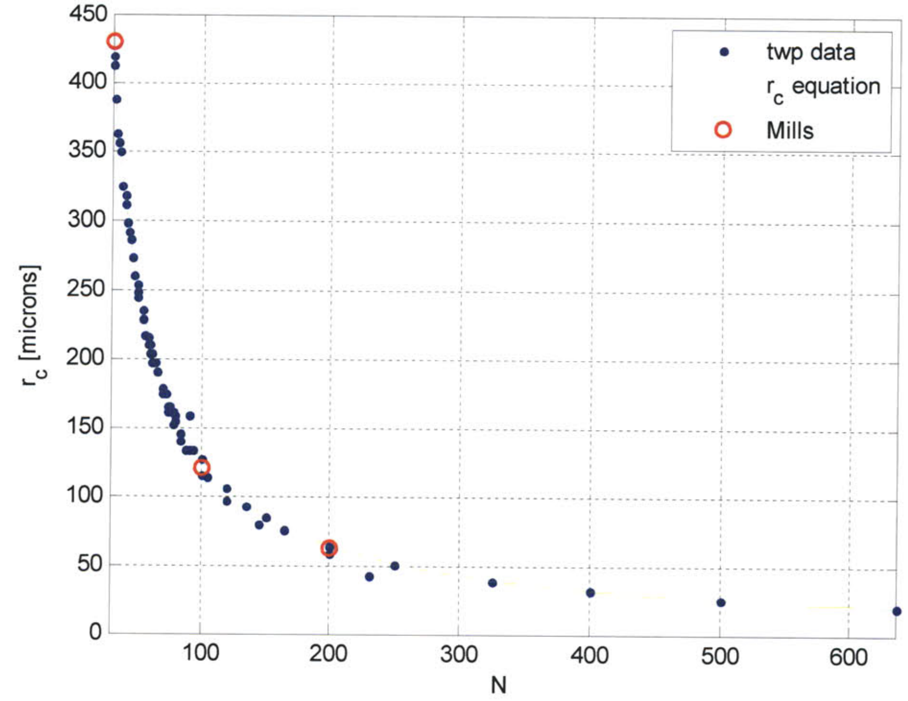

Figure D.1 Pore radius for various mesh number

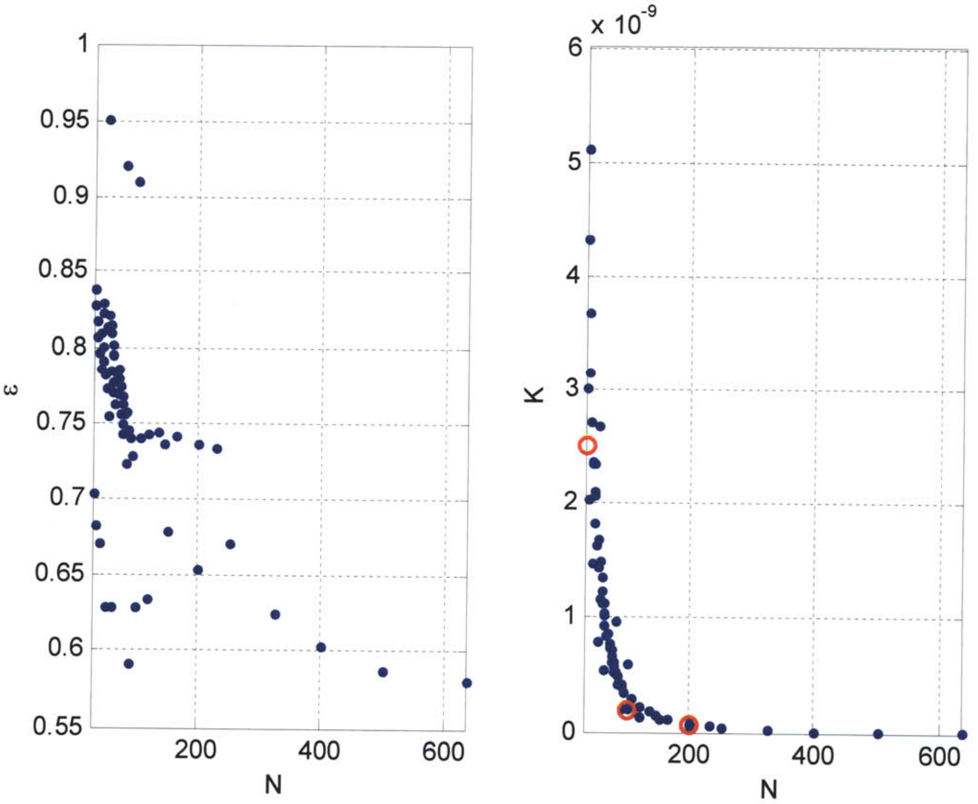

Figure D.2 Void fraction and permeability for various COTS mesh numbers

Using the COTS data for the mesh, the ratio of pore radius to permeability is shown in Figure D.3. Again the Mills data is shown by the red circles are correlates well with some COTS meshes.

The result for a single mesh heat pipe with four layers is shown in Figure D.4. The pipe diameter is 40 mm and the effective length is 1 m. It is concluded that the COTS meshes are similar and achieving a multiple mesh design analyzed in Section 4.2 (summarized in Table 4.3) is feasible.

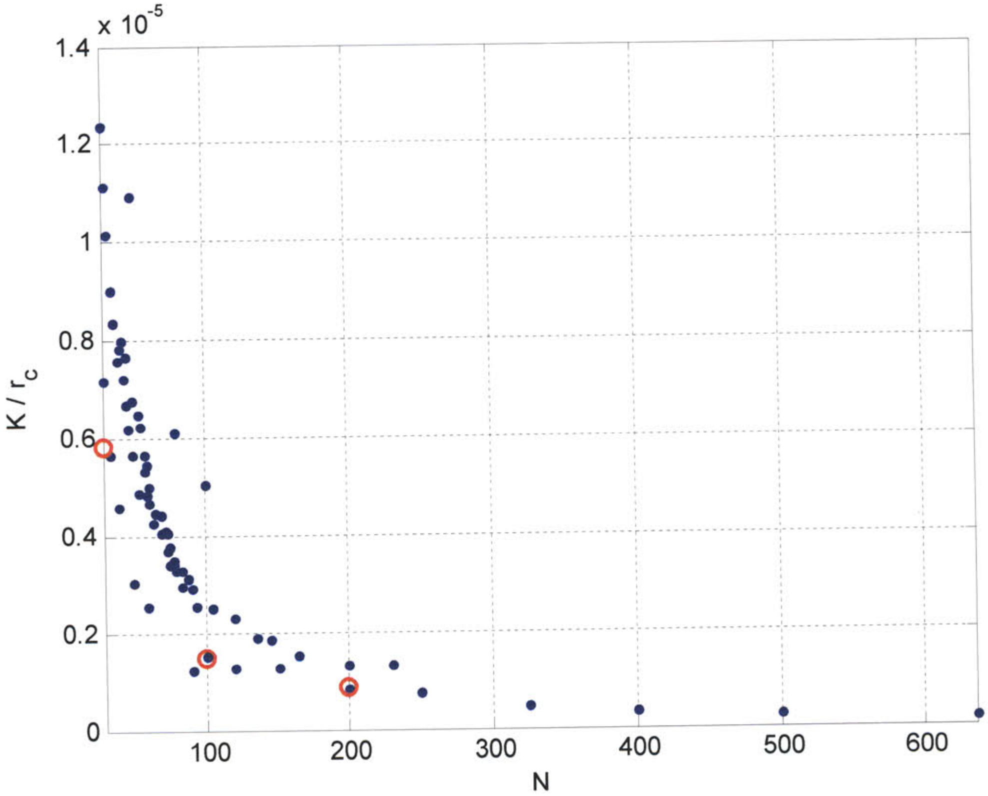

Figure D.3 Ratio of permeability to pore radius for COTS mesh

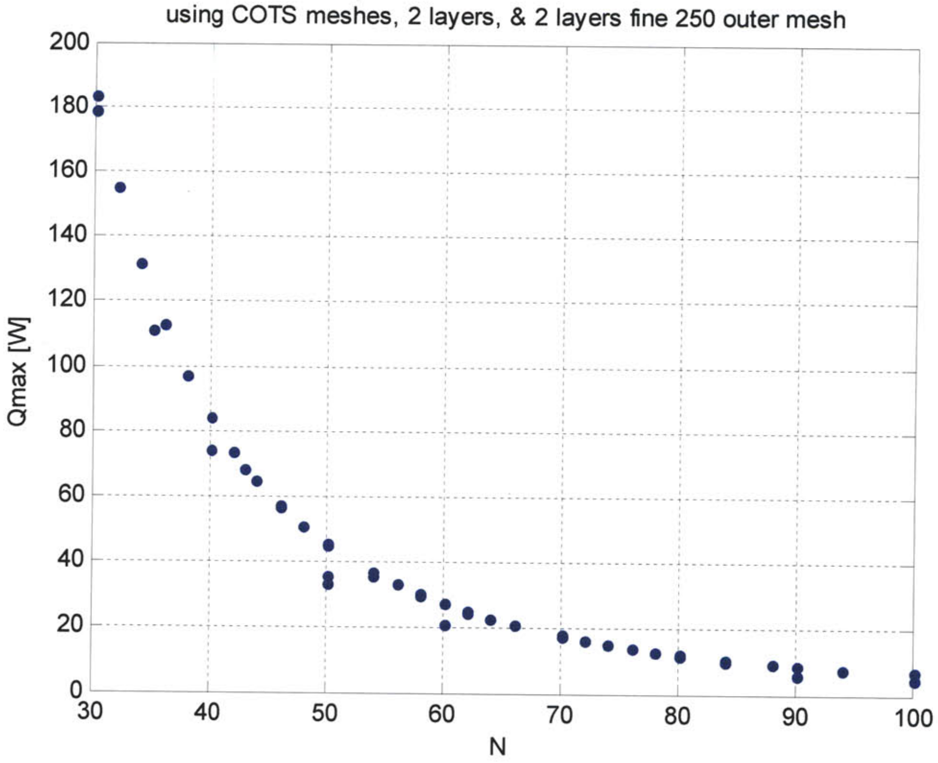

Figure D.4 Single mesh heat pipe, 4 layers, using COTS mesh, 1 m length, 40 mm diameter

In addition to determining the mesh number and number of layers, the material used for the mesh is another trade worth examining. A copper mesh is also available from vendors such as TWP Inc. Compared to a stainless steel mesh, a copper mesh exhibits a higher thermal conductivity and lower thermal resistance, which are more favorable thermal characteristics. The thermal resistance is related to the inverse of the thermal conductivity as $R \sim \frac{1}{K}$. The energy required to cool each material is also a second issue. The thermal conductivity and the specific heat for copper and stainless steel are given by

$$\begin{aligned} K_{\text{Cu}} &= 400 \ {}^{\text{W}}\!/_{\text{m}\cdot\text{K}} \quad K_{\text{SS}} = 15 \ {}^{\text{W}}\!/_{\text{m}\cdot\text{K}} \\ C_{\text{Cu}} &= 385 \ {}^{\text{J}}\!/_{\text{kg}\cdot\text{K}} \quad C_{\text{SS}} = 477 \ {}^{\text{J}}\!/_{\text{kg}\cdot\text{K}} \end{aligned} \tag{D.7}$$

For the size of the meshes used in the straight heat pipe, the thermal resistance of stainless steel mesh is approximately 27 times larger than the thermal resistance of a copper mesh. In addition, the energy required to cool a copper mesh is comparable to the stainless steel mesh, but slightly favors the copper mesh. Therefore, thermally the properties of copper are more favorable. However, the effect of pore sizes for stainless steel and copper meshes on the heat pipe performance is also worth investigating.

For a higher power capacity, a small pore size and large κ are favorable. For the COTS meshes, a copper mesh has a larger κ than the stainless steel meshes in general. More specifically, this is true for the #50 mesh, which is part of the design. So, the copper mesh is a more favorable coarse mesh material. However, very fine meshes do not exist commercially for a copper material. The finest mesh available is a #200 mesh. There is no #250 mesh number for a copper mesh. Therefore, stainless steel is a more favorable fine mesh material since it has a smaller r_c that allows for greater capillary pressure. This is especially true when comparing a copper #200 mesh with a stainless steel #250 mesh. Therefore, while the thermal properties of copper are more favorable, a stainless steel mesh is able to obtain a higher power capacity because of a finer mesh. While using multiple materials for a coarse and fine mesh is a possibility, it increases the complexity of the system and because of this was not chosen for the design of the heat pipe.

D.4 Flowmeter Testing

The flowmeter used to measure the amount of working fluid is an Omega FMA-1600A series. The flowmeter accounts for the temperature and pressure of the flow and outputs a volumetric flow rate, $\dot{Q}_f$ corrected to standard temperature and pressure (14.696 psi and 25°C). The Omega flowmeter was set to output $\dot{Q}_f$ in units of standard cubic centimeters per minute (sccm). The flowmeter is connected to a computer via RS-232 Serial cable. A Matlab program was developed to continuously read the flow rate and determine the total mass flow whenever working fluid is injected. The amount of mass measured during a single loop in the program was determined by

$$\Delta Mass = \dot{Q}_f \cdot \rho \cdot \Delta t \tag{D.8}$$

where the density of the gas, ρ, is at standard conditions, and Δt is the time for a single loop. By integrating mass for every time step, the cumulative mass can be determined.

A flowchart of the process to read the flowmeter is shown in Figure D.5. The flowmeter outputs the pressure, temperature, volumetric flowrate, and mass flowrate. In the Matlab code these quantities are "P, T, Vf, Mf" [sccm] respectively. The flowmeter can be set to constantly output data and Matlab reads the flowmeter data at each loop using the function stest.m, which reads in a block of data using Matlab's fscanf function. One example string is "+014.66 +027.32 +000.03 +000.02   N2 ". This is an exact character by character string including the spacing. The code checks for the 'N' character, then parses P, T, Vf, Mf, from the string respectively. In addition, the code records maximum flowrate, to let the user know if the maximum flowrate was breached. If this occurs, there could be measurement errors. The algorithm ends calculating the mass after a user defined maximum number of loops is reached. For reference, 700 loops takes approximately 40 seconds.

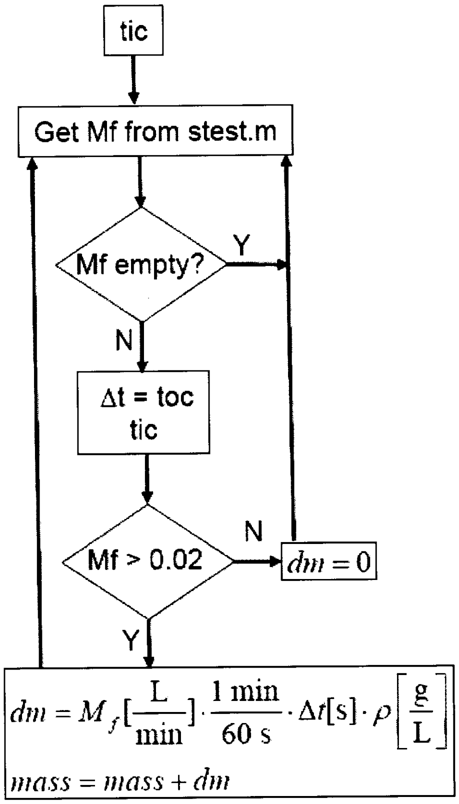

Figure D.5 Flowmeter algorithm flowchart

Two tests were conducted to validate the flowmeter system. First the circular heat pipe was filled with air at various pressures and this mass was measured. The amount of mass measured by the flowmeter was then compared to the theoretical amount of mass in the pipe according to the ideal gas law. Three different pressures were tested, each with multiple trials and the results are shown in Table D.1. For each of the cases, the flowmeter was within 1% of the theoretical mass. In addition, the flowmeter was found to have good repeatability, because the pipe under pressure was vented back to atmospheric conditions for each trial and this amount of air was also measured to be within 1%.

Table D.1 Testing the flowmeter accuracy by filling the circular heat pipe with air at various pressures

Pressure	# trials	Flowmeter	Actual	% error
20.2 psi	4	10.55 g	10.60 g	0.41%
24.7 psi	4	12.86 g	12.89 g	0.26%
30.3 psi	6	15.74 g	15.87 g	0.85%

A second test was conducted to test the flowmeter. This required filling up a small tank of CO_2. The amount of CO_2 filled was weighed using a postal scale and compared to the mass calculated by the flowmeter system. Comparison of these results is shown in Figure D.6. The flowmeter was also shown to be accurate with all trials having less than 3% difference with the weighed mass. The postal scale was sensitive to any vibrations or movement by the CO_2 filling station, which may have contributed to some of the errors. Overall, these tests have demonstrated confidence in the performance of the flowmeter system.

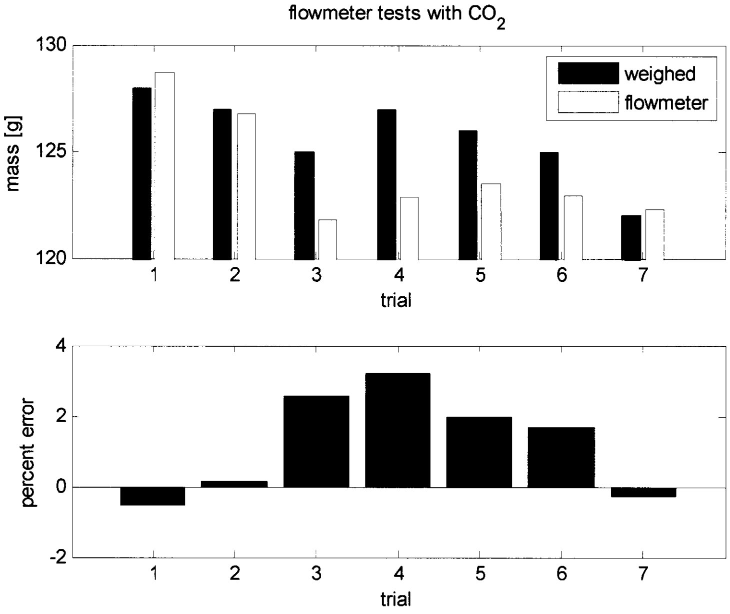

Figure D.6 Flowmeter calibration with CO_2 gas

D.5 Prototype Short Straight Heat Pipe with HTS

Before HTS wires were inserted into the straight heat pipe in Chapter 4, a short prototype system was built to practice the manufacturing process. A short copper pipe without a screen mesh and with an aluminum block with HTS wires were used. This system is shown in Figure D.7. Recall that the function of the aluminum block was to function thermally as a stack of HTS wires, and the HTS wires inserted into the block reached a superconducting state only after an entire 'stack' or in this case, the block was cold. The aluminum block was rectangular with a channel cut into it for the HTS wires. A longer section of the rectangular aluminum block shown in Figure D.7 was later cut into the cylindrical shape, with one inch diameter, that was used for the straight heat pipe in Chapter 4. This was because it was difficult to slide the rectangular block into a pipe that had a screen mesh without crunching the mesh. For the prototype system, the copper pipe was approximately 10 cm long. Two HTS wires are insulated with Kapton tape on both sides to prevent electrical contact with the aluminum or copper. Similar to the system described in Chapter 4, the HTS wires were tied at one end and fed out of the pipe via electrical connectors with a copper bus.

Figure D.7 Prototype copper pipe with HTS wires inside aluminum block

One of the objectives of the prototype system was to ensure that the HTS could be inserted without any damage. The first challenge was ensuring the HTS wires were not bent too much while sliding the copper cap on. The following were the steps taken to seal the HTS into the pipe.

1. Connect HTS to copper bus using screw connectors
2. Slide copper pipe cap onto copper bus to obtain a 'loose connection' (it is not really connected)
3. Check conductivity
4. Slide aluminum bar assembly into pipe
5. Solder cap, while taking temperature data
6. Slide Teflon on copper bus and tighten Swagelok fittings

The second major challenge was to solder the cap on without damaging the HTS wire, since the wire can delaminate at temperatures greater than 300°F and be destroyed. This is why the Teflon and Swagelok fitting are not inserted until after the cap is soldered. There is an air gap that exists between the copper bus and the Swagelok that can be used for cooling. The prototype system also had a single gas line to mimic the function of the N_2 gas feed. This feed was then connected to lab vacuum to suck air in through the gap to keep the HTS wires cool. A thermocouple also resided in the air gap to measure the temperature. The temperature measured while soldering on the cap is shown in Figure D.8. The cap took approximately 150 seconds to solder on and the peak air temperature was always less than 300°F.

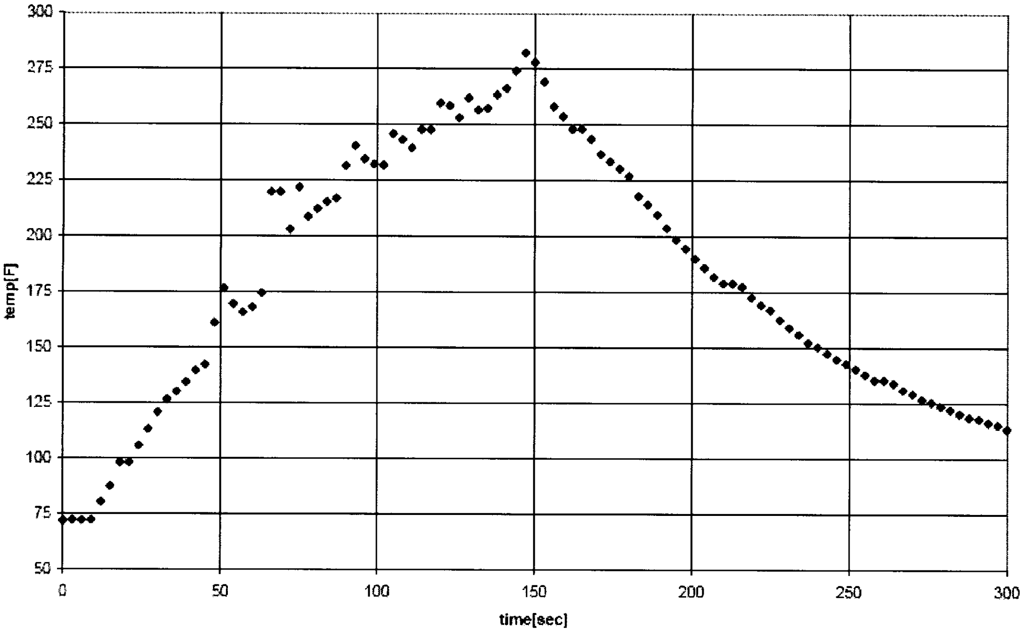

Figure D.8 Temperature near HTS wires while soldering on copper pipe cap

After the copper cap was soldered on, the pipe was pressurized using lab air. They system held a constant pressure of 61 psi. To make sure the superconductor was intact, the entire pipe was dunked into LN2 and the resistance of the HTS wire was measured using the same Wheatstone bridge from Chapter 4. This system measured the expected drop in resistance for the HTS wires and proved that the soldering process safely seals on the copper cap.

In addition to laying out the procedure for HTS insertion, there were several lessons learned from the prototype short straight heat pipe. Soldering on the copper cap in a rapid amount of time while still ensuring a leak tight bond was formed was a difficult process. The actual cap took three tries to attach and the last two already had the Teflon over the copper bus. It is advised for future processes to solder on the cap on a single try because taking off a partially soldered cap is extremely difficult. For the straight heat pipe without the HTS wire in Chapter 4 the hole for the N_2 gas feed was through a section where the copper cap and pipe overlapped. Since attempting to solder on a copper cap, dealing with the N_2 gas feed, and the HTS wires is difficult, the straight heat pipe with HTS placed the N_2 gas feed slightly away from the copper cap. This separated alignment of the gas feed and the HTS wires with the copper cap and simplified the process because there were fewer things to solder simultaneously. In addition to minimizing the bending of the HTS wires, the distance between the end of the aluminum block and the copper bus was increased for the final version.

D.6 Equipment List

The following is a brief list of the equipment that may be needed for a future flight heat pipe, recommended by Faghri [77]. Some of this equipment includes: a leak detector, welding equipment, filling equipment, coil springs, and release values.

The leak detector is used to determine the quality of the welds. The procedure for detecting leaks is to apply a vacuum to the heat pipe and connect a mass spectrometer to one end. By passing small amounts of Helium gas via a hypodermic needle, the mass spectrometer can determine if any He enters the pipe through leaks.

Argon arc welding is recommended for a copper container. The advantage of using welding over soldering is that no flux is required keeping the inside of the pipe clean and free of contamination. Filling can be accomplished by a attaching a small diameter tube to an end cap. A coil spring is used to maintain contact between the mesh and the container wall. Close contact between the wall and mesh is necessary to avoid local hot spots from occurring. For the multi-mesh type design, at the ends of the pipe the fine mesh should be wrapped around the end of the coarse mesh to ensure that the liquid layer is maintained in the wick structure. This is because the liquid-vapor interface occurs in the fine mesh for maximum capillary rise. For the heat pipe built in this research, coil springs were not used. The fine #250 mesh does not tend to open up a significant amount. However, if the screen is inserted without much handling, the mesh maintained good contact with the walls. The fine #250 mesh tends to conform to small rolled up radius smaller than the pipe cross-section if the fine mesh is handled too much. Therefore, it is important to insert the screen on the first attempt, if possible.

D.7 Effect of wetting angle

In Chapter 4, the analysis for the heat pipe power capacity assumed the maximum wetting angle or contact angle in the model for the capillary pressure (Equation (4.2)). In reality, the most favorable wetting angle may occur. More detailed modeling on capillary forces and contact angles are examined in Israelachvili [88]. The capillary pressure as a function of contact angle for the #250 mesh with nitrogen is shown in Figure D.9. The % reduction in ΔP_c compared to the maximum ΔP_c ($\theta = 0°$) is also shown in Figure D.9.

One topic for future heat pipe modeling is to measure and incorporate a more accurate wetting angle. In addition, calibration of the mesh pore size r_c, κ is important so that known quantities can be used instead of values either deduced or calculated from a specification sheet.

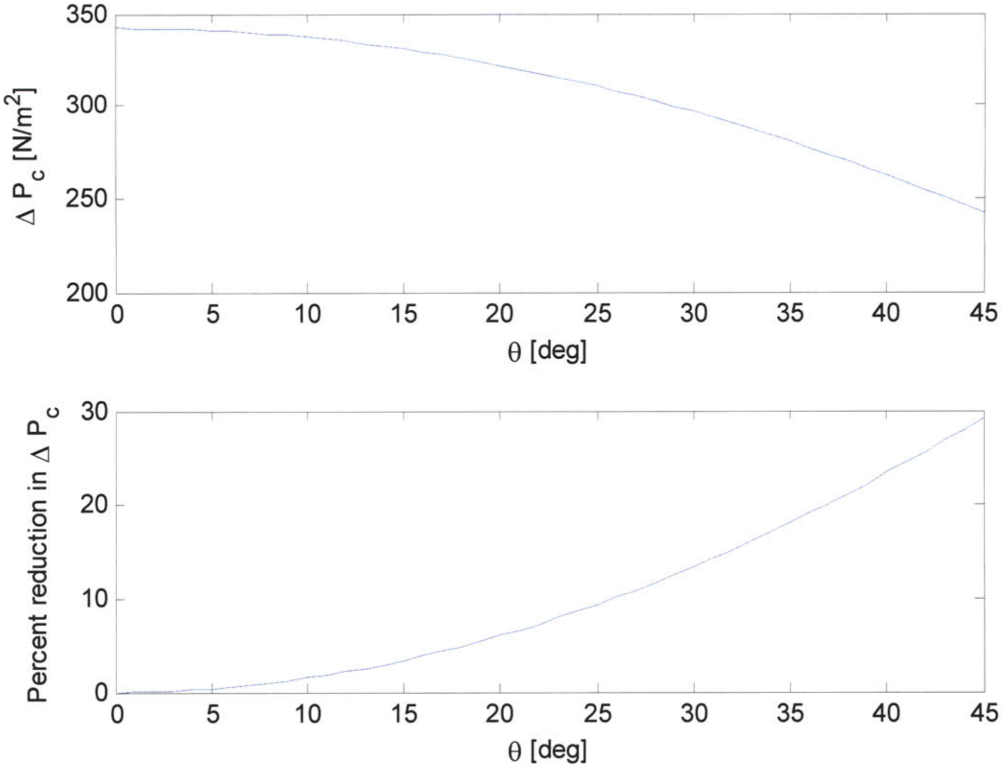

Figure D.9 Change in capillary pressure as a function of wetting angle

D.8 Maximum EMFF Rotation Rate

For the heat pipe operating in space there is no gravitation pressure head that the capillary pressure must overcome. However, there are other possible sources of pressure which could lead to heat pipe failure, given insufficient capillary pumping pressure. One possible failure scenario is if the EMFF vehicle is rotating at a fast enough rate to induce dryout of the wick. This scenario is shown in Figure D.10. In this case, the cryocooler is located at the axis of rotation. The possible location for dryout due to rotation of the vehicle may occur $\pi/2$ radians away from the cryocooler.

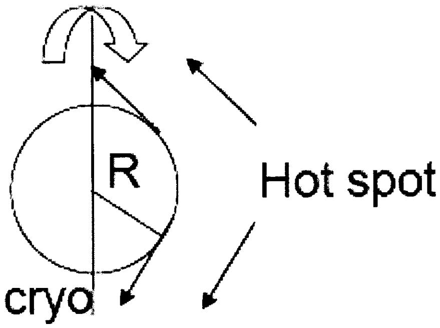

Figure D.10 Sketch of the effects of a rotation for an EMFF coil

In this scenario, the capillary pressure must overcome the liquid pressure drop and effect of the rotation, assuming negligible amount of vapor pressure drop

$$\Delta P_c = \Delta P_l + \Delta P_{rotation} \tag{D.9}$$

Using Equation (D.2), Equation (D.9) can be simplified so that the capillary pressure must overcome the acceleration, g, of the working fluid in the wick caused by rotation.

$$\Delta P_c - \Delta P_l \cong 0.2\Delta P_c = \rho g h \tag{D.10}$$

This simple model assumes a column of liquid the entire length of the wick. Solving the acceleration necessary to dry out the wick is given by

$$g = 0.2\frac{2\sigma}{r_c}\frac{1}{\rho h} \tag{D.11}$$

In this case, the maximum acceleration in the direction along the wick at h occurs approximately three quarters of the way away from the cryocooler at $3\pi R/4$ away. The maximum rotation rate can be determined by solving for ω in:

$$g = \omega^2 R_{\text{max g's}} \tag{D.12}$$

The maximum rotation rate is shown in Figure D.11 as a function of COTS screen meshes. In general, the maximum rotation rate given by this simple analysis is on the order of one revolution per minute. For the circular heat pipe designed in Chapter 5, using a #250 fine mesh, the maximum rotation rate is approximately 1.5 revolutions per minute.

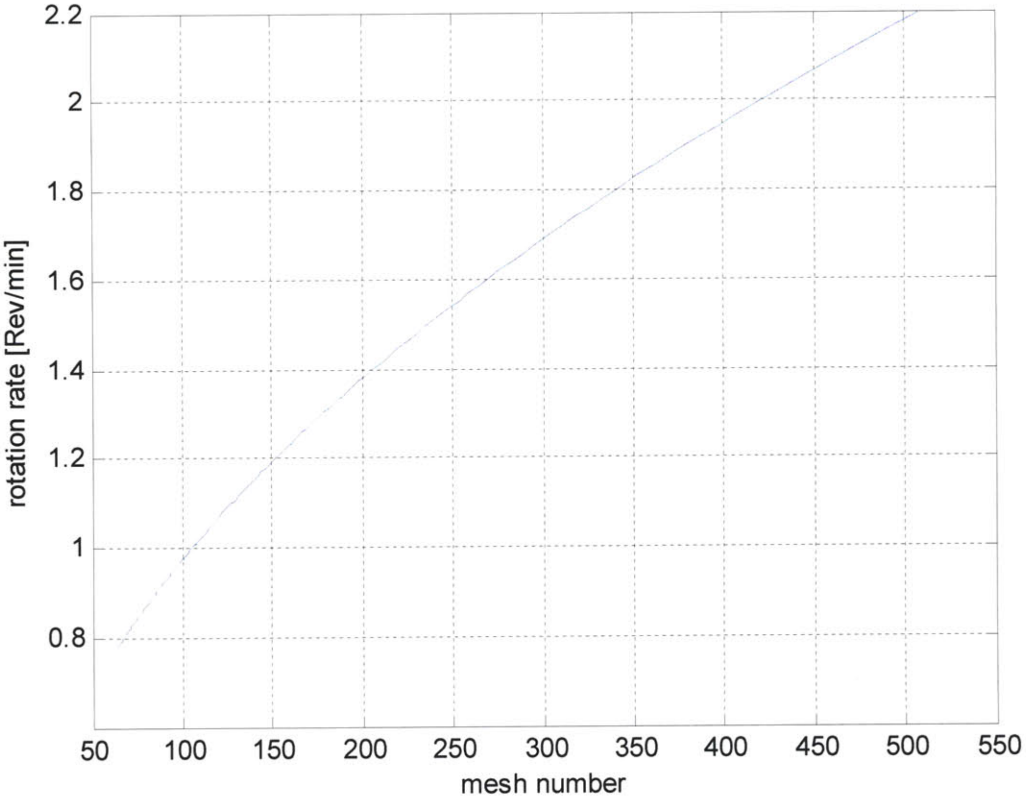

Figure D.11 Maximum allowable rotation rate for EMFF vehicle as a function of mesh number

Appendix E Improving HTS Performance

The HTS wire critical current density, I_c, varies according to the temperature and magnetic field. This variation for the COTS wires from American Superconductor is shown in Figure 4.40. On the y-axis is the critical current normalized by the critical current at 77 K, with no magnetic field. On the x-axis is the magnetic field. The family of curves in Figure 4.40 varies with temperature. Notice that as magnetic field increases, the critical current compared to the critical current with no field, decreases. Decreasing the temperature increases the critical current density. The following function is defined to describe the variation in I_c due to the temperature and magnetic field.

$$\eta_I = \frac{I_c}{I_c(77\text{K, no field})} \tag{E.1}$$

For EMFF, a single HTS wire is wrapped into a coil that has n-number of turns. Figure E.1 illustrates a cross-sectional cut of the coil. For simplicity the wire is approximated as a line current. Each line current produces a magnetic field, which affects the other wires. For example, the field that the top wire in the stack, called wire 1, sees from wire 2 is approximated as parallel to the surface of wire 1, using the line current approximation. In fact, all wires in the stack affect wire 1. The total magnetic field due to n turns is given as

$$B_n = \frac{\mu_o}{2\pi}\sum_{j=2}^{n}\frac{i_j}{(j-1)r} \tag{E.2}$$

It is the wires at the end of the stack that experience the maximum amount of magnetic field, and thus limit the critical current. In the testbed the HTS stack has 33 turns, which results in a maximum magnetic field of

$$B_{33} = 0.1958 \text{ Tesla} \tag{E.3}$$

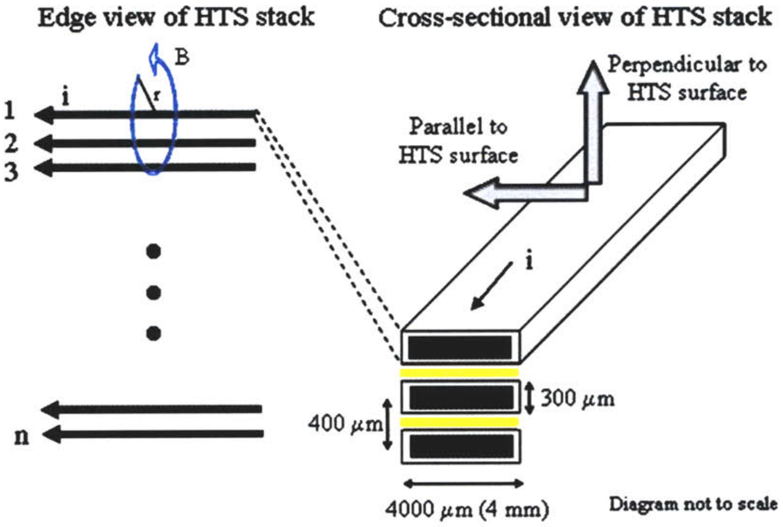

Figure E.1 Geometry of HTS coil turns

The testbed coils, shown in Figure D.2, are actually three stacks of 33 turns each. The perpendicular magnetic field seen by the top wire on the stack from neighboring stacks also acts to reduce the current. This is given by

$$B_{\perp} = \frac{\mu_o i}{2\pi r} = \frac{4\pi \cdot 10^{-7} \cdot 95}{2\pi \cdot 0.0125} = 0.00152 \text{ Tesla} \tag{E.4}$$

The perpendicular field is a higher order effect and can effectively be ignored if the neighboring stack is far enough away.

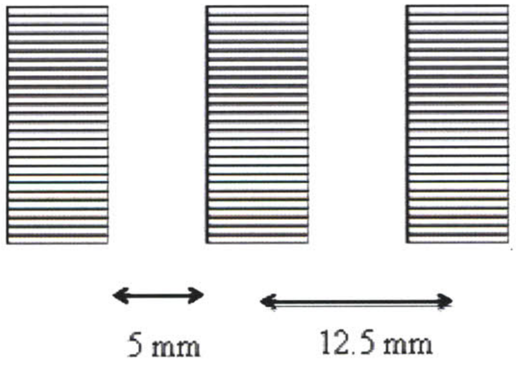

Figure E.2 HTS wire stacks for the MIT-SSL EMFF testbed

In the testbed, the maximum observed current was 95 A at 77 K. The theoretical maximum current is 115 A for a 100 m wire length [8]. This yields a reduction to approximately 83% of the value for no magnetic field.

$$\frac{I_{(\text{B-field})}}{I_{(\text{no B-field})}} = \frac{95\text{ A}}{115\text{ A}} \rightarrow \eta_I = 0.83 \tag{E.5}$$

The analysis so far is a summary of research conducted by Kwon [5] on the characterization of the HTS wires stacks due to magnetic fields. In order to improve the performance of the HTS coil, the HTS stack design can be modified to reduce the effect of magnetic field. A toroidal stack configuration shown in Figure E.3 has the potential to accomplish this. Shown is the cross-sectional area of the toroidal stack. The toroidal minor radius is *r*, and the major radius is R_c (not shown). The cross-section of some individual HTS wires is shown in Figure E.3. The wires wrap around the major radius of the toroidal. Neighboring wires are shown next to each other in Figure E.3. The toroidal stack configuration still produces the same magnetic moment as an equivalently designed stack based on the testbed.

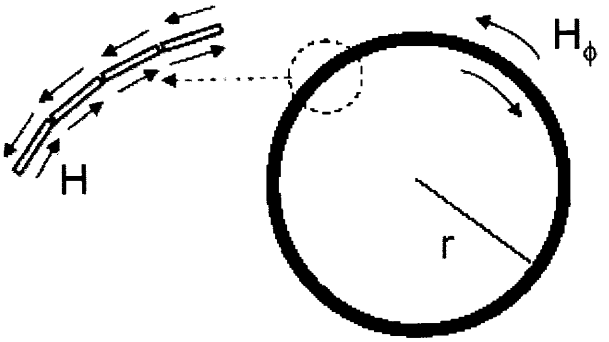

Figure E.3 Toroidal stack design

In the toroidal stack, the radial magnetic field components for neighboring wires cancel each other out. Therefore, there is no perpendicular field that is seen by the wires. The ϕ components of the magnetic field of neighboring wires add together. This total magnetic field, Bϕ is parallel to the wires. The reduction in performance due to the parallel field is less than the effect of the perpendicular field. Therefore, the toroidal stack design is an improvement compared to the EMFF testbed stacks. In order to determine the magnetic field, Ampere's law from Maxwell's equations can be applied [89].

$$\oint_L H \cdot dl = \int_S J_f \cdot dS + \frac{d}{dt}\int_S D \cdot dS \tag{E.6}$$

The magnetic field is then a function of the enclosed current, I_{enc}, assuming there is no time changing displacement field, *D*. In order to increase the magnetic field produced by a coil, but keeping a toroidal minor radius constant, additional layers of wire can be laid around the minor radius. Additional layers of wire will act to reduce the total current because neighboring layers will see the magnetic field from neighboring layers. To calculate this effect, Equation (E.6) is applied to a single layer toroidal stack with 100 turns and 100 amps.

$$B_\phi = \frac{\mu_o I_{enc}}{2\pi r} = \frac{4\pi \cdot 10^{-7} \cdot 10^{4}}{2\pi \cdot 0.05} = 0.04 \text{ Tesla} \qquad \text{(E.7)}$$

The field calculated is the parallel field effect on a neighboring wire layer, if one exists. This value of 0.04 T is significantly lower effect on the testbed stack because the field effect is parallel rather than 0.2 T perpendicular field of the testbed. Figure E.4 shows total current for a single layer in toroidal stack configuration and compares the result with a testbed stack accounting the magnetic field, and a stack with no magnetic field effects. A toroidal stack greater than a 0.05 m radius has a higher total current than the testbed stacks. This system requires 78 turns, which is less than the 100 turns in the 3 testbed stacks. In conclusion, different HTS wire stack configurations exist that minimize the effect of the magnetic field on performance. The implementation of these stacks remains one of the challenges to future stack designs.

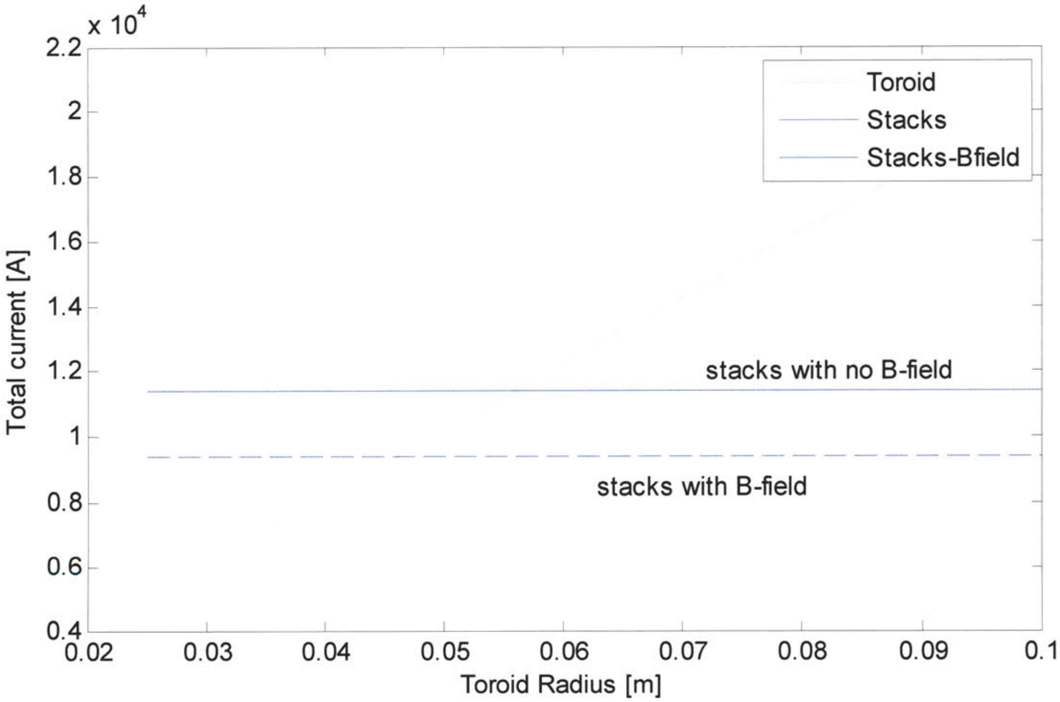

Figure E.4 Total current versus toroidal minor radius for the improved stack design

REFERENCES

[1] Terrestrial Planet Finder webpage, URL: http://planetquest.jpl.nasa.gov/TPF-I/ [cited 9 Sept. 2008].

[2] ESA Darwin mission webpage, URL: http://www.esa.int/esaSC/120382_index_0_m.html [cited 9 Sept. 2008].

[3] Brown, O., and Eremenko, P., "Fractionated Space Architectures: A Vision for Responsive Space," 4th AIAA Responsive Space Conference, Washington, D.C., 2006.

[4] Kong, E. M. C., Kwon, D. W., Schweighart, S. A., Elias, L. M., Sedwick, R. J., Miller, D. W., "Electromagnetic Formation Flight for Multisatellite Arrays," Journal of Spacecraft and Rockets, Vol. 41, No. 4, July-Aug. 2004, p. 659-666.

[5] Kwon, D. W., and Miller, D. W., "Electromagnetic Formation Flight of Satellite Arrays," S.M. Thesis, Space Systems Laboratory, Rept. 2-05, Massachusetts Inst. of Technology, Cambridge, MA, Jan. 2005.

[6] Gardner, P.G., "A Study of Selected Aspects of Electromagnetic Formation Flight," M.S. Thesis, Univ. of Maryland, Sept. 2008.

[7] Elias, L. M., Kwon, D. W., Sedwick, R. J., and Miller, D. W., "Electromagnetic Formation Flight Dynamics including Reaction Wheel Gyroscopic Stiffening Effects," Journal of Guidance, Control, and Dynamics, Vol. 30, No. 2, Mar-Apr. 2007, pp. 499-511.

[8] American superconductor, "Bi-2223 High Strength Wire," URL: http://www.amsuper.com/ [cited 2 Feb. 2007].

[9] Neave, M., "Dynamic and Thermal Control of an Electromagnetic Formation Flight Testbed," S.M. Thesis, Space Systems Laboratory, Rept. 07-05, Massachusetts Inst. of Technology, Cambridge, MA, June 2005.

[10] Schweighart, S. A., "Electromagnetic Formation Flight Dipole Solution Planning," Ph.D. Thesis, Space Systems Laboratory, Rept. 9-05, Massachusetts Inst. of Technology, Cambridge, MA, June 2005.

[11] Ahsun, U., "Dynamics and Control of Electromagnetic Satellite Formations," Ph.D. Thesis, Space Systems Laboratory, Rept. 12-07, Massachusetts Inst. of Technology, Cambridge, MA, June 2007.

[12] Sakaguchi, A., "Micro-Electromagnetic Formation Flight of Satellite Systems," S.M. Thesis, Space Systems Laboratory, Rept. 20-07, Massachusetts Inst. of Technology, Cambridge, MA, June 2007.

[13] Kaneda, R., Hashimoto, T. and Saito, H., "The Relative Position Control in Formation Flying Satellites using Super-Conducting Magnets", 2nd International Symposium on Formation Flying Missions and Technologies, Washington DC, Sept. 14-16, 2004.

[14] Wawrzaszek, R., and Banaszkiewicz, M., "Dynamics of 2 and 3 Satellite Formations Controlled by Electromagnetic Forces," COSPAR 2006, July 2006.

[15] King, L. B., Parker, G. G., Deshmukh, S., and Chong, J.H., "NIAC Phase I Final Report: Spacecraft Formation-Flying using Inter-Vehicle Coulomb Forces," Michigan Technological University, Jan. 2002.

[16] Schwenterly, S.W., Carter, M.D., Chang-Diaz, F.R., and Squire, J.P., "HTS Magnets for Advanced Magnetoplasma Space Propulsion Applications," Cryogenic Engineering Conference/International Cryogenic Materials Conference CEC/ICMC 1999 Symposium, Montreal Quebec, Canada, July 12-16, 1999.

[17] Van Sciver, S.W., "Cryogenic systems for superconducting devices," Physica C 354, 2001, pp. 129 – 135.

[18] Iwasa, Y., "Case Studies in Superconducting Magnets," Plenum Press, 1994.

[19] Flynn, T. M., "Cryogenic Engineering," Marcel Dekker, New York, 2nd Edition, 2005.

[20] Radebaugh, R., "Development of the Pulse Tube Refrigerator as an Efficient and Reliable Cryocooler," Proc. Institute of Refrigeration, 1999-2000.

[21] Kopera, L., Melisek, T., Kovac, P., and Pitel, J., "The Design and Performance of a Bi-2223/Ag Magnet Cooled by a Single-stage Cryocooler," Institute of Physics Publishing, Superconductor Science and Technology, p997-984, June 2005.

[22] Burgoyne, J.W., Daniels, P., Timms, K., Vale, S., "Advances in Superconducting Magnets for Commercial and Industrial Applications," IEEE Transactions on Applied Superconductivity, Vol. 10, Issue 1, March 2000, pp. 703-709.

[23] Spitzer Space Telescope website, URL: http://www.spitzer.caltech.edu/technology/cryostat.shtml [cited 10 Sept. 2008].

[24] Blau, B., Harrison, S.M., Hofer, H., Horvath, I.L., Milward, S.R., Ross, J.S.H., Ting, S.C.C., Ulbricht, J., and Viertel, G., "The Superconducting Magnet System of AMS-02 – A Particle Physics Detector to be Operated on the International Space Station," IEEE Transactions on Applied Superconductivity, Vol. 12, No. 1, March 2002.

[25] James Webb Space Telescope website, URL: http://www.jwst.nasa.gov/ [cited 10 Sept. 2008].

[26] Lallo, M., Bely, P., Cox, C., and Petro, L., "Thermal Considerations for a Passively Cooled NGST," The Next Generation Space Telescope: Science Drivers and Technological Challenges, 34th Liege Astrophysics Colloquim, June 1998, Edited by B. Kaldeich, pp. 307.

[27] Ross, R, "Cryocoolers 12," Springer, 2003.

[28] Keiter, D. E., and Wilson, K. B., "Sunpower Cooling Solutions," Sunpower Inc., Athena, Ohio.

[29] Shirley, K., Banks, S., Boyle, R., and Unger, R., "Design and Qualification of the AMS-02 Flight Cryocoolers," Space Cryogenics Workshop, Colorado Springs, CO, Aug. 25-26, 2005 and KAS and ISB,

"Cryogenic Thermal Performance (EM#1) at 0°C," PowerPoint Presentation slides, NASA Goddard Space Flight Center, Cryogenics and Fluids Branch.

[30] MAST Copernicus website, URL: http://archive.stsci.edu/copernicus/ cited [15 September 2008].

[31] Beam, J., Brennan P. J., and Bello, M., "Design and Performance of a Cryogenic Heat Pipe Experiment (CRYOHP)," AIAA 92-2867, AIAA 27th Thermophysics Conference, Nashville, TN, July 6-8, 1992.

[32] Silverstein, C.C., "Design and Technology of Heat Pipes for Cooling and Heat Exchange," Hemisphere Publishing Corp., 1992.

[33] Silvares, O. M., "Design and Test of a Cryogenic Heat Pipe," S.M. Thesis, Massachusetts Inst. of Technology, Cambridge, MA, Jan. 1973.

[34] Harwell, W., Quadrini, J., Sherman, A., and McIntosh, R., "Cryogenic Heat Pipe Experiment: Flight Performance Onboard a Sounding Rocket," AIAA 10th Thermophysics Conference, AIAA Paper 75-729, Denver, CO, May 27-29, 1975.

[35] Reay, D. A., Kew, P. A., "Heat Pipes," Elsevier, Boston, 5th Edition, 2006.

[36] Peterson, G.P., and Compagna, G.L., "Review of Cryogenic Heat Pipes in Spacecraft Applications," Journal of Spacecraft and Rockets, Vol. 24, No. 2, March – April 1987, pp. 99-100.

[37] Daugherty, M. A., Prenger, F. C., Hill, D. D., Daney, D. E., and Woloshun, K. A., "HTS Current Lead Using a Composite Heat Pipe," IEEE Transactions on Applied Superconductivity, Vol. 5, No. 2, June 1995.

[38] Prenger, F. C., Hill, D. D., Daney, D. E., Daughtery, M. A., Green, G. F., and Roth, E. W., "Nitrogen Heat Pipe for Cryocooler Thermal Shunt," Cryogenic Engineering Conference, Columbus, OH, July 17-21, 1995.

[39] Prager, R.C., Basiulis, A., "The State-of-the-Art of Cryogenic Heat Pipes," AIAA 18th Aerospace Sciences Meeting, AIAA Paper 80-0211, Jan. 14-16, 1980.

[40] Kreeb, H., and Molt, W., "Experimental Evaluation of Cryogenic Heat Pipes with Various Heat Carriers and Capillary Structures," AIAA Paper 78-421.

[41] Couto, P., Mantelli, M. B. H., and Ochterbeck, J. M., "Experimental Analysis of Supercritical Startup of Nitrogen/Stainless Steel Cryogenic Heat Pipes," Journal of Thermophysics and Heat Transfer, Vol. 20. No. 4, Oct. – Dec. 2006, pp. 842-849.

[42] Winglee, R., Ziemba T., et al., "Magnetized Beamed Plasma Propulsion (MagBeam)," NIAC Fellows Meeting Presentation, NASA's Institute for Advanced Concepts, March, 2005.

[43] Kwon, D.W., Sedwick, R.J., de Luis, J., "Low Mass, Low Power Superconducting Magnets for Defensive Counter-Space," DoD STTR proposal, Topic Number AF07-T036, March 2007.

[44] Hoffman, J., Batishchev, O., "Use of Superconducting Magnet Technology for Astronaut Radiation Protection," Final Report for NIAC Phase I Contract CP 04-01, May 2, 2005.

[45] Maignan, M., Brevart, B., Trollier T., Madrangeas V., Zanchi C., "Potentialities of HTS superconductor technology in telecommunication satellites," 1st International Symposium on Potentially Disruptive Technologies and Their Impact in Space Programs, Marseille, France, July 4-6, 2005.

[46] SAFIR mission webpage, URL: http://safir.jpl.nasa.gov/ [cited 12 Sept. 2008].

[47] Leisawitz, D., et al., "The space infrared interferometric telescope (SPIRIT): High-resolution imaging and spectroscopy in the far-infrared," Advances in Space research 40, 2007, pp. 689-703.

[48] Leisawitz, D., "NASA's far-IR/submillimeter roadmap missions: SAFIR and SPECS," Advances in Space research 34, 2004, pp. 631-363.

[49] Hoang, T. T., O'Connell, T. A., Swanson, T. D., Butler, C.D., and Ku, J., "Large Area Cryocooling for Far Infrared Telescopes," Cryogenic Optical Systems and Instruments X, Proceedings of SPIE Vol. 5172, 2003.

[50] Harrison, S., Milward, S., McMahon, R., Bieth, C., Kantas, S., and Pascal S., "High-Temperature Superconducting Magnets for Use in Electron Cyclotron Resonance Ion Sources," IEEE Transactions on Applied Superconductivity, 2005.

[51] Geschiere, A., Willen, D., Piga, E., and Barendregt, P., "HTS cables open the window for large-scale renewables," Journal of Physics: Conference Series 97, 2008.

[52] Demko, J.A., Lue, J.W., Gouge, M.J., Stovall, J.P., Martin, R., Sinha, U., and Hughey, R.L., "Cryogenic System for a High-Temperature Superconducting Power Transmission Cable," Cryogenic Engineering Conference/International Cryogenic Materials Conference CEC/ICMC 1999 Symposium, Montreal Quebec, Canada, July 12-16, 1999.

[53] Schippl, K., "Very Low Loss Cryogenic Envelope for long HTS-Cables," 6th European Conference on Applied Superconductivity, EUCAS 2003, Sorrento, Napoli, Italy, Sept. 14-18, 2003.

[54] Oomen, M.P., van Hasselt, P., Proelss, N., Leghissa, M., Kruip, M., Lister, S., Atkin, A., and Gilgrass, G., "A Pulsed HTS Coil Cooled by Heat Pipes as Part of a Pre-Polarized Magnet System," IEEE Transactions on Applied Superconductivity, Vol. 16, No. 2, June 2006.

[55] Wertz, J. R., and Larson, W. J., "Space Mission Analysis and Design", 3rd Edition, Microcosm Press, 1999.

[56] Barron, R. F., "Cryogenic Heat Transfer," Taylor & Francis, 1999.

[57] Gilmore, D. G., "Satellite Thermal Control Handbook," Aerospace Corporation Press, El Segunda, California, 1994.

[58] Siegel, R., "Thermal Radiation Heat Transfer," Taylor and Francis, 4th Edition, 2001.

[59] Sunpower Inc., Website, URL: http://www.sunpower.com/ cited [15 September 2008].

[60] Fortescue, P., Stark, J., and Swinerd, G., "Spacecraft Systems Engineering," Wiley, 3rd Edition, 2003.

[61] Mcmaster-Carr, Catalog 114, URL: http://www.mcmaster.com

[62] Jaluria, Y., and Torrance, K. E., "Computational Heat Transfer," Taylor and Francis, New York, 2nd Edition, 2003.

[63] Sinda/G User's Guide, Ver 2.4, Network Anaylsis, Inc., Feb. 2005.

[64] Lienhard, J. H., "A Heat Transfer Textbook," Phlogiston Press, Cambridge, Massachusetts, 3rd Edition, 2006.

[65] Frederking, T. H.K. and Yuan, S. W.K., "Cryogenics: Low Temperature Engineering and Applied Sciences," Yutopian Enterprise, Inc.

[66] Edmund Scientific, URL: http://www.scientificsonline.com/ [cited 25 September 2008].

[67] Mills, A.F., "Heat and Mass Transfer," Prentice Hall, New Jersey, 2nd Edition, 1999.

[68] TWP Inc., "Stainless Steel Mesh," http://www.twpinc.com [cited 8 August 2008].

[69] Chi, S.W., "Heat Pipe Theory and Practice: A Sourcebook," McGraw-Hill, 1976.

[70] Collier, J. G., and Thome, J. R., "Convective Boiling and Condensation," Clarendon Press, Oxford, 3rd Edition, 1996.

[71] Mills, A.F., "Heat and Mass Transfer," Prentice Hall, New Jersey, 2nd Edition, 1999.

[72] Peterson, George P., "An Introduction to Heat Pipes: Modeling, Testing, and Applications," John Wiley & Sons, Inc., New York, 1994.

[73] Sonntag, R. E., Borgnakke, C., and van Wylen, G. J., "Fundamentals of Thermodynamics," Wiley, 5th Ed., 1998.

[74] Paul Bauer, MIT Department of Aeronautics & Astronautics, Research Specialist, [private communication, 2007].

[75] Kurt J. Lesker Company, URL: http://www.lesker.com [cited 15 October 2008].

[76] Smithells, C.J., and Ransley, C.E., "The Diffusion of Gases through Metals," Proceedings of the Royal Society of London, Series A, Mathematical and Physical Sciences," Vol. 150, No. 869, May 1, 1935.

[77] Faghri, A., "Heat Pipe Science and Technology," Taylor & Francis, 1995.

[78] Ekin, J. W., “Experimental Techniques for Low-Temperature Measurements: Cryostat Design, Material Properties, and Superconductor Critical-Current Testing,” Oxford University Press, 2006.

[79] CRC Handbook of Chemistry and Physics, 65th Edition, CRC Press, Inc., Boca Raton, FL, pp. F-114 – F-120, 1984-85.

[80] Bickford, W. B., “Mechanics of Solids: Concepts and Applications,” Irwin, Inc., 1993.

[81] Richardson, R. C., Smith, E. N., “Experimental Techniques in Condensed Matter Physics at Low Temperatures,” Perseus Books, April 1988.

[82] Emerson & Cuming: A National Starch & Chemical Company, Stycast 1266 A/B, Two Component, Low Viscosity, Epoxy Encapsulant

[83] Microcosm, Inc., “Magnetic Torquers for Spacecraft Attitue Control,” URL: http://www.smad.com/analysis/torquers.pdf [cited 12 September 2008], further information also available at Zarm Technik GmbH.

[84] Incropera, F. P., Dewitt, D. P., Bergman, T.L., and Lavine, A.S., “Fundamentals of Heat and Mass Transfer,” John Wiley and Sons, 6th Edition, 2007.

[85] Hildebrand, F. B., “Advanced Calculus for Applications,” Prentice-Hall, Inc., New Jersey 2nd Edition, 1976

[86] Ozisik, M. N., “Heat Conduction,” John Wiley & Sons, Inc., 2nd Edition, 1993.

[87] Carslaw, H.S., and Jaeger, J.C., “Conduction of Heat in Solids,” Clarendon Press, Oxford, 1986.

[88] Israelachvili, J. N., “Intermolecular and Surface Forces,” Academic Press, 1991.

[89] Zahn, M., “Electromagnetic Field Theory: a problem solving approach,” Kreiger Publishing Company, Malabar, Fl, 1979.